Experimental Studies and Parametric Investigation on Laser Directed Energy Deposition based Additive Manufacturing of Hastelloy-X Thin Walls and Bulk Structures

By

Jinoop A N

ENGG03201604001

Raja Ramanna Centre for Advanced Technology, Indore

A thesis submitted to the

Board of Studies in Engineering Sciences

In partial fulfillment of requirements

for the Degree of

DOCTOR OF PHILOSOPHY

of

HOMI BHABHA NATIONAL INSTITUTE

May, 2021

Homi Bhabha National Institute

Recommendations of the Viva Voce Committee

As members of the Viva Voce Committee, we certify that we have read the dissertation prepared by **Mr. Jinoop A N** entitled "Experimental **Studies and Parametric Investigation on Laser Directed Energy Deposition based Additive Manufacturing of Hastelloy-X Thin Walls and Bulk Structures**" and recommend that it may be accepted as fulfilling the thesis requirement for the award of Degree of Doctor of Philosophy.

Prof. J Chattopadhyay, BARC	Chairman	J. Chattopadhyay 27/5/2021
Dr. C P Paul, RRCAT	Guide / Convener	27/05/2021
Prof. Nilesh J Vasa, IIT Madras	Examiner	N. J. Vasa 27/05/2021
Prof. R Balasubramaniam, BARC	Member	27/5/21
Dr. I A Palani, IIT Indore	Member	27/5/2021
Dr. Prabhat Kumar Gupta, RRCAT	Member	27/5/2021

Final approval and acceptance of this thesis is contingent upon the candidate's submission of the final copies of the thesis to HBNI.

I hereby certify that I have read this thesis prepared under my direction and recommend that it may be accepted as fulfilling the thesis requirement.

Date: 27.05.2021

Place: INDORE

27/05/2021

Signature

Guide

STATEMENT BY AUTHOR

This dissertation has been submitted in partial fulfillment of requirements for an advanced degree at Homi Bhabha National Institute (HBNI) and is deposited in the Library to be made available to borrowers under rules of the HBNI.

Brief quotations from this dissertation are allowable without special permission, provided that accurate acknowledgement of source is made. Requests for permission for extended quotation from or reproduction of this manuscript in whole or in part may be granted by the Competent Authority of HBNI when in his or her judgment the proposed use of the material is in the interests of scholarship. In all other instances, however, permission must be obtained from the author.

Jinoop A N

DECLARATION

I, hereby declare that the investigation presented in the thesis has been carried out by me. The work is original and has not been submitted earlier as a whole or in part for a degree / diploma at this or any other Institution / University.

Jinoop A N

List of Publications arising from the thesis

I Journal

Published and Accepted

1. "Laser Assisted Direct Energy Deposition of Hastelloy-X", A N Jinoop, C P Paul, K S Bindra, *Optics and Laser Technology*, **2019,** *109*, 14-19
2. "Effect of post heat-treatment on the microstructure and mechanical properties of Hastelloy-X structures manufactured by laser based Directed Energy Deposition", A N Jinoop, J Denny, C P Paul, J G Kumar, K S Bindra, *Journal of Alloys and Compounds*, **2019**, *797*, 399-412.
3. "Laser Assisted Directed Energy Deposition of Nickel Super Alloys: A Review", A N Jinoop, C P Paul, K S Bindra, *Journal of Materials: Design and Applications, Proc. of Institute of Mechanical Engineers.,* **2019**, *233*, 2376–2400.
4. "Laser Additive Manufacturing using directed energy deposition of Inconel-718 wall structures with tailored characteristics", A N Jinoop, C P Paul, S K Mishra, K S Bindra, *Vacuum*, **2019**, *166*, 270-278
5. "Hot deformation behavior of Hast-X preforms built using directed energy deposition based laser additive manufacturing", A N Jinoop, V A Kumar, C P Paul, R Ranjan, K S Bindra, *Materials Letters*, **2020**, *270*, 127737.
6. "Laser Additive Manufacturing of Hastelloy-X Thin Walls using Directed Energy Deposition: Parametric Investigation and Multi-Objective Analysis", A N Jinoop, C P Paul, J Denny, S K Nayak, P Vamsi Krishna, K S Bindra, *Lasers in Engineering*, **2020**, *46*, 15-34.
7. "Effect of Laser Energy per unit Powder Feed on Hastelloy-X Walls built by Laser Directed Energy Deposition based Additive Manufacturing", A N Jinoop, C P Paul, S K Nayak, J Ganesh Kumar, K S Bindra, *Optics & Laser Technology,* **2021***, 138,* 106845.
8. "Influence of Heat Treatment on the Microstructure Evolution and Elevated Temperature Mechanical Properties of Hastelloy-X Processed by Laser Directed Energy Deposition", A N Jinoop, C P Paul, J Ganesh Kumar, V Anilkumar, R Singh, S Rao, K S Bindra, *Journal of Alloys and Compounds,* **2021***,* 66, 70-80.

To be communicated

9. "Elucidating the Effect of Sequential Layer-by-layer Laser Directed Energy Deposition and Remelting of Hastelloy-X Bulk Structures", A N Jinoop, C P Paul, J Ganesh Kumar, R Singh, A Sagdeo, K S Bindra, *Journal of Manufacturing Processes.*
10. "Effect of interlayer delay on Hastelloy-X Walls built by Laser Directed Energy Deposition based Additive Manufacturing", A N Jinoop, C P Paul, K S Bindra, *International Journal of Advanced Manufacturing Technology*

II Chapters in books and lectures notes

1. A N Jinoop, C P Paul, K S Bindra, "Advancements in Post-Processing of Metal Additive Manufactured Components", Manufacturing and Industrial Engineering: Theoretical and Advanced Technologies, Eds. Pankaj Agarwal, Lokesh Bajpai, Chandra Pal Singh, Kapil Gupta, J Paulo Davim, CRC Press (Accepted).
2. C P Paul, A N Jinoop, K S Bindra (2018), "Metal Additive Manufacturing using Lasers", in "Additive Manufacturing: Applications and Innovations", Eds. Rupinder Singh and J. Paulo Davim, pp. 37 – 94, CRC Press, Boca Raton.

III Conferences

1. A.N. Jinoop, C. P. Paul, K. S. Bindra, An Innovative Approach for Directed Energy Deposition based Laser 3D Printing of Metallic Compact Heat Exchangers, National Aerospace Manufacturing Seminar, NAMS 2019, Dec 06 – 07, 2019, Trivandrum (Best Paper Award)
2. Jinoop A.N., Paul C.P., Nayak S.K., Kumar H., Bindra K.S., Effect of Scan Strategy on the Geometry of Laser Additive Manufactured Wall Structures, Proceedings of International Conference on Precision, Meso, Micro and Nano Engineering (COPEN 2019), December 12-14, 2019, IIT Indore.
3. A N Jinoop, S. Yadav, C P Paul, U Kumar, K S Bindra (2018) Investigating fabrication of Overhang Walls using Direct Energy Deposition based Laser Additive Manufacturing, National Laser Symposium-27, RRCAT, Indore.
4. A N Jinoop, C P Paul, K S Bindra (2017), Parametric Study on Laser Additive Manufacturing and Subsequent Post Processing of Inconel 718 Thin Walled Structures, ASME 2017 Gas Turbine India Conference, Bangalore.
5. A N Jinoop, C. P. Paul, C H Premsingh, U Kumar, K. S. Bindra (2018), Laser Additive Manufacturing using Hast-X: Process Development and Characterization, RSM-HBNI-2018 on Materials Science and Engineering of Nuclear Materials, IGCAR, Kalpakkam.

Other publications during the PhD work

1. "Experimental Studies on Laser Additive Manufacturing of Inconel-625 Structures using Powder Bed Fusion at 100 µm Layer Thickness", S K Nayak, S K Mishra, A N Jinoop**,** C P Paul, K S Bindra, *Journal of Materials Engineering and Performance,* **2020**, *29*,7636–7647.
2. "Laser Directed Energy Deposition based Additive Manufacturing of Copper: Process Development and Material Characterizations", S Yadav, C P Paul, A N Jinoop, A K Rai, K S Bindra, *Journal of Manufacturing Processes*, **2020**, *58*, 984-997.
3. "Investigating Build Geometry Characteristics during Laser Directed Energy Deposition based Additive Manufacturing", A C Paul, A N Jinoop, C P Paul, P Deogiri, K S Bindra, *Journal of Laser Applications*, **2020**, *32*, 042002.
4. "Effect of Heat-Treatment on the Microstructure, Mechanical Properties and Corrosion Behaviour of SS 316 Structures Built by Laser Directed Energy Deposition Based Additive Manufacturing", K Benarji, Y Ravi Kumar, A N Jinoop, C P Paul, K S Bindra, *Metals and Materials International*, **2020**, DOI: 10.1007/s12540-020-00838-y
5. "Fatigue Crack Propagation Behaviour of Inconel 718 Structures Built using Directed Energy Deposition based Laser Additive Manufacturing", J Denny, A N Jinoop, C P Paul, R Singh, K S Bindra, *Materials Letters*, **2020**, *276*, 128241.

6. “Parametric Investigation and Characterization of Laser Directed Energy Deposited Copper-Nickel Graded Layer”, S Yadav, A N Jinoop**,** N Sinha, C P Paul, K S Bindra, *International Journal of Advanced Manufacturing Technology*, **2020**,*108*, 3779–3791
7. “Effect of energy density on laser powder bed fusion built single tracks and thin wall structures with 100 µm preplaced powder layer thickness”, S K Nayak, S K Mishra, C P Paul, A N Jinoop, K.S. Bindra, *Optics & Laser Technology*, **2020**, *125*,106016.
8. “Experimental Investigation on Laser Directed Energy Deposition of Functionally Graded Layers of Ni-Cr-B-Si and SS316L”, S M Banait, C P Paul, A N Jinoop, H Kumar, R S Pawade, K S Bindra, *Optics & Laser Technology*, **2020**,*121*, 105787.
9. “Parametric investigation and characterization on SS316 built by laser-assisted directed energy deposition”, K Benarji, Y Ravi Kumar, C P Paul, A N Jinoop, K S Bindra, *Proceedings of the Institution of Mechanical Engineers, Part L: Journal of Materials: Design and Applications*, **2020**, *234*, 452-466.
10. “Post-processing of Laser Additive Manufactured Inconel 718 using Laser Shock Peening”, A N Jinoop, S Kanmani Subbu, C P Paul, I A Palani, *International Journal of Precision Engineering and Manufacturing*, **2019**, *20*, 1621–1628.

Jinoop A N

Dedicated to Family and Teachers

ACKNOWLEDGEMENTS

First and foremost, I would like to express immense gratitude to my supervisor *Prof. C. P. Paul*. It has been a great learning experience working with him and a lot of credit for my achievements and accomplishments goes to him. His constant support and guidance have always motivated me to work and aided me to channelize my energy in the correct path. More than anything, working together as a team with him has been intellectually enriching, inspiring, and a joyful experience. I hope to carry this learning for myself and for the generations succeeding mine. His multitasking and management skills are something I would like to learn and carry on in the future. I learnt a lot of new things, both in career as well as life, during the time I spent with him. He is a mentor who is true to his position.

I am very grateful to the doctoral committee members *Dr. J. Chattopadhyay, Dr. R. Balasubramaniam, Dr. I. A. Palani* and *Dr. P. K. Gupta* for their timely inputs and suggestions. I am also thankful to the former doctoral committee chairman *Dr. G. R. Reddy* for his suggestions and advice. I acknowledge the support offered by *Dr. K. S. Bindra*, Associate Director Laser Group, RRCAT and Head Laser Technology Division for his continuous support. I am grateful to *Mr. S. V. Nakhe*, Director, Laser Group for encouragement and support. I would like to thank *Dr. Arup Banerjee*, Dean Academic HBNI-RRCAT for his advices and instant help during my PhD tenure. Thanks to the financial assistance from Department of Atomic Energy, RRCAT and HBNI Mumbai.

I am grateful to *Dr. S. Kanmani Subbu*, my M.Tech. supervisor for motivating me to do PhD and sowing the first seeds of research on me. I am really thankful to many researchers and scholars who have directly or indirectly helped me in this journey. I acknowledge the support of members of Laser Additive Manufacturing Lab, RRCAT for their kind support throughout this journey. Thanks are due to *Mr. S. K. Mishra, Mr. Upendra Kumar, Mr, C. H. Premsingh, Mr. C. S. Mandloi, Mr. Anil Adbol, Mr. Sokhen Tudu* and *Mr. Lalit* of RRCAT for their technical assistance during the course of work. I am also grateful to *Dr. A. K. Rai* and *Dr. Atul Kumar* for their suggestions and advices in metallurgy and modeling, respectively. I am also thankful to *Mr. S. K. Nayak, Mr. Sunil Yadav* and *Mr. Dileep Kumar* for providing useful insights into my research, especially the late-night discussions. I am thankful to my senior *Dr. S. Shiva* (Assistant Professor, IIT Jammu) and *Dr. S. S. Mani Prabhu* (Post-doctoral fellow, IIT Delhi) for their advice and suggestions. I am obliged to *Dr. V. Anilkumar and team*, VSSC, Trivandrum and *Dr. J. Ganesh Kumar*, IGCAR Kalpakkam for their support during the course

of work. I am really thankful to *Mr. G. V. Kane, Dr. (Mrs.) A. Sagdeo, Dr. (Mrs.) P. Gupta, Mrs. M. Baral, Mrs. R. Singh, Mr. A. Bose, Mrs. S. Bhartiya, Mrs. P. Pokhriyal, Mr. V. Bharadwaj* and *Mr. A. Chaturvedi* of RRCAT for allowing me to use characterization equipment for this research work. I am thankful to *Prof. Sushil Mishra* and *Mr. Deepak Soman* for EBSD characterizations at IIT Bombay. Thanks are also due to the past scholars at our lab, *Mr. S. Saxena, Mr. Denny John, Ms. S. Banait, Mr Derek John, Mr. Anshu Sahu, Ms. Nidhi, Mr. Diljith P. K., Mr. B. Srinivasulu* and *Ms. Poonam Deshmukh* for their help during the course of work. Thanks to the collaborators *Dr. S. Bontha* and *Mr. J. Chaurasia*, NIT Surathkal; *Dr. Y. Ravikumar* and *Mr. K. Benarji*, NIT Warangal; *Dr. N. Sinha*, IIT Kanpur. I am also thankful to my batch mates at RRCAT, all junior and senior friends for the joyful moments at RRCAT Hostel.

On a special note, I would like to acknowledge the affection, support and moral encouragement provided by my father *Mr. A. P. Narayanan* and mother *Mrs. Rajamoni K.* I am always thankful for their prayers and support and for listening to all my issues during my tough phase. Their prayers helped me to move forward in life. I am also thankful to my in-laws, *Mr. A. M. Mohanan Nair* and *Mrs. S. Leela* for their continuous support and prayers. They always motivated me to do better and kept belief in me. Thanks are also due to my sister *Mrs. Jini Rengith* and brother-in- laws *Mr. Rengith Menon* and *Mr. Arun M.L.* for their motivation and support during the course of my research.

Last but not the least, I am eternally grateful to my wife *Mrs. Parvathy M L* for travelling with me throughout this research journey. I thank her for the indefatigable support on personal front, without which it would not have been possible to complete this research work. Though I spent most of my time in my research being away from her, she continuously supported me during my hard days and stayed with me in achieving my goal. Her prayers and motivation always helped me to come back to research with a fresh mind after tough and low periods.

Jinoop A N

CONTENTS

LIST OF FIGURES

LIST OF TABLES

Chapter 9 : Conclusions and Future Scope

9.1 Conclusions

The present research work comprehends and contributes to the existing understanding on the Laser Directed Energy Deposition (LDED) of Hast-X structures from single tracks to multiple overlapped and multi-layer tracks under different process conditions yielding thin walls and bulk structures in terms of processing, geometry, microstructural and mechanical characteristics. It provides insights on to the effect of in-situ treatments and ex-situ post-processing on the behaviour of LDED built Hast-X components. The work also contributes to the development of process methodology for building Printed Circuit Heat Exchangers (PCHEs) using LDED. On the basis of the research work, the followings are the conclusions:

a) The geometry of LDED built single tracks show that the track width and track height increase with an increase in laser power and powder feed rate, while the same effect in track width and track height is observed with the reduction in scan speed. Laser power is found to be dominant process parameter for track width, while powder feed rate is the significant process parameter for controlling track height. The developed analytical modelling confirms the parametric dependence of track width and track height.
b) The identified processing window indicates that an optimum value of Laser Energy per unit Powder Feed (LEPF) is mandatory for defect free deposition of Hast-X. For higher values of LEPF, cracks are observed primarily due to combination of higher thermal stresses and elemental segregations. For lower values of LEPF, the deposits are found to be discontinuous primarily due to unavailability of sufficient laser energy. The optimum value of LEPF for Hast-X is identified in the range of 8.2 - 13.2 kJ/g for continuous and crack free deposition. Within the process window, the area fraction density of continuous tracks

is found to be > 99.5% and the porosity increases with a reduction in LEPF and increase in scan speed. The process parameter combination yielding higher area fraction density and build rate are deployed for overlapped multi-track deposition.Defect-free deposition in the micro scale with fine cellular and dendritic grain structure is achieved.

c) One of the exciting applications of LDED is the development of wall structures and the properties of the wall structures can be tailored by varying the thermal conditions, which can be achieved by depositing at different process parameters or providing interlayer delay between layers using idle time period. The effect of LEPF on the geometry of the wall structures shows that the variation in wall height increases with an increase in LEPF, while the variation in wall width decreases with an increase in LEPF. It is also observed that the average wall height decreases and average wall width increases with an increase in LEPF due to increase in the outward flow of melt pool. The microstructural studies show that grain structure is a mix of cellular and dendritic growth within the range of LEPF used for the study. The size of cellular/dendritic growth increases slightly with an increase in LEPF due to reduction in the cooling rate. Investigations on the mechanical properties illustrates that the micro-hardness, yield strength and ultimate strength decreases slightly with an increase in LEPF, with higher values of yield strength and micro-hardness as compared to conventional wrought sample. Numerical simulation aids to elucidate the above results and show that the preheat temperature on the previously built layer increases with an increase in LEPF.

d) In case of walls built with different interlayer delay, it is observed that the average wall height increases and average wall width decreases with an increase in the interlayer delay period due to reduction in the outward flow of melt pool. The cellular and dendritic growth is observed at all conditions and it is observed that size of growth decreases slightly with an increase in the interlayer delay period primarily due to higher cooling rate. In addition,

the studies on mechanical properties show that strength values increase with an increase in interlayer delay supporting the observations from the microstructural studies. Numerical simulation aids to the explanation of the above results and shows that the pre-heat temperature on the previously built layer reduces with an increase in interlayer delay leading to an increase in cooling rate.

e) Bulk structures are integral for building dense Hast-X engineering components using LDED. Thus built bulk structures show few pores at isolated locations (relative density ~ 99.5%), which are a mix of lack of fusion porosity and gas porosity. The microstructural analysis shows the presence of cellular and dendritic growth, with an increase in the size of growth from the bottom layer to the top layer owing to reduction in cooling rate as the deposition moves from bottom layer to top layer. The elemental segregations of C, Si and Mo are observed in the samples due to non-equilibrium solidification in LDED and the presence of Mo based carbides are also observed, which are formed due to higher number of thermal cycling experienced by the material during the layer-by-layer deposition. The orientation of the grain growth is largely random orientation with some preferred texture along the (100) plane and the grain size is observed to be finer that the conventional wrought samples. Surface analysis of the built structure show that the residual stress on the sample surface is primarily tensile and the higher surface roughness on the as-built surface is attributed to the presence of partially melted powders on the sample surface. The micro-hardness, yield strength and ultimate tensile strength of LDED built Hast-X are higher than that of conventionally processed wrought samples and wall structures deposited at same process parameters. Further, mechanical properties measured at elevated temperature show that the yield strength and ultimate strength decreased by 33% and 32%, respectively with an increase in test temperature to 873 K. The yield strength of LDED samples is greater

than the conventional counterparts at all temperature conditions mainly due to higher dislocation densities in LDED samples.

f) LDED built bulk components are observed to have higher surface roughness, localized lack of fusion porosity and non-equilibrium microstructure. Thus, LDED built structures are subjected to SLLR (a process involving laser remelting after LDED of each layer) to improve the density and surface quality; and solution treatment to achieve uniform microstructure. It is observed that relative density of LDED built Hast-X structures increased with SLLR and the lack of fusion porosity disappeared primarily due to localized material re-distribution during SLLR. The average surface roughness reduced by 71.5% after SLLR due to melting of partially melted powders observed on as-built LDED surface. The cellular and dendritic growth of LDED samples show a little refinement with SLLR. Presence of random grain orientation is observed after SLLR due to re-distribution of thermal history generated during LDED. A small increase in the microhardness by 12% and yield strength by 7% is observed after SLLR due to relatively finer dendritic microstructures in SLLR samples.

g) Microstructural and mechanical studies on the solution treated Hast-X structures show the presence of recrystallized and coarsened equiaxed grains with random orientation and significant reduction in segregation and carbide precipitation. Reduction in the average micro-hardness is observed after solution treatment and the hardness values are found to be closer to micro-hardness of conventional wrought Hast-X. The yield strength of solution treated sample is similar to the yield strength of conventionally wrought Hast-X taken from literature at all test temperatures from room temperature to 873 K, which can be due to coarsened grain structure and reduction in the dislocation density. It is observed that the yield strength and ultimate strength of the solution treated samples reduced by 27% and 25%, respectively with an increase in test temperature from room temperature to 873 K.

h) One of the potential applications of Hast-X is the development of PCHE. LDED of PCHE is challenging due to the difficulty in building completely overhang parts using the generic 3-axis configuration. To achieve the same, overhang walls are built by varying the distance between the laser spot centre and vertical shift of the co-axial nozzle after each layer. The maximum lateral shift possible for fabricating overhang structures without failure is found to be 15%. PCHE channels built at different combination of process parameter show that the process parameter selection, channel size and overlap percentage between layers influences the quality of channels. Further, PCHE is built using a combination of straight walls, overhang walls and bulk structures using the acquired know-how from the above comprehensive studies.

9.2 Future Scope

The future scope of the work includes the following:

a) The fatigue, corrosion and oxidation behaviour of LDED built Hast-X in as-built and post-processed conditions may be explored.
b) Effect of LEPF and preheat on the properties of LDED built bulk Hast-X structures may be analyzed.
c) Effect of different SLLR parameters and solution treatment temperatures on LDED built bulk structures may be investigated.
d) Studies may also be carried out on the development of PCHEs for design duty conditions using LDED and its performance evaluation.
e) Studies may be carried out to explore the optimization of machining parameters for LDED built Hast-X as it can pave a path for hybrid LDED process.
f) Studies on the effect of slurry-based machining may be carried to out to improve the surface quality of LDED built channels.
g) Uncertainty analysis of track geometry can be performed.

h) Effect of channel surface roughness on the performance of the PCHE can be carried out.

i) Accelerated testing of LDED built Hast-X can be performed.

SUMMARY

Laser Additive Manufacturing (LAM) is one of the advanced manufacturing technologies for building near-net-shaped engineering components in a layer-by-layer fashion using high power lasers as an energy source. LAM shows a rising demand in aerospace and power sector to build high-performance components subjected to extreme duty conditions. Hastelloy-X (Hast-X) is one of the nickel-based superalloys suitable for high-temperature applications due to the appropriate blend of high-temperature strength, toughness and resistance to degradation in a corrosive or oxidizing environment. The applications of Hast-X include components for various advanced power generation cycles, combustion zone components in gas turbine engines and intermediate heat exchanger for high temperature reactor applications. Laser Directed Energy Deposition (LDED) based LAM technique of Hast-X has potential for building components used in aerospace and power sector. Literature survey indicates that there are no comprehensive studies available in public domain on LDED of Hast-X. The present thesis is focused on the engagement of the versatile LDED to deposit defect free Hast-X thin-wall and bulk structures, and comprehensively investigate their behaviour at different process and service conditions experimentally.

Single tracks being the basic building unit in LDED, investigations on single tracks are carried out to evaluate the effect of process parameters on geometry and build quality. The geometrical analysis show that the track width and track height increase with an increase in laser power and powder feed rate, while the similar effect in track width and track height is observed with the reduction in scan speed. A simple analytical model is developed for faster predictions of track geometry and it finds good match with the experimental results. The effect of process parameters on track quality shows that an optimum value of Laser Energy per unit Powder Feed (LEPF) in the range of 8.2 - 13.2 kJ/g for Hast-X is required for continuous and crack free deposition for scan speed 0.3 - 0.7 m/min. The reasons for discontinuous deposits at lower LEPF are attributed to lower energy available for deposition, while the cracking at higher LEPF

is primarily due to combined effect of higher thermal stresses and elemental segregations. The process parameter combination yielding higher area fraction density and build rate is selected from the identified process window for overlapped multi-track deposition and it is observed that the deposition is defect-free at the micron scale with fine cellular and dendritic grain structure.

Wall structures deposited using different values of LEPF and interlayer delay period are studied using geometrical, microstructural and mechanical characterisations. The variations in the wall height and wall width at different LEPF values are investigated and it reveals that the variation in wall height increases with an increase in LEPF, while the variation in wall width decreases with an increase in LEPF. The microstructural studies show that grain structure is a mix of cellular and dendritic growth with small increase in the grain size with an increase in LEPF. Investigations on the mechanical properties illustrates that there is a small decrease in the micro-hardness, yield strength and ultimate strength with an increase in LEPF. The comparison with conventional wrought sample show that LDED built walls have higher values of yield strength and micro-hardness. For walls built at different interlayer delay, it is observed that the average wall height increases and average wall width decreases with an increase in the interlayer delay period. The cellular and dendritic growth is observed with smaller grain growth with an increase in the interlayer delay period. In addition, the studies on the mechanical properties shows that the strength values increase with an increase in interlayer delay confirming the observations made during the microstructural studies.

Qualification of bulk structures is required for building dense Hast-X engineering components using LDED and the relative density is found to be ~ 99.5% at identified parameters. The microstructure of Hast-X bulk structure shows the presence of fine cellular and dendritic growth having largely random orientation with some preferred texture along the (100) plane. The elemental segregations of C, Si and Mo and presence of Mo based carbides are observed.

The surface of the built structure is characterized by tensile residual stress and higher surface roughness. The mechanical properties of the bulk structures at room temperature are higher than that of conventionally processed wrought samples and the wall structures deposited at same process parameters. The evaluation of mechanical properties at elevated temperature shows a gradual reduction in strength with higher yield strength at all temperature conditions as compared to its conventional counterparts. Studies on the effect of Sequential Layer by Layer Remelting (SLLR) on LDED built bulk components shows improvement in relative density, reduction in surface roughness and the presence of relatively refined cellular and dendritic growth. There is a small increase in microhardness and yield strength with the deployment of SLLR. Microstructural and mechanical studies on the solution treated Hast-X structures show the presence of recrystallized and coarsened equiaxed grains with random orientation. A significant reduction in segregation and carbide precipitation is also observed. There is a reduction in the average micro-hardness after solution treatment and the hardness values are found to be closer to micro-hardness of conventional wrought Hast-X. The yield strength of solution treated sample is similar to the yield strength of conventionally wrought Hast-X taken from literature at all test temperatures from room temperature to 873 K.

One of the potential applications of Hast-X is the development of Printed Circuit Heat Exchanger, generally used in advanced power sectors. LDED of PCHE is challenging due to the difficulty in building overhang geometries. The overhang tracks are built to make overhang structure by varying the lateral shift and vertical shift for each layer. PCHE channels are investigated at different combination of process parameter to identify the optimum process window. Subsequently, PCHE is fabricated using a combination of straight walls, overhang walls and bulk structures employing the acquired know-how from the above comprehensive studies.

Chapter 1 : Introduction & Motivation

1.1 Background

Manufacturing is the process of converting raw materials, parts or components to a desired final product that satisfies a customer's expectations or specifications. Manufacturing can be primarily classified into three different categories, like - Formative Manufacturing, Subtractive Manufacturing and Additive Manufacturing [1]. Formative manufacturing refers to the process by which components in the desired shape and size are built by changing the shape of the raw material. The examples of formative manufacturing processes include die forging, injection moulding, etc. Subtractive manufacturing is the process by which desired components are built by removing material from the bulk raw material, like - milling, drilling, turning, etc. [2]. Traditionally, the manufacturing sector is dominated by subtractive and formative manufacturing techniques. However, the continuously increasing demand for high-performance components in engineering, medical, automotive and other sectors necessitated complex-shaped components (such as components having undercuts, lattice structures, overhangs, etc.) with high strength to weight ratio and motivated engineers to use advanced manufacturing processes. In addition, machining generates material wastage, which leads to high buy-to-fly ratio[3]. The buy-to-fly ratio is defined as the ratio between the weight of the raw material purchased to the weight of the final part[4]. Typically, the buy-to-fly ratio in conventional machining is close to 10[5][6], which means that only 10% of the raw material is used for developing the component and the remaining 90% is scrapped. Conventional manufacturing also increases the lead time due to the time required for procurement of material and tool. Further, the limited capabilities of conventional manufacturing processes to build

multi-material components or join metallurgically incompatible materials also attracted the deployment of advanced manufacturing processes.

Additive Manufacturing (AM), a "process of joining materials to make parts from 3D model data, usually layer upon layer, as opposed to subtractive manufacturing and formative manufacturing methodologies" [7], introduced by Charles Chuck Hull in the year 1986 paved a way to solve most of the above issues associated with the conventional manufacturing processes. AM was initially used for fabricating models and prototypes for various industrial and academic applications. However, with the advent of technology, AM progressed to become a "true manufacturing platform that develops the form, fit and function of a component"[8]. AM is one of the disruptive technologies, which is being used to build highly complex structures by exploiting its design freedom at reduced time and cost. AM is also attractive due to its ability to build highly customized components paving the way for the fabrication of "mass customized" products[9]. AM reduces material wastage[10], lead time [11] and product development cycle [12]and also provides manufacturing flexibility.

Figure 1.1 presents a general product development cycle using conventional manufacturing and AM. Generally, the product development cycle involves three stages, i.e., design, production and application. Figure 1.1a presents the typical product development cycle used in conventional manufacturing. The design stage comprises of synthesis, design analysis, documentation and drawing. In the design stage, design need is taken from various sources such as market survey reports and feedbacks. In this stage, several concepts are identified and are analysed in the next stage. The analysis stage involves design analysis, optimization, evaluation and communication. By the end of the analysis stage, the developed design is completely examined to assess its performance. The final design obtained at the end of this stage will be sent for documentation and drawing. The second stage, i.e., the production stage

involves planning, tool procurement, raw material procurement and machine code generation for manufacturing. At the end of the second stage, the product is sent for manufacturing as per the design and production guidelines. Thus, the manufactured product enters into the third stage, i.e., the application stage, where the quality of the product is checked. If the product qualifies the quality checks, it will be sent for packaging, which is followed by shipping and delivery. After delivery, the customer feedback is taken as an input to synthesis stage and the process continues.

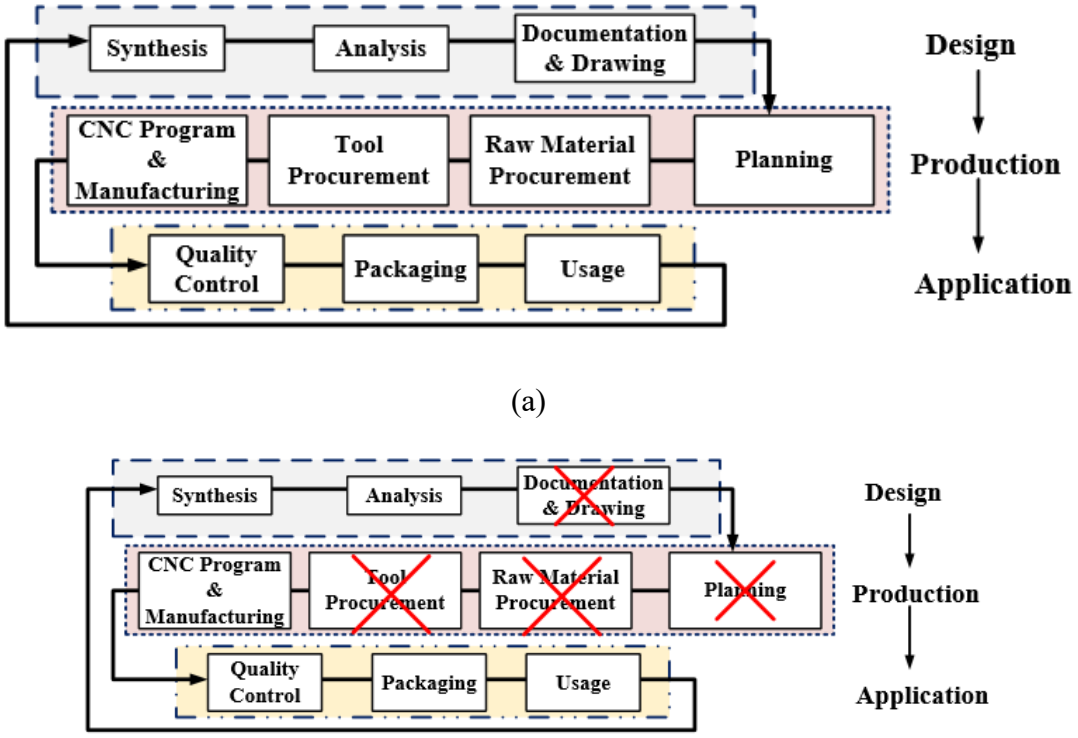

Figure 1.1: Typical Product Development Cycle (a) conventional (b) Additive Manufacturing [13]

Figure 1.1(b) presents the product development cycle with the implementation of AM. By using AM, some of the stages in the product development cycle are either completely or partially removed. The model made at synthesis and analysis stage contains all the information and does not need separate efforts for preparation of general layout and detailed drawings, fabrication

procedure and stage-wise precaution document. Hence, the model is directly used as reference document removing the documentation and drawing stage. Since AM system is used for building the component, there is no need of further process planning and machine/ equipment allocation. The planning for building component is automatically carried out by the AM system itself. In most cases, the raw material is predefined based on the component application. As AM uses shapeless raw material, the raw material procurement can be initiated before the full design is finalised. This facilitates the initiation of raw material procurement prior to completion of design yielding time saving. The deployment of AM does not require any special tooling and hence, tool procurement stage is also eliminated. Thus, the introduction of AM process results in large saving in terms of expenditure and time proving it viable for many applications, specifically for product development[13].

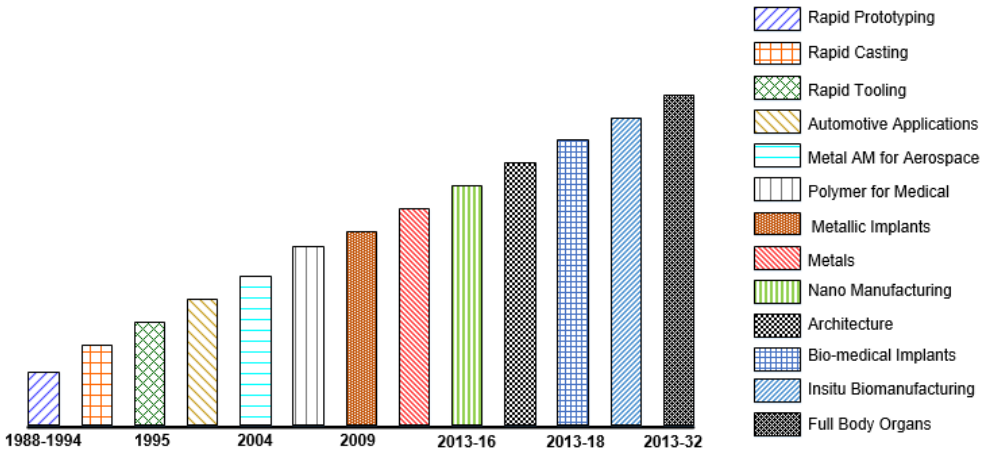

Figure 1.2: Evolution and Future Projection of AM [14]

Figure 1.2 presents the evolution of AM during the last three decades and the future projections of AM. As discussed earlier, AM was initially used for fabricating models and prototypes, most commonly known as Rapid Prototyping (RP). Afterwards, AM extended to casting applications for fabricating patterns required for developing a mould for casting, which is commonly known as Rapid Casting. Subsequently, AM is used as a technique for fabricating moulds for various

processes, like – vacuum casting, injection moulding, blow moulding, hot forging, cold forging, etc. This process is called Rapid Tooling. In the late 1990s and early 2000s, a trend towards the use of Metal AM (MAM) processes for Automotive, Aerospace and Medical sectors emerged. In addition, application of polymer AM for bio-medical applications started in mid - 2000's. Research in the direction of micro and nano-manufacturing using AM also became attractive during the last few years. Further, the use of AM in various other sectors, like - fashion, jewellery, architecture, food, constructions, etc. also gained attention. With the current pace, it is estimated that by the early 2030's human body organs can be developed using AM[14].

In the past decade, huge adoption and advancements in AM are seen and as per the annual report by Wohlers Associates in 2019, the global revenue from AM production and related services is expected to be $15.8 billion in 2020 and it is expected that the revenue will climb to $23.9 billion in 2022 and $35.6 billion in 2024 [15,16]. Figure 1.3 presents the applications of AM in different sectors as per the Wohlers report, 2019. It shows that the largest application of the technology in 2018 is for end-use parts, followed by functional prototypes. A combined 18.5% of the total application by jigs, fixtures, and other tooling demonstrates an important range of applications in industries.

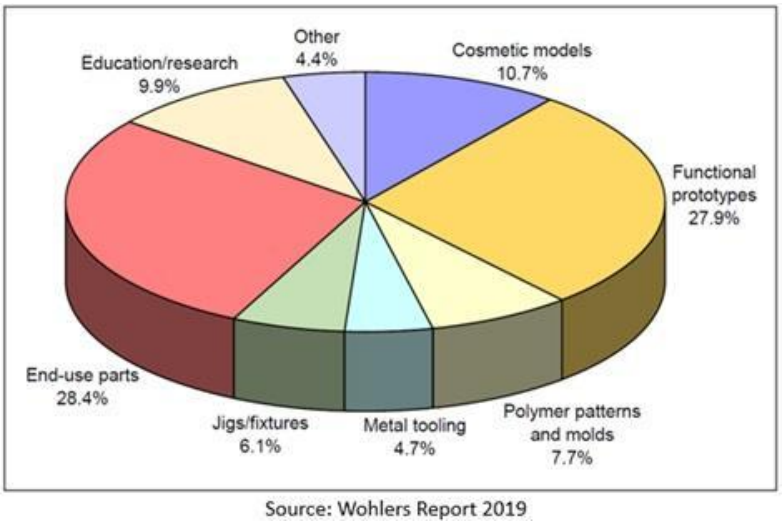

Figure 1.3: Applications of AM in different sectors as per Wohlers report 2019 [16]

It is seen that several industries are attracted to use AM, which is mainly due to the various freedoms it offers. The freedoms offered by AM are as follows:

a) **Shape design freedom:** AM provides the opportunity for "feature-based design and manufacturing" [17] and allows the fabrication of complex geometries with undercuts, lattice structures, honeycomb structures, etc. This aids the fabrication of components with reduced weight and material usage. Further, fabrication of the entire component is possible as a single unit without joining separate parts. With the advent of design for AM tools, it is possible to use advanced computational tools to retain material only at locations where it is necessary, without compromising the part strength and functionality. This aids to reduce material usage and wastage by adding materials at specific locations as per the requirement. Besides, in contrast to conventional manufacturing, cost per part is independent of the design complexity in AM as presented in Figure 1.4. In conventional manufacturing, the cost per part increases with an increase in design complexity. However, in AM, the cost per part is only a function of build time and material usage. This attracts the deployment of AM for various engineering applications[18]. Figure 1.5(a) presents a typical complex geometry built using AM [19].

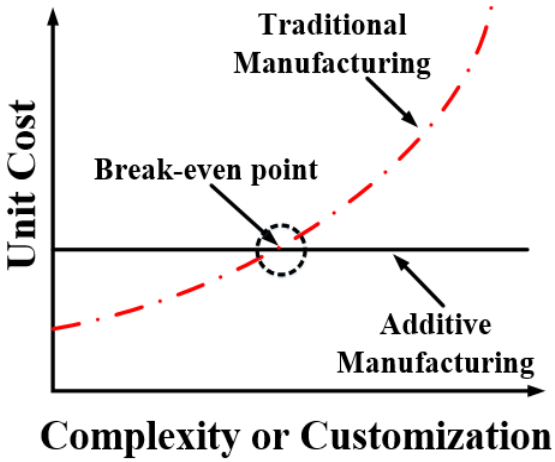

Figure 1.4: Unit manufacturing cost for additive and conventional manufacturing with product complexity

b) **Material design freedom:** AM provides the opportunity to add multiple materials in a single component mainly due to the layer-by-layer build-up approach and selective material fusion/ deposition principle. AM also allows the fabrication of components with multi-materials in a single layer or different materials at different layers. This gives the freedom to join metallurgical incompatible materials by bringing a buffer material compatible with both the materials in between them. The materials having a large variation in thermo-physical properties can be joined by providing appropriate composition gradient between the two materials. This aids to avoid steep gradient in the properties and allows to improve the interface strength of the joint, which makes it suitable for applications under hostile conditions[20]. Figure 1.5(b) presents a photograph of a typical functionally graded structure built by AM involving a metal (Ti6Al4V) and ceramic (Al_2O_3)[21].

(a) (b)

Figure 1.5: Freedoms offered by AM (a) Shape Design [19] (b) Material Design [21]

c) **Logistics freedom:** AM aids to reduce the gap between manufacturer and consumer with the availability of cyber technologies. It enables the design, manufacturing and property evaluation of the components at distant and remote locations. The number of stages involved in the component fabrication is reduced with the use of AM and it reduces the supply-chain management[22].

d) **Post-processing freedom:** Post-processing is the final stage in AM used for achieving the desired mechanical, surface and microstructural properties[23]. During AM, building strategy can be selected according to the post-processing requirements. Dimensionally critical parts can be derived using machining and appropriate tolerance can be provided to such parts during the design stage itself.

In the engineering sector, MAM transformed AM from a process for prototyping to a process for fabricating near-net shaped end-use components. Laser, a tool of power and precision is the most commonly used energy source in MAM and it is termed as Laser Additive Manufacturing (LAM). Lasers can be used for processing any material that can absorb the laser energy at a particular wavelength. Lasers can be focussed tightly to a small spot size, which helps in

achieving high energy density. The wide deployment of LAM provided the biggest leap for AM and brought it to the category of disruptive technologies. LAM is the most commonly used MAM process globally and the recent trend indicates an increasing demand for LAM built components to fabricate high-performance components, like – compact heat exchangers [24], developing coatings to withstand high operating temperatures[25], fabrication of sensor-embedded smart components for real-time monitoring[26], fabrication of functionally graded materials[27], gas turbine engine components[28], etc. in aerospace and power sector.

In the power sector, the power cycles are always motivated to improve their thermal efficiency. Rankine or Brayton power cycles are most commonly power cycles for generating electricity at the utility level, where the heat input is provided from thermal sources, like - fossil fuels, solar, nuclear fission, etc. Carnot law states that a larger temperature difference between the thermal source and thermal sink improves the maximum thermal efficiency of a power cycle. As the atmosphere is the sink in most of the cases and reducing its temperature is difficult, an increase in the source temperature is the only possible way to improve the thermal efficiency of the power cycle [29]. Figure 1.6 presents the variation of thermal efficiency with the turbine inlet temperature. It shows that with an increase in the turbine inlet temperature, the thermal efficiency of the power cycle increases. An example in this line is the Generation IV nuclear reactors, which includes Sodium cooled Fast Reactor, Lead cooled Fast Reactor, Gas-cooled Fast Reactor, Super-Critical Water-cooled Reactor, Very High-Temperature gas-cooled Reactor, and Molten Salt Reactor. These reactors work at a higher temperature of 500 – 900°C as compared to conventional water-cooled reactors, which operates at a temperature of 300°C [29].

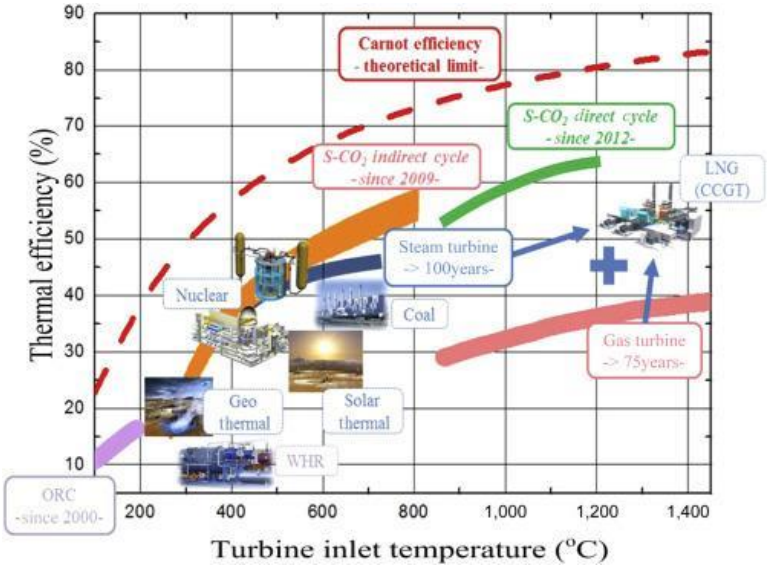

Figure 1.6: Variation of thermal efficiency with turbine inlet temperature [29]

Some of the material challenges involved in component manufacturing for advanced power sectors are [30]:

- The material will be exposed to a high temperature (≥ 800 °C), which can cause a loss in mechanical strength.
- Materials will be exposed to highly corrosive environments due to the presence of contaminants, like - N_2, CO, CO_2, H_2, CH_4 and H_2O.
- Operation life up to 60 years is compelling the long-term material stability.

Thus, the materials suitable for these applications should possess high melting point, good strength, good oxidation resistance and good corrosion resistance at elevated temperatures.

In the aerospace sector, many components have complex geometry, which involves parts with integrated functions, aerofoil shapes with internal cooling channels, thin-walled components, etc. As light-weighting is important in the aerospace sector, fabrication of thin-walled components is highly significant [31]. Fabrication of thin-walled components is difficult by subtractive manufacturing on account of distortions of thin-walled components due to cutting forces during the machining [5]. The aerospace sector also requires lightweight components

with high strength to weight ratio to have systems with good fuel efficiency and reduced emissions. Some of these components require high-performance claddings on the surface to improve the corrosion [32] and tribological behaviour[33], while some require functionally graded components[34]. Another aspect that attracts the use of LAM in the aerospace sector is the need for customized components[35]. Lower buy to fly ratio and reduced lead time also interest the use of LAM in the aerospace sector [35].

Nickel-based superalloys are the most preferred materials for the advanced power sector applications and aerospace applications due to their ability to retain superior properties at elevated temperatures close to 70% of the melting point [36]. Hastelloy-X (Hast-X) is one of the nickel superalloys suitable for high-temperature applications in the power and aerospace sector[37]. It is suitable for Advanced Ultra Supercritical Steam (AUSC), Supercritical CO_2 (SCO_2), Concentrated Solar Power (CSP) plants and other unique power generation methods[38]. Few examples indicating the applications of Hast-X in the power sector are:

a) Structural components in high-temperature gas-cooled reactors (HTGR) in Japan Atomic Energy Research Institute (JAERI) [39].
b) Intermediate heat exchanger components in the very high-temperature gas-cooled reactor (VHTR) for transferring heat to the secondary side [40].

In addition, Hast-X is used in gas turbine engines for combustion zone components such as transition ducts, combustor cans, spray bars and flame holders, etc. [37].

1.2 Motivation of the Thesis

LAM is an advanced manufacturing process that has several inherent advantages for building complex-shaped engineering components for advanced engineering applications. These components are exposed to hostile conditions and are made up of materials that can withstand

extreme duty conditions. Nickel superalloys are preferred materials for enormous applications under hostile conditions (elevated temperature and high pressure). Hast-X is one of the nickel superalloys widely used for high temperature applications due to their ability to retain mechanical strength, corrosion resistance and oxidation resistance at elevated temperature. However, the fabrication of Hast-X components using conventional machining is challenging due to severe tool wear and lower material removal rate owing to excellent mechanical properties retention by material at elevated temperature and self-hardening. LAM of Hast-X can bring the components to a near-net shape reducing the need for excessive machining. However, the major challenge in processing Hast-X using LAM is its susceptibility to hot or solidification cracking. Thus, there is a need to develop the process for building Hast-X structures using Laser Directed Energy Deposition (LDED) based LAM to build near net-shaped components. LDED of Hast-X can pave the way for building engineering components operating at elevated temperatures. The characterisations, including the geometrical studies, microstructure, evaluation of room temperature and high-temperature mechanical properties of LDED built Hast-X structures, are significant to qualify the built material for various engineering applications. LDED built thin-wall and bulk structures are important for the potential fabrication of various engineering applications, especially the fabrication of compact heat exchangers, gas turbine components, etc. It is necessary to develop the process methodology to build a prototype power sector component, like - compact heat exchanger using LDED for building multi-material heat exchanger systems. Thus, the motivation of this thesis is to use LDED based LAM technique to deposit defect-free Hast-X for building thin-wall and bulk structures and investigate its behaviour at different conditions.

1.3 Scope of the Work

The thesis work aims to employ the versatile LDED technique to deposit Hast-X for defect-free deposition of the thin-wall and bulk structures. Therefore, the research aims to investigate

the effect of key process parameters on the single-track deposition to identify the process window and understand the parametric dependence for geometry and material behaviour. Further, the identified process window will be used for building thin-wall structures and bulk structures. The acquired know how will be used to correlate the effect of the process on the various properties including geometrical characteristics, microstructure formation and mechanical behaviour. The study will also be extended to understand the effect of in-situ and ex-situ treatments on the behaviour of the built structures. Finally, a process methodology will be developed to build a prototype Printed Circuit Heat Exchanger (PCHE) using LDED. These studies will fill the gap for an immediate need of the LAM community through a systematic acquisition of knowhow on the processing and properties of LDED built Hast-X.

1.4 Organization of Thesis

Chapter 1 introduces the problem. A detailed literature review along with some preliminary trials on nickel superalloys are presented in Chapter 2. Chapter 3 explains the various experimental systems and tools used for LDED and characterisation of Hast-X structures. Chapter 4 discusses the modelling and experimental studies on track geometry along with experimental investigations on process window development for defect-free deposition and defect-analysis during LDED of Hast-X single tracks. Chapter 5 presents the experimental and numerical investigations on the effect of Laser Energy per unit Powder Feed (LEPF) and interlayer delay on LDED built thin-walls. Chapter 6 discusses the microstructural and mechanical characteristics (room and elevated temperatures) of LDED built bulk structures in the as-built condition. Chapter 7 analyse the effect of in-situ SLLR and post heat-treatment on the properties of LDED built Hast-X structures. Chapter 8 presents the LDED of overhang walls and process methodology evolved based on the results of the present investigation to build Printed Circuit Heat Exchanger (PCHE). Chapter 9 presents the conclusions of the entire study and future scope.

Chapter 2 : Literature Review[1]

2.1 Introduction

In the past decade, MAM technology has grown significantly mainly due to the challenges involved in the machining of advanced materials and increasing demand from aerospace and power sector for customized solutions. Among the various MAM processes, LAM processes are most commonly used in industries and research. This chapter reviews the MAM processes with a focus on LAM technology. Further, the various aspects of LDED process are discussed with respect to process mechanisms, systems, advantages and limitations. In addition, the chapter will review the literature available on LDED of nickel superalloys. The chapter ends with a discussion on the aim and objectives of the present work and flowchart of the present work.

2.2 Laser Additive Manufacturing

2.2.1 Additive Manufacturing

Additive Manufacturing (AM) is growing as a potential disruptive technique and the global production trend shows that with the advancements in AM, mass-customization and localized manufacturing will be the future of manufacturing [8]. AM is termed as a "disruptive technology", because it is an invention/technology that is creating a new market and value network by replacing and pushing behind the existing market and value network. Till recent times, AM was used primarily for prototyping or building models. However, with an increase in the number of materials that can be processed by the technology, advancements in

[1] This chapter is partially reproduced with permission from SAGE Publications (Journal - S. No. 3), Elsevier (Journal - S. No. 4) and CRC Press (Chapters in books and lectures notes - S. No. 1) - See Letters of Copyright Permission (Page No: 208, 209 and 210).

technology and availability of high energy density sources, applications of AM are increasing in numerous industries. ASTM/ ISO 52900 classified AM into seven different categories and they are as follows:

a) **Vat photopolymerization (VP):** VP is defined as **"***an additive manufacturing process in which liquid photopolymer in a vat is selectively cured by light-activated polymerization*".

b) **Binder Jetting (BJ):** BJ is defined as **"***an additive manufacturing process in which a liquid bonding agent is selectively deposited to join powder materials"*.

c) **Material Jetting (MJ):** MJ is defined as **"***an additive manufacturing process in which droplets of build material are selectively deposited"*.

d) **Sheet Lamination (SL):** SL is defined as **"***an additive manufacturing process in which sheets of material are bonded to form an object*".

e) **Material Extrusion (ME):** ME is defined as **"***an additive manufacturing process in which material is selectively dispensed through a nozzle or orifice"*.

f) **Powder Bed Fusion (PBF)**: PBF is defined as **"***an additive manufacturing process in which thermal energy selectively fuses regions of a powder bed"*.

g) **Directed Energy Deposition (DED)**: DED is defined as *"an additive manufacturing process in which focused thermal energy is used to fuse materials by melting as they are being deposited"*. [7]

Figure 2.1 presents a comparison of the various aspects of different AM processes based on the material, the form of the material, state of the material and principle involved in AM. The basic methodology involved in all the processes are same i.e., layer-by-layer addition of material to build 3D component. However, the basic difference lies in the methodology used for material feeding, joining technique, the form of material and state of the material. VP uses

photosensitive polymer in liquid form as the raw material and solidification are achieved through polymerization by using UV light to build a single layer. MJ uses selective deposition of photosensitive material as liquid droplets from the print head and uses a UV light to solidify the material to generate a solidified layer as per the geometry requirement. BJ uses a pre-placed bed of powder (metal, polymer or ceramics) and selective deposition of binders from deposition head as per the required geometry to form a single layer. ME uses the raw material in wire form/ filaments and it is heated to molten form by the heating nozzle. The molten material is deposited as per the geometry requirement to form a layer. SL uses sheets (paper, metal, wood, etc.) as the raw material and they are joined by adhesives/ solid-state welding process and the extra portion is removed using the subtractive technique as per the required geometry to form a layer [41][42]. PBF processes start with a layer of powder spread on the substrate or build plate and high energy density sources, like – lasers or electron beam is used to melt the powder (polymer, metal or ceramic) selectively as per the required geometry[41][43]. DED uses a high energy density source to melt dynamically fed raw-material (wire or powder) to deposit the material as per the required geometry, which aids to build a layer[27].

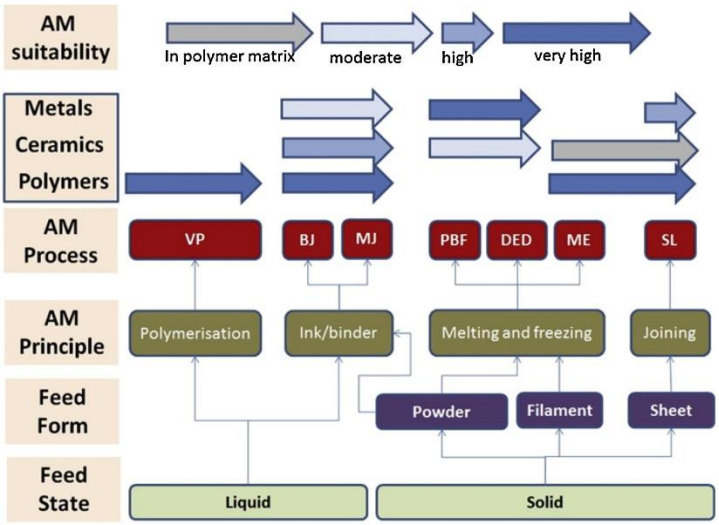

Figure 2.1: Comparison of various AM processes [42]

2.2.2 Metal Additive Manufacturing

MAM is an advanced version of AM that transformed AM to industrial manufacturing for building high-performance functional end-use components. Among the different AM processes seen in Figure 2.1, ME, BJ and VP can build metallic components indirectly by using polymer-metal mix raw material as feedstock. In all these processes, the metal remains in solid-state and thus, a green part is obtained, which is a blend of metal and polymer. ME uses filaments with a blend of thermoplastic polymer and metallic material, where the polymer material is heated to the molten state and deposited to build the green part[44]. BJ uses binder to join metal powder particles and a green part is built[45]. VP uses metallic powders in the photo-polymer liquid and the polymer is cured using UV radiation[46]. The green part built using the above techniques is subsequently kept in a furnace for debinding and the polymer is burned out from the green part. This leaves behind a metallic part with porosity. The debinding stage is followed by a sintering stage to improve the density of the build part[44]. Due to the indirect manufacturing procedures and low strength of these components, they are not deployed for functional applications generally.

SL, PBF and DED are the AM processes that build complete metallic components in its entirety during the process[47]. SL is used to join metallic sheets by using a combination of ultrasonic welding and milling operation. Ultrasonic welding is used to join the metallic sheets by using a solid-state welding technique, while the milling operation is used to generate intricate geometries[48]. SL is a hybrid form of manufacturing, which uses a combination of additive and subtractive technologies for building engineering components.

Commercially, high energy source based MAM processes is most commonly used to build functional components. Figure 2.2 presents the classification of MAM processes involving high energy sources for melting and solidification of feedstock material. The various high

energy sources used in MAM are laser beam, electron beam and arc[49]. The types of feedstock used in MAM are wire and powder. Another way to classify the process is the methodology used for material feeding. It can be of two types: powder bed-based (pre-placed bed) or dynamic feeding based. Based on this, MAM can be classified primarily as DED and PBF. DED and PBF use high power energy sources for melting the raw material and deposit them in the layer-by-layer fashion. DED uses dynamic material feeding approach, while PBF uses a bed of powder as raw material. DED uses either a laser beam or electron beam or arc as the energy source, while PBF uses a laser beam or electron beam to melt the raw material[49].

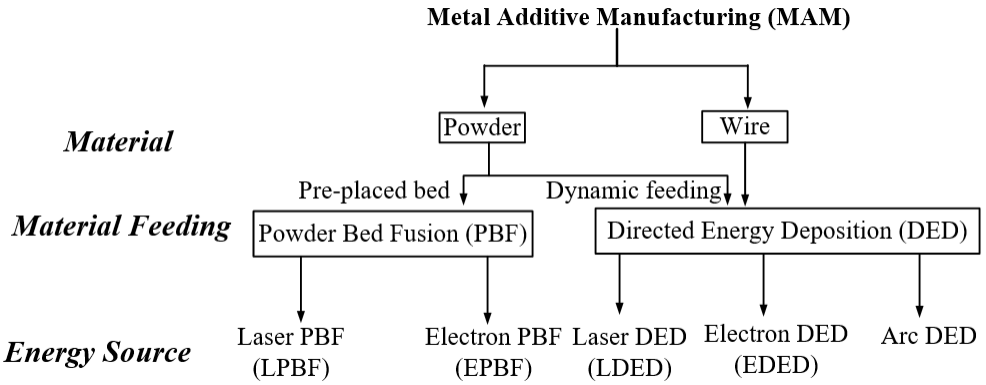

Figure 2.2: Classification of MAM process

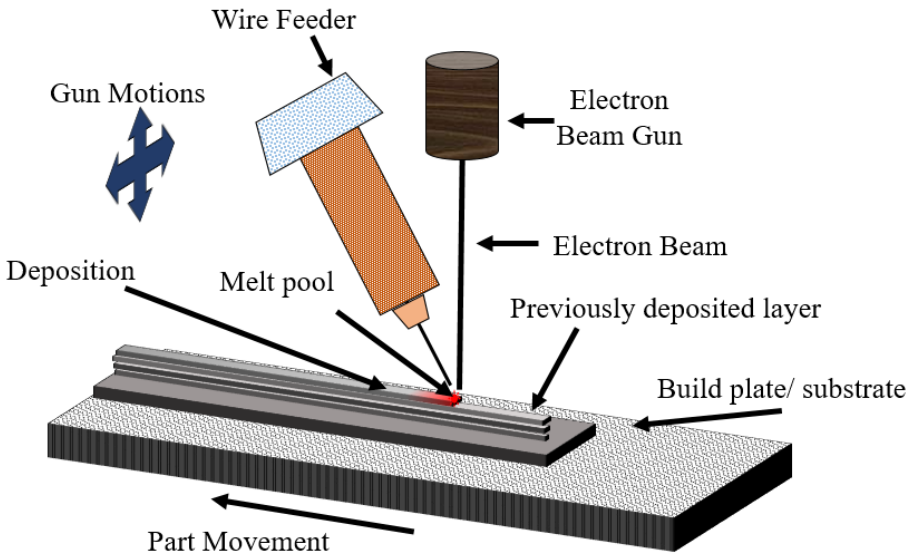

Figure 2.3: Wire Feed EDED System

Electron beam-based additive manufacturing (EBAM) can be primarily of two types: Electron Beam Powder Bed Fusion (EPBF) and Electron beam Directed Energy Deposition (EDED). EPBF, most commonly known as Electron Beam Melting (EBM) deploys high energy electron beam, to melt pre-placed layer of metallic powder using the layer-by-layer methodology, to shape the component. In EDED, electron beam from the electron gun is used to deposit laterally fed metallic wires as shown in Figure 2.3. The system can also be used with multiple wire feeders, which allow the deposition of multi-materials or functionally graded materials. CNC workstation is used for job manipulation in the X direction and the electron gun movement in the Y direction and Z direction[50].

EBAM is attractive due to the following reasons:

- The electron beam can be focused to a small spot to bring out the high-intensity beam.
- Melt pool contamination is not possible due to vacuum.
- The energy used for melting is independent of the absorptivity of the material.
- Pre-heating aids to achieve high density and strong parts.

However, the major limitations associated with EBAM are:

- Only metallic components can be built due to the process nature.
- High initial setup cost due to vacuum enclosure.
- X-rays generation during the process.

Arc based MAM processes follow the DED principle and are typically of two configurations: lateral and co-axial. The lateral configuration is used with Gas Tungsten Arc Welding (GTAW)[51], while the co-axial configuration is used with Gas Metal Arc Welding (GMAW). Figure 2.4 presents the typical schematic of a GMAW based system. Arc based MAM employs melting and deposition of the metallic wire using an arc as the thermal energy source. An arc generated between the substrate material and welding wire tip leads to melting of the welding wire tip and substrate, which results in metal droplet generation. The generated droplets are dropped on the melt-pool created on the substrate surface. With the movement of the welding torch as per the required trajectory, the molten metal, which gets accumulated is solidified and deposited[52][53].

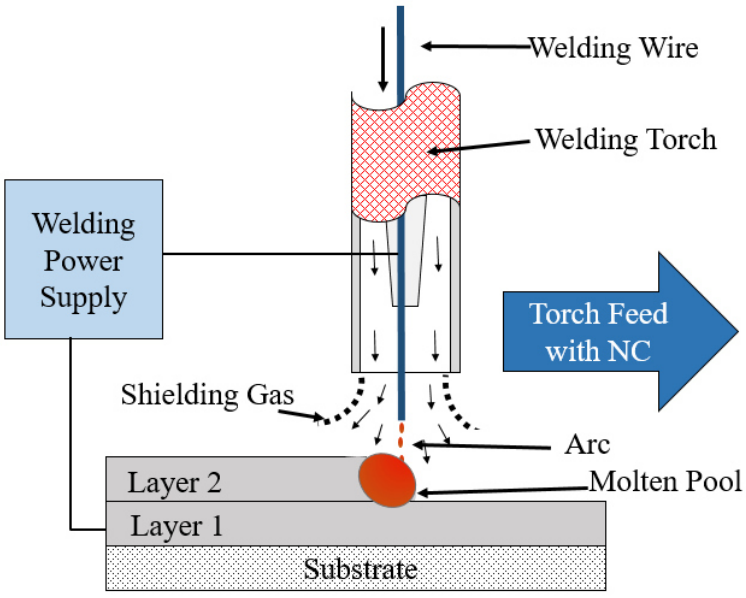

Figure 2.4: Gas Metal Arc Welding based MAM

2.2.3 Laser Additive Manufacturing

LASER (**L**ight **A**mplification by **S**timulated **E**mission of **R**adiation) is a device that produces light by optical amplification due to stimulated emission of electromagnetic radiation. The laser is one of the most incredible inventions of the last century, demonstrated with several sensational applications. The basic concept of the laser was first given by Charles Hard Townes Alexander Mikhailovich Prokhorov and Nikolai Gennediyevich Basov, who shared the coveted Nobel Prize (1964). However, TH Maiman from Hughes Research Laboratory, California, demonstrated laser for the first time experimentally by flashing light through a ruby crystal, in 1960 [54][55][56]. The major differences between laser and ordinary light can be understood with the aid of an analogy. If several pebbles are thrown to a pool together, the waves generated by each pebble will cancel each other as they are thrown randomly. This permits the waves to move only a short distance. If the pebbles are thrown to the pool one by one at the same location at constant time intervals between them, the generated waves will strengthen and can travel a longer distance. This is because the waves travel coherently. Thus, the light waves are exactly in step with each other and have a fixed phase relationship in lasers [56]. This makes lasers suitable for materials processing applications. The main features of laser that attracts its use in material processing are coherence (spatial and temporal), high intensities and fluence, short to ultra-short pulse durations, no need of vacuum for propagation and feasibility of transportation through flexible optical fibres. The use of lasers in the manufacturing industry has following advantages over conventional methods:

a. Laser-based techniques are non-contact processes suitable for processing various advanced engineering materials such as brittle materials, soft and thin materials, electric and non-electric conductors, etc.
b. Being a thermal process, materials with adequate thermal properties can be effectively processed irrespective of their mechanical properties.

c. It is a flexible process [56].

The two major processes involved in LAM of metals are Laser-based PBF (LPBF) and Laser-based DED (LDED). LPBF uses a laser as an energy source for fusing a pre-placed layer of powder and it is primarily classified into Laser Sintering (LS) and Laser Melting (LM). Figure 2.5 presents the typical schematic of an LPBF system, which consists of a high power laser, Galvanoscanner, build platform, powder hopper and powder spreader. Both LS and LM have a similar arrangement and the major difference lies in the mechanism involved in bonding.

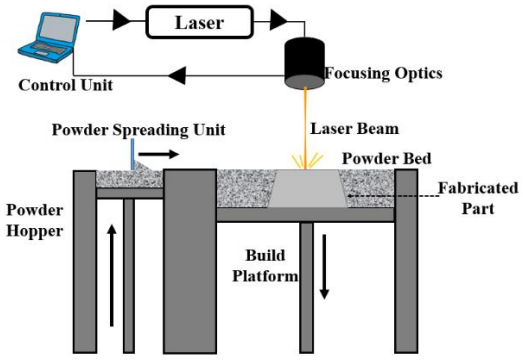

Figure 2.5: Schematic arrangement of LPBF system

LS: It is the first AM process that used the PBF principle to build 3-dimensional components using laser energy. The process was generally used to process polymers or polymer-coated metal powders to build polymer components and metallic components, respectively. LS is a prominent process for building polymer components. However, the use of LS for building metallic components was mainly due to the unavailability of high-power lasers to melt metals completely. Thus, polymer-coated metal powders were used to bond the polymers together to build a green structure.

Like other AM process, LS starts with 3D model data, which is sliced into several layers. The powder is filled in the powder hopper/ dispenser and powder spreading unit (roller or blade) is used to spread a layer of powder (15 - 100 microns) on the build plate. The LS process begins with preheating of powder particles to a temperature that is below the melting point/ glass

transition point of the polymer. The advantages of pre-heating are reduced laser energy required for material fusion/ bonding and reduced distortion due to a reduction in the thermal gradient during the initial stages of the build. Consequently, the laser selectively scans the regions of the powder bed and sinters the powder particles as per the required geometry. The laser power required for fusing the powder is the excess energy required to elevate the powder temperature from preheating temperature to melting point temperature. Once one layer is built, the build platform moves down by a distance equal to the layer thickness and powder dispenser moves up. Further, the powder is spread over the previously built layer followed by pre-heating and selective laser scanning. Extra powder surrounding the part will act as support structures to a greater extent and it also allows fabrication of overhang components[57,58]. LS is well established for single-component systems, which are generally polymers and multi-component systems (multi-material powder particles or pre-alloyed powders). The multi-material powder particles will consist of a low melting point material (used as binder material) and high melting point structural material. The main feature of LS is that the powder particles are not completely melted, but it is sintered or partially melted[59].

LM: LM process was developed to build components with full density (~ 99.99%) without post-processing. The availability of high-power lasers helped in developing LM based systems and these systems are commercially available by diverse vendor-specific names, like – selective laser melting, direct metal laser sintering, laser cusing, etc. System arrangement is similar to LS and the basic differences between LS and LM are the use of high-power lasers (like - diode-pumped Nd: YAG laser or fibre laser), smaller layer thickness and fine beam spot diameter to melt the powder particles completely. High laser power, small layer thickness and fine beam diameter help to provide sufficient laser energy density to completely melt the powder particles to achieve a higher density with good metallurgical bonding [59].

2.3 Laser Directed Energy Deposition (LDED) Process

2.3.1 Process Mechanism

LDED is a LAM process that uses high power lasers to create a melt pool on the surface of the substrate or previously built layer onto which the feed material is added. LDED can be classified as powder fed deposition (PFD) or wire fed deposition (WFD) based on the feedstock material used for deposition [49].

a) Powder Fed based Directed Energy Deposition

Powder feeding is the most commonly used approach in LDED, which generally consists of a powder feeder (single-channel or multi-channel), high power laser source, workstation (CNC or robotic) and deposition head (generally a co-axial nozzle) as shown in Figure 2.6. The carrier gas is used for carrying the powder from powder feeder to the deposition zone through the deposition head. In addition, shielding gas is used to protect the melt-pool from oxidation. The commonly used shielding gases are Argon, Helium and Nitrogen. Nitrogen cannot be used for processing all materials due to its reactivity with some metals. Argon and Helium gases are used often due to their inert nature to prevent contamination of the molten pool. Helium has the advantage of higher ionisation potential, while argon has the advantage of higher density. In Indian context, Argon is the most-commonly used shielding gas owing to its inert nature, higher density, and easy availability.

During LDED, the laser beam is delivered to the deposition zone using a co-axial nozzle along the vertical axis in the centre of the nozzle array and focused by a lens near the workpiece. The co-axial nozzle consists of three passages, with the central passage used for the laser beam and shielding gas; the next outer passages used to inject the powder to form a co-axial laser-powder stream; the outermost passages are used to provide a converging conical jet of shielding gas. Focusing height of laser is manipulated by moving the lens and nozzle in the Z-direction. XY

movement is achieved either by moving the workpiece or laser head by using a computer-controlled drive system to form the desired cross-sectional geometry.

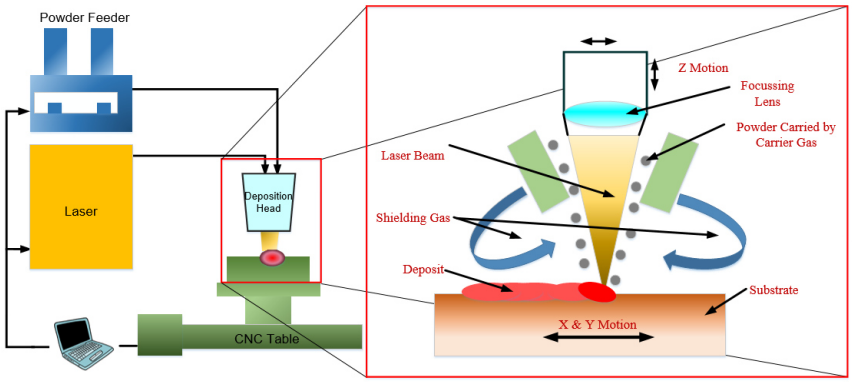

(a)

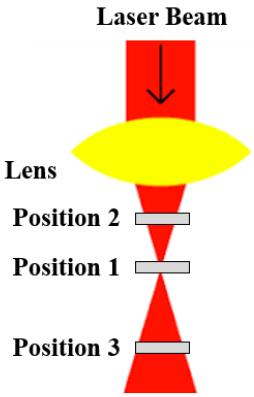

(b)

Figure 2.6: Schematic arrangement of PFD based DED (a) system (b) substrate positioning

PFD starts with a laser generating a melt pool on the substrate, where it interacts with the substrate. Generally, the size of the melt-pool is a function of process parameters and beam diameter. During this stage, the powder fed using co-axial nozzle undergoes pre-heating due to multiple internal reflection and absorption of the laser beam. Once the melt pool is created, the powder is injected to the melt-pool using a co-axial nozzle and it undergoes complete melting as it enters the melt-pool. As the laser moves away, the melt pool solidifies and deposition is obtained. The basic building block in DED, i.e., a single line deposit is defined as a track, which is achieved by moving the deposition head or sample linearly in the X-Y plane. By depositing

overlapping tracks with 50% - 60 % overlap of track width, a single layer is built as per the required geometry of the first slice. Once a layer is built, the co-axial nozzle moves up by a distance equal to the layer thickness and a melt-pool is created on the previously deposited layer. The procedure repeats until the complete three dimensional part is built[17][60].

During LDED, the substrate can be positioned at three different locations as presented in Figure 2.6 (b). They are:

• At the laser focus (Position 1) – When the laser beam is positioned at the focus point on the substrate, the beam spot is the smallest and it results in lower build rate during LDED as a greater number of tracks and a larger number of layers are required to build the same geometry. Hence, it is not the optimum choice.

• Before the laser focus (Position 2) – When the laser beam is positioned before the laser focus on the substrate, the converging laser beam interacts with powder and substrate. Any local high point in the layer undergoes a lower laser density and results in improper melting and discontinuity in the deposit. Hence, it is not preferred choice.

• After the laser focus (Position 3) - When the laser beam is positioned after the laser focus on the substrate, the diverging laser beam interacts with powder and substrate. In this case, any local high point in the layer undergoes melting and spreads over the surface. This results in deposition of uniform layer. Generally, diverging laser beam is used for LDED applications due to this inherent advantage.

In WFD based AM technique, the material is deposited by feeding the wire through a nozzle and melting the fed wire with the laser beam. The molten metal forms a metallurgical bond with the substrate/ previously deposited material and by relative motion between substrate and laser head and/ or wire feeder, a metal track is generated after solidification of molten metal.

To protect the oxidation of molten metal, the nozzle is integrated with either suitable inert gas shielding arrangement or a controlled atmosphere chamber. The advantage of WFD over PFD lies over the fact that the deposition rate is 100%, with minimal material wastage. In addition to this, fewer health hazards may occur as compared to PFD. WFD can be primarily of two types: lateral wire feeding and co-axial wire feeding[17]. Figure 2.7a presents a schematic of typical lateral Wire feed LAM System, where the wire makes an angle with the laser beam. In lateral wire feeding based system, the angle between the laser source and wire is an important process parameter along with other LDED process parameters.

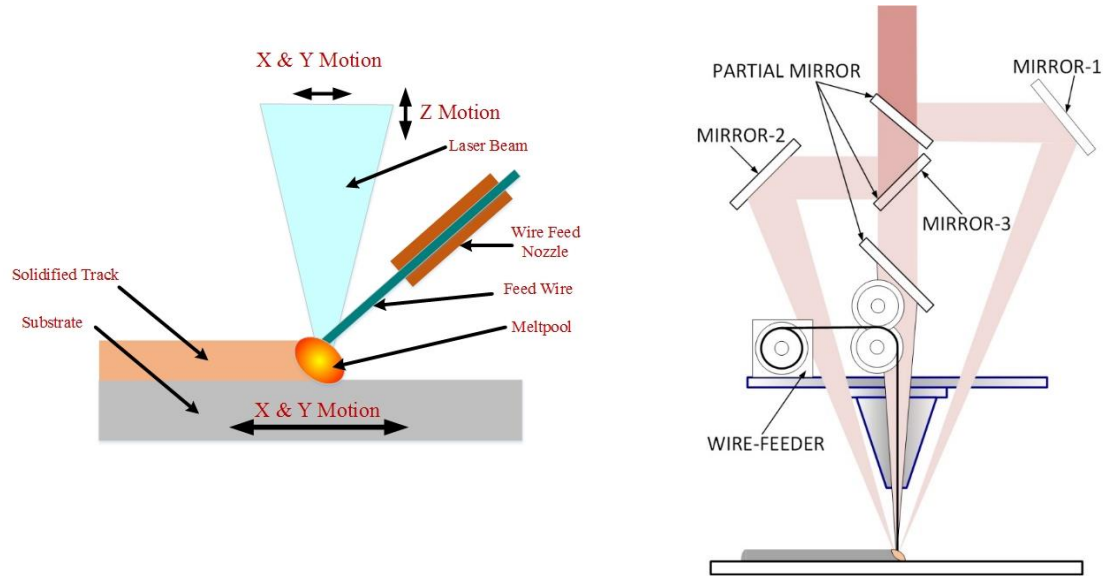

(a) (b)

Figure 2.7: Wire Feed LDED System (a) Lateral (b) Co-axial

Co-axial laser wire feeding is one of the latest developments in WFD and it deploys metallic wire and laser beam fed co-axially to build three-dimensional components[61]. The system comprises of a co-axial wire feeding nozzle, high power laser beam, beam splitters and beam reflectors as shown in Figure 2.7b. The principle behind co-axial wire feedings is that the beam is split into three different beams using beam splitters, reflected by reflectors and focused at a single point keeping horizontal orientation 120° apart. The metallic wire is melted using the focused laser beam and can be used for making complex 3D components from CAD model

data. The major advantage of this wire feeding system is the omnidirectionally it offers as compared to lateral wire feeding.

Even though WFD systems have many advantages over PFD, the wide deployment of WFD is limited by the smaller processing window, relatively low surface quality, reduced precision and larger feature size in WFD due to the typical wire diameter in mm scale. In addition, the coupling of wire and laser is another challenge in WFD based DED.

2.3.2 Process Parameters

The most common process parameters that influence LDED process are:

a) **Laser power:** Laser power is the rate at which energy is released from the laser or the energy released per unit time. If all the other process parameters remain constant, a very high laser power will lead to cracking of the material and very low laser power will result in incomplete melting and irregular deposition [62]. However, the deposition rate and material catchment efficiency increase with an increase in laser power.

b) **Laser beam diameter/ spot diameter:** It is the diameter of the laser beam on the surface of the substrate or the previously deposited layer. The laser beam diameter defines the intensity of the laser beam. The intensity of the laser beam is the ratio between laser power (P) and beam spot area (A_b)[63].

$$\text{Laser beam intensity} = \frac{P}{A_b} \tag{2.1}$$

c) **Material feed/ flow rate:** Material feed rate is the rate of flow of the feedstock in DED systems and it can be the wire feed rate or powder feed rate. Wire feed rate is typically represented in m/min and powder feed rate is represented in terms of g/min. For a given laser power density and interaction time, the deposition rate increases with the increase in material feed rate up to a critical value [62].

d) **Scan speed:** The scan speed determines the interaction time between the laser beam and substrate/ previous layer, which defines the laser energy per unit length. This decides the size

of the melt pool along with the beam diameter. Scan speed also defines the interaction time between the laser and material fed, which defined material fed per unit length. The effect of basic parameters can be accounted with Laser energy per unit length (equation 2.2) and material fed per unit length (equation 2.3).

$$Laser\ Energy\ per\ unit\ length = \frac{P}{V} \tag{2.2}$$

$$Powder\ fed\ per\ unit\ traverse\ length = \frac{m_p}{V} \tag{2.3}$$

where, P stands for laser power, V stands for scan speed and m_p stands for powder feed rate. The parameters "laser energy per unit traverse length" and "powder fed per unit traverse length" govern the laser energy and the material available for the single track deposition, respectively [17].

e) **Transverse Traverse Index/ Degree of overlap:** Transverse traverse index is defined as the ratio between the displacement of the nozzle head to the track width during multi-track deposition (refer equation 2.4) as presented in Figure 2.8. When LDED has to be performed for a larger area, several tracks should be laid adjacent to one another. The overlap between the adjacent tracks governs the density of the built structure. If the overlap between two adjacent tracks is too low, it results in a large amount of porosity. If the overlap percentage is too large, it will result in larger energy at the same location, which can lead to cracking and distortion. Typically, 50 – 60% overlap is preferred to build bulk structures and < 40% is used to build porous components [17].

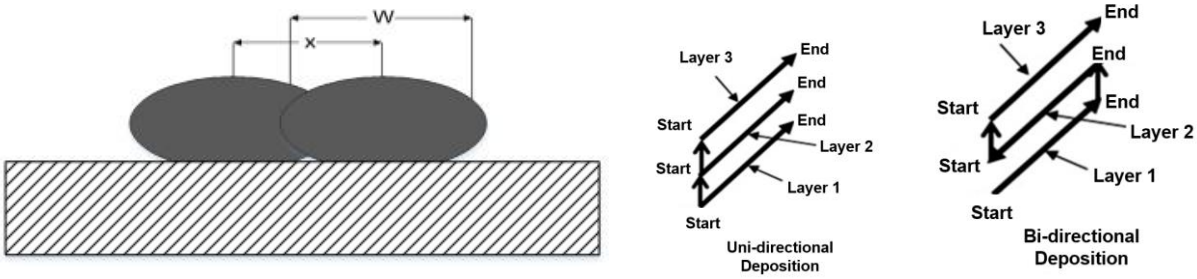

(a) (b)

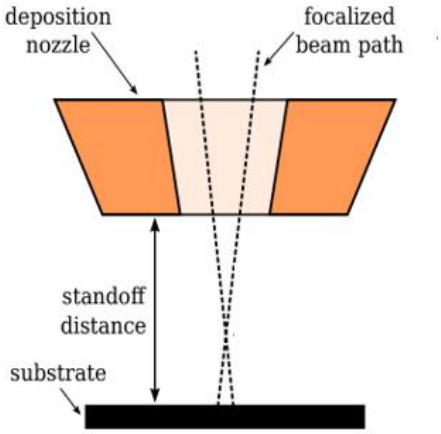

(c)

Figure 2.8: Schematic representing (a) transverse traverse index (b) Uni-directional and bi-directional deposition (c) Standoff distance [64]

$$\text{Transverse traverse index (i)} = \frac{x}{w} \qquad (2.4)$$

f) **Scan strategy:** Scan strategy refers to the path followed by the heat source during selective deposition of materials during LDED. Contrary to PBF, scan strategies in DED are relatively simple due to the limitation levied by workstation movement. Uni-directional and bi-directional fills are the most commonly used scan strategies in DED as shown in Figure 2.8b [47].

g) **Standoff distance:** Stand-off distance is the distance between the tip of the nozzle to the substrate surface. Figure 2.8c presents the schematic representing standoff distance. Generally,

a diverging beam is used for LDED as shown in Figure 2.8c [64] and the stand-off distance is kept constant to ensure the appropriate gas shielding and powder feed for various beam diameters**.**

h) **Gas flow rate:** In LDED systems, the gas flow is used for two major purposes. It acts as a carrier gas to deliver the powder to the melt pool and shielding gas to prevent oxidation of the melt pool. Argon gas is the most commonly used gas for both purposes. A lower value of carrier gas flow results in lack of enough energy to carry the powder. However, higher carrier gas flow rate results in a higher gas velocity for the same tube section, which results in powder ricocheting at the impingement point.

2.3.3 Advantages and Limitations

The various advantages of LDED are:

a) **High deposition rate**: LDED brings higher deposition rates as compared to PBF mainly due to in-situ melting of feedstock using high energy density sources. In LDED, separate time is not required for powder spreading and levelling. The typical deposition rate of LDED is in the range of 230 cc/hr at a laser intensity of 3.8 kW/cm^2 [47].

b) **Dense and strong parts**: LDED involves melt-pool generation on the surface/ previous layer surface onto which the molten feed material is added. This leads to good metallurgical bond resulting in highly dense components[65]. LDED can build components with a density close to 100%.

c) **Multi-material range**: LDED can use multiple materials at the same time, which allows to build components with customized material, functionally graded joints, etc. [66].

d) **Larger parts**: In PBF, the maximum size of the component that can be built in the chamber depends on the size of the build chamber. LDED can build large components

and it depends on the maximum distance that can be moved by the workstation[67]. Movable pallets can be used to further increase the volume in one direction.

The limitations of LDED process are as follows:

a) **Low dimensional accuracy**: LDED built components have low resolution and poor surface finish due to the high energy, larger beam diameter and higher melt pool flow[68].

b) **Support structures – not preferred:** Support structures are generally not preferred in LDED mainly due to the nature of how the LDED technology builds parts[69]. Thus, highly intricate geometries like - undercuts, lattice structures are difficult to build.

c) **Thermal distortion:** As LDED uses high energy density sources, thermal distortion and residual stresses are usually observed[70], which can also result in cracking or delamination of the built parts [71].

2.3.4 Post-processing

The bulk and surface properties as well as geometry achieved in LDED built material is influenced by distortions due to heating, partially melted powders, solidified melt droplets, surface variations brought by the laser movement and processing strategy. However, the as-deposited surface roughness, dimensional accuracy and properties are inadequate for many industrial applications. Therefore, a certain amount of post-processing is required for LDED components [72].

The first stage of post-processing is the removal of the part from the substrate. This is usually done using wire electrical discharge machining or sawing. The next stage of post-processing depends on the application. This can be surface property, aesthetic and bulk property enhancements. Surface property enhancement of LDED components is also performed laser-based techniques such as laser shock peening (LSP), laser remelting, laser micromachining and laser annealing (LA). Surface finish enhancements are done using conventional subtractive

manufacturing techniques, like - computer numerical control (CNC) milling and polishing, glass blasting, or ultrasonic machining [41]. Surface property enhancements can also be done with non-thermal techniques, like - shot peening. Shot peening is a mechanical surface treatment technique in which small balls are impacted on the surface of a component. The repeated impacts of the balls induce compressive residual stress and refine the microstructure. This helps in delaying the crack initiation and hinders the crack propagation [73]. Thus, the mechanical properties and microstructure can be tailored as per the requirement by shot peening.

Post-processing heat treatment is also applied to LDED components to adapt the bulk properties of the components to the working conditions or to reduce the induced thermal stress [74]. Thus, the desired microstructure and mechanical properties for service conditions can be achieved by various heat treatment procedures. The recipe of these heat treatment procedure is material dependent. These treatments alter the grain size, grain orientation, porosity and mechanical properties.

Relieving of internal stress is another aspect associated with heat treatment. As discussed earlier, LDED components have internal residual stress due to the high thermal gradient. Thus, annealing is performed on LDED components for reducing the internal residual stresses [75]. Solution treatment and ageing procedures are common for precipitation hardened materials, like - nickel based superalloys. Solution treatment helps in dissolving the undesirable phases, while ageing enables the formation and growth of precipitation phases. These processes are usually done sequentially. The processing conditions and time for solution treatment should be properly selected for dissolving the precipitates. Once solution treatment is done, ageing is carried out to generate strengthening precipitates [47].

2.3.5 Applications

a) Near-net-shaped Parts

LDED is useful in fabricating near-net-shaped components for various applications, particularly when the application demands hard to machine materials. Machining of hard materials will be a slow and expensive process as it involves excessive machine and tool wear. It can be accelerated, if LDED is used to build those components to near net shape, only final finishing can be done using conventional machining. This involves the fabrication of large sized aerospace components, which are generally built using nickel superalloys or titanium alloys. Nickel superalloys possess self-hardening nature, while low thermal conductivity of titanium limits its machinability [76,77]. Hence, these components can be near net-shaped using LDED and brought to final shape by machining. Some of the examples include the development of Titanium brackets [78] and SS 316 housing [79] by Sandia National Laboratory.

b) Feature Addition

LDED can also be used to add features onto existing components and this is effective when the feature to be added is expensive to be built using conventional manufacturing. These features can be of same material as that of existing surfaces or new material, which is metallurgically compatible with existing material [80].

c) Biomedical

LDED is useful to build porous biomedical implants as compared to conventional techniques, mainly due to its unique advantages of tailoring porosity and mechanical properties (i.e., Young's Modulus) by varying process parameters. It is also possible to include diverse materials together and build functionally graded materials to achieve optimal properties. The process is compatible to build custom implants for patient-specific needs [81]. Some of the

common alloys used for biomedical applications are Titanium and its alloys [82], Co-based alloys [83], 316L stainless steel [84], and Ni-Ti based alloys [85].

d) Clad layers of high-performance materials

Cladding is a surface modification technique used for adding one material over another material in a controlled manner, which is typically used to develop a protective layer. Cladding generally improves the corrosion resistance and tribological properties by adding layers of superior material over the base component. It also helps to improve the life cycle of parts and to reinstate their functionality [60]. At the process end, LDED is an extension of the cladding process and thus, it is being continuously deployed globally for cladding applications. One of the examples is the life-improvement of boiler pressure components in Waste to Energy (WTE) industry. Inconel 625 (IN625) coatings of 0.070 to 0.100-inch-thick are deployed for protection against corrosion and erosion. IN625 provides enhanced pitting and corrosion resistance caused by chloride contamination for boiler components. The major advantage is the cost savings resulting from deployment of less expensive material as boiler material and providing IN625 coating on the surface rather than fabricating the entire component with IN625 [86].

e) Repairing of Components

Repair is one of the most common applications of LDED[87], especially in the aerospace sector. As repairing of a worn-out/ damaged part is cost-effective than building or purchasing the new part, most of the aerospace companies prefer LDED. Some of the common examples of LDED based repair is the repairing a gas-turbine blade using Ni-based superalloy[88] and repairing of steam circuit parts at thermal power stations using Cobalt alloy deposition [89] for high-temperature mechanical properties, etc.

2.4 LDED of Nickel Superalloys

2.4.1 Nickel Superalloys

Superalloys are materials that can be used for applications involving extreme duty conditions i.e., operating temperature close to 70% of melting point temperature. In addition to withstanding the high temperature, they can retain the mechanical properties (static, fatigue and creep loading conditions) over a long period at this temperature. They can be Ni-based, Ni-Fe based and Co-based [90,91].

Among the superalloys, many of the advanced applications use Nickel Superalloys due to outstanding blend of corrosion resistance, strength, toughness, metallurgical stability, fabricability and weldability. Due to their exceptional combination of heat and corrosion resistance, they are employed to build components requiring good chemical resistance and strength at elevated temperature [92], like - turbines, rockets, heat exchangers, etc. The primary reasons for the exceptional characteristics of these superalloys are listed below:

a. The face-centred cubic structure permits a lower creep rate and controlled phase transformations.
b. Significant solubility of alloying elements into the matrix.
c. Controlling solidification can eliminate the grain boundaries preventing material failures at elevated temperatures and its usage in single-crystal form.
d. Precipitation phases can be formed that enhances high-temperature properties [91,92].

The composition and properties of common Nickel superalloys are provided as Annexure 1.

2.4.2 Summary of LDED of Important Nickel Superalloys

a) Inconel 718

There is a substantial quantity of research work published on LDED of Inconel 718 (IN718) due to its extensive applications in aerospace applications, like - turbine disk, shafts and compressor

blades, which demands high-temperature mechanical strength. Research on LDED of IN718 initiated with CO_2 lasers [93] and gradually moved on to fibre lasers in recent years[94]. The mechanical properties of LDED built IN718 samples are observed to be lower than wrought samples[95]. IN718 is precipitation hardened alloy and thus, solution treatment followed by ageing is the most common post-processing treatment for IN718 to precipitate the strengthening phases. With ageing, the mechanical properties can be brought close to the properties of wrought samples[95]. Precipitation of the phases during LDED can be modified by varying the process parameters or laser mode of operation[96,97]. Cracking phenomenon is not seen considerably during LDED of IN718 and can be controlled by fine-tuning the process parameters, if any[98].

b) Inconel 625

Inconel-625 (IN625) is a solid solution strengthened nickel superalloy, which is highly corrosive and oxidation-resistant with outstanding strength and toughness. LDED of IN625 initiated in mid-2000s using CO_2 lasers [62] and it is continuing with novel innovations in the fabrication of graded structures[99], composites[100], layer remelting[101], etc. for exciting engineering applications. The mechanical properties at different rastering pattern are observed to better than hot rolled and annealed material[62]. Solution treatment shows promising results to obtain tailored properties[102]. Corrosion and fatigue crack propagation properties of as-built IN625 are similar to that of wrought material[103,104]. The microstructure is mainly dendritic and the growth texture can be changed by altering LDED process parameters[105,106]. Further, high-temperature mechanical properties of LDED built IN625 shows the compatibility of the material for extreme duty applications[107].

c) Inconel 100

Inconel 100 (IN100) is a precipitation-hardened superalloy manufactured normally by casting or powder metallurgy. LDED of IN100 is not much attempted due to the solidification stress

cracking, which may occur in the heat-affected zone during rapid cooling. The cracking in the built samples is controlled by meticulously controlling laser energy input and the microstructure is mainly dendritic with carbide formation. The mechanical properties in the as-built condition are observed to be higher than conventionally built samples[108].

d) Inconel 690

Inconel 690 (IN690) is another high-performance nickel superalloy used in extremely corrosive and high-temperature application. The material is also susceptible to cracking, specifically ductility-dip cracking, which is generally developed due to the huge amount of strain generated during LDED[109,110]. Researchers are also working on to improve the properties of LDED built IN690 by building composites using ceramic reinforcements (like – TiC)[111].

e) Inconel 738

Inconel 738 (IN738) is a nickel superalloy showing exceptional high temperature and hot corrosion resistance. This is primarily due to the precipitation of γ′ phases (Ni_3 (Al,Ti)) [112]. One of the earlier works by Zhong et al. used CO_2 laser-based deposition and it was seen that cracking decreased with a reduction in laser energy. The mechanical strength in the as-built and heat-treated samples (aged condition) is found to be higher than that of as-cast samples, while the ductility in LDED and heat-treated samples are higher than that of as-cast samples[112]. However, reports on IN738-LC, a lower carbon variety of IN738 shows reduced cracking tendency with pre-heating at 1050°C[113]. Yield strength and ultimate strength of LDED built IN38-LC samples are ~ 14% higher than as-cast samples, while the elongation is ~ 44% higher than as-cast samples[113].

f) Rene Alloys

Rene based alloys, like - Rene41[114,115], Rene 104 [116]and Rene n5 [117]are investigated in some of the published research works. The research efforts are primarily focussed on process development for defect-free deposition by optimizing LDED processing parameters. Efforts to

understand the effect of post-processing, like – heat treatment and hot isostatic pressing is being pursued to improve the mechanical properties[114,116]. In addition to microstructural and mechanical characteristics, studies on oxidation behaviour are also investigated in the literature[117].

g) Waspaloy

Waspaloy is a precipitation-hardenable nickel superalloy generally deployed in aerospace applications. It is seen from the published literature that the efforts in the LDED of Waspaloy are primarily limited to the process window development and microstructural studies. The cracking tendency is generally seen in these alloys using continuous-wave and pulsed laser-based deposition[118,119].

2.4.3 Hastelloy-X

Hastelloy-X (Hast-X) is a Ni-Cr-Fe-Mo based superalloy that has been used for applications requiring high strength at elevated temperatures. The material is a single-phase alloy with FCC structure and the strength is obtained by solid solution strengthening from Cr, Mo and W. The presence of carbide will also provide strength to the material. The higher chromium content increases the oxidation and corrosion resistance of the material. The major advantage of deployment of Hast-X for applications involves the combination of strength, performance and corrosion resistance at elevated temperatures[120].

The history of the development of Hastelloy grade goes back to 1900s. The patent was granted to Haynes International in the year 1921 for a Ni-Mo based alloy, which aids the development of several trademarked alloys, including Hastelloy® B alloy. In 1922, the trade name Hastelloy® was invented by taking letters from the **Ha**ynes **Ste**llite A**lloy** = Hastelloy®. In 1931, Hastelloy® C alloy, the first of the entire family of C alloys, is introduced for the use in chemical plants, as well as aircraft engine components. During 1950s, there was a huge demand for high-temperature alloys and thus, new high temperature wrought alloys were developed.

MULTIMET® is one such alloys with Ni-Co-Cr-Mo-W as the major elements, which appeared in the year 1949. In 1950, a Co-based alloy called HAYNES® 25 alloy, was first manufactured. During this time, Haynes International received a contract to develop a gas turbine jet engine for various military and aerospace applications. In 1952, Hastelloy® X (Hast-X) was invented and just at the time of its invention, Pratt & Whitney was searching for a replacement material for its failed combustor for their JT-3 jet gas turbine engine. The alloy showed good performance during testing and it was used for JT-3 engine, which powered the first Boeing 707. Later, the material was deployed for JT-8D engine by Pratt & Whitney, which powered the first Boeing 727 aircraft. With time, Hast-X alloy remained as one of the commonly used nickel-base alloys for gas turbine hot section components[121].

Hast-X shows superior oxidation resistance to temperatures close to 982°C (1800°F) and higher. The specifications of Hast-X are covered in Section VIII of ASME Boiler and Pressure Vessel Code and part 7 of ASTM standards. The material is allowed to be used up to 900°C under Case 1321-2 (Special Ruling) to Sect. VIII, in unfired pressure vessels. The material is attractive for fabricating steam-based High-Temperature Gas Cooled Reactor (HTGR) components, like – lower cross ducts and upper cross ducts[122]. The nominal design temperature for the hot duct is 788°C, with chances of peak temperature rising up to 927°C[122]. The use of Hast-X is also permitted for applications in direct cycle HTGR with a nominal temperature of 816°C (1500°F). The material is also one of the candidates for fabricating components for gas-cooled reactor process-heat plants (VHTR)[123]. The composition and properties of Hast-X are provided in annexure 1 and annexure 2.

There has been a considerable amount of work done on LAM of Hast-X using LPBF. Wang et al. reported the processing of Hast-X using LPBF for the first time in 2011 using an EOS 270 system. It is observed that energy density in the range of 1.2 – 1.6 J/mm^2 is ideal for building components with minimum surface roughness and better dimensional accuracy.

Macroscopic density > 99.5% is achieved at laser energy density above 1.4 J/mm^2 and cracking is minimized when the laser energy density is greater than 2 J/mm^2. The mechanical properties for the built structure are yield strength of 800 MPa, the ultimate strength of 900 MPa and ductility of 28%, which is higher than conventional forged samples. Thus, the authors conclude that the LPBF built Hast-X is suitable for structural applications[124]. Wang et al. investigated the effect of hot isostatic pressing (HIP) on the mechanical properties of LPBF built Hast-X at room and elevated temperatures. The tensile properties of both LPBF and LPBF+HIP samples are higher than hot forged samples at room and elevated temperatures. The fatigue property is improved and scatter in fatigue performance is reduced by HIP process [125]. Tomus et al. investigated on controlling the microstructure of LPBF built Hast-X to build components without cracks and minimal porosity, by varying the scanning speed and composition of Mn and Si. It is observed that a low composition of Mn + Si is ideal for minimal cracking. However, low scanning speed and high composition of Mn + Si are ideal for achieving maximum density for the built structures [126]. However, Harrison et al. observed that cracking could not be eliminated during LPBF of Hast-X by varying the process parameters. It is also concluded that the most significant parameter affecting the cracking is laser power and scan speed is important in controlling the porosity of the built samples. Precipitation or grain boundary segregation is not observed in the samples and the composition mapping do not reveal any visible change in the composition across the crack. The authors attempted to modify the composition of Hast-X by increasing the amount of solid solution strengthening elements and reducing the composition of tramp elements. It is observed that the crack density reduced by 65% and material strength increased at elevated temperatures [127]. Etter et al. observed anisotropy in the mechanical properties in LPBF built Hast-X samples with lower values of Young's modulus for samples measured parallel to the build direction. However, it is observed that the anisotropy reduced with heat-treatment. It is also observed that scan strategies have a

significant effect on the texture of the growth [128]. Tomus et al. investigated the effects of post-processing on the microstructure and mechanical properties of LPBF built Hast-X in as-built, HIPed, heat-treatment, HIP + heat-treated conditions. The crystallographic texture is random at all heat-treated conditions and yield strength of the as-built sample is higher than the conventional wrought sample. Heat treatment and HIP reduces the yield strength, while ultimate strength reduces with heat-treatment and increases with HIP. This is also supported by an increase in ductility after HIP treatment. However, it is seen that a combination of HIP and heat-treatments increased the ductility to a value close to the ductility of conventionally processed samples. HIP improved the relative density of the samples significantly and the effect of heat-treatment on the porosity is negligible. As the material has low carbon content, it is observed that only a less number of finely dispersed carbides are present and it does not change significantly in size/ number density after heat treatment [129]. According to another work by Tomus et al., the major cracking mechanism during LPBF of Hast-X are hot-tearing and thermal cycling. Hot-tearing is the major factor governing the crack initiation, while thermal cycling governs the propagation of the crack. As per the study, the strain-induced during thermal cycling is lower than the maximum strain that can be taken by the material at high temperature. Thus, thermal cycling cannot be a reason for crack initiation. The hot tearing tendency can be controlled by varying the composition of Si and C, while the effect of Mn is found to be insignificant [130].

Marchese et al. performed an in-depth analysis of the microstructure and cracking during LPBF of Hast-X. It is observed that the melt pool is mainly consisting of fine growth with cellular and columnar shapes. The cracks are covered by the bright phases and the composition analysis on the bright phases along the cracks show the enrichment in Mo correlated with depletion of Ni, which indicates the presence of carbides. The presence of carbides coupled with high induced residual stress during the process acts as a source for crack formation [131]. Mertens

et al. investigated the effect of pre-heating on the porosity generation in LPBF built Hast-X and it is seen that when the combination of scan speed and laser power leads to lower value of laser energy density, the application of pre-heating can increase the part density [132].

Han et al. investigated the effect of the HIP on the microstructure, density, cracking and mechanical properties of LPBF built Hast-X. It is observed that the relative density increases from 99.3% to 99.98% after HIP treatment, though the gas porosity inside the built sample is not closed. Further, all the microcracks generated during the process are closed after the HIP. HIP processed samples has lower yield strength and ultimate strength as compared to that of the as-built sample. However, the fatigue life of LPBF built Hast-X samples increases after HIP treatment [133].

Marchese et al. investigated the behaviour of LPBF built Hast-X in as-built, HIP and heat-treated conditions. It is observed extremely fine precipitates of Mo-rich M_6C carbides along with other possible metastable Mo-rich carbides. The presence of globular and square-shaped Mo-rich M_6C carbides inside the grains and mix of elongated Mo-rich M_6C and Cr-rich $M_{23}C_6$ carbides at grain boundaries is observed. Subsequent solution annealing results in the dissolution of carbides at grain boundaries, but the globular and square Mo-rich M_6C carbides remains unchanged [134]. Kong et al. investigated the microstructural, mechanical and corrosion behaviour of LPBF built Hast-X and compared it with the wrought counterpart. The presence of M_6C carbide is detected and the mechanical properties are found to be higher than the wrought samples as observed by the other researchers. However, the corrosion resistance of LPBF built Hast-X is found to be better than the wrought samples in less aggressive medium, while LPBF built Hast-X corroded faster in severe environments. This is due to the fast dissolution of the voids and melt pool boundaries [135].

Sistiaga et al. performed an in-depth investigation on micro-crack free Hast-X built using LPBF in the as-built and heat-treated conditions. The heat-treated conditions used in the study are 2h

at 1177 °C + argon cooling (HT1) and 2h at 800 °C + argon cooling (HT2). It is observed that there is no change in the grain size after HT1 and HT2. However, HT2 has carbides at intergranular and transgranular regions, while HT1 samples do not contain carbides and a smaller amount of dislocations. The high-temperature tensile test indicates a decrease in yield and ultimate tensile strength for all conditions when the testing temperature is increased. A significant decrease in elongation is observed when tensile testing is performed at 750 °C. This is attributed to the carbide formation at the grain boundaries independent on the initial microstructure of the test specimens. High-temperature tensile test indicates a reduction in the yield strength and ultimate strength values for all the sample conditions when the test temperature is increased. However, a small reduction is only seen at 750 °C, which is primarily attributed to carbide formation at grain boundaries[136]. Sistiaga et al. also attempted to deploy a high power laser for LPBF of Hast-X and to improve the build rate. The authors could achieve a build rate of 16 mm^3/s using high power LPBF as compared to 6 mm^3/s using low power LPBF. The use of high laser power increases the melt pool width and results in coarser sub-grains and high dislocation density. Further, the effect of HIP on the mechanical properties of LPBF built Hast-X is investigated and HIP helped in attaining competitive mechanical properties as compared to conventionally processed Hast-X parts[137].

Keshavarzkermani et al. investigated to control the microstructure and mechanical properties of LPBF built Hast-X by varying the scan speed from 500 to 2050 mm/s at a laser power of 195W, a layer thickness of 0.04 mm, hatching spacing of 0.09 mm, 5mm stripe width with rotating scanning vectors (67°)[138].

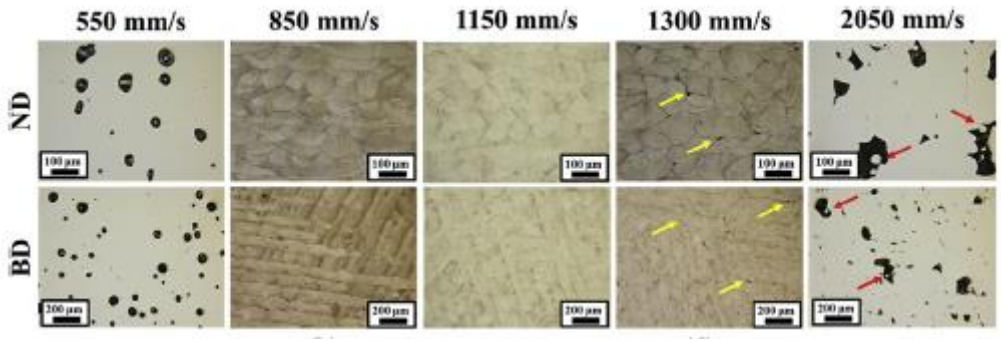

Figure 2.9: Variation of porosity with scan speed [139]

Figure 2.9 presents the variation of porosity with scan speed along the build direction (BD) and normal to build direction (ND). Major porosities are not observed at 850 mm/s, 1150 mm/s and 1300 mm/s, while 550 mm/s and 2050 mm/s samples show keyhole porosity and lack of fusion porosities, respectively. A reduction in grain size from 136 µm to 51 µm is seen when the scan speed is increased from 850 mm/s to 1300 mm/s. Maximum ductility of 65% is obtained at a scan speed of 850 mm/s and the highest yield strength and ultimate strength of 489 MPa and 706 MPa, respectively are obtained at a scan speed of 1050 mm/s[139].

2.5 Preliminary trials on LDED of Nickel Superalloys

It is observed from the literature that the most commonly processed nickel superalloy in LDED is Inconel 718. To understand the processing, microstructure, mechanical properties and post-processing on LDED built nickel superalloys, preliminary investigations are carried on LDED built Inconel 718. The built structures are subjected to post-heat treatment using an indigenously developed furnace (maximum temperature of 1200°C) as summarized in Table 2.1. The temperature for post-heat treatment is selected from the range of temperature provided in the literature for the solution treatment of IN718 [140].

Table 2.1: Post-heat treatment parameters

Treatment	Solution treatment
HT950	At 950°C for 1 hour soaking time followed by water quenching

HT1050	At 1050°C for 1 hour soaking time followed by water quenching

The microstructures of thin walls built by LDED (in as-built and post heat-treated conditions) are studied using an optical microscope. Figure 8a presents the micrograph of the sample in the as-built condition.

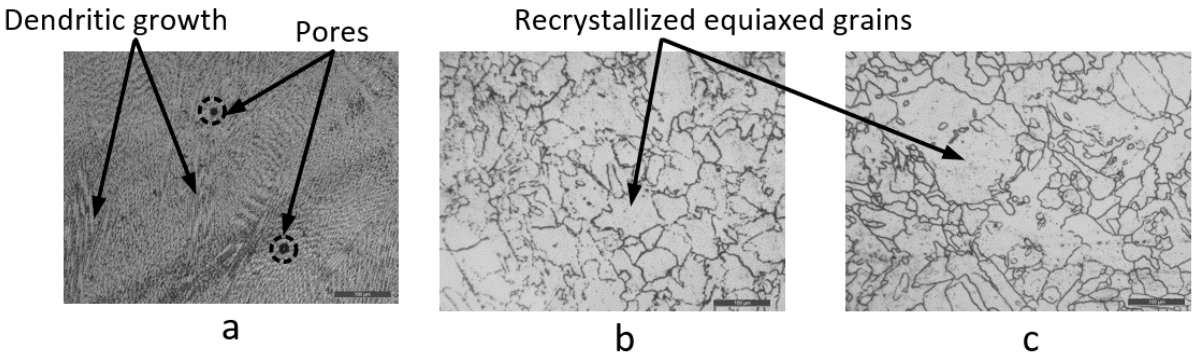

Figure 2.10: Microstructure of a) as-built b) HT950 c) HT1050 samples

Few pores at isolated locations in the deposits are also observed. The typical size of these pores is less than 15 microns. Microstructure examinations of LDED deposits of IN718 reveal dendritic structure as shown in Figure 2.10a. The direction of dendrite growth is along the direction of deposition due to preferential cooling. The dendritic microstructures are developed as a result of the rapid cooling rate during LDED. Figure 2.10b and 2.10c present the microstructure of the deposit after heat treatment at 950°C (HT950) and 1050°C (HT1050), respectively. After post-heat treatment, the homogenized microstructure is observed in all samples with dissolved dendrites. The columnar grains present in the as-built samples are not visible in the HT950 and HT1050 samples. Recovery, recrystallization and grain growth takes place during post-heat treatment. During recovery, the internal stresses are relieved and mainly takes place at a lower temperature without affecting the mechanical properties of the material. During recrystallization, new grains are formed with the same lattice structure with

approximately the same dimensions in all directions as appropriate conditions are provided. Thus, recrystallized equiaxed grains are formed during post-heat treatment. Further, the coalescence of grains during grain growth increases the size of grains leading to a reduction in strength and hardness with enhanced ductility. The micro-hardness of IN718 samples are examined in as-built and post-heat treated condition. Figure 2.11 presents the variation of the hardness along the cross-section. It can be observed that as-built samples have higher hardness than post-heat treated samples. The average hardness of as-built, HT 950 and HT1050 are 234 ± 7 $HV_{1.96N}$, 220 ± 6.1 $HV_{1.96N}$ and 206 ± 5.9 $HV_{1.96N}$, respectively. Higher hardness of as-built sample can be due to the fine dendritic microstructure usually observed in LDED samples owing to the high cooling rate [105]. A reduction of 6 % and 12 % in micro-hardness is observed for HT950 and HT1050 samples, respectively as compared to that of as-built samples. Grain agglomeration and coarsening due to the post-heat treatment can be the reason for the reduction in microhardness of post-heat treated samples as per Halls-Petch relationship. Further, the result is compared with IN718 samples made by LPBF and it was observed that the average micro-hardness is 319 $HV_{1.96N}$, 307 $HV_{1.96N}$ and 260 $HV_{1.96N}$ in the as-built, HT950 and HT1050 condition, respectively [141]. It may be observed that the trend remains similar while the higher hardness is observed in LPBF samples. This can be due to the faster scanning rate as compared to LDED, which results in finer microstructures.

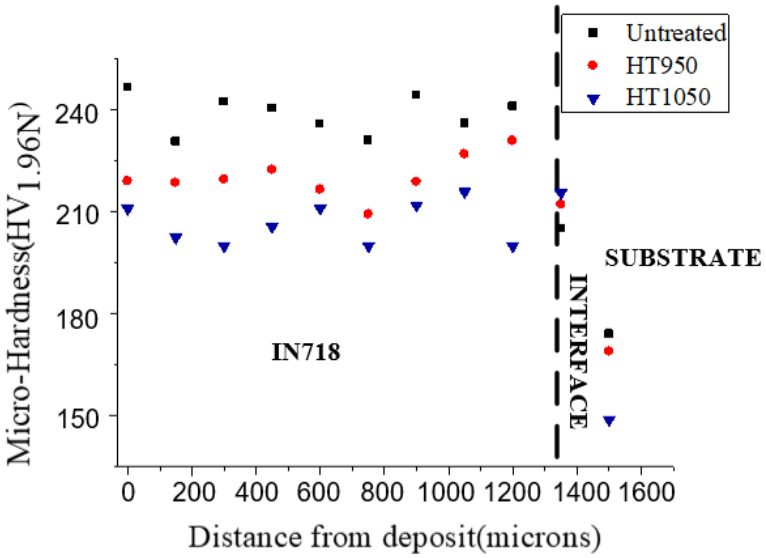

Figure 2.11: Variation of hardness along the cross-section

Ball indentation tests (BI) are performed for comparing the energy storage capacity and maximum displacement of the material using a single cycle with a maximum load of 80 N at a rate of 0.1 mm/min with unloading cycle till 10 N load. Figure 2.12 presents the typical load-displacement curve obtained during the BI of LDED samples. The maximum displacement for as-built, HT950 and HT1050 samples are 0.050 mm, 0.070 mm, and 0.079 mm, respectively. The relatively lower depth of penetration in the as-built sample is primarily attributed to the higher hardness. The areas under the loading and unloading curve represent the entire work performed during loading and the reversible elastic contribution of the total work, respectively. The difference between the two areas represents the energy absorbed in plastic deformation, which can be correlated to the energy stored by the material. The area under the curves of as-built, HT950 and HT1050 samples are 0.49 N-mm, 1.09 N-mm, and 1.7 N-mm, respectively. BI studies reveal the improvement in energy storage capacity by 2.22 and 3.46 times for HT950 and HT1050, respectively to that of as-built samples.

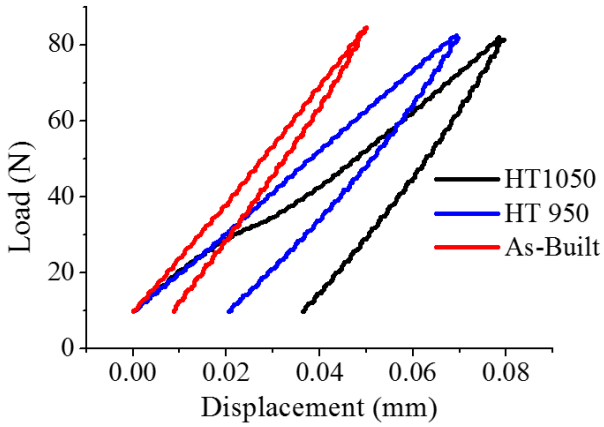

Figure 2.12: Load displacement curve during BI

2.6 Gap Areas

It is observed from the literature that LDED has inherent advantages making it suitable for several applications in engineering, medical, etc. The freedoms offered by LDED includes an optimum combination of shape design freedom and material design freedom along with logistics freedom and post-processing freedom. It is essential to deploy LDED technique for fabricating challenging engineering components to utilize the various freedoms offered by the technology. Even though the applications of LDED are more common for cladding, coating and repairing since its inception, the technology is also explored to build complex-shaped functional components. Some of the renowned industries using LDED for building large scale components are: GKN aerospace and Mitsubishi Electric. One of the studies performed by Optomech clearly shows the advantages of using LDED for building complex shaped engineering components. As per the case-study published by Optomech, the average time for building a rocket nozzle conical part using LDED and LPBF are 16 hours and 240 hours, respectively. This difference in build time reflected on to the estimated price as $3,200 and $16,800 for LDED and LPBF, respectively[142]. LDED receives an edge over LPBF in terms of build time and cost associated with fabrication of components due to the high deposition rate in LDED. This shows that an LDED system is suitable for building relative large components with intricate geometries.

The technology is also useful to build near-net-shaped components of difficult to machine materials, as it facilitates minimization of the energy and time to be spent in machining the components. The machining of difficult to machine materials, like – nickel superalloys, can result in excessive tool wear and minimal material removal rate. In addition, nickel superalloys are significant for various extreme duty applications. The literature review indicates that only limited number of nickel superalloys are explored by LDED. It is found that the significant amount of works on nickel superalloys are carried out on Inconel 718 and Inconel 625, with a few published works on Inconel 100, Inconel 690, Inconel 738, Rene and Waspaloy. Most of the studies presented in the literature are focused on the microstructure and mechanical properties of the LDED built structures. The literature indicates that material-specific processing strategies are essential for defect-free deposition and the mechanical properties are of LDED built components is a function of microstructure, processing strategies and parameters.

Further, Hast-X is one of the materials suitable for high-temperature applications in the power sector and it is suitable for fabricating structural and heat-exchanger components for advanced power sectors [37,38,123] and aerospace applications. Thus, it is necessary to develop LDED technology to process Hast-X. The literature survey summarizes that there is some amount of work done on LPBF of Hast-X, which includes the process window development for defect-free parts, post-processing, characterisation and methods to improve the build quality. It was concluded by several researchers that the process window development is critical for processing Hast-X. It is also critical to tailor the microstructure, mechanical properties and surface properties to qualify the components for intended applications. The gaps identified from the literature are summarized as:

a) There is limited published literature on LDED of Hastelloy grade materials, like - Hast-X, showing a knowledge gap especially on the effect of process parameters on the track geometry and track quality for defect-free deposition using LDED.
b) LDED built thin wall structure (multi-layer deposition) is basic block for building complex engineering components and thus, it is necessary to understand the characteristics of thin walls. There is a lack of comprehensive studies on the effect of process parameters and interlayer delay conditions on the geometry, microstructure and mechanical properties of LDED built nickel-based superalloy wall structures.
c) Bulk structures (multiple overlapped tracks and multi-layer deposition) are necessary to build complex-shaped engineering components with higher build rate. Literature shows the studies on the microstructure and mechanical properties of fusion welded [143]and Laser Powder Bed Fusion (LPBF) processed Hast-X[124,125,134–138,126–133]. However, there is no literature available on the microstructure and mechanical properties of LDED built Hast-X bulk structures.
d) LDED built bulk structures are generally subjected to several in-situ and ex-situ treatments for defect rectification and tailoring its properties [47]. In-situ Sequential Layer-by-layer Laser Remelting (SLLR) can be deployed for reducing the porosity, grain refinement and improving the surface finish of LDED built components. Hast-X, being a solid solution strengthened superalloy, requires probing into the microstructural and mechanical characteristics of LDED built Hast-X in solution treated condition. There is no study available in the open literature on the effect of in-situ SLLR and solution treatment on the behaviour of LDED built Hast-X components.
e) Literature confirms the suitability of Hast-X for building heat exchangers[40]. However, there is no study available in the public domain defining the LDED methodology using wall and bulk structures for building Hast-X heat exchanger.

In view of the above, there is a strong need for in-depth scientific understanding and detailed investigations on the processing, analysis of microstructure and mechanical properties of LDED built Hast-X thin wall and bulk structures at different process conditions. Thus, it is proposed to take up the research on LDED of Hast-X in the present work, which involves the process development, geometry analysis, characterisation of bulk and wall structures, post-processing of built structures and lastly, the development of prototype heat exchanger to demonstrate the applications of LDED built Hast-X.

2.7 Aim and Objectives

The thesis work aims to employ the versatile LDED to deposit Hast-X thin wall and bulk structures; and investigate their properties comprehensively through experimental studies. The primary objectives of the work are:

a) Experimental Analysis and Modelling of LDED built Hast-X Single Tracks.
b) Effect of Laser Energy per unit Powder Feed and interlayer delay period on LDED built Hast-X thin walls.
c) Elucidating the microstructural and mechanical behaviour of LDED built bulk structures.
d) Understanding the effect of In-situ Sequential Layer by Layer Re-melting (SLLR) and post heat-treatment of Hast-X bulk structures.
e) Process methodology for LDED of Printed Circuit Heat Exchanger using thin wall and bulk structures.

2.8 Flowchart of thesis

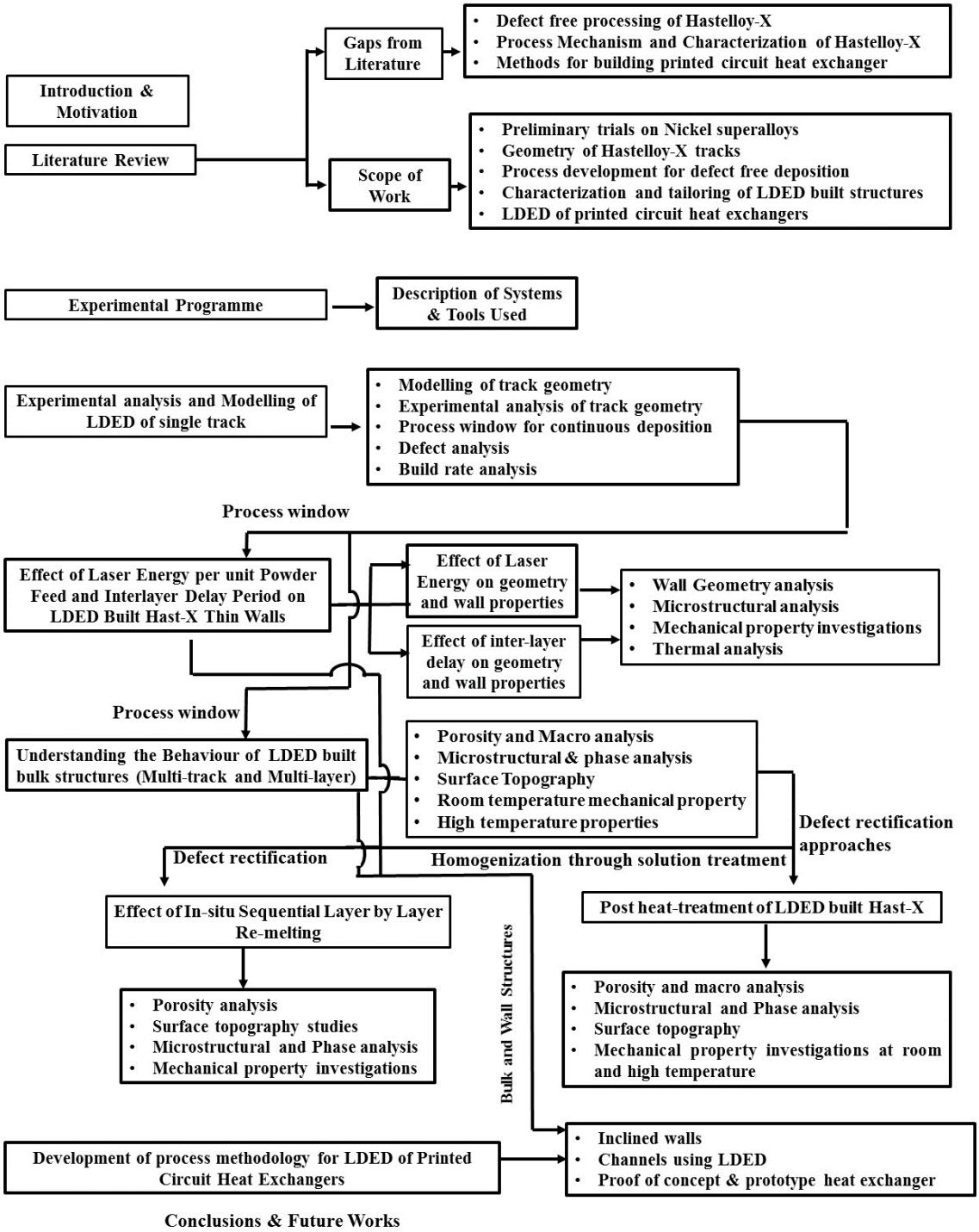
Introduction & Motivation
Literature Review
Gaps from Literature
Defect free processing of Hastelloy-X
Process Mechanism and Characterization of Hastelloy-X
Methods for building printed circuit heat exchanger
Scope of Work
Preliminary trials on Nickel superalloys
Geometry of Hastelloy-X tracks
Process development for defect free deposition
Characterization and tailoring of LDED built structures
LDED of printed circuit heat exchangers
Experimental Programme
Description of Systems & Tools Used
Experimental analysis and Modelling of LDED of single track
Modelling of track geometry
Experimental analysis of track geometry
Process window for continuous deposition
Defect analysis
Build rate analysis
Process window
Effect of Laser Energy per unit Powder Feed and Interlayer Delay Period on LDED Built Hast-X Thin Walls
Effect of Laser Energy on geometry and wall properties
Wall Geometry analysis
Microstructural analysis
Mechanical property investigations
Thermal analysis
Effect of inter-layer delay on geometry and wall properties
Process window
Understanding the Behaviour of LDED built bulk structures (Multi-track and Multi-layer)
Porosity and Macro analysis
Microstructural & phase analysis
Surface Topography
Room temperature mechanical property
High temperature properties
Defect rectification approaches
Defect rectification
Homogenization through solution treatment
Effect of In-situ Sequential Layer by Layer Re-melting
Post heat-treatment of LDED built Hast-X
Porosity analysis
Surface topography studies
Microstructural and Phase analysis
Mechanical property investigations
Porosity and macro analysis
Microstructural and Phase analysis
Surface topography
Mechanical property investigations at room and high temperature
Bulk and Wall Structures
Development of process methodology for LDED of Printed Circuit Heat Exchangers
Inclined walls
Channels using LDED
Proof of concept & prototype heat exchanger
Conclusions & Future Works

2.9 Summary

LDED captivates advantages of shape design and material design freedom, which attracts its deployment for several engineering applications. Hast-X is one of the materials suitable for high-temperature applications in the power sector and aerospace sector and its applications are increasing continuously. Further, there is no study available in public domain on LDED of Hast-X structures and investigations on its geometric, microstructural and mechanical properties. Thus, the present work aims to employ LDED technique to deposit Hast-X thin wall and bulk structures and investigate their properties comprehensively. The next chapter presents the experimental programme, which includes the LDED system details, various sample preparation systems and characterisation tools.

Chapter 3 : Experimental Programme

3.1 Introduction

In the present chapter, the experimental setup and characterisation tools used for Laser Additive Manufacturing, post-processing and analysis are described. It includes the range of tools from macroscopic to microscopic analysis and mechanical testing system. The details of experimental system used for building structures/ samples are described in the following passage.

3.2 Experimental Setup

3.3.1 Laser Directed Energy Deposition (LDED) System

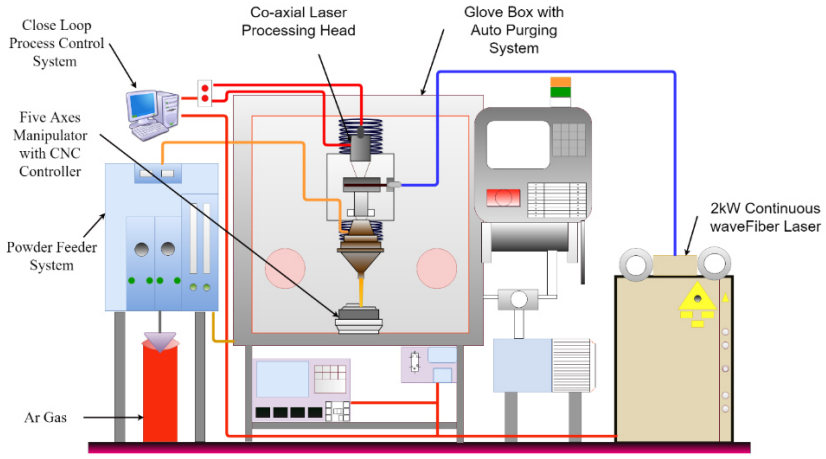

Figure 3.1: Schematic diagram of the LDED setup used for experiments

LAM activities at Raja Ramanna Centre for Advanced Technology (RRCAT), Indore, India are initiated in the year 2003. The indigenously developed AM technology at RRCAT was initially known as “Laser Rapid Manufacturing (LRM)”, which used high power CO2 lasers for material deposition. A number of materials were investigated using the developed LRM

system [13,17,144–148]. During 2012, LAM activities at RRCAT extended to the deployment of high power fibre lasers due to the inherent advantages offered by fibre lasers. Today, it is a full grown activity offering not only, system and process solutions to in-house DAE applications, but also extending the facility to various national labs and reputed academic institutes for front line research work in the area of LAM [149–156].

In the present work, an indigenously developed LDED system at Laser Additive Manufacturing Laboratory, RRCAT is used. Figure 3.1 presents the schematic of the LDED system used for experiments. The system uses a high-power laser energy source to melt the substrate/ previously deposited layer and feed material taken in powder form to build three-dimensional components in a layer-by-layer fashion. Figure 3.2 (a) presents the photographic view of the LDED system used for the experiments.

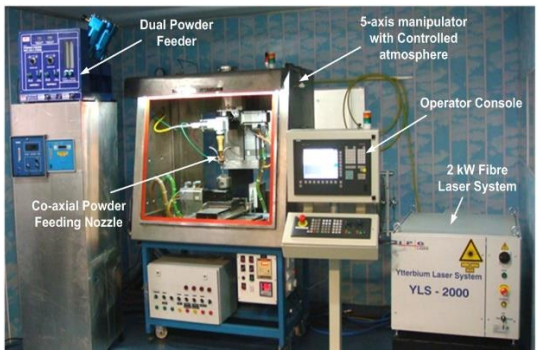

(a)

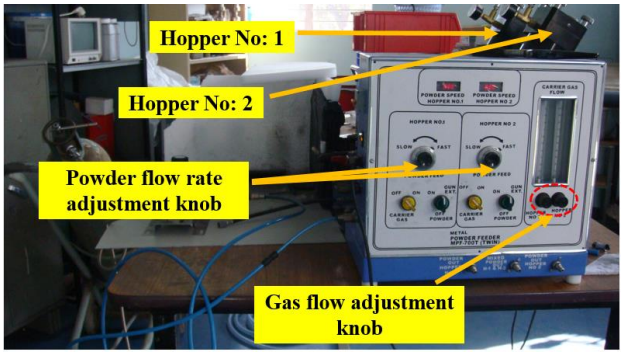

(b)

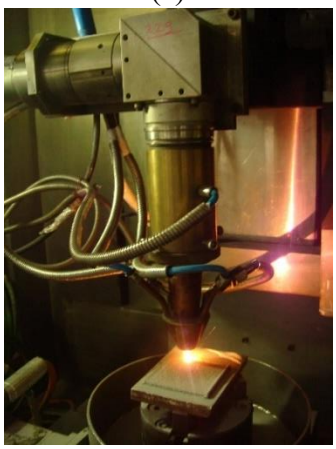

(c)

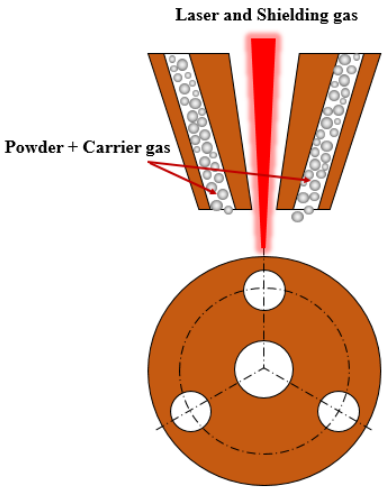

(d)

Figure 3.2: LDED system (a) photographic view (b) Twin powder feeder (c) Co-axial nozzle photograph (d) schematic of co-axial nozzle

The system consists of the following sub-systems such as:

i. Computer Numerical Control (CNC) System
ii. Five-axis Computer Numerical Control (CNC) manipulator in controlled atmosphere chamber
iii. 2 kW fibre laser system
iv. Twin powder feeder system
v. Coaxial powder feeding nozzle
vi. Operator console
vii. Oxygen and Moisture Analyser

The detailed system description is as follows:

i. Computer Numerical Control (CNC) System

Computer numerically controlled (CNC) systems are used to control the machine and processes by providing capabilities ranging from simple point-to-point linear movement to complex algorithms with simultaneous multiple axes movement. Siemens 810 D controller is used as the CNC controller in the present system. In addition to the job manipulation, it also controls the laser on/ off, central gas on/ off and powder on/ off.

Table 3.1 Different Axes of the LDED system

Axes	**Description**	**Stroke length/ Rotation**
X	linear traverse of the work table to the X direction, mutually perpendicular to Y & Z axes	250 mm
Y	linear traverse of the work table to the Y direction, mutually perpendicular to X & Z axes	250 mm

Z	linear traverse of the Nozzle head to the Z direction, mutually perpendicular to X & Y axes	250 mm
V	tilt axis about Y-axis for tilting laser head	±110°
W	the continuous rotational axis of the work table about the Z-axis	360º

ii. Five-axis Computer Numerical Control (CNC) manipulator in a controlled atmosphere chamber

The system uses a 5 axis workstation placed inside controlled atmosphere chamber (glove box). However, in the present work, 3 axes, i.e. X, Y and Z are only used for experiments. Preloaded ball screws with linear motion guides are used in the workstation. Table 3.1 presents the details about the axes of the LDED system. Y-axis is mounted over the X-axis and W-axis and Z-axis and V-axis are mounted on the top. Repeatability, accuracy and resolution of the machine are ± 5 µm, ± 10 µm and 1 µm, respectively. The glove box with appropriate gas feeding system facilitates the usage of inert gas to provide an inert atmosphere for LDED process. The glove box is provided with an antechamber for loading/ unloading of components/ parts on the workstation during the processing without impeding the control atmosphere.

iii. 2 kW fibre laser system

LDED system consists of a 2 kW continuous wave Ytterbium fibre laser as the thermal energy source for melting the powder particles. The laser system used has a nominal output power ranges from 50 W -2050 W with a wavelength of 1080nm and output modulation rate of the laser system is 50 kHz. The system has switching on/off time of 80 µs. The laser beam is randomly polarized with a beam product parameter value less than four. The overall size of the laser system is 1.2 m × 1.2 m × 0.75 m. The laser system also consists of a fibre delivery system with a core diameter of 50 µm. The system has a collimator of 160 mm focal length facilitating

laser beam of 20 mm and it is focused with refractive optics (material: Quartz) of 200 mm focal length. The focusing optics is the part of the co-axial nozzle used for deposition.

iv. Twin powder feeder system

Twin powder feeder system is used to supply powder to nozzle head. The make and model of the twin powder feeder used are MC Thermal Spray Equipment, India and MPF-700T, respectively. Figure 3.2 (b) presents the photographic view of twin powder feeder used for LDED. The powder feeder is volumetric controlled type. Twin powder feeder provides the capability for the system to feed two materials simultaneously in pre-set ratio to melt pool for building bimetallic components, functionally graded structures, composites, etc. The powder feed rate ranges from 2 -40 g/min with a reproducibility of ± 0.2 g/min.

v. Coaxial Powder Feeding Nozzle

LDED deploys a co-axial nozzle consisting of a central hole and three concentric holes of 2 mm diameter at 120º apart. The central hole carries the laser beam and central gas, while the outer holes carry the powder with the help of carrier gas. Figure 3.2 (c) and (d) presents the photographic view and schematic of the coaxial nozzle used for LDED, respectively. Argon is used as the carrier gas and shielding gas. Highly pure Argon gas with >99.9993 % purity having oxygen and moisture less than 2 ppm, nitrogen less than 3 ppm and total hydrocarbon less than 0.2 ppm is used.

vi. Operator Console

It acts as an interface between the user and the controller. It facilitates the data entry (G & M codes), safe operation and monitoring. It provides three mode of operation: jog, manual data input and automatic. The system has a dedicated button for emergency stop to be used in case of exigency. It has Siemens 810 D control panel and multi-level soft touch keyboard with E-stop and feed control.

vii. Oxygen and Moisture Analyser

There are oxygen and moisture sensors installed in the system for getting the information about the existing level of oxygen and moisture content inside the glove box. To achieve the desired level of purity in the glove box, chamber is evacuated to 50 mbar lower than the atmospheric pressure and Argon gas is purged with higher rate. Normally, it takes ~ 30 hours to achieve purity < 20 ppm.

The process parameters used for LDED experiments are presented in Table 3.2.

Table 3.2: Process parameters used for LDED experiments

Process parameter	**Value**
Laser power	600 – 1600 W
Scan speed	0.3 -0.7 m/min
Powder feed rate	5 - 8 g/min
Laser spot diameter	~ 3 mm
Argon gas flow rate	6 - 8 litres per minute

3.3.2 High-Temperature Furnace

To study the effect of heat-treatment on the microstructure and mechanical properties, solution treatment is carried out using a high temperature muffle furnace with quenching facility (Make: Therelek, Model: Bottom Loading Furnace). The maximum temperature at which the furnace can operate is 1400°C. Solution treatment is carried out by raising the temperature of the sample from room temperature (30 °C) to 1177° C. The samples are heat-treated by soaking for a time duration of 60 – 120 minutes depending on the section thickness followed by water quenching to room temperature.

3.3 Sample Preparation and Characterisation Tools

This section describes the various sample preparation systems and characterisation tools used in the study. They are as follows:

3.3.1 Sample Preparation

i. Sectioning and Mounting

Sectioning is the process of cutting the samples from the deposits for metallographic analysis and characterisations. Sectioning is carried out using a *Concord* make and *DK7732* model Wire Electric Discharge Machining (WEDM) as per the requirements. In order to prepare the samples for microscopy and microhardness, the samples are epoxy mounted. Mounting aids to improve the handling of samples during polishing and characterisation. For cold mounting, hardener and resin are mixed in the ratio of 1:2. Dobeckot 505C epoxy resin is used for mounting because of its low viscosity and capability to cure in moist conditions. Hardener EH411 is used to harden the resin. For efficient mounting without any leakage, a small amount of grease is applied on the surface before keeping the mould. After placing the sample inside the mould, the resin-hardener mixture is poured into it. The mixture is then kept to cure for 8 - 12 hours. After mounting, the bottom surface of the mould is subjected to facing operation using Lathe to obtain a surface parallel to the top surface of the mould.

ii. Grinding and Polishing

The grinding and polishing step in metallographic specimen preparation is used to obtain a mirror finish surface for porosity examination and micro-hardness measurements. Further, the polished samples in etched condition will be used for microstructural analysis. Grinding and polishing are performed by using a *Chennai Metco* make and *Bainpol* model semi-automatic polishing machine. Initially, the mounted samples are subjected to coarse grinding in wet condition using 80 and 180 grit silicon carbide adhesive papers of 8'' diameter. The final objective of coarse grinding is to achieve a flat surface. Further, medium and fine grinding is carried out using 240, 320, 400, 600 and 1000 silicon carbide adhesive papers of 8'' diameter. The speed of the disc is set to 200 rpm for grinding and pressure applied against the mounting

is 1 bar. Subsequent to fine grinding, polishing is used to obtain the mirror finish on the sample surface. It includes the use of abrasives (suspended in a water solution) on a cloth-covered electrically powered wheel. Final mirror finishing on the samples is done using velvet cloth polishing with the help of colloidal silica solution.

iii. Electrolytic Etching

The electrolytic etching is used to reveal the microstructural features and it is a metal etching process working on the basis of electrolysis. The system involves the deployment of an electrolyte, an anode, and a cathode. The sample to be etched is used as the anode and is connected to the positive terminal of the direct electric current. SS 304L rod is used as the cathode for etching in the present work. A *Scientific* make and *PSD3005* model voltage sources are used as direct current source for electrolytic etching.

The etchant for Hastelloy-X is selected according to ASTM standard E 407-99. The oxalic acid solution is used for electrolytic etching with 10 gram of oxalic acid mixed in 100 ml of distilled water. The etching is carried out at 12 V for 5 – 10 seconds.

3.3.2 Characterisation

i. Stereo Microscope

Stereo microscope is a variant of optical microscope used for low magnification observation of samples. It has two spatially separated optical paths and when the user looks through a stereo microscope, the two light paths image the specimen at slightly different angles, which is interpreted as the stereo vision. A *Leica* make and *S APO* model stereo microscope is used in the present work to measure the track geometry and analyse surface topography of the built samples.

To measure the track geometry, the deposited tracks are analysed in the polished and etched condition. Leica software is used to measure the geometrical features such as track width and track height. To analyse the surface topography, the as-built LDED surface is analysed directly under the stereomicroscope from 1 X to 8 X magnification.

ii. Optical Microscope

An optical microscope generates a magnified image of a sample using an objective lens and enlarges the image additionally using an eyepiece permitting the user to observe the sample by the naked eye. Inverted optical microscope of *Omnitech* make and *Metagraph – A* model is used for the analysis of sample.

The mirror polished samples are used for analysing porosity and quantified using *Quantimet* software. The etched and polished samples are subjected to microstructural studies and the microstructural images are acquired using 4X – 40X magnification. *Quantimet* software attached to the optical microscope is used to measure the size of the microstructural features.

iii. 3D Scanner

3D scanner works on the principle of laser triangulation, which uses a laser beam projected at a known angle onto a sample and the time period of travel of the reflected laser ray from the sample is used to capture the point on the sample surface. LDED built walls are scanned using a *Hexagon* make and *RA-7525 SEI* model laser scanner having a repeatability of 20 µm and accuracy of 29 µm. The developed 3D model data in the as-built condition is analysed using *INSPECT 5.5 plus* software for geometrical studies.

The scanned 3D model is imported to the *INSPECT 5.5 plus* software and alignment using 321 principle is carried out to align the 3D model in such a way that the top surface of the substrate is normal to Z-axis, length of the wall is aligned along the x-axis and a point on the datum plane

(substrate surface) is fixed to be the origin of the coordinate system. Thus, X-axis corresponds to the direction along the length of the wall, Y-axis relates to a direction indicating the distance between walls and Z-axis shows the build direction or height of the wall.

iv. X-ray Fluorescence

X-ray Fluorescence (XRF) is an analytical technique that uses the interaction of X-rays with a material to determine the chemical composition of elements. When a sample is exposed to X-rays, the atoms in the sample absorb the energy by ionizing. This leads to ejection of electrons from the lower energy levels and they are substituted by electrons from higher energy orbital. This results in energy release as characteristic X-rays indicating the type of atom present. A *Bruker* make and *S1 TITAN 600* model handheld XRF analyser is used in the present work.

XRF technique is used to confirm the composition of the major elements present in the powder used for deposition. Rh X-ray source having a beam spot diameter of 5 mm is used for the analysis.

v. Scanning Electron Microscopy and Electron Back Scattered Diffraction

Scanning Electron Microscope (SEM) uses focused beam of electrons and they are scanned along the sample to obtain information about the surface topography, microstructure and chemical composition. When the electrons interact with atoms in the sample, various signals are produced and they contain information about the surface topography and composition of the sample. The secondary electrons generated during the electron-sample interaction is used to obtain the microstructure and surface topography. Characteristic X-rays generated during the electron-sample interaction is used for detecting the composition of the elements in the sample. In Electron Back Scattered Diffraction (EBSD) analysis, an electron beam interacts with a titled sample and the diffracted electrons generate a pattern on the fluorescent screen. This pattern is characteristic of the crystal structure and orientation of the region under study.

A *ZEISS* make and *Zigma* model field emission SEM with an Energy Dispersive Spectroscopy (EDS) attachment is employed to observe morphology, surface topography, microstructure and composition. A *Zeiss* make and *Gemini 300* model SEM having an EBSD attachment is used for EBSD analysis.

Powder morphology is analysed by spreading the powder particles on the conductive carbon adhesive tapes. Surface topography is analysed on the as-built surface in secondary electron mode. The microstructure is examined on the polished and etched samples using secondary electron mode. EDS is used to analyse the composition of the samples using elemental mapping. EBSD is carried out on a mirror-polished sample to evaluate the grain orientation and grain size along the cross-section.

vi. X-ray Diffraction

X-ray diffraction (XRD) uses the dual wave/particle nature of X-rays for extracting information related to the crystal structure of the materials. XRD uses diffraction pattern for identification and characterisation of compounds. XRD uses monochromatic X-rays and when these X-rays strike the target material, it undergoes scattering and the scattered X-rays undergo constructive and destructive interference. This process is known as diffraction and it follows the Bragg's law. A *Bruker* make and *D8 Advance* model XRD system is used for analysing the samples.

XRD analysis is carried out from 30 – 80° using a step size: 0.02° and dwell time: 0.5 s. Cu Kα radiation (λ = 1.54 Å) at 40 kV and 40 mA is used in a continuous scan mode.

vii. Confocal Microscope

In a confocal microscope, laser light is focused onto a specific spot at a definite depth within the sample, which leads to the emission of fluorescent light. The optical signals that are out of focus will be cut off using a pinhole inside the optical pathway, which allows only the

fluorescence signals from the illuminated spot to reach the light detector. The images of a single optical plane are obtained by scanning the sample in a raster pattern. An *Olympus* make and *LEXT 3D* model Confocal microscope is used in the present work. The microscope has a planar resolution of 0.12 μm and an unevenness resolution of 5 nm. The microscope features both high pixel density and high inclination sensitivity, which enables measurements on surfaces with fine irregularities and steep angles.

Confocal microscope is used to measure surface roughness and depth profiling. For roughness analysis, cut-off length of 800 μm and evaluation length of 4000 μm are used. Gaussian filter is used for the analysis and 50X objective lens is used.

viii. X-ray based Residual Stress Tester

X-ray diffraction can measure residual stress using the distance between crystallographic planes (d). The standard d-$\sin^2\varphi$ method is used for measuring residual stress. A *Proto Manufacturing* make and *iXRD* model X-ray residual stress measurement tester is used in the present work.

The deposit is subjected to residual stress measurement at different points on the top surface without machining or separation from the substrate. The (311) diffraction peak at 155° is used for residual stress measurement using XRD principle. MnKα source having a wavelength of 2.1 Å and a spot diameter of 2 mm is deployed for stress measurement.

ix. Micro-hardness

Vickers micro-hardness test is used to measure the microhardness of the material, which consists of a diamond indenter in the form of a pyramid with opposite phases kept in an angle of 136°. In this test, the diamond indenter is pressed gently over the surface of the mirror polished sample for applying plastic deformation. The indenter is allowed to give the plastic deformation to the material until the dwell time is finished. After the dwell time, the indenter

is released and the diagonal of the indentation is measured by using optical technique. *Omnitech* make and *F.Auto* model Vickers micro-hardness tester is used for the test.

Micro-hardness testing is carried out using 1.96 N load and 10 second dwell period on a mirror polished sample. Equation 3.1 is used for calculating the micro-hardness values.

$$HV = \frac{\text{Constant} \times \text{Test Force}}{(Average\ Indent\ Diagonal)^2}\ (\text{kgf/mm}^2) = \frac{1.8544 \times F}{(davg)^2}, \quad (3.1)$$

$$d_{avg} = \frac{d_1 + d_2}{2}$$

Where, d_1 and d_2 are the two diagonals of the indentation and F is the applied load.

x. Micro-tensile testing

Micro-tensile testing is carried out using *Zwick Roell* make *Kappa CS* model Universal Testing Machine (UTM). Micro-tensile testing is carried out using a load cell having a maximum loading capacity of 1 kN. The micro-tensile testing is performed to evaluate the yield strength, ultimate strength and ductility of the LDED built Hast-X bulk structures. The dimensions used for preparing the micro-tensile samples are presented in Figure 3.3. The testing is carried out at a strain rate 10^{-3} s^{-1}.

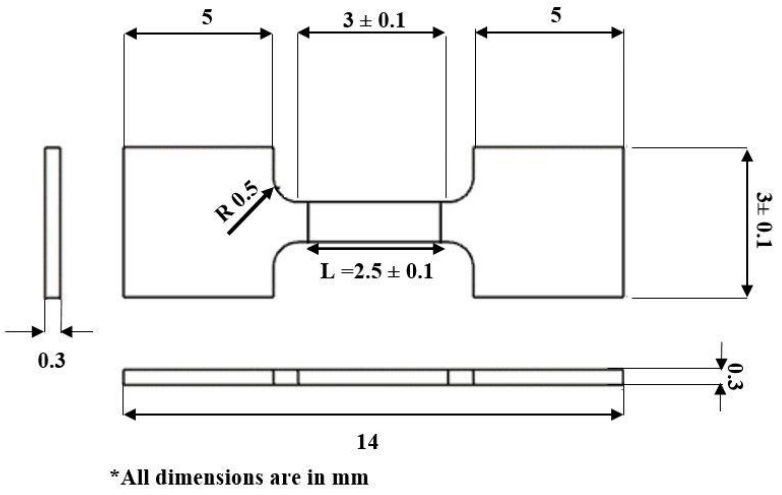

Figure 3.3: Drawing of micro-tensile samples

xi. High-temperature Automated Ball Indentation

Automated Ball Indentation (ABI) uses the applied load and measured depth of indentation to determine the mechanical properties of the material. It employs theories of elasticity and plasticity along with semi-empirical relations, which govern the material behaviour during loading [20]. The strain and stress at any time are functions of penetration depth and indentation force, respectively. The plastic strain is determined using periodic partial unloading and is estimated by subtracting elastic depth from total depth. Figure 3.4a displays loading pattern used in ABI, where P_1, h_{p1}, h_{p3}, h_{e1}, and h_{t1} are the load applied during the first cycle, plastic depth of indentation after first indentation cycle, plastic depth after third indentation cycle, elastic recovery depth after first indentation cycle, total depth (plastic and elastic depth) after first indentation cycle, respectively. Indentation force vs depth data is used to calculate the true stress and true plastic strain values using elasticity and plasticity theories and Holloman equation is used for estimating materials strain-hardening exponent (n) and ultimate strength (US).

For each cycle, the total depth of penetration (h_t) is measured during loading and total indentation diameter (d_t) is determined from the measured depth using the Equation 3.2. Plastic depth h_p is deployed for calculating plastic diameter d_p by iterating Equation 3.3 where, E_{spec} is the Young's modulus of the specimen, E_{ind} is Young's modulus of indenter [20] and D is the indenter diameter (D = 0.76 mm).

$$d_t = 2\,(D\,h_t - \mathrm{h}_t^2)^{1/2} \tag{3.2}$$

$$d_p = \sqrt[3]{2.735\,P\,D\;\frac{[\frac{1}{E_{spec}} + \frac{1}{E_{ind}}][4\mathrm{h}_p^2 + \mathrm{d}_p^2]}{4\,\mathrm{h}_p^2 + \mathrm{d}_p^2 - 4\,h_p\,D}} \tag{3.3}$$

Equations 3.4 and 3.5 are used for calculating values of true stress (σ_t) and true plastic strain (ε_p), respectively, where δ is the constraint factor [21].

$$\varepsilon_p = 0.2\ \frac{d_p}{D} \tag{3.4}$$

$$\sigma_t = \frac{4\ P}{\pi\ \mathrm{d}_p^2\ \delta} \tag{3.5}$$

The data points collected from all the cycles are fit to Equation 3.6, where, m and A are Meyer's coefficient and yield parameter, respectively calculated using regression analysis. On obtaining the value of A, Equation 3.7 is used to calculate the yield strength of the material (σ_y), where b_m and B are material yield slope and yield offset constant (in MPa), respectively [21].

$$\frac{P}{\mathrm{d}_t^2} = A\ (\frac{d_t}{D})^{\,m-2} \tag{3.6}$$

$$\sigma_y = B + b_m\ A \tag{3.7}$$

The ultimate tensile strength (UTS) is obtained by taking the value of ε_u = n in Holloman as presented in Equation 3.8, where, K is the strength coefficient.

$$UTS = K\ (\frac{\varepsilon_u}{e})^n,\ \mathrm{e} = 2.71 \tag{3.8}$$

Figure 3.4a presents the high temperature ABI setup deployed for the present study showing the indenter and the sample fixture. ABI experiments are performed using an *Advanced Technology Corporation* make and *SSM-B4000* model system on a mirror-polished sample of size 20 mm x 20 mm x10 mm for the bulk samples and cross-section for wall samples. ABI setup having a maximum loading capacity of 4.45 kN and operating temperature up to 850 °C is used for the study. Tungsten Carbide indenter and Silicon Carbide indenter of diameter 0.76 mm is used for room temperature and elevated temperature testing, respectively. ABI testing is carried out from room temperature to 873 K, with each test using seven cycles of loading and partial unloading (40 % of maximum load in each cycle).

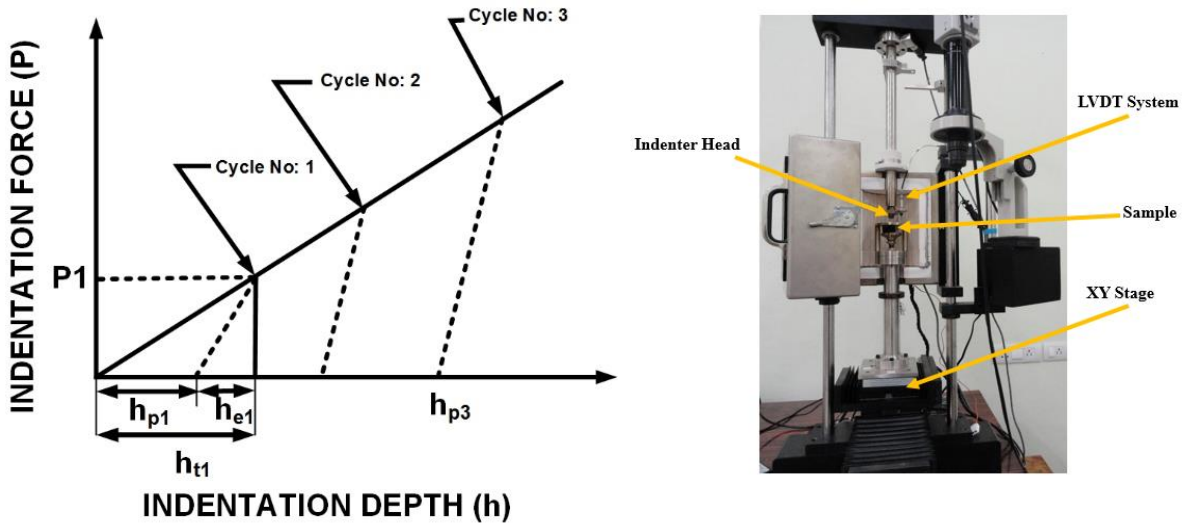

(a) (b)

Figure 3.4: ABI a) Typical loading pattern b) experimental setup

3.4 Summary

The present chapter discussed on the experimental system used for building structures/ samples, sample preparation systems and characterisation tools. The subsequent chapter deals with studies on the LDED built Hast-X single tracks including track geometry analysis, process window development and defect analysis.

Chapter 4 : Experimental Analysis and Modelling of LDED built Hastelloy-X Single Tracks[2]

4.1 Introduction

The basic building unit in Laser Directed Energy Deposition (LDED) is the single track deposition. The geometry and quality of the single track is a function of the LDED process parameters and the major LDED process parameters governing the single track characteristics are: laser power, scan speed and powder feed rate for a particular laser beam diameter and laser beam profile. It is necessary to probe into the variation in the geometry and quality of the single tracks at different combination of LDED process parameters. Examining the geometry of the tracks is important to elucidate the variation in the melt-pool behaviour at different process parameters. The melt-pool behaviour is a complex phenomenon in LDED, which is mainly a combination of surface tension forces and viscous forces [157,158]. These forces vary with the melt-pool temperature and material chemistry. Thus, analysis of the melt-pool behaviour and geometry will aid to select the process parameters for building engineering components. In addition, the systematic study of the deposit quality is primary requisite to develop a material-specific processing recipe for building defect-free components.

This chapter deals with experimental and modelling studies on the LDED of Hast-X single tracks. The chapter begins with the characterisation of commercially available Hast-X powder for its morphology, particle size distribution and composition of major elements. An analytical

[2] This chapter is partially reproduced with permission from Elsevier (Journal - S. No. 1) and Old City Publishing (Journal - S. No. 6) – See Letters of Copyright Permission (Page No: 208 and 209).

model for predicting the track geometry is proposed. The track width and track height values predicted using proposed analytical modelling are compared with the experimental values. Subsequently, Hast-X single tracks are deposited at different laser power, scan speed and powder feed rate and the variation in the track width and track height are analysed at different combinations of LDED process parameters. Table 4.1 presents the range of process parameters used for the study. Further, the process window is identified by analysing the single tracks using topography analysis, composition examination, porosity check and build rate analysis. Subsequently, overlapped track deposition is carried out and they are examined in the macro and micro scale.

Table 4.1: Process parameters used for LDED single track experiments

Process parameter	**Value**
Laser power	600 – 1600 W
Scan speed	0.3 -0.7 m/min
Powder feed rate	5 - 8 g/min

4.2 Powder Characterisation

Powder quality is one of the basic factors governing the characteristics of the structures built using LDED. Powder characteristics such as morphology, particle size distribution, composition and phases are the major characteristics that need to be known before initiating the deposition. In the present work, commercially available gas atomized Hast-X powder is procured from M/s Sandvik, United Kingdom. Figure 4.1 (a) and (b) presents the morphology of the Hast-X powder particles obtained using Scanning Electron Microscopy (SEM). Powder morphology is an important feature that directly influences the flowability in LDED[47]. Powder morphology is mainly dependent on the powder manufacturing route. Gas atomized powders typically yield spherically shaped powders. It can be seen that the powder particles used in the present work are primarily spherical with some surface irregularities. The surface irregularities are mainly due to the presence of satellite particles on the surface of the powder

particles. These satellites are generated due to the difference in solidification rate between smaller molten particles that adhere to partially molten particles of a larger size.

The particle size distribution is another significant parameter for uniform deposition during LDED process. If the powder particles are too fine, the powder particles will not be able to reach the melt-pool during dynamic blowing in LDED. This is due to the lighter nature of the powder particles, which gives the powder a tendency to disperse/ scatter during the flight from nozzle to the substrate. However, if the powder particles are too coarse, it will result in incomplete melting of the powder particles. Thus, an optimum range of powder particle size is required for deposition. Powder size is measured using the SEM morphology images with the aid of Image- J software. Typically, powder size varies between 50 – 100 µm in LDED process and the measured range of powder particle size is in the range of 50 – 110 microns with maximum particles in the zone of 60 – 70 µm as seen in Figure 4.2.

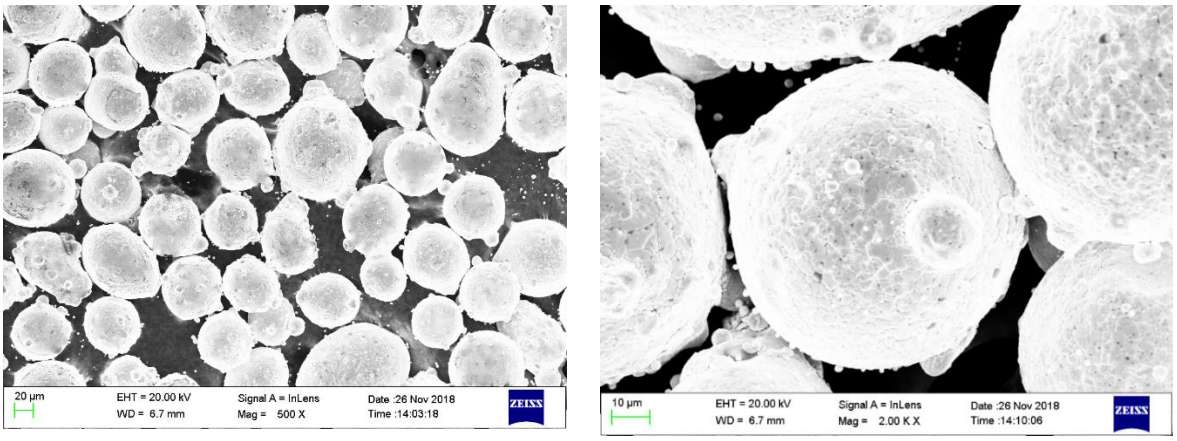

(a) (b)

Figure 4.1: Morphology of Hast-X Powders

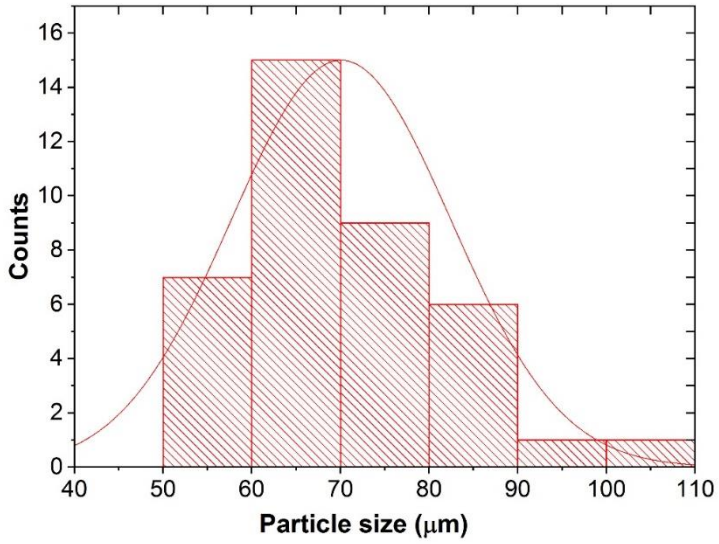

Figure 4.2: Powder particle size distribution

Table 4.2 presents the nominal composition of the Hast-X powder and composition of the major elements measured using X-ray fluorescence (XRF) technique. XRF technique can detect the presence of higher atomic mass elements with accuracy and thus, the elemental composition of lighter and trace elements is not detected. It is confirmed that the chemical composition of the major elements of the powder used for LDED deposition is within the range of composition as per the standards.

Table 4.2: Composition of Hast-X powder (UNS N06002)

Element	**Nominal** [136]	**Measured using X-ray Fluorescence**
Chromium	20.5 – 23.0	20.9
Iron	17 – 20	19.04
Molybdenum	8 -10	10
Cobalt	0.5 - 2.5	0.93
Tungsten	0.2 -1.0	0.6
Silicon	1.0 max	-
Manganese	1.0 max	0.2

Phosphorous	0.04 max	-
Sulphur	0.03 max	-
Carbon	0.15 max	-
Nickel	Balance	47

Figure 4.3a presents the X-ray diffraction (XRD) of the powder used for deposition. XRD analysis of the powder shows strong diffraction peaks of (111), (200), (220) plane of face-centred cubic (FCC) crystal structure, which are originated from the γ-Ni phase. The peak positions of the powder are 43.48°, 50.69° and 74.57° for (100), (200) and (220) planes, respectively. Figure 4.3b presents the peaks available in the standard database and it is observed that peaks of the Hast-X powder have a very close match with the peaks reported in the standard database (PDF number: 00-004-0850).

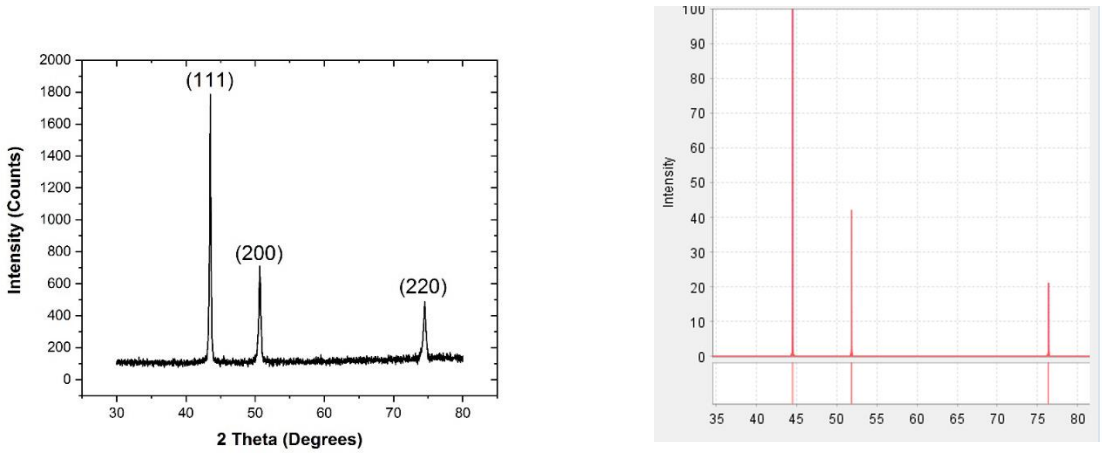

(a) (b)

Figure 4.3: XRD pattern (a) Hast-X powder (b) standard peaks from PDF card

4.3 Modelling of Track Geometry

Prediction of track geometry is carried out to understand the relation between the process parameters and the track geometry. This is important for process control to improve the consistency and stability of the process. Numerical models based on finite element method can

be difficult for applying in process control owing to their high computational cost. Time-efficient empirical-statistical models and analytical relations are great platforms for process optimization and process control [146]. In the present work, a simple methodology for predicting the track geometry is proposed by discretization of a Gaussian beam using Rosenthal point source heat equation.

4.3.1 Assumptions and Simplifications

- **Heat Losses:** In LDED, conduction is the major mode of heat transfer and convection and radiation losses are negligible. Thus, convection and radiation heat transfer are neglected in the present work.
- **Material properties:** The material is assumed to be isotropic and homogenous. Thermophysical properties are assumed to be temperature independent. The average value of the temperature range provided in Table 4.3 is considered for calculation of thermophysical properties. A similar approach is used by Huang et al [159].

Table 4.3: Thermophysical properties of Hast-X [160]

Properties (Unit)	Values (at Temperature)
Density (kg/m^3)	8220 (300 K) – 7400 (1628 K)
Melting Temperature Range (K)	1530 – 1628
Thermal Conductivity (W/m.K)	10 (300 K) – 30 (1628 K)
Specific Heat (J/(kg·K)	450 (300 K) – 680 (1628)

- **Laser absorptivity:** Laser absorptivity of 0.3 is considered for the calculation. It is assumed that the laser absorptivity/ reflectivity is not dependent on the inclination of laser beam relative to the melt pool surface
- **Marangoni flow:** The Marangoni flow is counted by modifying the thermal conductivity with a correction factor of μ, which is taken as 2.5 in the present work [146].

- **Laser energy distribution:** The laser beam is assumed to be TEM_{00} mode with a Gaussian distribution.

4.3.2 Model description

During LDED, the laser beam strikes at the surface of the substrate/ previously deposited layer and the attenuation of laser power takes place due to absorption, reflection and scattering due to the powder particles. The laser energy after being attenuated inside the powder cloud reaches the substrate surface, where it undergoes, reflection and absorption. The absorbed laser power is taken from the melt pool surface to deposit and substrate/ previous layer through heat conduction and Marangoni flow. Marangoni effect is considered by using modified thermal conductivity as discussed earlier. Thus, the problem gets converted to a heat conduction problem, where the laser heat source is kept on the melt pool top surface.

Rosenthal point heat source equation as shown in equation 4.1 provides the temperature distribution due to a point heat source, where, q_o, K, V, α are laser power, material thermal conductivity, scan speed and material thermal diffusivity, respectively. R signifies the distance from the point of interest to the laser heat source and x-vt is ξ [161].

$$T_p(x,y,z) = T_0 + \frac{P}{2\pi K_m R} \exp\left(-\frac{V(R+\xi)}{2\alpha}\right) \qquad \text{Where, R} = \sqrt{\xi^2 + y^2 + z^2} \qquad (4.1)$$

Equation 4.1 is suitable to obtain the temperature distribution by solving the heat conduction problem on a semi-infinite surface due to an instantaneous point heat source. The temperature distribution due to a continuous heat source, i.e., a Gaussian laser source can be calculated by considering a number of point sources. The Gaussian laser distribution is discretised into 5 different point heat sources and energy available at each point source is selected as per the Gaussian distribution. Figure 4.4 presents the representation of laser power discretization for moving heat sources labelled as 1, 2, 2',3 and 3'. By applying superposition principle, the effect of each point sources at different points inside the melt-pool is estimated, where the

temperature at any point (x,y,z) due to any of the discretized point source T_p is given by equation 4.1, where *p* can be point sources 1, 2, 2',3 and 3'.

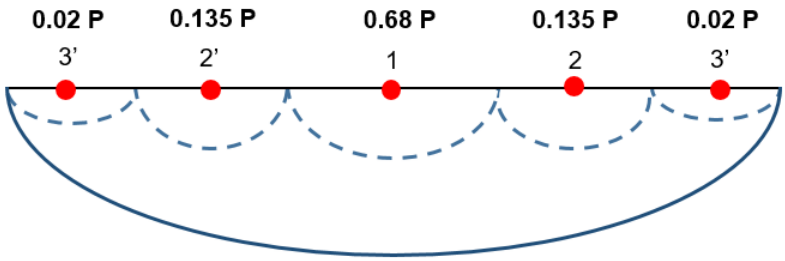

Figure 4.4: Representation of laser power discretization for moving heat source

The substrate over which the point heat sources are moving is considered as semi-infinite and it is discretised. The temperature at a point T (x, y, z) can be represented as per equation 4.2.

$$T(x, y, z) = \sum T_p \tag{4.2}$$

The temperature at different nodal points along the width is estimated and the limiting point at which the temperature is just equal to the melting point is used to estimate the track width.

To estimate the track height, the melt-pool boundary is obtained by relating the calculated enthalpy with the enthalpy of the material at the melting point for every node. This is followed by the enthalpy balance approach reported by Kumar et al. [162,163] to estimate the track height. Excess enthalpy above the melting point is calculated at all nodal points for estimating local track height at each node. This is followed by balancing the excessive enthalpies above the melting point. The cumulative difference between element enthalpy (H_s) and enthalpy at the melting point (H_m) is calculated to define the extra enthalpy available. The enthalpies H_s and H_m are given by equation 4.3 and 4.4.

$$H_s = h_e \rho \left[C_p (T_m - T_i) + L \right] \tag{4.3}$$

$$H_m = h_{melt} \rho \left[C_p (T - T_m) + L \right] \tag{4.4}$$

T_m, T_i, T, ρ, L and C_p are the melting temperature, temperature of powder, temperature of the melt pool, density, latent heat of fusion and specific heat, respectively.

Further, mass balance is applied for estimating the local track height $h_m(x)$ by using the conservation of mass, as represented by equation 4.5 [158], where η, m_p *and* r_l are catchment efficiency, powder feed rate, the radius of laser beam, respectively.

$$h_m(x) = \frac{\eta m_p}{2\rho r_l V} \tag{4.5}$$

$$h_{new} = h_e \cap h_m \tag{4.6}$$

Actual track height h_{new} is minimum of the two heights, i.e., h_e and h_m as presented in equation 4.6; h_e is maximum possible height due to energy conservation and h_m is maximum possible height due to powder mass conservation.

4.3.3 Comparison with Experimental Results

Further, the model is validated using experimental values. Figure 4.5 presents a comparison between the experimental and modelling results for continuous tracks (presented in section 4.4) deposited at 8 g/min.

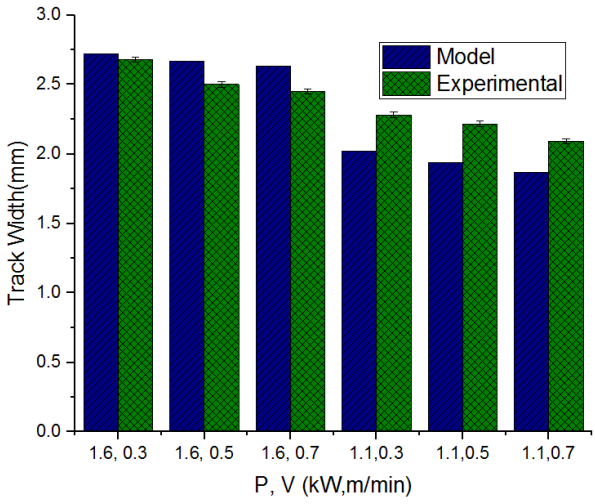

(a)

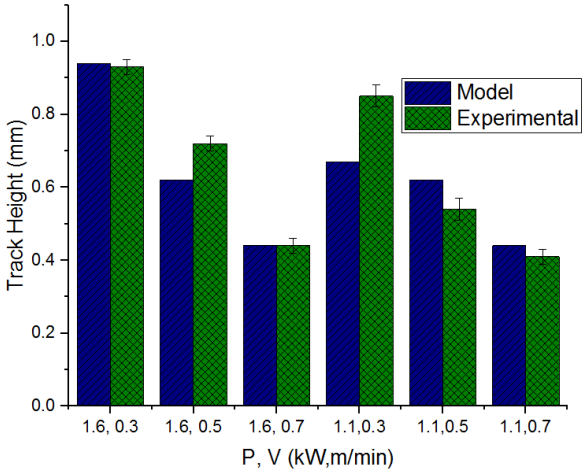

(b)

Figure 4.5: Comparison of experimental and modelling results at powder feed rate of 8 g/min (a) Track width (b) Track height

As mentioned earlier, track width is predicted by considering the limiting point at which the temperature is greater than or equal to the melting point. It is noted that with the increase in the laser power and decrease in scan speed, the distance between the melting point boundary (the point at which the temperature is greater than the melting point) and center of laser beam increases, which leads to increase in the track width. This is primarily due to availability of more energy for the deposition at higher laser power and increased interaction time between laser beam and material at lower scan speed. This leads to higher melt-pool temperature resulting in enhanced heat-transfer. In case of track height, it is observed that for the analysis carried out at scan speed of 0.3 m/min, the actual track height is governed by track height predicted using enthalpy balance. It is also observed from equation 4.5 that the track height predicted using mass balance is directly related to powder feed rate and inversely related to scan speed. Thus, more interaction time between the powder source and laser beam leads to higher values of track height from mass balance. While, at other process conditions, i.e., at scan speed of 0.5 m/min and 0.7 m/min, the track height is governed by the mass balance as the energy available for deposition is sufficient for melting the available quantity of powder. This also indicates that the process

conditions deploying scan speed of 0.5 m/min and 0.7 m/min depicts stable deposition as the amount of energy available for deposition is sufficient for the given quantity of powder. It is observed that the maximum deviation in track width and track height are 12% and 18%, respectively as shown in Figure 4.5.

The proposed model provides a simple and quick approach for predicting the track width and track height with reasonable accuracy. It provides an overall understanding into the effect of process parameters on LDED track geometry and can aid for quick process parameter selection. The model can be further extended to process control by improving its accuracy through the use of a larger number of point heat sources, by considering convection and radiation heat source, temperature dependent thermophysical properties, etc.

4.4 Track Geometry Analysis

For a given laser spot diameter, the most important process parameters affecting the track geometry are laser power, scan speed and powder feed rate. Hence, these three parameters are selected for the parametric investigation. For the study, the laser power (P) is varied from 600 – 1600 W at three levels, scan speed (V) is varied from 0.3 - 0.5 m/min at three levels each at two levels of powder feed rate (F) (5 and 8 g/min). Stainless steel 316L (SS 316L) substrate of 75 mm diameter and 10 mm thickness is used. Figure 4.6 presents the cross-section images of the LDED deposited single tracks.

	Power(W)			Scan Speed (m/min)
Powder Feed Rate (g/min)	600	1100	1600	
5	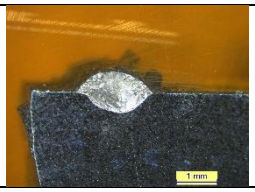	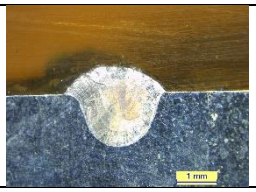		**0.3**

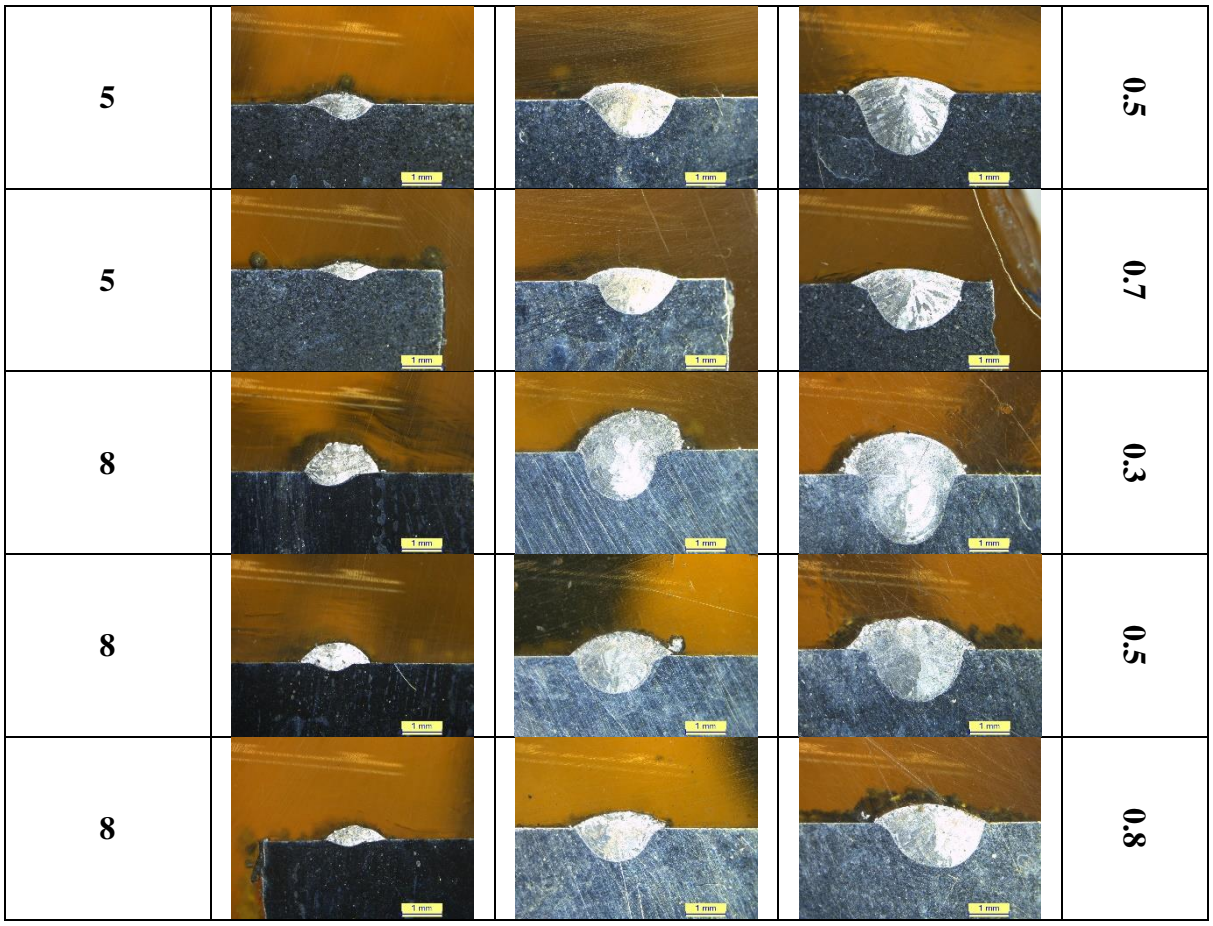

Figure 4.6: Track Geometry at different process parameters

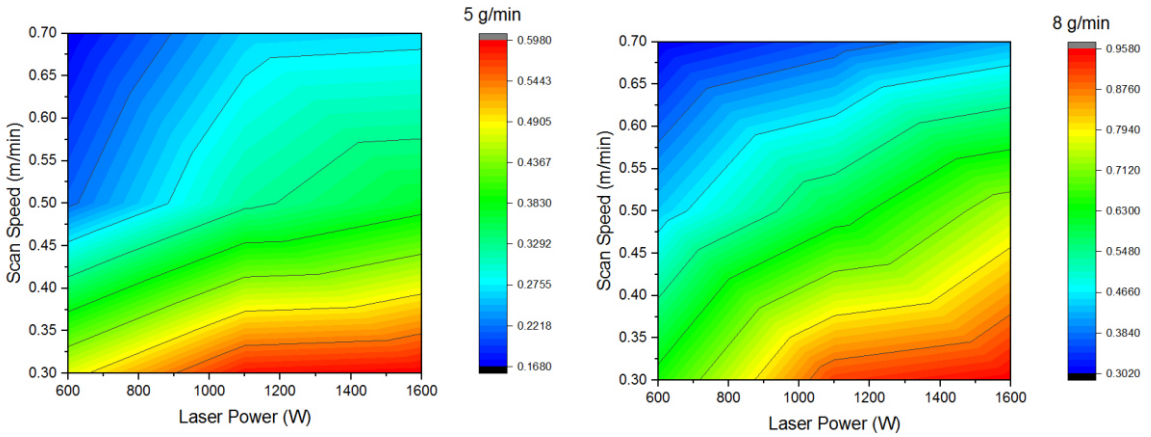

(a) (b)

Figure 4.7: Variation of track height with laser power and scan speed at different powder feed rate (a) 5 g/min (b) 8 g/min

Figure 4.7a and 4.7b presents the variation of track height with laser power and scan speed at a powder feed rate of 5 g/min and 8 g/min, respectively. It is observed that the track height increases with an increase in the laser power and reduces with an increase in the scan speed at a particular powder feed rate. The reason for the above can be explained with the help of a combined process parameter called "Laser Energy per unit Length (LEL)" shown in equation 4.7. It can be seen that LEL is directly proportional to laser power and inversely proportional to the scan speed. As the laser power increases, the energy available for melting the fed powder particle and substrate increases, which further increases the catchment efficiency of the deposition and energy available in the melt-pool. Catchment efficiency is defined as the ratio between the amount of material deposited to the amount of material fed to the melt-pool for deposition. With an increase in catchment efficiency, more amount of powder particles will be melted and deposited. On the other side, a reduction in the scan speed increases the interaction time between the laser beam and powder particle/ substrate. Interaction time is defined as the ratio between the beam diameter and scan speed. An increase in the interaction time increases the amount of powder captured by the melt-pool and the availability of more amount of energy in the melt-pool, which increases the deposit height. The effect of scan speed on the track height can also be explained with the help of a combined parameter called "Powder Feed per unit Length (PFL)" as shown in equation 4.8. PFL is a ratio of powder feed rate and scan speed. As the scan speed reduces, the powder fed per unit length of deposition increases, which increases the track height. Thus, the combined effect of LEL and PFL are the major reasons for the increase in track height with an increase in laser power and scan speed.

$$\text{Laser Energy per unit Length (LEL)} = \frac{Laser\ Power}{Scan\ speed} = \frac{P}{V}\ \text{(J/m)} \tag{4.7}$$

$$\text{Powder Feed per unit Length (PFL)} = \frac{Powder\ Feed\ Rate}{Scan\ Speed} = \frac{F}{V}\ \text{(g/m)} \tag{4.8}$$

A comparison of Figure 4.7a and 4.7b shows the direct relationship between powder feed rate

and track height. As the powder feed rate increases, the PFL increases, which shows that more amount of powder is available for deposition. This leads to an increase in track height with an increase in powder feed rate. In the present experimental matrix, minimum track height of 0.16 mm is obtained at a combination of minimum value of LEL and PFL of 51 J/m and 7 g/m, respectively. Maximum track height of 0.95 mm is obtained at the combination of maximum value of LEL and PFL of 320 J/m and 26 g/m, respectively. It is also observed that the effect of powder feed rate on the track height is maximum, followed by scan speed and laser power.

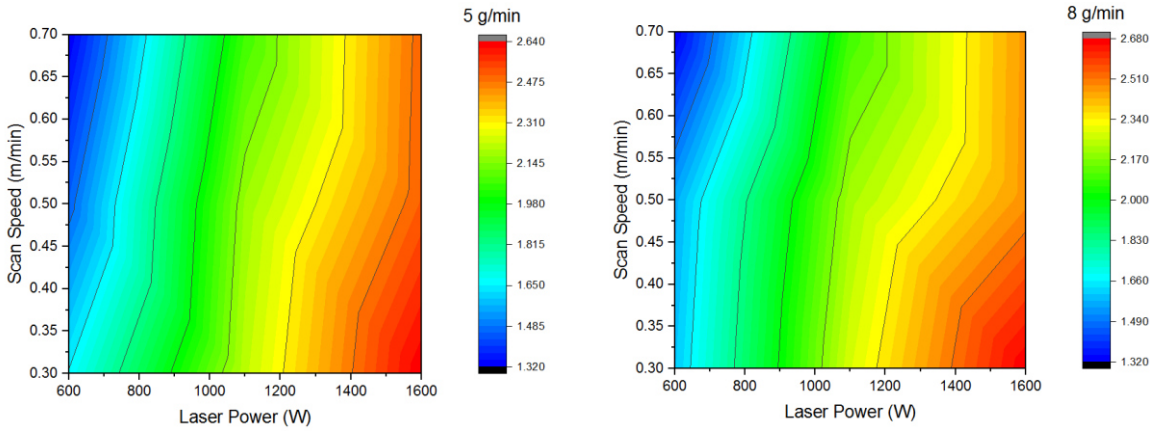

(a) (b)

Figure 4.8: Variation of track width with laser power and scan speed at different powder feed rate (a) 5 g/min (b) 8 g/min

Figure 4.8a and 4.8b presents the variation of track width with laser power and scan speed at a powder feed rate of 5 g/min and 8 g/min, respectively. In case of track width, at a particular beam diameter and powder feed rate, the track width increases with an increase in the laser power and decreases with an increase in scan speed. The increase in track width with an increase in laser power is mainly due to an increase in LEL. On the other side, a reduction in scan speed also leads to an increase in LEL. The increase in the laser energy available in the melt-pool raises the temperature of the melt-pool. During LDED, the center of the melt-pool will be at a higher temperature than the edges, which can be due to more heat transfer at the edges. The difference

in the temperature inside the melt-pool leads to variation in the thermophysical properties within the melt-pool. The major factors governing the melt-pool dynamics are surface tension gradient and variation in viscous forces inside the melt-pool. Marangoni effect results in the mass transfer inside the melt-pool as fluid moves from the region of lower surface tension to the region of higher tension. Thus, the Marangoni flow inside the melt-pool is primarily dependent on the surface tension gradient ($d\gamma/dT$) within the melt-pool. It can be seen from figure 4.9 that a negative $d\gamma/dT$ results in the reduction of surface tension with an increase in the temperature, which allows for outward melt-pool flow. This results in the formation of wider melt-pool during LDED. On the other side, a positive relationship between the surface tension and temperature results in an inward flow of the melt-pool leading to a narrow melt-pool. Hast-X being a nickel superalloy, the surface tension typically shows a negative relationship with temperature [164,165]. Thus, with an increase in the laser energy per unit length, the width of melt-pool increases.

A comparison of Figure 4.8a and 4.8b shows the direct relationship between powder feed rate and track width. As the powder feed rate increases, the PFL increases, which shows that more amount of powder is available for deposition. However, the effect of the powder feed rate on track width is relatively less. In the present experimental matrix, the minimum track width of 1.32 mm is obtained at the minimum combination of LEL and PFL of 51 J/m and 7 g/m, respectively. The maximum track width of 2.68 mm is obtained at the combination of maximum value of LEL and PFL of 320 J/m and 26 g/m, respectively. It is also observed that the effect of laser power on the track width is maximum, followed by scan speed and the effect of powder feed rate is the least. This is because the availability of laser power and the interaction time are the major factors governing the melt-pool width/ track width.

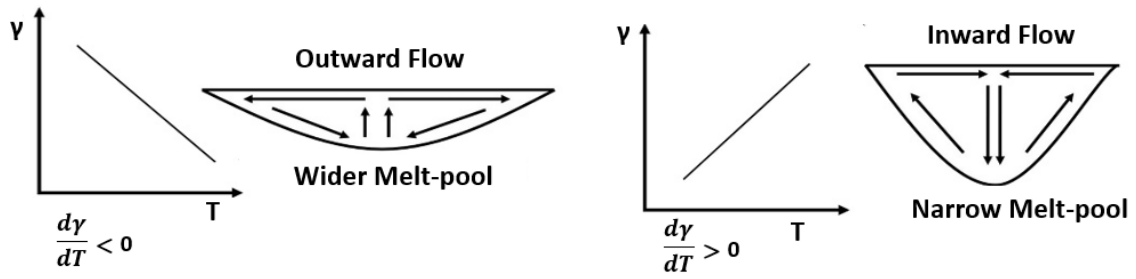

(a) (b)

Figure 4.9: Schematic diagrams of fluid flow patterns within melt-pool for: (a) negative surface tension gradient, and (b) positive surface tension gradient [149]

Aspect ratio is defined as the ratio between the track width and track height. Track width and track height increases with an increase in laser power, reduction in scan speed and increase in powder feed rate. The calculation of aspect ratio will help to understand the relative variation of track width with respect to track height, when the process parameters are changed. Figure 4.10a and 4.10b present the variation of aspect ratio with laser power and scan speed at a powder feed rate of 5 g/min and 8 g/min, respectively. It can be observed that the aspect ratio increases with an increase in laser power and scan speed, and decreases with an increase in the powder feed rate. As the laser power increases, the increase in the width of melt-pool is more than the increase in the track height. This leads to an increase in aspect ratio with an increase in laser power. On the other side, an increase in scan speed leads to more reduction in track height than the reduction in track width, which results in an increase in aspect ratio with an increase in scan speed. Similarly, a change in the powder feed rate results in more variation on the track height than track width. It can also be observed that the contribution of laser power to the aspect ratio is low as compared to scan speed and powder feed rate. It is observed that at a constant LEL, as PFL increases, the aspect ratio shows a significant reduction primarily due to relatively larger increase in track height as compared to track width. In addition, at a constant PFL, an increase in LEL leads to a slight increase in aspect ratio. This is mainly due to the

competing nature of track width and track height. As LEL increases, track width and track height increase mainly due to the significant effect of laser power and scan speed, respectively.

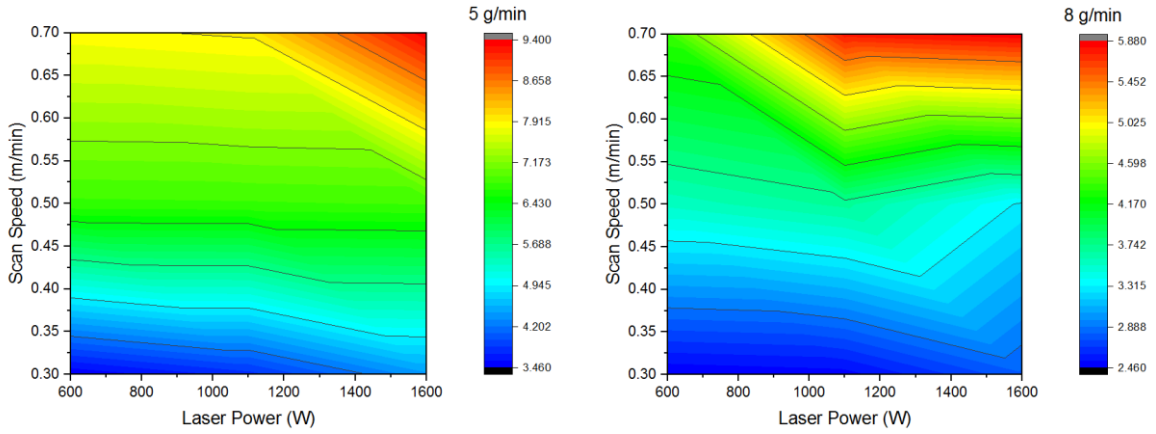

(a) (b)

Figure 4.10: Variation of aspect ratio with laser power and scan speed at different powder feed rate (a) 5 g/min (b) 8 g/min

4.5 Process Window Development

Table 4.4 presents the process parameters and corresponding results for material deposition as per full factorial design of experiment. Surface topography examination using a stereo microscope reveals that there are regular, irregular and cracked deposits as shown in Figure 4.11. The experimental result matrix is evaluated using combined parameter, laser energy per unit powder feed (LEPF = Laser Power/ Powder Feed Rate) at different scan speeds. All deposits at LEPF = 4.5 kJ/g and 7.2 kJ/g yielded irregular deposits, while deposits at LEPF=19.2 kJ/g resulted in cracked deposits. Uniform deposits without cracks are observed for the value of LEPF in the range of 8.25 kJ/g to 13.2 kJ/g for the range of scan speed used for the study. When the LEPF is lower than 4.5 kJ/g the amount of energy available for continuous deposition of material is not available, which resulted in the formation of irregular deposition. However, at LEPF values of 19.2 kJ/g, cracks are formed and the analysis of the

cracks are provided in the subsequent section. All combination of process parameters for the laser power of 1100 W yields uniform deposition, as it is within the optimum range of LEPF.

Table 4.4: Process Parameters and Corresponding Observations

Specimen ID	Laser Power (W)	Scan Speed (m/min)	Powder Feed Rate (g/min)	LEPF (kJ/g)	Remarks
Hast-X-01	600	0.3	5	7.2	Irregular
Hast-X-02	600	0.5	5	7.2	Irregular
Hast-X-03	600	0.7	5	7.2	Irregular, discontinuous
Hast-X-04	1100	0.3	5	13.2	Regular
Hast-X-05	1100	0.5	5	13.2	Regular
Hast-X-06	1100	0.7	5	13.2	Regular
Hast-X-07	1600	0.3	5	19.2	Crack
Hast-X-08	1600	0.5	5	19.2	Crack
Hast-X-09	1600	0.7	5	19.2	Crack
Hast-X-10	600	0.3	8	4.5	Irregular
Hast-X-11	600	0.5	8	4.5	Irregular
Hast-X-12	600	0.7	8	4.5	Irregular
Hast-X-13	1100	0.3	8	8.25	Regular
Hast-X-14	1100	0.5	8	8.25	Regular
Hast-X-15	1100	0.7	8	8.25	Regular
Hast-X-16	1600	0.3	8	12	Regular
Hast-X-17	1600	0.5	8	12	Regular
Hast-X-18	1600	0.7	8	12	Regular

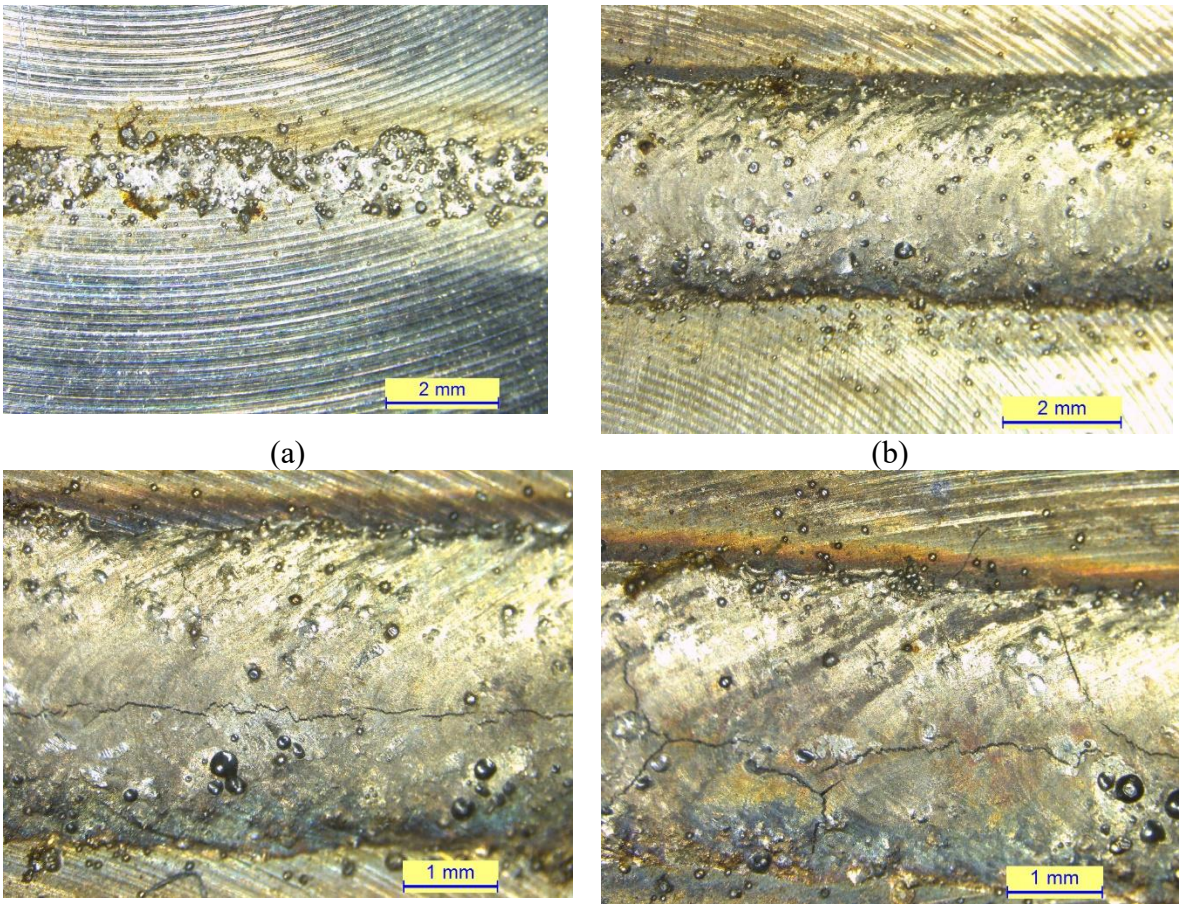

(a) (b)

(c)

Figure 4.11: Surface analysis of cracks at various LEPF (a) discontinuous tracks, LEPF= 7.2 kJ/g (b) continuous tracks, LEPF=12 kJ/g (c) continuous tracks with cracks LEPF=19.2 kJ/g.

4.6 Defect Analysis

Elemental mapping is carried out to understand the possibilities of segregations induced cracking as shown in figure 4.12. Carbon (C) and Silicon (Si) segregations are observed along the crack, which indicates the possibilities of hot cracking due to their segregations. Manganese (Mn) segregations are also observed near to the cracks. These observations are in line with the literature available for the same alloy system. The major impact of C and Si on the hot cracking sensibility is mainly due to the increasing amount of the eutectic phase and reducing the solidification range [130,131]. Dacian et al. [130] reported that lower concentrations of Si, Mn, and C can result in the minor formation of micro-segregation along the grain boundaries,

consequently generating less crack. Dacian et al. also proposed that cracking mechanism is mostly controlled by Si and C, whereas Mn has a negligible effect. It was also proposed that Si and C have a notable influence on the hot cracking susceptibility coupled with high thermal residual stresses. It is also reported in the literature for another grade of Hastelloy that Si increases the quantity of M_6C carbides alongside the grain boundaries, giving a broad supply of crack initiation [166].

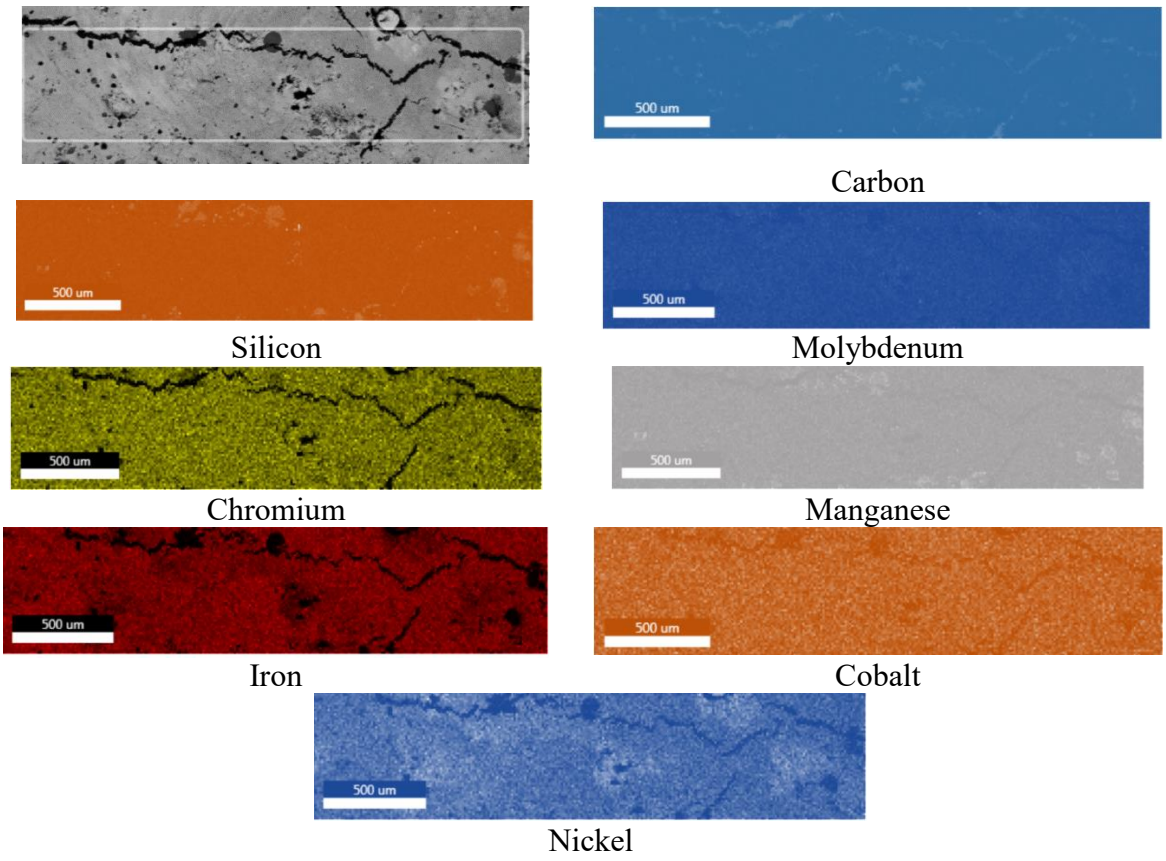

Figure 4.12: Element mapping along the crack

As the cracking observed on the surface of the laser tracks is at higher LEPF, it can also be due to the excessive laser energy used for deposition, which results in larger thermal gradients within the melt-pool. Mukherjee et al. [164] proposed a relation between the thermal strain in the melt-pool and thermal gradient during LDED process as shown in equation 4.10. The thermal strain increases with an increase in the thermal gradient inside the melt-pool, which depends on the LEPF used for deposition. As the LEPF increases, thermal gradient increases,

which results in a large amount of thermal strain inside the melt-pool. Harrison et al. [127] suggested that cracks occur when thermal residual stresses overcome the ultimate tensile strength (UTS) of the alloys at a precise point and temperature. Thus, cracking during higher LEPF can be due to the larger values of residual stresses at higher LEPF. Therefore, it can be concluded that the cracking during LDED of Hast-X is primarily a combination of thermal stresses and elemental segregation.

$$\varepsilon = \frac{\beta \Delta T}{EI} \frac{tH^{3/2}}{F_O \sqrt{\rho}} \tag{4.10}$$

where β, ΔT, EI, H, t, Fo, ρ is the volumetric coefficient of thermal expansion, temperature increase during LDED, flexural rigidity, heat input per unit time, characteristic time, Fourier number and density of the alloy, respectively.

As continuous and crack free deposition is observed with a LEPF of 8.2 – 13.2 kJ/g, the single tracks in the above LEPF zone are subjected to porosity analysis. Porosity is analysed along the cross-sections as shown in Figure 4.13. It is observed that all the samples are highly dense with relative density > 99.5%. It can be seen that the average area fraction porosity decreases with an increase in the LEPF values, with maximum porosity observed at 8.2 kJ/g followed by 12 kJ/g and 13.2 kJ/g. The reduction in the average area fraction porosity with an increase in LEPF is primarily attributed to the increase in the energy available for deposition of a unit mass of powder. Further, within a particular LEPF, it is observed that the average percentage of porosity increases with an increase in the scan speed. This is mainly due to the reduction in the amount of energy available for complete consolidation at higher scan speed. It can also be seen that the shape of porosity is a mix of elongated/ non-uniform pores and uniform/ spherical pores. The elongated pores can be defined as lack of fusion pores, which are mainly formed due to unavailability of sufficient energy for complete material consolidations at few locations.

These porosities are seen in large proportion in tracks built at 8.2 kJ/g, due to the lower value of laser energy available for melting unit mass of powder. The spherical pores are known as gas porosities, which are formed as a result of the gas trapping during LDED processing. Gas porosity can also be formed due to vaporization of alloying elements at some locations, where the temperature exceeds the boiling point of the elements present in the alloy [81]. It is observed that slightly higher porosity is obtained at 13.2 kJ/g than 12 kJ/g at a scan speed of 0.5 m/min. The major reason for the above is the lower laser energy per unit length (LEL) used for depositing the tracks at LEPF of 13.2 kJ/g. LEL used for depositing tracks at 13.2 kJg/ and 0.5 m/min is 132 kJ/m, while the LEL used for depositing tracks at 12 kJg/ and 0.5 m/min is 192 kJ/m. The lower LEL deployed for depositing the single track at 13.2 kJ/g can lead to the formation of lack of fusion defects. The minimum porosity is observed for tracks deposited with LPEF of 13.2 kJ/g at a scan speed of 0.3 m/min, followed by LPEF of 12 kJ/g at a scan speed of 0.3 m/min and LPEF of 12 kJ/g at a scan speed of 0.5 m/min.

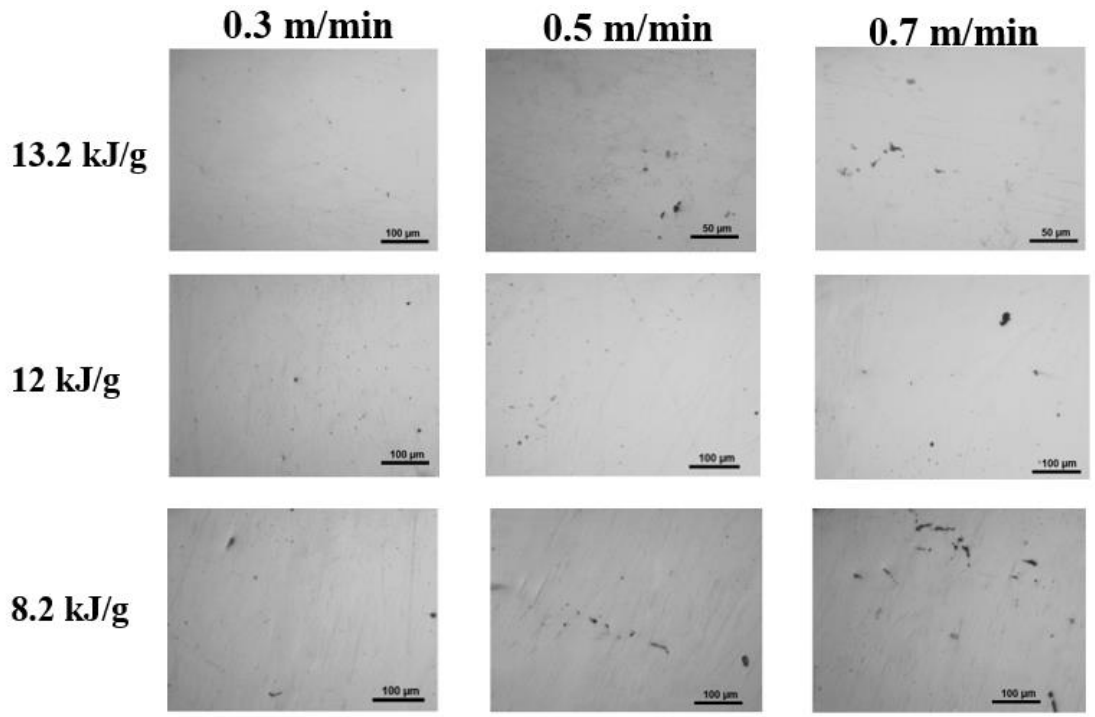

Figure 4.13: Porosity analysis of single track

4.7 Build Rate Analysis and Process Parameter Selection

As the samples are dense, process parameters for building bulk samples can also be selected by considering the build rate in addition to the track continuity and porosity. Build rate is an essential factor as it governs the amount of time required for building a component. Build rate is estimated using equation 4.11, where A is the area of the track and V is the scan speed for tracks with LEPF in the range of 8.2 -13.2 kJ/g. Area of the track is calculated using equation 4.12, by assuming the shape of the track geometry as a parabolic segment [159].

$$Build\ rate = A_t \times V \tag{4.11}$$

$$A_t = \frac{2}{3} \times track\ width \times track\ height \tag{4.12}$$

Table 4.5 presents the variation in track area with process parameters and combined process parameters. It can be seen that the track area is directly related to the laser power and powder feed rate and inversely related to the scan speed. This is in-line with the variation in the track height and track width with the change in LDED process parameters. As laser power increases, the area of the melt-pool increases and catchment efficiency increases, which results in a larger track area. In addition, an increase in powder feed rate also increases the amount of material available for LDED deposition, which increases the track area. The inverse relation between scan speed and track area is due to the reduction in the interaction time between the laser energy and powder/ substrate material with an increase in scan speed.

Build rate is basically material deposition rate, which can be estimated with track area and scan speed. Build rate is observed to increase with an increase in the laser power and powder feed rate. However, the variation in the build rate with scan speed shows that the build rate is maximum at 0.5 m/min at LEPF of 8.2 kJ/g and 12 kJ/g. At 0.3 m/min, the interaction time between the laser source and powder material is more, which results in a larger track area.

However, the lower speed of deposition reduces the build rate of the track. At the scan speed of 0.7 m/min, even though the laser scan speed is high, the smaller interaction time between the laser source and material results in a reduction in the track area. Thus, the maximum build rate is obtained at a scan speed of 0.5 m/min. However, at LEPF of 13.2 kJ/g, the variation in build rate at different scan speed was found to be insignificant due to the competing nature of track area and scan speed. In the present experimental matrix, maximum build rate is obtained at laser power – 1600 W, scan speed – 0.5 m/min, powder feed rate – 8 g/min with a LEPF value of 12 kJ/g. As the above combination of process parameter also results in lower porosity, it is selected for multi-track deposition.

Table 4.5: Variation in track area and build rate with process parameters

S.No.	Laser Power	Powder Feed Rate	Scan Speed	LEPF	Track area	Build rate
	W	g/min	m/min	kJ/g	mm^2	mm^3/min
1	1100	8	0.3	8.2	1.37	0.42
2	1100	8	0.5	8.2	0.87	0.43
3	1100	8	0.7	8.2	0.49	0.35
4	1600	8	0.3	12	1.69	0.50
5	1600	8	0.5	12	1.22	0.61
6	1600	8	0.7	12	0.68	0.47
7	1100	5	0.3	13.2	0.86	0.25
8	1100	5	0.5	13.2	0.46	0.23
9	1100	5	0.7	13.2	0.35	0.24

The overlapped track deposition is carried out by using unidirectional deposition strategy (deposition head adds material only in one direction and remains idle in the return stroke) using 50% overlap between the adjacent layers to obtain sound metallurgical bonding between the tracks. The overlapped track deposits are subjected to microscopy analysis to confirm the defect-free deposition. Figure 4.14 presents the macro-structure of the overlapped track layer. Overlapped laser deposition tracks are observed in Figure 4.14 (a) and (b). No cracks are observed in the overlapping zone during the overlapped multi-track deposition as observed in the single tracks at the same process parameter. The overlapping zone is a potential area of inter-track porosity due to lack of fusion zones. In addition, the presence of macro scale porosities is not observed along the cross-section. These macro porosities are majorly contributed by gas porosity, trapped foreign material, and material absence due to contraction. The absence of cracks and macro-porosities indicates that the deposit is defect-free with a sound metallurgical bond between the tracks in the macro scale. Figure 4.14 (c) presents the macroscopic view of the deposit top surface. It is observed that the deposit is crack-free confirming the suitability of process parameters for deposition of bulk structures. However, layer-wise pattern and partially melted powder particles are visible on the top surface of the deposited layer. The layer-wise pattern is due to the linear scan path followed by the laser, which is true for all additive manufacturing processes. The presence of partially melted powders is primarily due to the inability of the laser to melt the fed powder completely, which results in the presence of partially melted powders. These powders did not receive enough energy to melt and form a continuous deposit. However, the powder particles got sufficient energy to just form a bond with the built layer. Spatter formation during LDED process is also a source for the presence of partially melted particles on the deposit surface. These are generated from the melt-pool due to the strong temperature gradients inside the melt-pool leading to temperature-dependent and multifaceted hydrodynamic flows in the melt-pool.

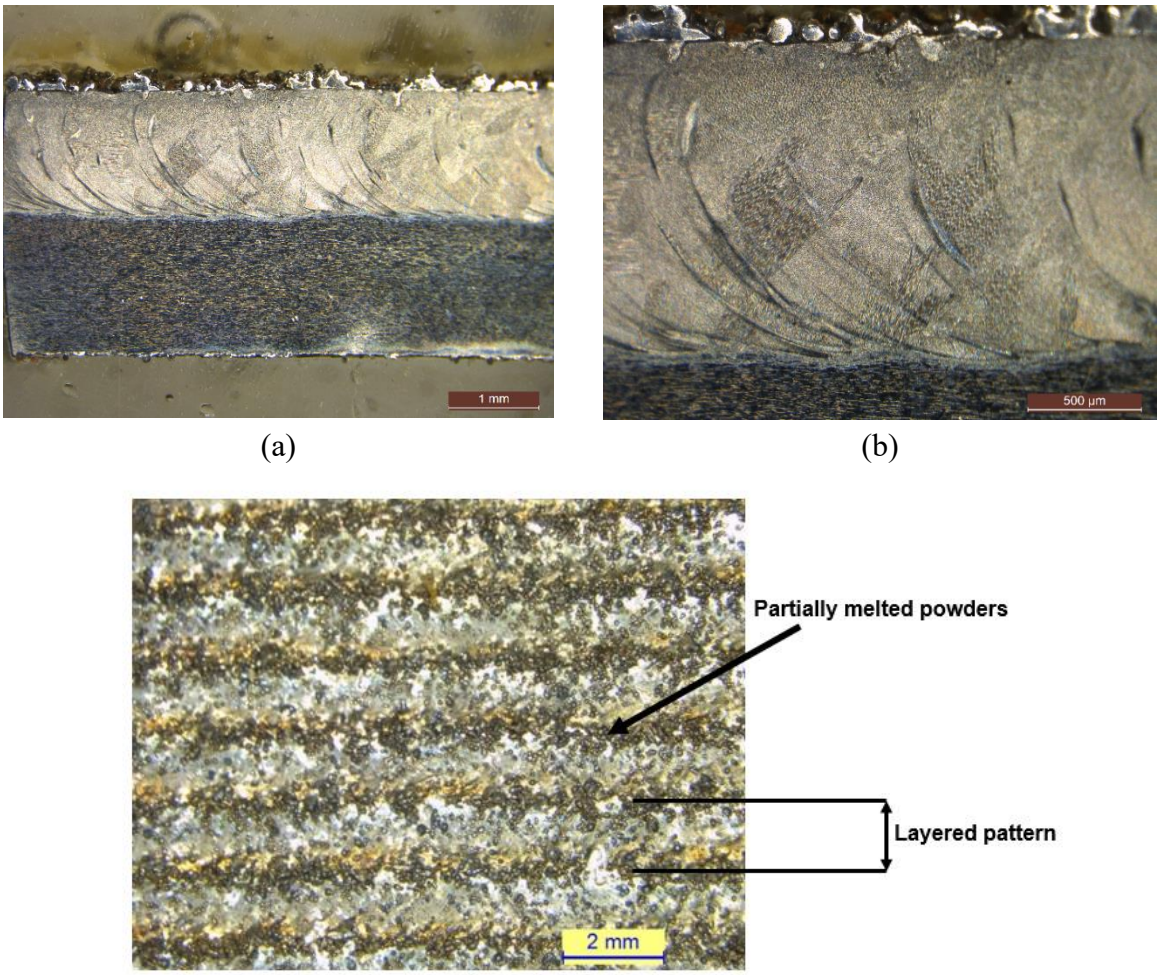

(a) (b)

(c)

Figure 4.14: Overlapped track deposition (a) Macro-structure at lower magnification (b) macro-structure at higher magnification (c) top-surface

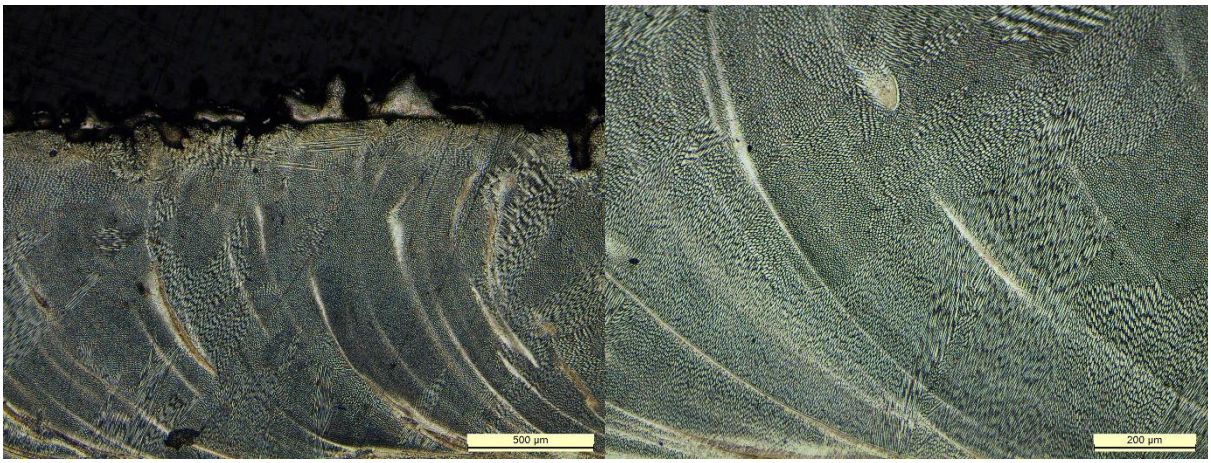

(a) (b)

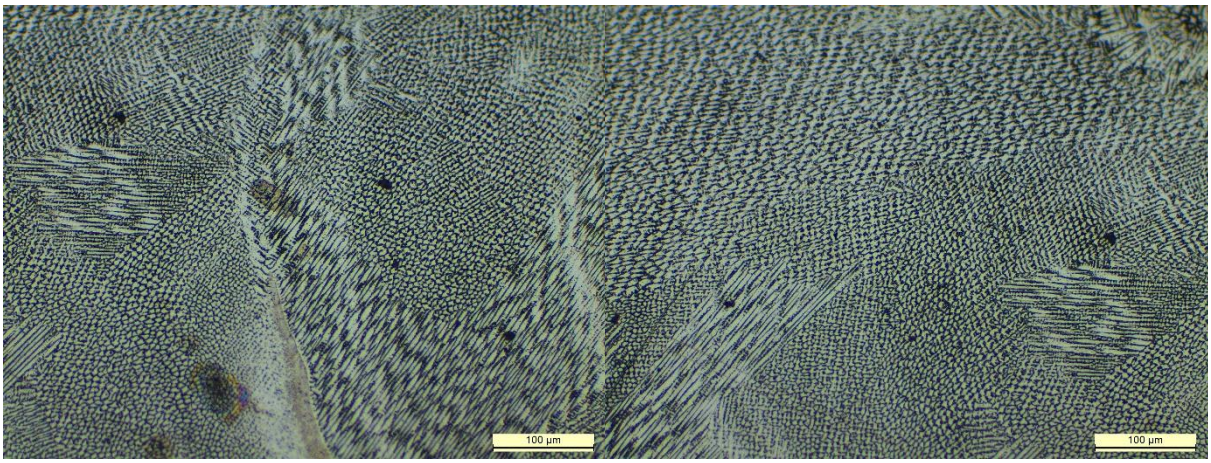

(c) (d)

Figure 4.15: Microstructure of the single-layer overlapped track deposition at different locations

Figure 4.15 presents the microstructural analysis of the overlapped track deposited layer. It is observed that deposited layer is crack free in the micro-scale also, with the presence of few isolated porosities. The thermal history in the form of heat affected zone (HAZ) for overlapped melt-pool path is visible in the deposited layer. The columnar growth is observed and the microstructure is a combination of cellular and dendritic growth. This is primarily due to the higher thermal gradient associated with the process. Cellular growth is mainly seen at the deposit-substrate and track-track interface due to the higher thermal gradients. The grain structure is fine due to the higher cooling rate during the deposition process. The defect-free nature of the deposited layer in the micro-scale also confirms the suitability of the process parameter for bulk deposition.

4.8 Summary

As the commercially available Hast-X powder is used in the investigation, it is first characterized for morphology and chemical composition to confirm the quality and suitability for LDED deposition. Parametric investigations of track geometry show that the major factor governing track width and track height is laser power and powder feed rate, respectively. An

analytical model for predicting the LDED built single track geometry using an extension of Rosenthal equation shows good agreement with the experimental results. The cracking is observed at higher Laser Energy per unit Powder Feed (LEPF), which can be due to a combination of elemental segregations and higher thermal stresses. The process window for the defect-free deposition without cracks and discontinuity is observed with LEPF in the range of 8.2 - 13.2 kJ/g at a scan speed of 0.3 – 0.7 m/min. Porosity analysis of the tracks shows that the area fraction density of the continuous tracks is found to be greater than 99.5%. Further, a combination of the build rate analysis and porosity analysis is used to select the process parameter combination for overlapped-track deposition. The overlapped-track depositions are analysed and observed to be defect-free in the macro and micro scale.

Chapter 5 :Effect of Laser Energy per unit Powder Feed and Interlayer Delay Period on LDED Built Hast-X Thin Walls [3]

5.1 Introduction

One of the exciting applications of LDED is the building of thin walls for manufacturing components having complex shapes with improved material utilization. During LDED, the deposited material undergoes rapid cooling enabling the building of a structure/ wall with a low aspect ratio (ratio of width-to-height). However, the precise control on the thin wall geometry during LDED is a challenge due to distortions generated on account of larger thermal gradients and resulting thermal stresses. This can be controlled by appropriate selection of LDED process parameters [167,168].

On the application side, thin-walls are used for shaping many engineering components, like-blades of an impeller or turbine, heat exchanger walls, and heat exchangers fins, widely used in aerospace and power sectors [169]. In some applications, thin-walled metallic parts are used to increase the machine functionality without expanding the machine's size and to assemble small machines [170]. Literature shows that the thin walls are deposited by LDED for varying width ranging from 1 mm to 6 mm [171]. In most of these applications, LDED built thin-walled components are post-processed to meet the end-use requirements [172]. The total manufacturing process of a complex thin-walled component using conventional techniques is time-consuming and yields higher material wastage. However, LDED may save the machining

[3] This chapter is reproduced with permission from Elsevier (Journal – S. No. 7) – See Letters of Copyright Permission (Page No. 210)

time up to 80% and the overall cost by 20 – 50% for building components having thin walls as major feature [168]. Further, conventional machining of thin-walled structures for aspect ratio greater than 10 is more challenging due to buckling of the machined wall as a result of cutting forces [168].

Several researchers are working on the building of thin wall structures by LDED. One of the major issues associated with LDED of wall structures is the deviation in the wall dimensions primarily due to the accumulation of thermal energy leading to temperature rise during continuous layer by layer deposition. According to Lee et al. [165], a bulge is observed during multi-layered LDED due to the combined effect of surface tension, gravitational force during laser interaction time, and fluid convection inside the melt pool. Surface tension generally tends to provide a round shape to the melt pool surface for minimizing the surface energy. However, the gravitational forces acting at the edges of the deposit prevents it from forming a perfect circular cross-section. In addition to this, the top surface of the pre-deposited layer is at a higher temperature at the beginning of deposition for any layer as compared to that at the previous layer. This is primarily due to insufficient time for input heat to dissipate during the continuous layer by layer deposition. This increase in the melt pool fluid volume leads to a larger and deeper melt pool. The average temperature of the melt pool also increases causing a reduction in viscosity and density. This is also supported by gravity forces and thermo-capillary convection, providing a combined downward force and offers the melt pool a tendency to slide down to the deposit edges. This results in sidewalls with bulged edges and larger width as compared to the single-track width. In order to control the geometry of the wall structures, temperature accumulation should be controlled. This can be done by varying the laser energy input within the defined process window for material or by providing idle time between each layer.

In the previous chapter, the process was developed for building continuous and crack free Hast-X structures using LDED. The developed process window showed that the Laser Energy per unit Powder Feed (LEPF = Laser Power/Powder Feed Rate) of 8.2 - 13.2 kJ/g resulted in continuous and crack free structures at scan speeds ranging from 0.3 – 0.7 m/min. The literature survey shows that there is no comprehensive study available in the public domain on the effect of LEPF and interlayer delay on LDED built wall structures, especially on nickel superalloys. Thus, in the present chapter, a detailed investigation is carried out to understand the effect of LEPF and interlayer delay (time delay between successive layers) on the wall geometry and Hast-X material property. Finite element based numerical simulation is also used for explaining the effect of LEPF and interlayer delay on the temperature distribution and its correlation with wall geometry and material properties.

5.2 Effect of LEPF on LDED built Thin Wall Structures

5.2.1 Experimental Details

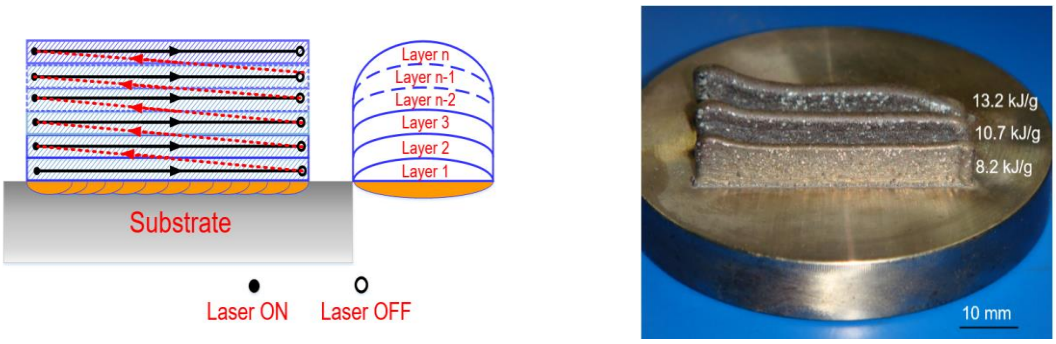

(a) (b)

Figure 5.1: LDED built walls at different LEPF (a) Deposition Strategy (b) Pictorial view

Wall structures are built at three different LEPF values i.e., 8.2 kJ/g, 10.7 kJ/g and 13.2 kJ/g using LDED. It is derived by varying laser power, while the scanning speed and powder feed rate are kept constant at 0.5 m/min and 6 g/min, respectively. The laser power deployed for the deposition is 820 W, 1070 W, 1320 W for 8.2 kJ/g, 10.7 kJ/g and 13.2 kJ/g, respectively.

Vertical shift equal to 0.4 mm is provided after depositing each layer for building wall structures. Unidirectional strategy as shown in Figure 5.1a is used, in which deposition takes place along one direction and laser is turned off during return path. Figure 5.1b presents the photographic view of LDED built Hast-X thin walls.

5.2.2 Geometrical Analysis

Figure 5.2a to 5.2d presents the 3D scanned model, plane along the length of the wall and normal to substrate, plane along the cross-section and normal to substrate and plane along the build direction and parallel to substrate, respectively to analyse the geometry variation. INSPECT software is employed for generating the 2D sections of the walls along the length, cross-section and build direction. Wall geometry is analysed by considering planes along the length of wall, cross-section and build direction. The obtained data is compared and analysed using statistical tools.

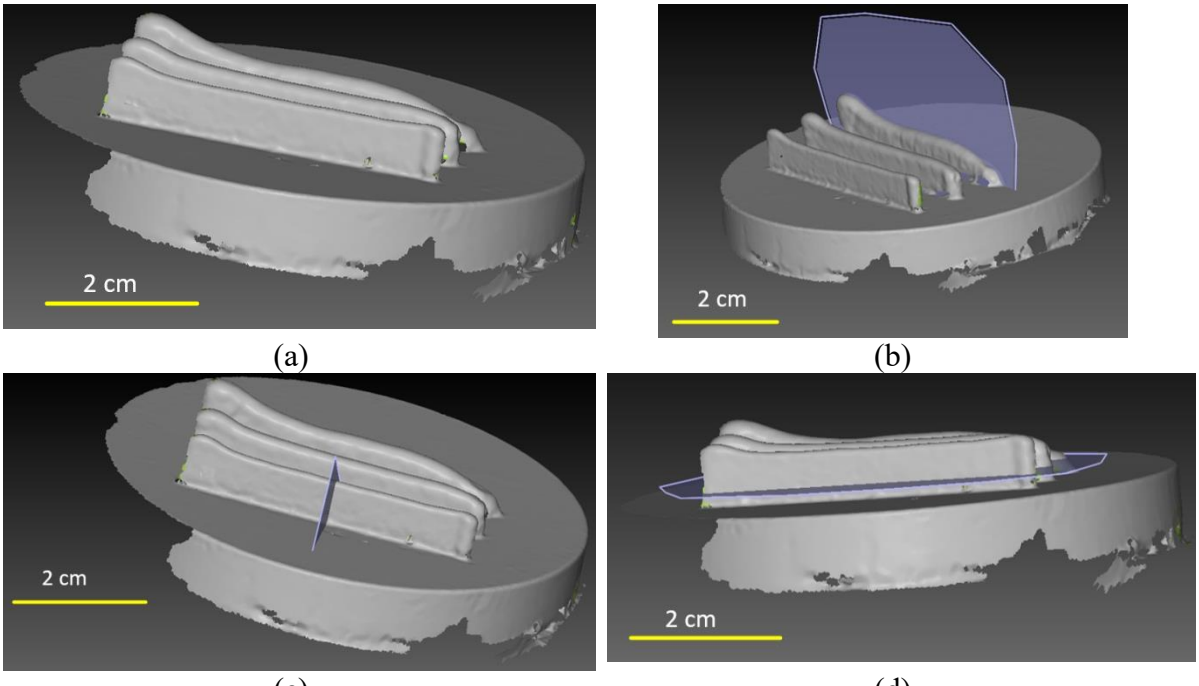

(a) (b)

(c) (d)

Figure 5.2: LDED built walls a) 3D Scanned Model b) Plane along the direction of track laying c) Plane along the cross-section d) Plane along the build direction

i. Wall Height

Figure 5.3a presents the variation of wall height along the length of the wall with a closer examination at the central region of the wall. It is seen from Figure 5.3a that the maximum wall height is observed at the start of deposition, which is primarily due to the inertia of the motion control system. Further, the excess amount of powder available on the surface of the previously deposited layer due to the unidirectional strategy (laser off during return, while powder is on) leads to an excess height at the starting point as compared to the endpoint of deposition as the laser gets off at this position. Further, as the layers build up, the standoff distance decreases due to more height at the starting point. The reduction in standoff distance results in a laser beam with higher energy density due to reduced beam width [173] and the higher value of energy density contributes to further increase in its height. Thus, there is a large difference in height between the starting point and other regions of the wall. The effect is more dominating for higher laser energy density. As a result, the maximum height at the starting position is observed for 13.2 kJ/g followed by 10.7 kJ/g and 8.2 kJ/g. However, it can be observed that as the laser moves from the starting position to the end position (in a layer), the height of 13.2 kJ/g wall gradually reduces. At the endpoint of the wall, the height of 13.2 kJ/g is minimum followed by 10.7 kJ/g and 8.2 kJ/g. Thus, the variation in wall height is more at 13.2 kJ/g, followed by 10.7 kJ/g with least variation for 8.2 kJ/g. For geometry analysis, a central region, as marked in Figure 5.3a, is used. Figure 5.3b present the box plot of the central region of the wall, respectively. The mean value of the wall height at the central region reduces with an increase in LEPF and the measured mean values of wall height are 6.79 mm, 6.66 mm and 6.42 mm for 8.2 kJ/g, 10.7 kJ/g and 13.2 kJ/g, respectively. The range of wall height is lowest for 8.2 kJ/g, while the value of the range of wall height increased by 75 % and 256 % when LEPF is increased from 8.2 kJ/g to 10.7 kJ/g and from 8.2 kJ/g to 13.2 kJ/g, respectively. It can also be noted that due to the preheat effect at higher layers, melt pool volume increases at higher layers, which leads to higher powder catchment. However, higher wall height results in

exposure to higher laser energy density and resulting in larger outward flow of the melt pool increases. These two competing phenomena yields the resultant wall height. An increase in the range of height at 13.2 kJ/g also shows that the variation in height increases with increase in LEPF. This is due to the higher amount of energy available at the melt pool during higher LEPF, leading to an increase in melt pool instability, which is explained using Figure 5.4.

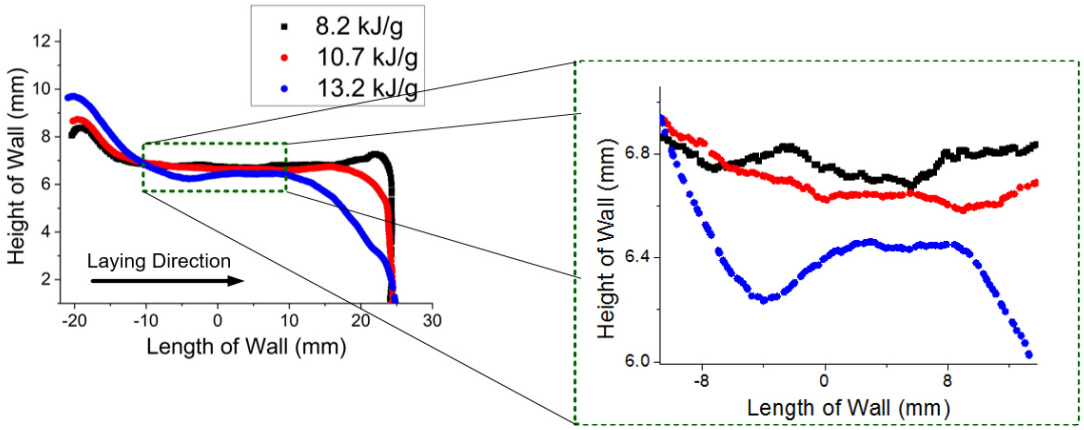

(a)

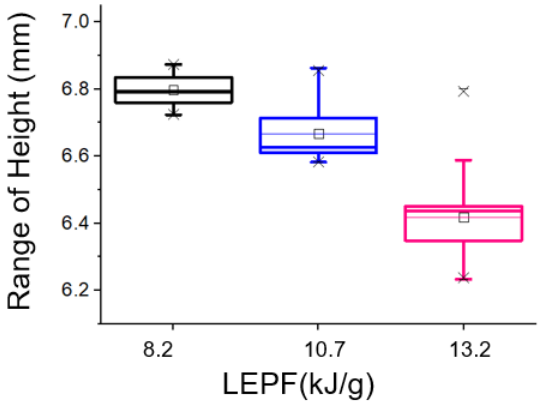

(b)

Figure 5.3: Measurements along the length of the wall at different process conditions a) Wall height b) Box plot of wall height in the central region

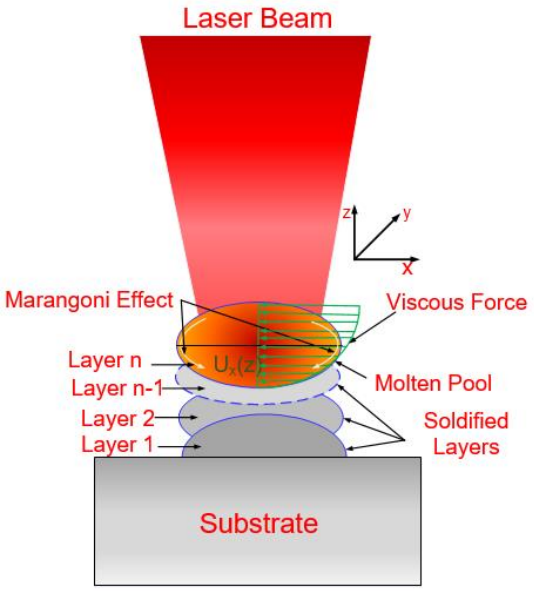

Figure 5.4: Schematic of the melt pool showing the various effects

The melt-pool instability generated during LDED and schematic are shown in Figure 5.4 can be explained as follows: During LDED, thermal conduction and thermo-capillary flow of molten metal are the major sources for carrying the absorbed laser power from the melt pool surface into the feed powder and the substrate/previously deposited layer [158]. The outward flow of the melt pool is aided by the thermo-capillary flow due to surface tension and restricted by the viscosity of the material. Thus, a 2-D configuration of the melt pool is presented in this section, where the melt pool shape is governed by surface tension and viscous forces as the laser beam moves away (as shown in equation 5.1) [164]. Equation 5.2 presents the variation in temperature distribution along the surface of the melt pool boundary [158].

$$\mu_L \frac{\partial u_x(z)}{\partial z} = \left(\frac{d\gamma}{dT}\right)\left(\frac{\partial T}{\partial s}\right) \tag{5.1}$$

$$\frac{\partial T}{\partial s} = \frac{h\,(T - T_0)}{K_m} \tag{5.2}$$

Integrating equation 5.1 with the boundary condition: $z = 0$ and $u_x(z) = 0$, equation 5.3 is obtained as:

$$\mu_L . U_x(z) = \left(\frac{d\gamma}{dT}\right) \times \left(\frac{h.(T - T_0)}{K_m}\right).z \tag{5.3}$$

Where, U_x (z), the fluid velocity is the ratio between fluid displacement (x_f) and interaction time (D/v). Thus, equation 5.3 can be rewritten as equation 5.4 and 5.5. Thus, the fluid spread *(x_f)* is a function of the temperature inside the melt pool, beam diameter, scan speed, viscosity, surface tension gradient $(\frac{d\gamma}{dT})$ and *z*.

.

$$\frac{\mu_L . x_f . \mathrm{v}}{D} = \left(\frac{d\gamma}{dT}\right) \times \left(\frac{h.(T - T_0)}{K_m}\right).z \tag{5.4}$$

$$x_f = \frac{D\,z}{v\mu_L}\left(\frac{d\gamma}{dT}\right) \times \left(\frac{h(T - T_0)}{K_m}\right) \tag{5.5}$$

Thus, at a constant beam diameter (*D*), scan speed (*v*) and material properties, the fluid spread in the melt-pool is a direct function of its effective fluid viscosity in the melt-pool. At higher laser power and higher layers, melt-pool temperature increases leading to reduction in the effective viscosity and surface tension. The availability of excessive laser energy leads to local vaporization of molten metal and unstable melt-pool and the larger volume of molten metal adds to melt-pool instability.

ii. Variation of wall width

Figure 5.5 presents the variation of wall width along the cross-section of the wall structures at the center of the wall length. Figure 5.5a presents the box plot showing the mean wall width and variation of wall width along the cross-section. The measured mean wall width is 1.47 mm, 2.47 mm and 3.36 mm for 8.2 kJ/g, 10.7 kJ/g and 13.2 kJ/g, respectively. The measured maximum value of wall width is 1.79 mm, 2.58 mm and 3.49 mm for 8.2 kJ/g, 10.7 kJ/g and

13.2 kJ/g, respectively. Thus, at higher values of LEPF, the width of the melt pool is larger resulting in larger wall width. Further, the fluid displacement and outward flow are also higher at higher LEPF leading to increased wall width as seen in the previous section. It is also observed that the wall width increases with the number of layers. This is because the top solid surface after (n-1) th layer deposition is at a relatively higher temperature before depositing the nth layer, which provides a preheating effect. This is mainly due to unavailability of adequate time to dissipate the heat energy (at the end of the (n-1) th layer) during multi-layered wall deposition. This leads to increased melt pool fluid volume resulting in a larger and deeper melt pool. Further, the increase in the average melt pool temperature leads to a reduction in viscosity and fluid density [174]. In addition, a convection phenomenon takes place inside the melt pool due to the temperature distribution as the temperature in the melt pool reduces from the center of melt pool to the edges due to the laser beam profile. Lower temperature leads to higher surface tension and this leads to liquid flow from low surface tension region to higher surface tension region. This results in an outward flow of molten material and provides a downward force for the melt pool. This offers a propensity for the melt pool to slide to the edges resulting in larger width values at higher layers. These observations are in line with the work published by Lee et al. [165].

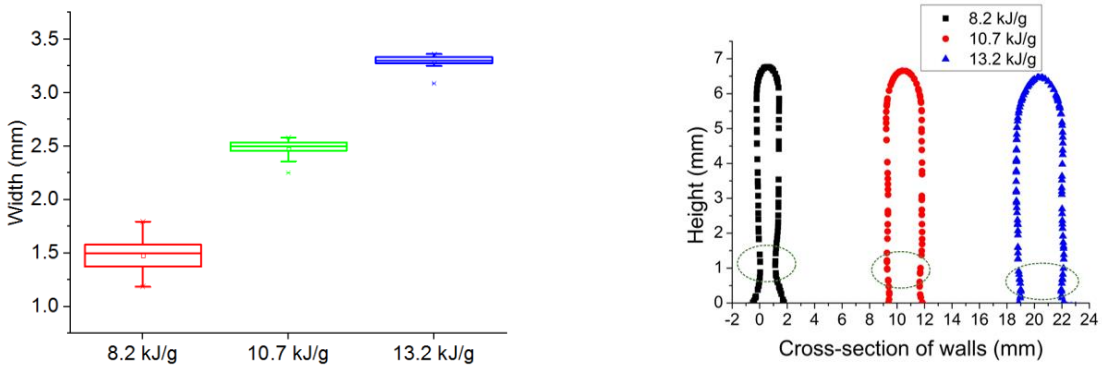

(a) (b)

Figure 5.5: Measurements along the cross-section of wall at different process conditions (a) Box plot (b) Cross-section

Figure 5.5b presents the cross-section image of the walls built at three different values of LEPF, where zero height represents the substrate surface. The variation in the wall width is visible. Neck formation is observed at the lower layers at all values of LEPF and it is found to be more pronounced at 8.2 kJ/g. At lower values of LEPF, the catchment is low due to the lower amount of available energy and higher ricocheting effect of feed powder. The feed powder along with the gas tends to shear the melt pool resulting in the neck formation. However, as the layers build up, the shearing effect reduces due to the increase in the powder catchment. The increased catchment at higher layers can be due to the preheating effect of previous layers and increase in the melt-pool surface area as the deposition goes from the flat substrate surface to the convex surface of the previous layer [17]. Reduction in the neck formation at higher LEPF is mainly due to higher catchment at higher LEPF and this leads to more uniform wall width. It can also be noted that the position of necking has moved to a lower height value with an increase in LEPF, which indicates that the wall attains stability at the lower height at higher LEPF as compared to walls built at lower LEPF. This is mainly due to the higher amount of laser energy available at higher LEPF, which leads to increased powder catchment.

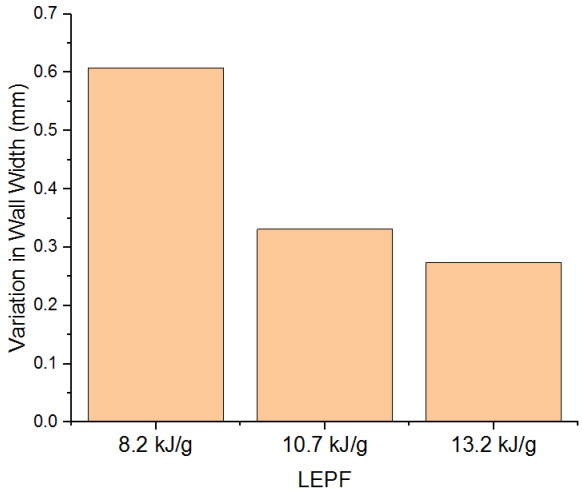

Figure 5.6: Maximum variation of width along the cross-section of the wall

It can be noted from Figure 5.6 that the maximum variation of wall width decrease continuously with an increase in LEPF. The higher variation at lower LEPF is mainly due to necking and the presence of stair-stepping effect as a result of reduced re-melting of previously deposited layers. With an increase in LEPF the variation in wall width reduces continuously due to reduction in the necking effect and stair-stepping effect. This is due to the increase in the re-melting of previous layers and reduction in the partially melted powders on the surface due to increased catchment.

iii. Variation of wall profile along the build direction

Figure 5.7 presents the variation in the wall width profile (in the XY plane) along the length at different values of height from the substrate (Z direction) for a central region of 20 mm (-10 to 10). Figure 5.7a presents the variation of wall width profile along the length at different z values such as 1 mm, 2 mm (for lower layers), 5 mm and 6 mm height (for higher layers) from the substrate surface. It is seen that the deviation in the profile is more for 8.2 kJ/g at lower layers i.e., z values of 1 mm and 2 mm. This is clearly due to the necking effect and the presence of partially melted powders at 8.2 kJ/g. However, at higher layers, i.e., z values of 5 mm and 6 mm, the deviation in profile along the length is more for 13.2 kJ/g with maximum deviation at

z = 6 mm. Figure 5.7b presents the values of the range of wall profile at different z values. At z = 1mm, the maximum range is observed for 8.2 kJ/g and minimum range is observed for 13.2 kJ/g. However, as the z increases, the trend reverses and at z = 6 mm, the maximum range is observed for 13.2 kJ/g and minimum range is observed for 8.2 kJ/g. Only slight variation in range values is observed for 10.7 kJ/g from z plane at 1 mm to 6 mm. The reduction in the range at 8.2 kJ/g with the increase in wall height is mainly due to the reduction in the amount of partially melted powders on the wall surface, lack of necking and improved catchment with an increase in the number of layers. On the other side, the increased deviation at higher layers for 13.2 kJ/g is due to increased melt flow at higher layers as a result of increasing melt pool temperature. Thus, the trend depicted by the range in figure 5.7b shows that spread in data is more for 8.2 kJ/g at lower layers, while the maximum spread is observed for 13.2 kJ/g at upper layers.

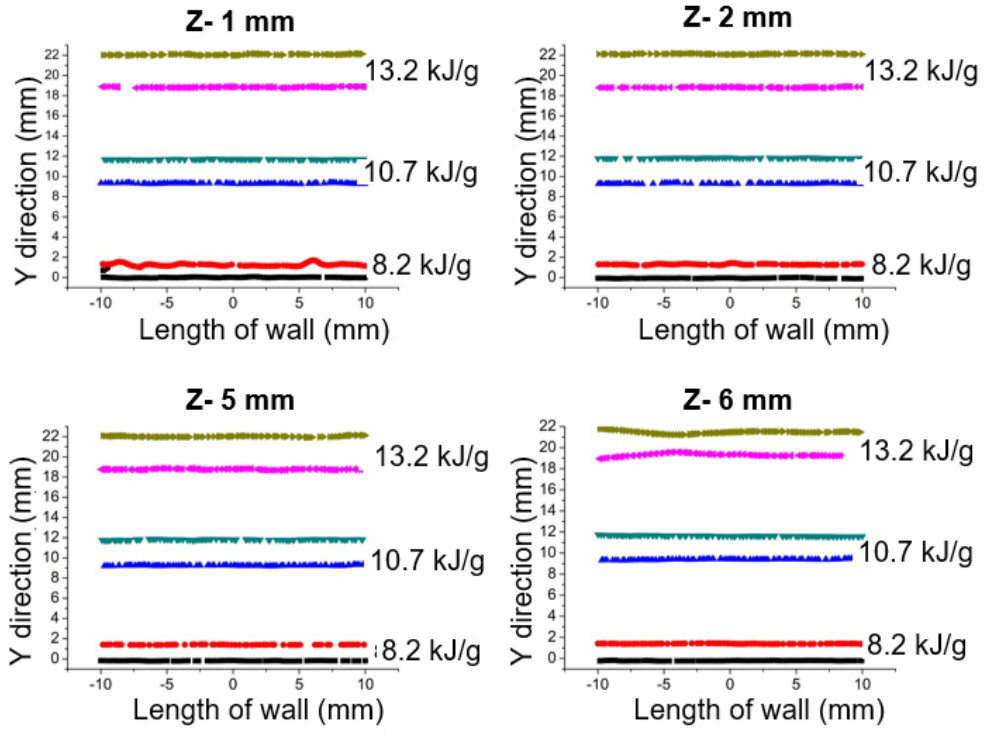

(a)

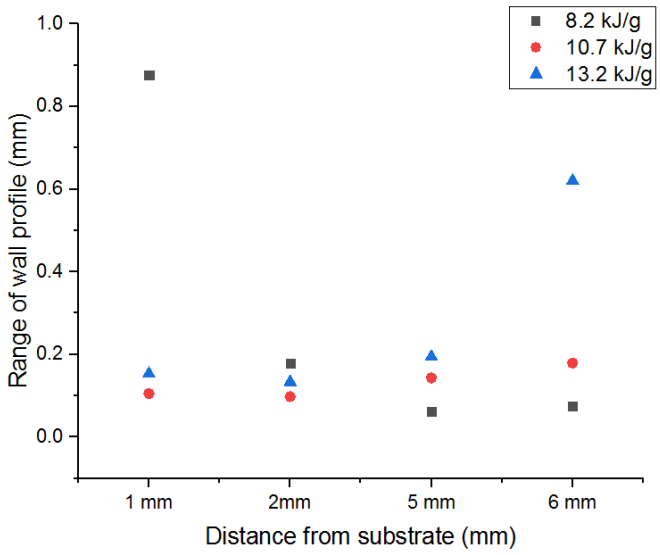

(b)

Figure 5.7: Measurement along z plane a) wall profile b) Range of wall profile in the central zone

5.2.3 Microstructural Characterisation

Macrostructure of thin wall structures built at 8.2 kJ/g, 10.7 kJ/g and 13.2 kJ/g is presented in Figure 5.8a, 5.8b and 5.8c, respectively. In the macrographs, the layered pattern is visible due to the heat effect during layer-by-layer deposition. The built structures are continuous and free from macro-defects (cracks or inclusions) at all three conditions. The morphology also indicates a coherent metallurgical bonding between consecutive layers. The presence of the partially melted powders is observed at the lower layers of 8.2 kJ/g, due to lower catchment at lower LEPF during the initial layers of deposition. The depth of the built walls on the substrate subsurface is 0.2 mm, 0.76 mm and 0.97 mm for 8.2 kJ/g, 10.7 kJ/g and 13.2 kJ/g, respectively. The higher depth at 13.2 kJ/g signifies more remelting of the previously deposited layers during multi-layered deposition, which results in reduced stair-stepping effect during LDED.

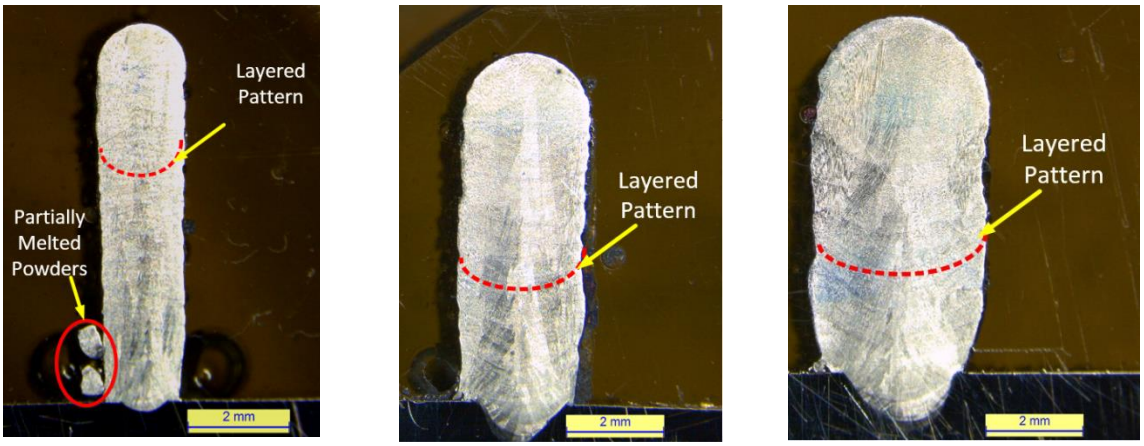

(a) (b) (c)

Figure 5.8: Macrostructure of wall structures a) 8.2 kJ/g b) 10.7 kJ/g c) 13.2 kJ/g

The microstructure during LDED is a function of two major parameters, i.e., temperature gradient (G) and growth rate (R) that govern the mode of grain growth and size of the grains. The temperature gradient is primarily dependent on the laser energy available per unit area for deposition, while the solidification velocity is directly related to the scan speed. Figure 5.9a presents the effect of G and R on the morphology and size of microstructure. G/R and G × R decides the grain morphologies and grain size, respectively. Higher values of G/R results in cellular growth and lower values of G/R leads to equiaxed microstructure during LDED. Further, as the G × R-value increases, the cooling rate increases, which results in finer grain structure [49]. The most commonly witnessed solidification microstructures in the LDED components are columnar and equiaxed. The columnar growth can be terminated at some solidification conditions and equiaxed structure are formed. The changeover from columnar to equiaxed takes place when nucleation of adequately several equiaxed dendrites occurs in the constitutionally under-cooled liquid contiguous to the columnar dendritic front[49].

Figure 5.9b, 5.9c and 5.9d present the microstructure of walls built at LEPF of 8.2 kJ/g, 10.7 kJ/g and 13.2 kJ/g, respectively. The microstructure is analysed at three different locations i.e., bottom, middle and top layers for all the three samples and the defects are not observed at

micro-scale also. The microstructure is a mix of cellular and dendritic growth and characterized by columnar growth at all the conditions. Dendrites with classical secondary arms are mainly observed at the top layers of 8.2 kJ/g and 10.7 kJ/g. However, dendrites with secondary arms are observed in the middle layers and top layers at 13.2 kJ/g. There is no evidence of equiaxed dendrite formation at the top layers of deposition. It is also found that the size of the dendrites increases with an increase in LEPF because of reduction in the cooling rate due to an increase in the preheat temperature during multi-layered deposition. Similarly, the size of dendrites increases from bottom to top layers because of increase in preheat temperature caused due to previously deposited layers. The measure value of average dendrite width at various location with different LEPF is presented in Table 5.1.

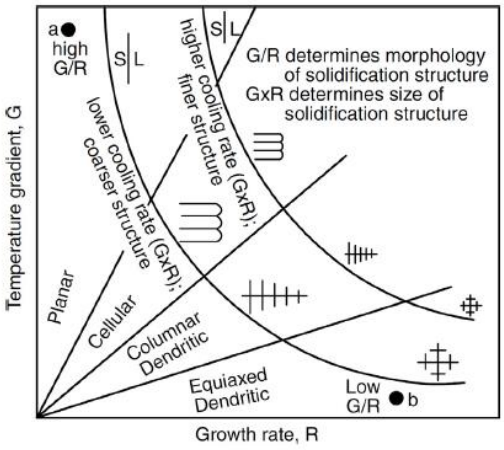

(a)

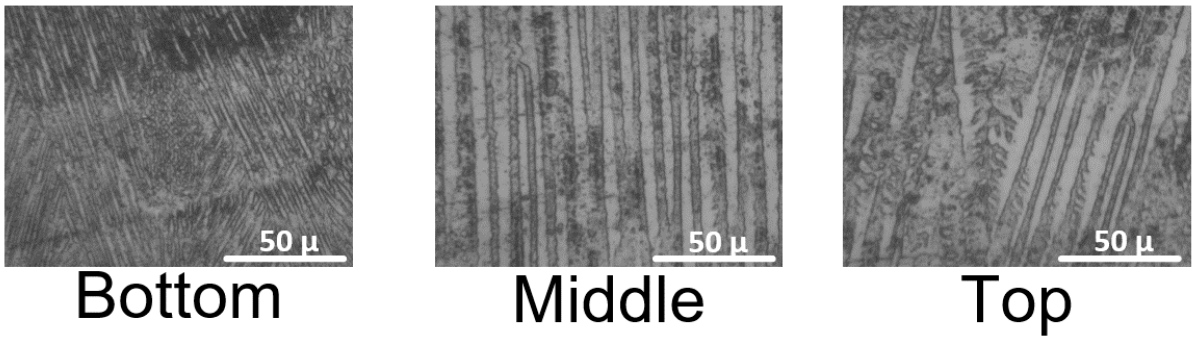

Bottom Middle Top

(b)

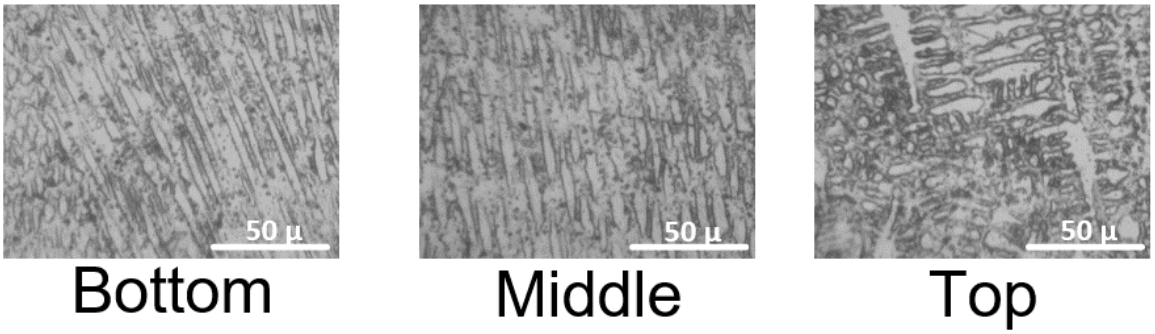

(c)

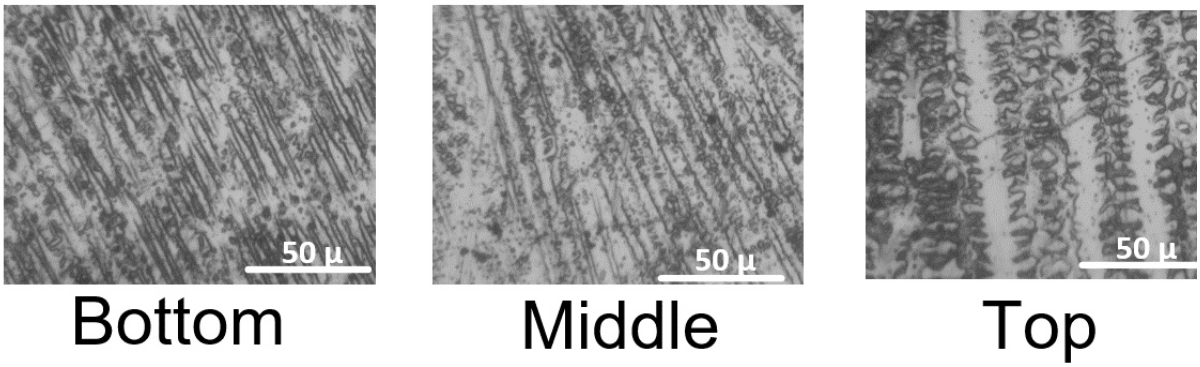

(d)

Figure 5.9: Microstructure a) effect of G and R [49] b) of wall structures at 8.2 kJ/g c) of wall structures at 10.7 kJ/g d) of wall structures at 13.2 kJ/g

Table 5.1: Average dendrite width at various location with different LEPF

LEPF (kJ/g)	Average dendrite width (µm) at various layers		
	Bottom	Middle	Top
8.2	2 ± 0.5	5 ± 0.4	7 ± 0.3
10.7	3 ± 0.3	5.5 ± 0.4	8 ± 0.4
13.2	5 ± 0.2	6 ± 0.5	11± 0.6

X-ray diffraction studies are performed from 30 to 80° for all the three conditions. The data is analyzed using PDF-4 software and the peaks are matched using the PDF Number: 00-004-

0850. The results show the presence of γ matrix as presented in Figure 5.10a. Slightly higher intensity of (200) plane indicates some preferred growth However, a slight shift in the peak is observed for all the samples. For instance, the peak position for the strongest peak corresponding to (200) plane is 50.83°, 50.73° and 50.57° at 8.2 kJ/g, 10.7 kJ/g and 13.2 kJ/g, respectively. Peak position shifts towards left (refer Figure 5.10b) is observed with a magnitude of 0.1° and 0.26° for 10.7 kJ/g and 13.2 kJ/g, respectively as compared to that of 8.2 kJ/g for the strongest peak. As per the Braggs law, as shown in equation 5.6, where n is an integer, λ is the X-ray wavelength, d is the lattice spacing and θ is peak position, the variation in peak position can be due to the variation in lattice spacing. This is mainly due to the difference in the lattice strain as the value of LEPF increases. In addition, the change in solubility of the elements into the matrix at different temperature due to variation in cooling rate with change in LEPF can also result in peak-shift.

$$n\lambda=2d\sin\theta \tag{5.6}$$

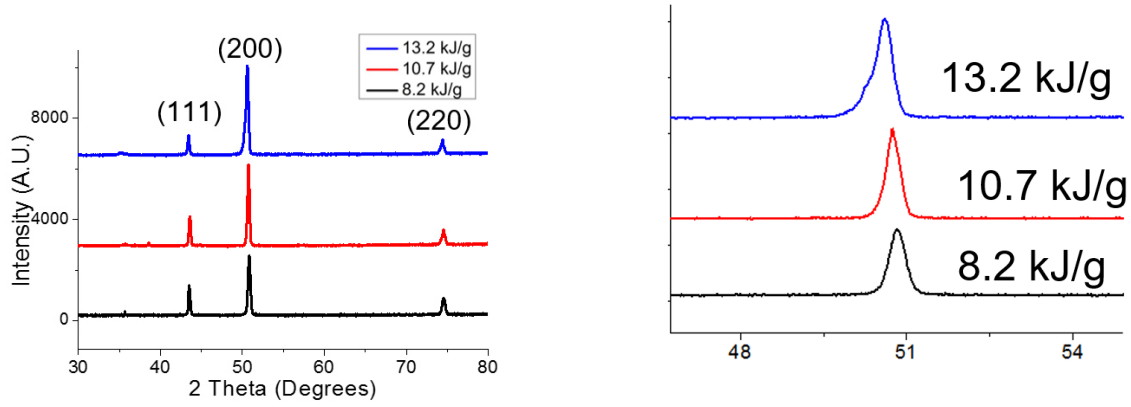

(a) (b)

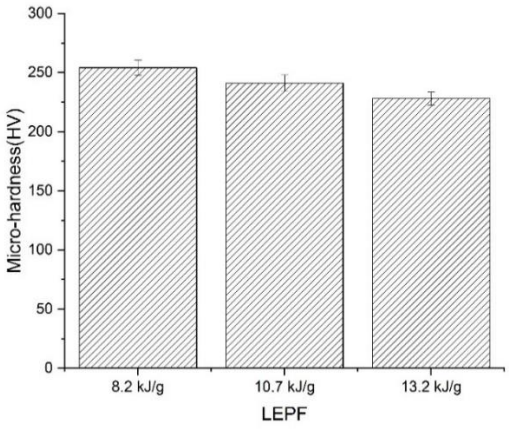

(c)

Figure 5.10: Effect of LEPF on a) XRD pattern b) XRD peak shift c) Microhardness

5.2.4 Mechanical Behaviour of wall structures

Microhardness is measured at three different locations on the cross-section of the sample. Figure 5.10c presents the average microhardness values obtained at three different LEPF. It is observed that the maximum value of average microhardness is obtained at 8.2 kJ/g and the minimum microhardness is obtained at 13.2 kJ/g. The difference in average microhardness between 8.2 kJ/g and 13.2 kJ/g is obtained as 10 %. Higher values of microhardness at lower LEPF is attributed to the finer microstructure as per Halls-Petch criteria [175,176]. These results are in line with the microstructural studies. The obtained value of microhardness is higher than the reported hardness values for conventional Hast-X (180 HV) [37].

Automated Ball Indentation (ABI) testing is carried out on LDED built thin walls to estimate the tensile behaviour as it is a non-destructive testing method. The suitability of using ABI for LDED samples is tested on bulk structures and it is presented in chapter 6. Load - indentation depth plot obtained on thin walls built at 8.2 kJ/g, 10.7 kJ/g and 13.2 kJ/g is presented in Figure 5.11a. It is observed that the load required for achieving same depth is higher for 8.2 kJ/g samples as compared to that of 10.7 kJ/g and 13.2 kJ/g, with only slight variation between 8.2 kJ/g samples as compared to that of 10.7 kJ/g. This is mainly due to relatively higher resistance to deformation offered by samples built at 8.2 kJ/g as compared to others due to relatively finer

microstructure. These are in line with results obtained during micro-hardness measurements and microstructural examinations. Figure 5.11b presents the flow curves of the built walls and it can be seen that the walls built at 13.2 kJ/g shows lower tensile strength than that of 8.2 kJ/g and 10.7 kJ/g. The samples built at 8.2 kJ/g and 10.7 kJ/g shows overlap in data depicting minimal variation in the flow curve with LEPF. The variation in the yield strength and ultimate strength with LEPF is presented in Figure 5.11c and it is seen that there is only a slight variation in strength between 8.2 kJ/g and 10.7 kJ/g. However, a drop in strength is observed at 13.2 kJ/g as compared to samples built at 8.2 kJ/g and 10.7 kJ/g. The obtained value of yield strength is slightly higher than the yield strength of the wrought Hast-X reported in the literature (340 MPa) [37]. These are in line with the results obtained during microhardness measurement.

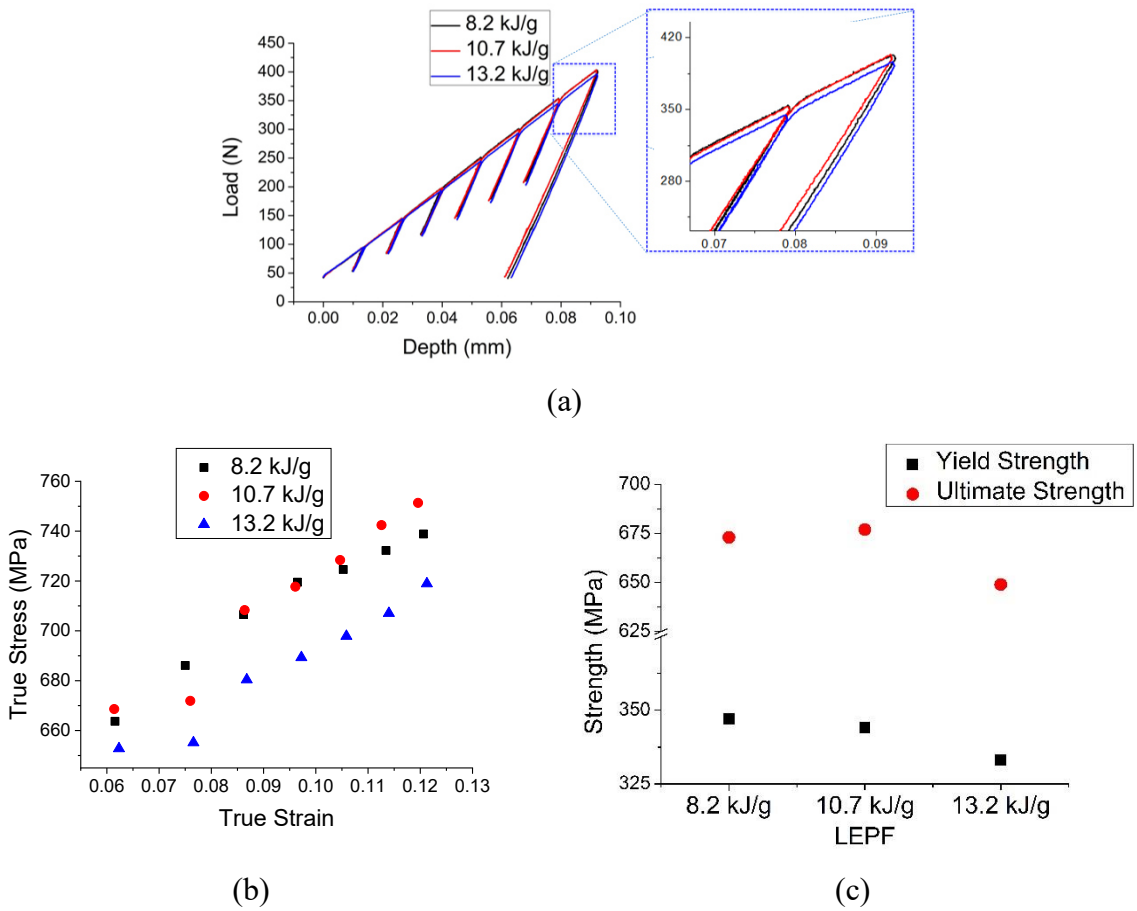

Figure 5.11: ABI on LDED Hast-X a) Load – displacement plot b) True stress – True Strain c) Variation of strength with LEPF

5.2.5 Thermal Analysis of Thin Walled Structures at different LEPF

Three-dimensional finite element simulations for thermal analysis of LDED process is performed using ANSYS (version 18.1) software to understand the effect of LEPF on the temperature distribution and preheat temperature during multilayer deposition

i Assumptions and Simplifications

- *Initial Conditions*: At the beginning of the deposition (t=0), the substrate is assumed to be at the room temperature (i.e. at 303 K)
- *Deposit Geometry*: The geometry of the LDED deposit is assumed to be rectangular in cross-section and the top surface is assumed to perfectly flat.
- *Heat Losses*: Convection losses are considered and radiation losses are neglected. Convective heat transfer coefficient (*h)* is taken as 20 W/m^2K for incorporating convection losses [177]
- *Material Properties*: The properties of the deposits are assumed as isotropic and homogeneous. Thermo-physical properties of Hast-X are taken from HAYNES International [37]
- *Laser Source*: The laser beam profile is assumed to be Gaussian and its effect is incorporated in the moving laser source by applying heat flux having a Gaussian beam distribution. It is assumed that 30% of the laser power is coupled with the surface for material deposition [178]. Figure 5.12 presents the schematic view of a layer built using LDED with the typical boundary conditions considered for the heat transfer analysis. The intensity distribution in the laser beam is considered as a Gaussian and moves along the y-axis in the XY plane.
- **Marangoni flow:** The actual thermal conductivity due to thermocapillary flow is more than the static melt conductivity. The effect of Marangoni flow is taken into account by modifying the thermal conductivity as shown in equation 5.7.

$$K^{*}=C\,K_{m},\ if\ T>T_{m} \tag{5.7}$$

Where, C is taken as 2.5 as mentioned by Kumar et al. [162].

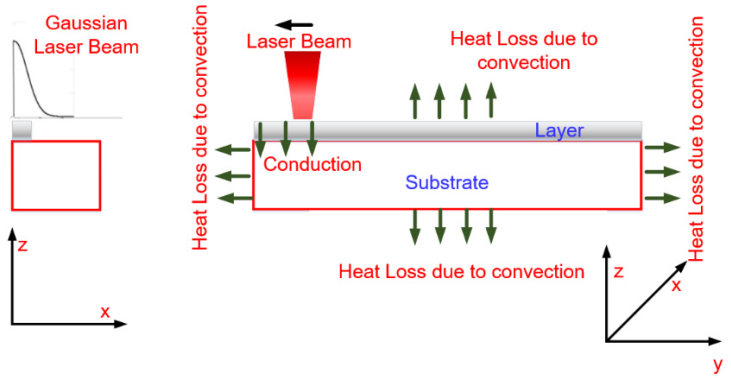

Figure 5.12: Boundary conditions used for Numerical Simulation

ii Governing Equations

Equation 5.8 and 5.9 presents the governing equation for energy conservation and boundary conditions, respectively. Heat conduction equation carries a significant role in the physical modelling of LDED process and thus, heat conduction equation in the three-dimensional Cartesian coordinate system is used as shown in equation 5.8 [179], in which the laser source moves in the y-direction. Boundary conditions are taken by considering the heat input, conduction and convection losses.

$$K^{*}\nabla^{2}\,T+\dot{Q}=\rho\,C_{p}\left(\frac{\partial T}{\partial t}-v\,\frac{\partial T}{\partial y}\right) \tag{5.8}$$

$$K^{*}\frac{\partial T}{\partial n}-q+h\left(T-T_{o}\right)=0 \tag{5.9}$$

iii Element and Meshing: Solid70 element type of ANSYS 18.1 is used for the thermal analysis and element birth and death technique is used to simulate the temperature. Before applying the proposed model, the mesh independency is checked using a dimensional parameter (δ) (ratio of laser beam diameter (D) to element size (e)) [162,179]. It was observed that the maximum variation in local temperature at all locations was less than

1.5% for δ > 25. Figure 5.13 presents the variation in local temperature with dimensional parameter. Thus, an element size of 0.1 mm is deployed for the present study.

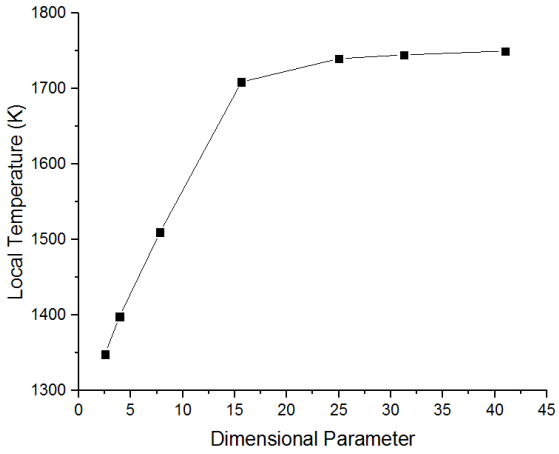

Figure 5.13: Variation of local temperature with dimensional parameter

iv Thermal Profile

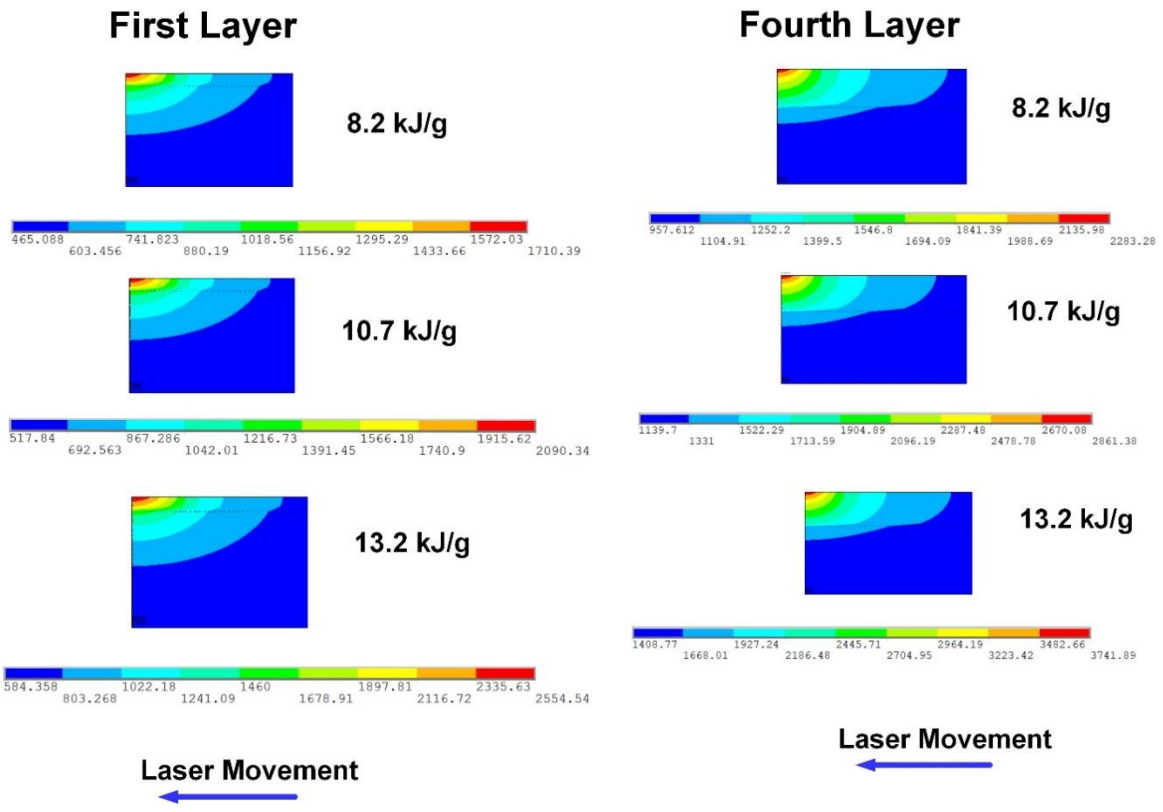

(a) (b)

Figure 5.14: LDED Temperature profile in YZ plane (a) first and (b) fourth layer with different LEPF

Figure 5.14 presents the thermal profile during 1st layer and 4th layer using ANSYS APDL at 8.2 kJ/g, 10.7 kJ/g and 13.2 kJ/g. The peak temperature is obtained at the center of the laser spot and decreases gradually with distance away from the center of laser beam. It can also be seen that the temperature of melt pool continuously increases with increase in LEPF values with thermal effect on the previously deposited layers and expanded heat affected zone. As the layers build up, heat transfer takes place through the previously deposited layers which are relatively at higher temperatures than the substrate temperature before deposition. This leads to increase in peak temperature at higher layers as compared to lower layers.

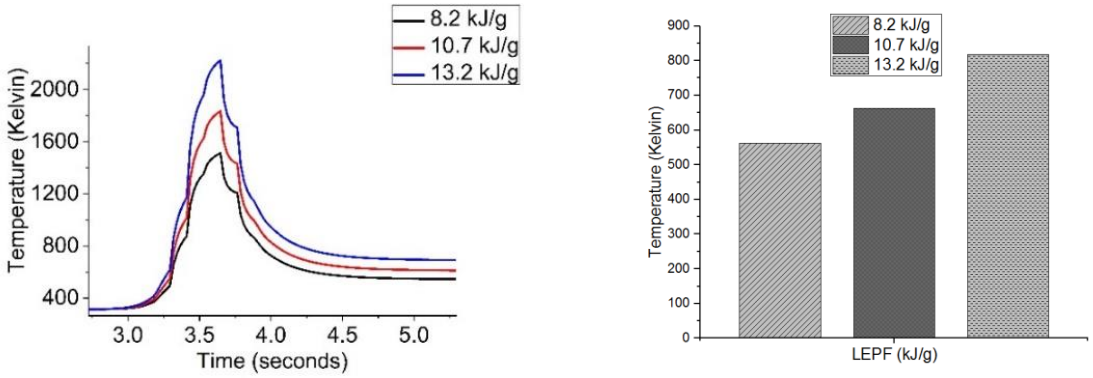

(a) (b)

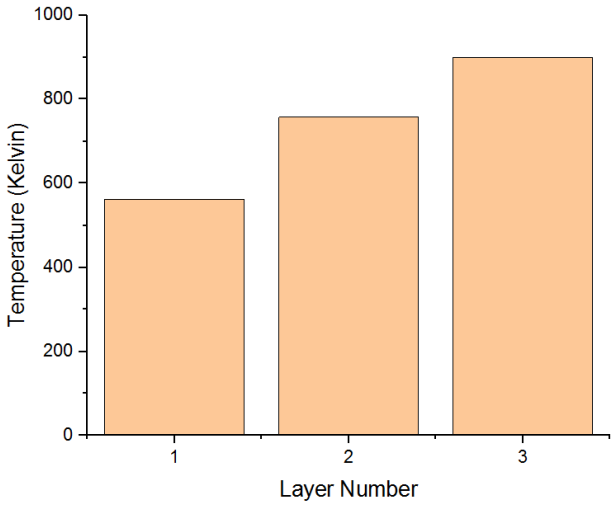

(c)

Figure 5.15: Numerical simulation showing a) Temperature distribution at a point on the first layer b) Effect of LEPF on preheat after the first layer of deposition c) Effect of layer number on preheat at a LEPF of 8.2 kJ/g.

Figure 5.15a presents a comparison of the temperature profile during the first layer of deposition at different LEPF values. As expected, the maximum temperature is achieved at a LEPF of 13.2 kJ/g due to the higher laser power used for deposition. Figure 5.15b presents the effect of LEPF on the preheating temperature. Preheating temperature presented in Figure 5.15b is the maximum temperature on the previously deposited layer before laying the next layer. The preheating temperature obtained after layer 1 is 552 K, 664 K and 824 K for 8.2 kJ/g, 10.7 kJ/g and 13.2 kJ/g, respectively. As the layers build up, a steady increase in the preheating temperature is observed as presented in Figure 5.15c. An increase in the preheating temperature with an increase in the number of layers can be due to the higher temperature at the previous layer leading to a reduction in the heat transfer. An increase in preheat temperature with LEPF is also obtained due to the increased amount of thermal energy available at the point of deposition. This increase in preheat temperature with an increase in the number of layers

and LEPF, results in increased wall width and reduced cooling rate leading to coarser grain structure and lower mechanical strength with increase in LEPF.

5.3 Effect of Interlayer delay on LDED built Thin Wall Structures

5.3.1 Experimental Details

In order to probe into the effect of interlayer delay on the geometry, microstructure, mechanical properties and thermal distribution of Hast-X wall structures, wall structures are built using laser power, scan speed and powder feed rate of 1600 W, 0.5 m/min and 8 g/min, respectively. The process parameter is selected from the process window based on the continuous deposition, minimal porosity and maximum build rate as presented in chapter 4. Wall structures are built by laying 10 layers one over the other with vertical shift of 0.42 mm. Unidirectional deposition strategy is deployed with an interlayer delay of 10 s, 20 s and 40 s between each layer. The delay is achieved by reducing the return speed to obtain the required delay period. During the delay period, the laser is turned off, but the powder and Argon flow is turned on continuously.

5.3.2 Wall Geometry

3D Laser Scanner is used to obtain the 3D model of the built wall and INSPECT plus software is used to analyse the geometry of the built walls. Figure 5.16a presents the typical 3D scan image of LDED built walls obtained from the laser scanner. Figure 5.16b and 5.16c present the planes along the build direction and direction of laser scan, respectively.

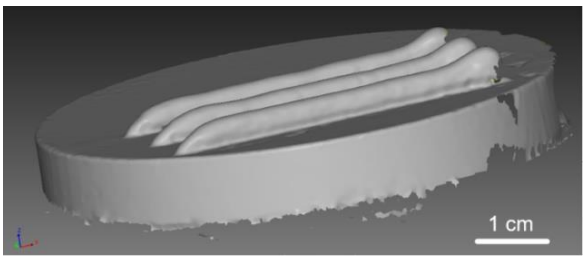

(a)

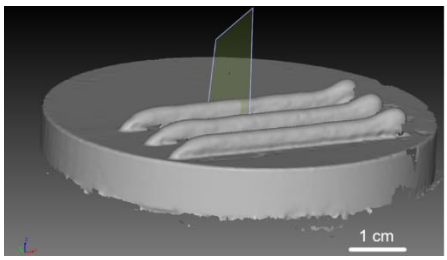

(b)

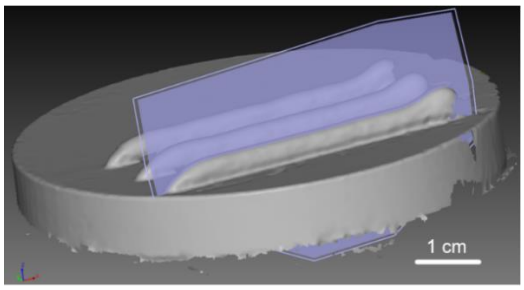

(c)

Figure 5.16: 3D laser scan images a) 3D model b) plane along the build direction c) plane along the direction of laser scan.

i. Wall height

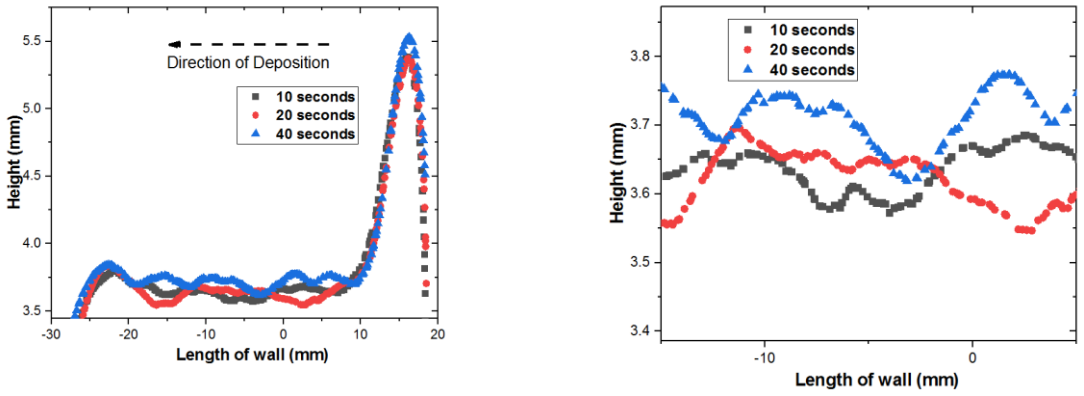

(a) (b)

Figure 5.17: Wall height along the length (a) total length (b) central region

Figure 5.17 presents the variation in wall height along the wall length. It can be observed that the maximum wall height is observed at the starting point, which can be attributed to the inertial (acceleration/deceleration) effects of the workstation. However, a significant difference in the starting point height is not observed between walls built with 10 s, 20 s and 40 s delay as opposed to the one seen in figure 5.3. This is primarily due to the same process parameters used for deposition. However, the maximum height of the wall obtained at the starting point is 5.5 mm for walls built with 40 s delay and 5.3 mm for walls built with 10 s and 20 s delay. The higher height for 40 s delay walls at the starting point is primarily due to lower preheat temperature and heat diffusion, which prevents the outward flow of the melt pool. The reduced

outward flow leads to an increase in the deposition height at the higher interlayer delay. In addition to the acceleration/ deceleration effects, due to higher laser power, the catchment is very high at the starting point as compared to the central region, which causes larger deviation in the wall height between the starting point and central region. The minimum height at the central region is primarily due to the continuous deposition and availability of laser energy and powder without inertial effect. However, the average height of the wall at the central region is slightly higher for 40 s delay wall as compared to that of 10 s and 20 s. The increasing trend seen in the wall height with an increase in the interlayer delay is very small primarily due to competing nature of reduced outward flow and reduced powder catchment at higher interlayer delay. One more interesting observation is that the variation in the wall height follows a wavy pattern, which can be a function of the process parameters. Higher laser energy per unit length results in higher melt pool flow and turbulence, which can result in a way pattern in the wall height.

ii. Wall width

Wall width is measured at three different locations (starting, center and middle) of the wall. The measurement is performed by considering a plane at the center of the wall, 10 mm from the start point and 10 mm from the ending point. Table 5.1 presents the width measured at the three different locations for the wall built at an interlayer delay of 10 s, 20 s and 40 s. It is observed that the wall width is maximum at the starting /ending zone and minimum at the center position for all the walls. The maximum width at the starting/ ending zone is due to the more amount of powder and laser energy available for deposition at the starting point and ending point due to inertial effect (acceleration/ deceleration) of the workstation. The width measured at the central region is minimum as the amount of laser energy and powder available is used for deposition continuously without inertial (acceleration/ deceleration) effect. Further,

it can be seen from Table 5.2 that there is a reduction in wall width with an increase in delay period between the subsequent laying of layers. A reduction of 7%, 6% and 3% is observed in the wall width at the center, start and endpoint of deposition, respectively when the delay is increased from 10 seconds to 40 seconds. This can be primarily due to the reduction in the melt pool temperature due to interlayer delay. At lower values of interlayer delay, the melt pool temperature is higher and this leads to lower viscosity and reduced surface tension. This results in bulging of the walls due to the flow of molten materials along the side walls when the new layer is deposited. Thus, the dimension of the wall can be controlled by providing an appropriate interlayer delay, which can reduce the preheat temperature before laying the next layer.

Table 5.2: Width measurement at different locations

Position	Interlayer delay (s)		
	10	20	40
Start	3.38	3.22	3.13
Center	3.20	3.16	3.00
End	3.35	3.29	3.24

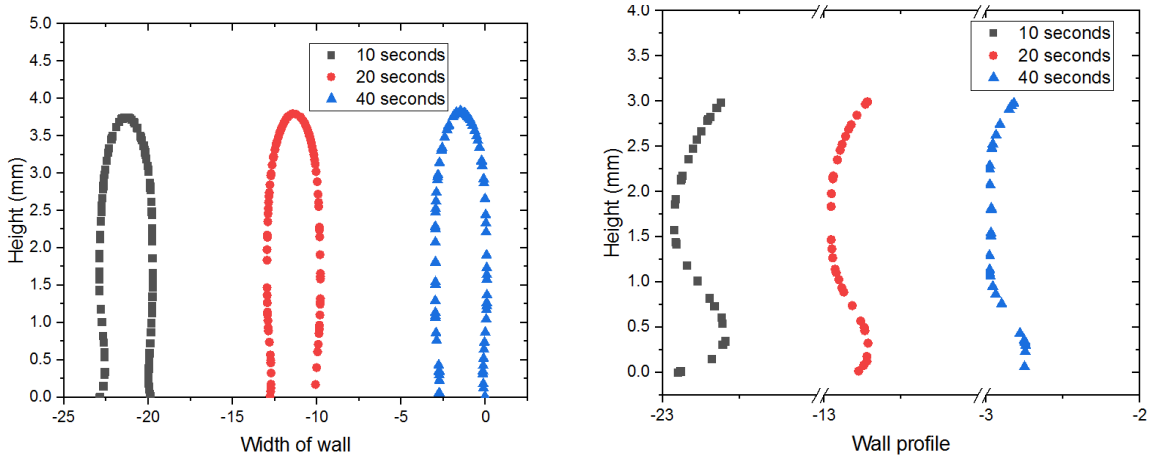

(a) (b)

Figure 5.18: LDED built walls (a) cross-section (b) wall profile

Figure 5.18 presents the cross-section of the LDED built walls with different values of interlayer delay. It is observed that necking is not prominent mainly due to the higher values

of laser energy used for deposition. It may be seen that the necking position shows a slight shift in the upward direction, with an increase in the interlayer delay mainly due to lower, preheat temperature available on the build surface at the higher interlayer delay. It can be seen that the walls built with 40 s delay is sharper than the walls built with 10 s and 20 s delay. Subsequently, the effect of delay period on the wall profile is analysed and it is observed that the deviation in wall profile decreases with an increase in the delay period. Statistical analysis up to 3 mm height shows that the range of wall profile deviation is 0.33 mm, 0.24 mm and 0.23 mm for walls built at 10 s, 20 s and 40 s, respectively. This can be due to the reduction in heat accumulation yielding reduced preheat temperature with an increase in the interlayer delay period.

5.3.3 Microstructural Characterisations

Figure 5.19 presents the macro-structure of the built wall cross-section analysed using a stereomicroscope. Sound metallurgical bonding is observed between the substrate and the built walls. It is also seen that the built walls are defect-free without any macro cracks. The melt pool boundaries are also visible in the macro-structure.

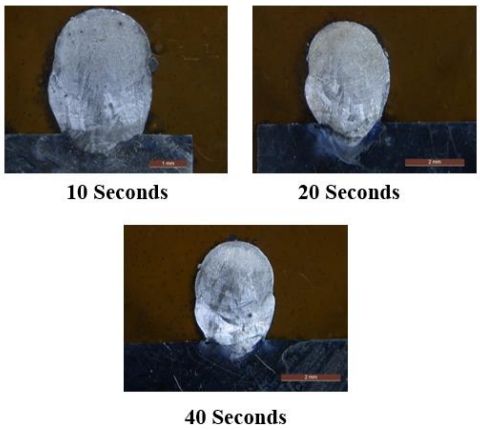

Figure 5.19: Macrostructure of the built walls at different interlayer delay

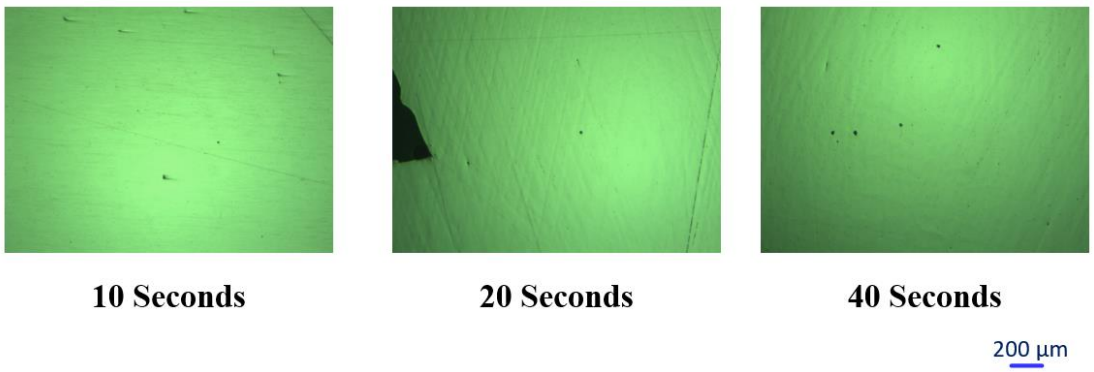

Figure 5.20: Typical porosity observed in LDED built walls at different interlayer delay

Figure 5.20 presents the porosity of walls built with different values of interlayer delay. The walls to largely defect-free (free from cracks and other bulk defects) at the micro-level as well. It is seen that the walls are dense with few spherical and irregular pores at isolated locations, which can be mainly due to trapped gas porosity and lack of fusion, respectively.

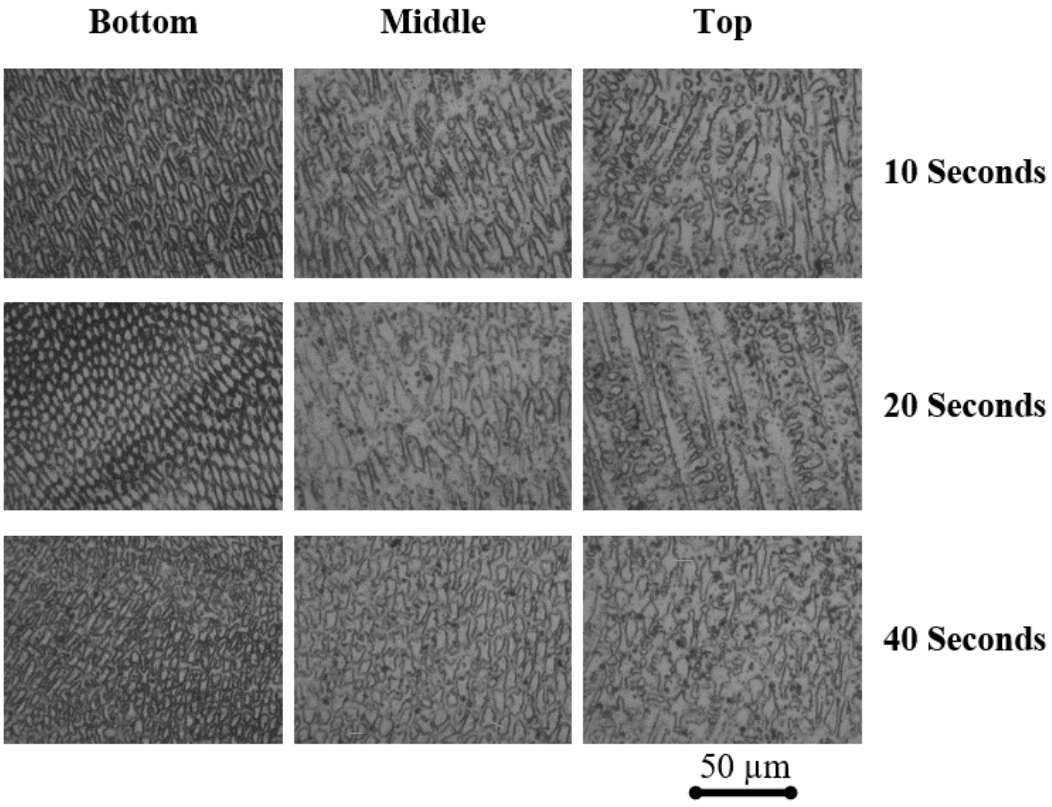

Figure 5.21: Microstructure of built walls along the cross-section

The microstructure of the built walls is analysed using an optical microscope as shown in figure 5.21. The microstructure is primarily a mix of cellular/dendritic growth, with cellular growth observed in the lower layers and dendritic growth observed in the middle and top layers. Cellular growth is observed at the bottom layers mainly due to the higher thermal gradient as the substrate act as a heat sink during the initial layers. However, as the layers build-up due to lower thermal gradient, dendritic growth with classical secondary arms is seen at the top layers. The mode of the microstructural growth is similar at all interlayer delay conditions, with no evidence of equiaxed dendrites. Thus, it can be concluded that the interlayer delay does not affect the mode of microstructural growth. As the interlayer delay period increases from 10 s to 40 s, the temperature of the melt pool reduces due to improved conduction through the previous layers. This reduction in the temperature of the previous layer before the addition of the next layer leads to reduced melt pool size and larger thermal gradient. As the thermal gradient increases, faster cooling is observed with a reduction in the size of the dendrites. This leads to the formation of relatively fine growth and reduced arm spacing at higher values of the delay period.

Figure 5.22 presents the elemental mapping of LDED built Hast-X walls at the different interlayer delay. The uniform distribution of Ni, Cr, Fe and Mn elements are observed in all the samples irrespective of the interlayer delay period. Further, the segregations of Mo, Si and C segregations are observed in the LDED wall structures. The tendency of segregation reduced slightly with an increase in the interlayer delay period due to an increase in the cooling rate. At very high cooling rates, solute atoms are trapped by fast-advancing solidification interface, and as a result, the micro-segregation gets reduced[180]. The presence of Mo rich carbides is also detected in LDED built walls primarily due to continuous thermal cycling during the process.

These carbides can be M_6C (M stands for Mo) as reported in previous studies on LPBF built Hast-X [134].

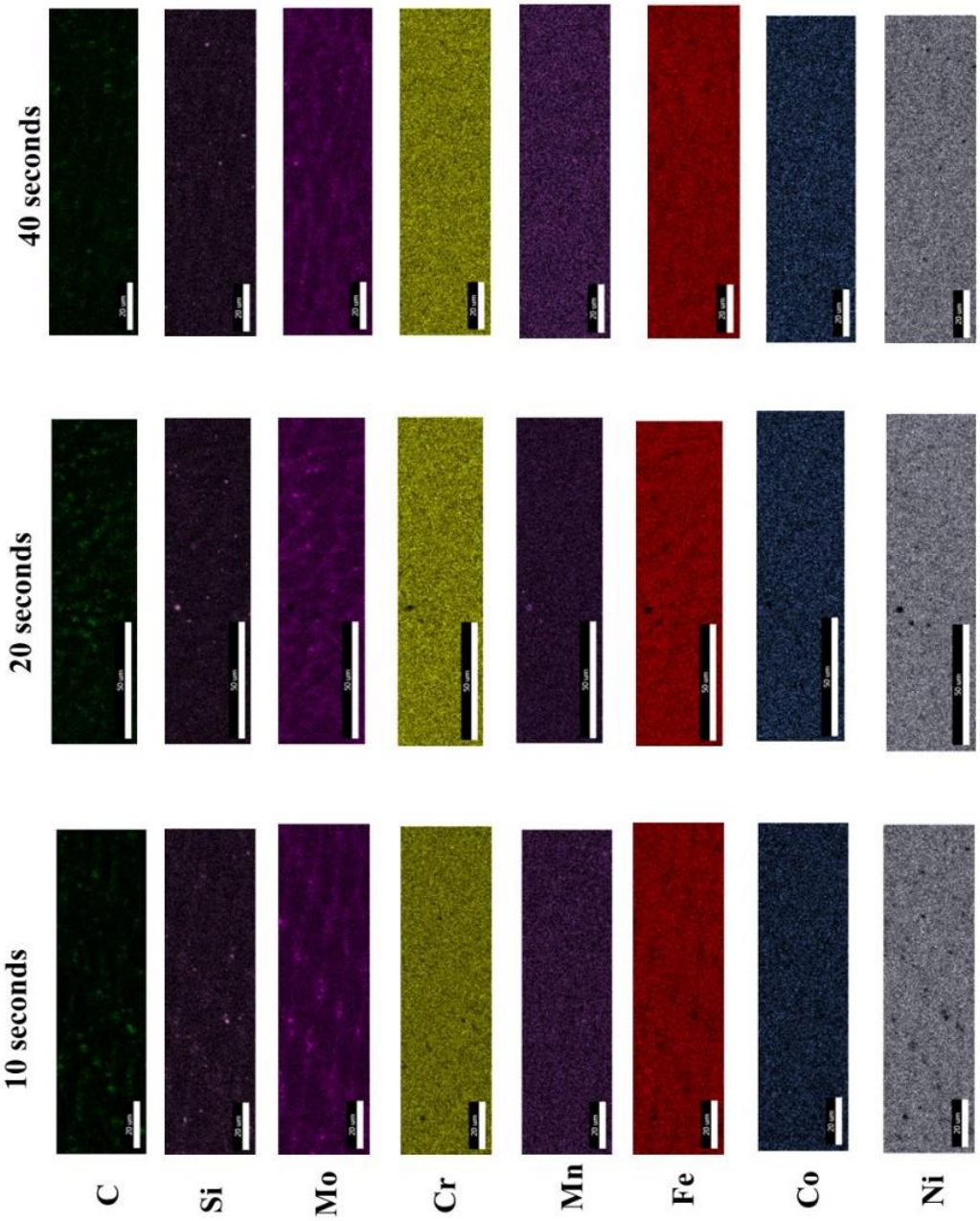

Figure 5.22: Elemental mapping of LDED built Hast-X walls at different interlayer delay

Figure 5.23 presents the XRD pattern of LDED built walls with interlayer delay 10 s, 20 s and 40 s. It can be seen from Figure 5.23a that the peaks confirm the presence of γ matrix phase. The presence of Mo rich carbides is not observed from XRD pattern, which can be due to the

lower volume fraction of the carbides. A slight shift in the peak position towards the left side is observed with an increase in the interlayer delay as shown in Figure 5.23b. This slight shift can be attributed to the variation in the lattice strain generated during the deposition, which can be mainly due to the difference in the thermal gradient during LDED. A shift in the peak position can correspond to the variation in the d spacing according to Braggs law as presented in equation 5.5[181].

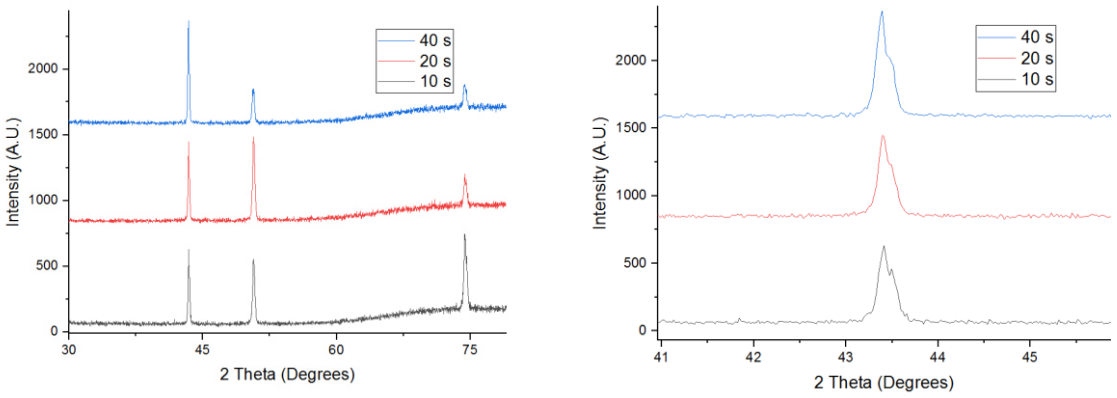

(a) (b)

Figure 5.23: XRD (a) pattern of walls built at the different interlayer delay (b) peak shift

5.3.4 Mechanical Properties

Figure 5.24a presents the micro-hardness of LDED built walls at the different interlayer delay. It is observed that the micro-hardness shows a slightly increasing trend with an increase in the interlayer delay. The slight increase in micro-hardness is mainly due to the higher cooling rate with an increase in the inter-layer delay period as discussed in the previous section. However, the variation in micro-hardness is not significant, which shows that the effect of interlayer delay on the resistance to deformation is low.

Further, in order to understand the effect of inter layer-delay on the yield and ultimate strength of the material, ABI studies are carried out. Figure 5.24b and Figure 5.24c presents the load-displacement plot and trues stress-strain plot of LDED built wall structures, respectively. It is

observed from Figure 5.24b that the load required to obtain same indentation depth is higher for walls built with 40 s interlay delay as compared to those built with 20 s and 10 s interlayer delay. This is primarily due to the higher resistance to deformation provided by walls built with 40 s interlay delay as compared to those built with 20 s and 10 s interlayer delay. These observations are in agreement with micro-hardness and microstructural results.

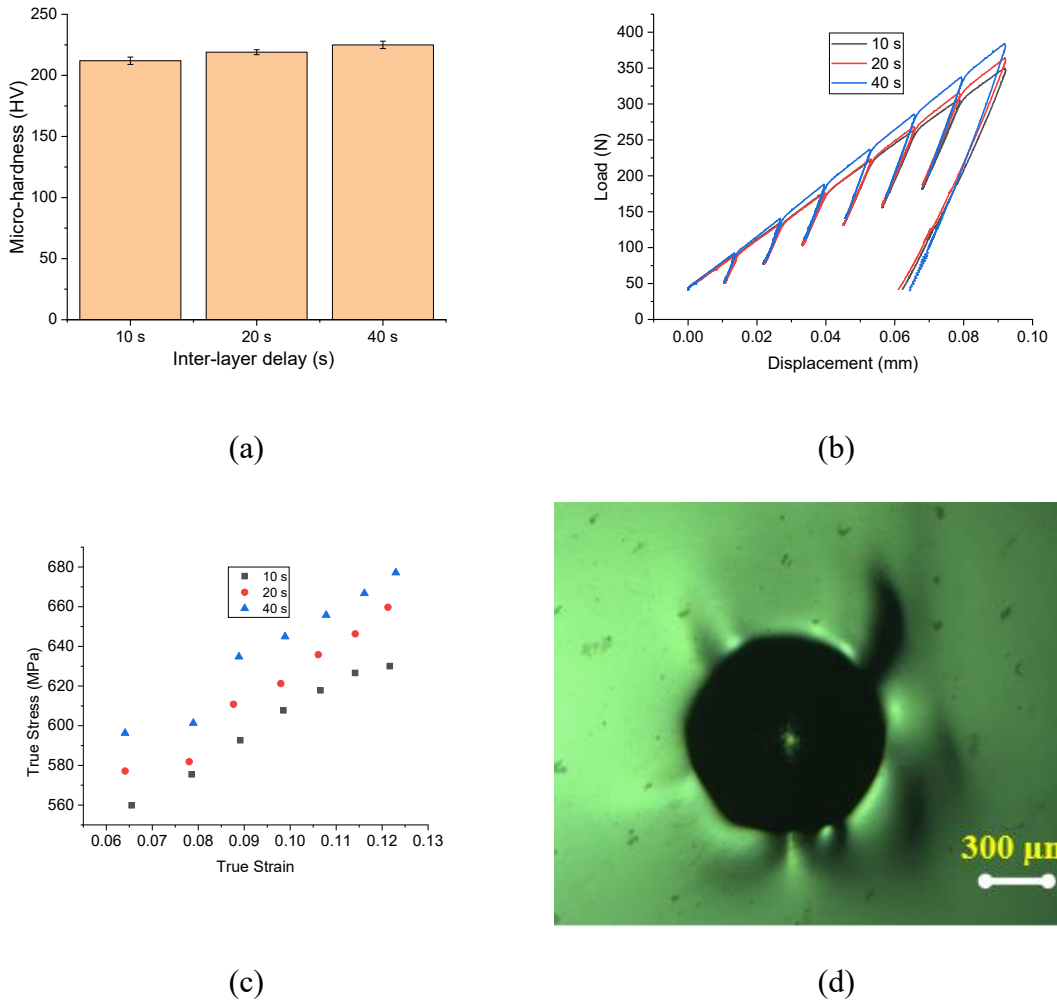

Figure 5.24: Mechanical properties of LDED built walls at different interlayer delay (a) Micro-hardness (b) load-displacement diagram (c) True stress-strain curve (d) Typical ABI indentation.

Figure 5.24c presents the flow curves of the walls and it can be seen from that the walls built with 40 s interlay delay show higher tensile strength as compared to those built with 20 s and

10 s interlayer delay. Table 5.3 presents the mechanical properties of walls built with different interlayer delay. The estimated yield strength is 323 MPa and ultimate strength is 598 MPa for walls built interlayer delay of 40 s. The estimated yield strength is 299 MPa and ultimate strength is 585 MPa for walls built interlayer delay of 20 s. The estimated yield strength is 278 MPa and ultimate strength is 525 MPa for walls built interlayer delay of 10 s. The obtained values of yield strength and ultimate strength are lower than the wrought standard [37] and higher than the cast standard for the material [182]. In order to understand the variation in ductility, yield ratio (YS/ UTS) is calculated. Yield ratio indicates the amount of deformation a material can undergo during plastic stage. A lower value of yield ratio indicates higher ductility for the material [183]. The calculated yield ratio values for walls built with 10 s, 20 s and 40 s delay are 0.52, 0.51 and 0.54, which shows minimal variation in ductility with increase in delay period. This is in line with the microstructural analysis of the built walls. Figure 5.24d presents a typical ABI indentation. Material pile-up around the indentation is observed due to plastic flow of the material around the indentation.

Table 5.3: Mechanical properties of walls built with different interlayer delay

Condition	Yield Strength (MPa)	Ultimate Strength (Mpa)	Yield Ratio
10 s	278	525	0.52
20 s	299	585	0.51
40 s	323	598	0.54

5.3.5 Thermal Analysis of Thin Walled Structures at different interlayer delay

In order to understand the effect of interlayer delay on the thermal profile and to correlate with the experimental results, numerical simulation is carried out on a 4 layer wall structure. The details of the numerical model are already presented in section 5.2.5. Figure 5.23 presents the effect of interlayer-delay on the temperature of the built walls. It can be seen from figure 5.25a

that the maximum preheat temperature on the surface of the previously built layer after deposition of a layer increases with an increase in the number of layers. However, the preheat temperature decreases with an increase in the interlayer-delay period. The increase in the preheat temperature with an increase in the number of layers is the primary reason for the reduction in the thermal gradient and cooling rate at higher layers. At the same time, reduction in the preheat temperature with an increase in the interlayer-delay period is the primary reason for the increase in cooling rate, which leads to variation in size of grains, segregation and mechanical properties. This is attributed to the fact that heat transfer from the melt-pool takes place at a brisk pace if the temperature of the previous layer is lower. The effect of the interlayer delay period on the cooling rate can be well elucidated from figure 5.25b, which shows that the slope of temperature vs time plot is higher for walls built with higher interlayer delay. This indicates that the cooling rate increases with an increase in the interlayer-delay period. Thus, the increase in thermal gradient and cooling rate with an increase in the interlayer-delay are the primary reasons for the variation in the microstructure and mechanical properties.

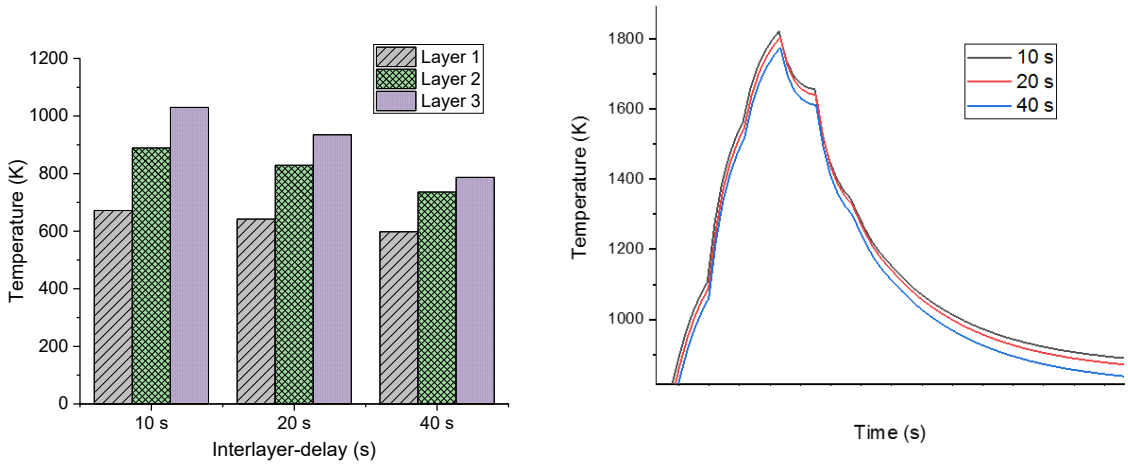

(a) (b)

Figure 5.25: Thermal analysis of LDED built walls (a) preheat after each layer (b) merged temperature profile

5.4 Summary

LDED is an attractive process particularly for the fabrication of thin walled components. In the present chapter, investigations are carried out to study the effect of LEPF and interlayer delay on the geometry, microstructure and mechanical properties of Hast-X wall structures built by LDED. In the case of walls built with different LEPF, it is observed that the variation in wall height increases with increase in LEPF, while the variation in wall width decreases with increase in LEPF. The geometry analysis along the build direction shows the maximum deviation for 8.2 kJ/g at the lower layer and 13.2 kJ/g at the top layer, while 10.7 kJ/g shows minimum deviation. Microstructural analysis shows cellular and dendritic growth at all conditions and a marginal reduction in mechanical properties with increase in LEPF. Numerical simulation is used to understand the effect of LEPF on the thermal profile and preheating temperature on the previously deposited layers and it is correlated with experimental results.

In the case of walls built with different interlayer delay, it is observed that average wall height increases with an increase in interlayer delay. However, the variation in wall width decreases and the value of wall width decreases with an increase in interlayer delay. Microstructural studies show the presence of cellular and dendritic growth at all conditions with relatively finer grain structure at higher interlayer delay period. The increase in cooling rate due to increase in interlayer delay lead to a reduction in elemental segregation and improved mechanical properties at the higher interlayer delay. Numerical simulation is used to understand the effect of interlayer delay on the thermal profile and preheating temperature on the previously deposited layers and it is correlated with experimental results.

Chapter 6 : Elucidating Microstructural and Mechanical Behaviour of LDED Built Hast-X Bulk Structures[4]

6.1 Introduction

In the previous chapter, detailed investigations on the LDED built Hast-X wall structures are carried out with a focus on the geometry, microstructure and mechanical properties. LDED also finds application in building bulk structures for various applications in engineering sectors, like - the bulk separation between fluids in heat exchangers, repair and remanufacturing, fabrication of automotive components, building aerospace components, etc. Bulk structures are defined as those structures built using multiple overlapped track deposition and multi-layer deposition. As the deposition of bulk structures involve multiple overlapped tracks and multi-layer deposition, the behaviour of bulk structures are expected to be different from wall structures. In addition, the deposited structures are exposed to a larger number of thermal cycles[47]. Due to the effect of a large number of thermal cycles, the microstructural and mechanical properties of LDED built bulk structures are expected to be different from the conventionally built components [184]. During conventional manufacturing, complete diffusion in the solid and liquid state takes place due to equilibrium solidification conditions. Thus, phases will be in equilibrium and composition agrees to that in the available phase diagram. During LDED, non-equilibrium solidification conditions exist. Thus, phase generation and changes are non-equilibrium and temperature at which the phase transformation takes place will also differ from equilibrium conditions[184]. As there is no literature available

[4] This chapter is partially reproduced with permission from Elsevier (Journal – S. No. 1, 2 and 5) – See Letters of Copyright Permission (Page Nos. 208 and 209)

in the public domain on the microstructure and mechanical behaviour of LDED built Hast-X bulk structures, it is necessary to probe into the microstructural and mechanical properties of these structures built at identified process parameters. In the present chapter, investigations are carried on the defect analysis followed by analysis on the microstructural behaviour, surface characteristics and mechanical testing at room temperature and elevated temperatures.

6.2 Experimental Details

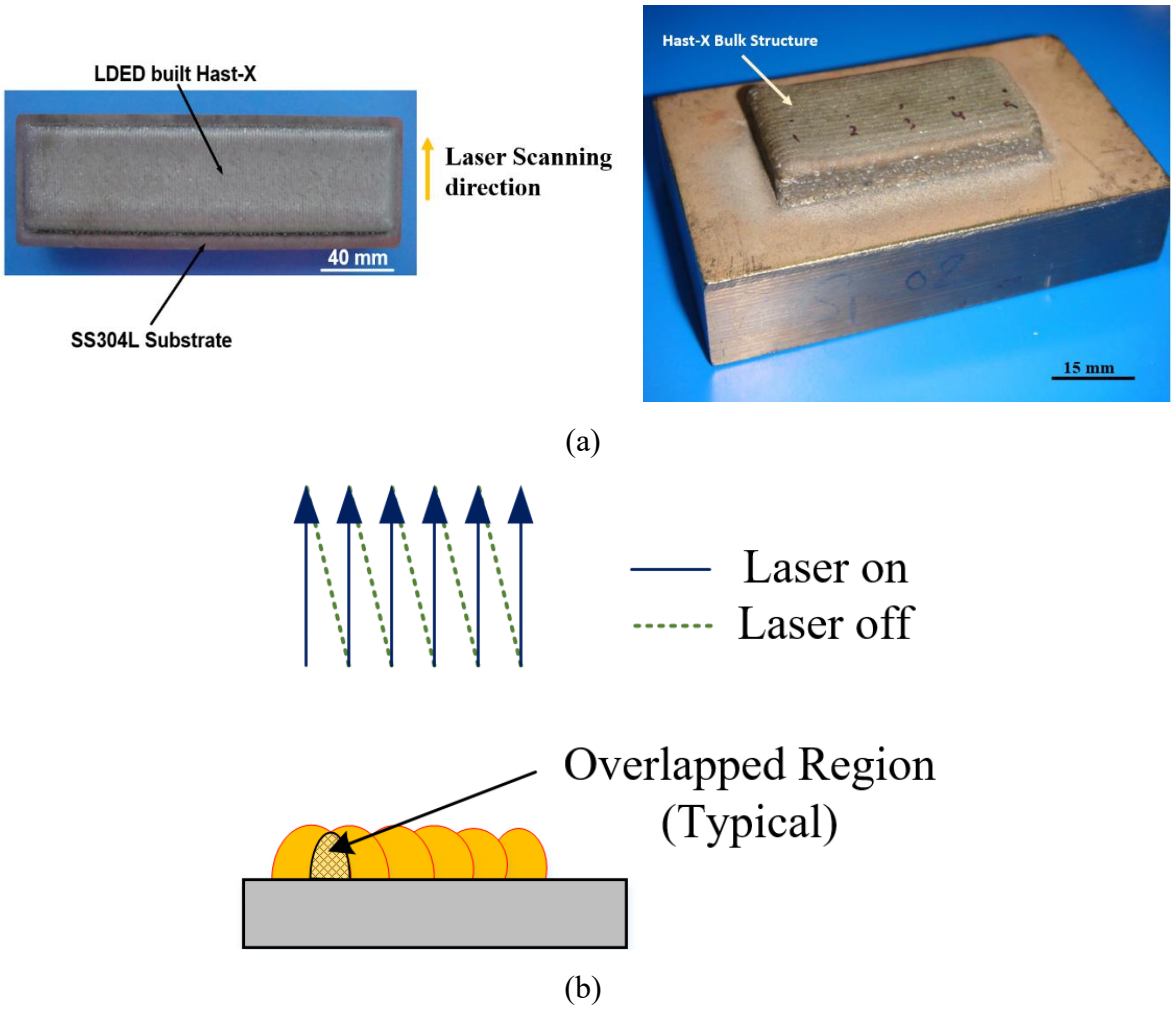

Figure 6.1: LDED built Hast-X Bulk Structures a) Photographic view b) Scan Pattern

The parameters used for the deposition of bulk structures are taken from the process window developed in chapter 4. From the derived process window, process parameter yielding a

combination of maximum build rate and minimum porosity is selected for bulk structure deposition. LDED process parameters deployed for depositing bulk Hast-X structures are laser power – 1600 W, scan speed – 0.5 m/min and powder feed rate – 8 g/min, with 50 % overlap between adjacent tracks as discussed in chapter 4. Argon gas with purity >99.9993% at a flow rate of 6 litres per minute (lpm) is used as the carrier gas and shielding gas for the LDED experiments. Figure 6.1a presents the photographic view of different bulk structures built using LDED for testing and characterisation. Unidirectional laser scanning strategy is used for deposition as shown in figure 6.1b.

6.3 Macro-Defect and Porosity Analysis

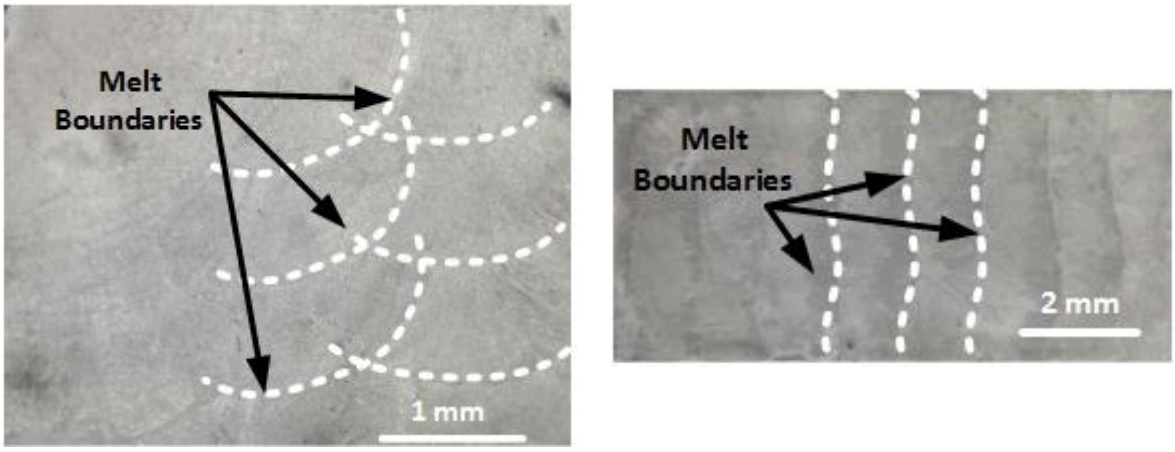

(a) (b)

Figure 6.2: Melt-pool boundaries along (a) cross-section (b) on top surface

Figure 6.2 (a) and (b) presents the macro-scale melt-pool analysis along the cross-section and top-surface of deposit, respectively. Overlapping melt-pools are visible along the cross-section and top surface of the deposit. It can be seen that the melt-pool boundaries are defect-free. Further, optical microscopy is used to analyse the micro-scale defects in the LDED built Hast-X structure. It is observed from Figure 6.3(a) that the LDED built samples are free of micro-cracks. Few pores are visible at isolated locations, which are a mix of gas porosity and process-

induced porosity (lack of fusion porosity). Gas porosity (marked with continuous circles) is generated either due to the porosity inside the powder due to the powder production technique or gas trapped inside the melt-pool during solidification. Process induced porosity (marked with dotted lines) can be due to insufficient material consolidation at localized regions[47]. The size of the pores ranges from 10 – 20 microns and the relative density estimated by the area fraction technique is ~ 99.5 %.

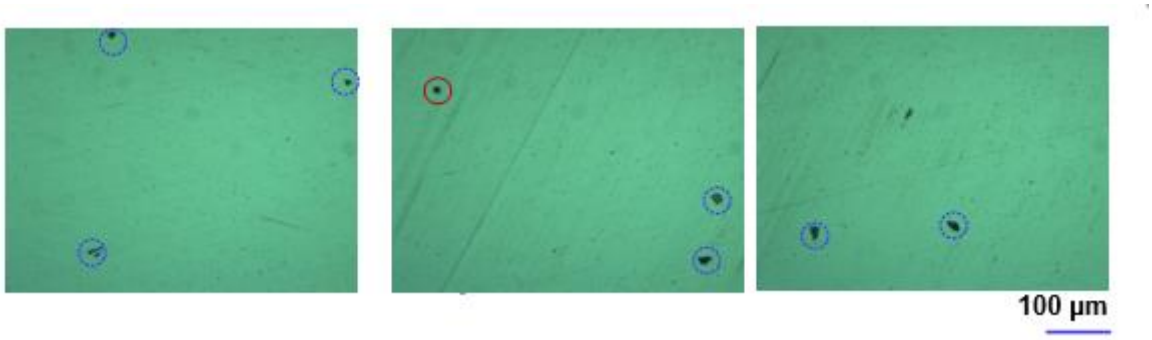

Figure 6.3: Porosity analysis of LDED built bulk structures

6.4 Microstructural and Phase Analysis

Microstructure in figure 6.4a shows a layered structure defining molten pool boundaries at the layer interface, because of the heat effect during subsequent layer deposition [96]. The remelting of the previously built layers is important to build high-quality components using LDED as it eliminates surface contaminants and allows to breakdown the oxide films [49]. Figure 6.4b shows that microstructure is a mix of cellular and dendritic growth with cellular growth mainly seen in the lower layers and dendrites with secondary arms in the upper layers. During LDED, the microstructure near the melt-pool boundary is controlled by the base metal. However, the microstructure is controlled by competitive growth in the subsequent layers. In upper layers, microstructure dominated by “long” and “straight” dendrites is seen. Columnar growth is seen epitaxially from the substrate, due to the high directional heat flow generated

during LDED. During LDED, the cooling is primarily due to conduction through the substrate or previously deposited layers and moderately via the neighbouring solidified layer grown from the trailing end of the melt pool. Further, the shape of the melt pool can be approximated to an elongated ellipse [185]. Figure 6.4c shows that the boundaries of the melt pool will be at an angle between 45° and 90° with the substrate and will be a function of scan speed. As the heat transfer is perpendicular to the solid-liquid interface as shown in Figure 6.4c, the microstructure growth follows the heat transfer waves and the growth direction of dendrites will be at an angle between 45° and 90° with the substrates' top plane. In the present work, the direction of dendritic growth is observed to be ~ 60° as shown with arrows in Figure 6.4b. These observations are in-line with work reported by Dinda et al. [105]. It can also be observed that the growth at the lower layers are finer due to higher cooling rate at the bottom layers and there is a gradual increase in the size of the columns from bottom to top layers. The primary arm spacing is measured approximately as 1 μm in the bottom layers, while it ranges from 6 μm to 8 μm in the middle layers. At the top layers, the dendrites with secondary arms are present due to the relatively lower cooling rate. The arm spacing in the top layer is in the range of 10 - 15 μm. The detailed microstructural analysis shows that the cooling rate of the melt pool is very high at the bottom layers due to the larger thermal gradient during LDED. Thus, the growth of secondary dendrites is inhibited in the lower layers. The upper layers cool slowly as compared to the lower layers due to the preheating effect yielding lower thermal gradient at the top layers. As a result, the grain structure is finer at the bottom layers and it gets coarsened with an increase in the build height. The overall primary arm spacing in LDED fabricated Hast-X is much lower than that of conventional casting (100 - 300 μm) [186]. Figure 6.4d presents the SEM image of microstructural growth in different directions due to the difference in direction of effective heat transfer. Figure 6.4e presents the typical SEM microstructure of the dendritic growth observed at the top layers of the built structure.

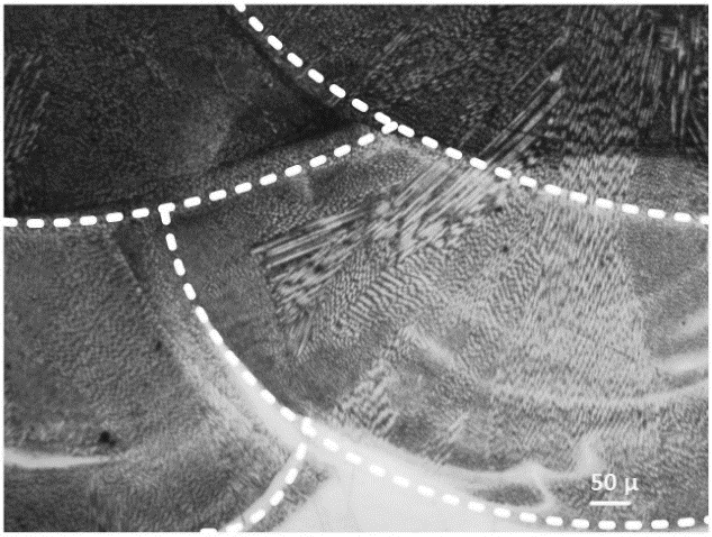
50 µ

(a)

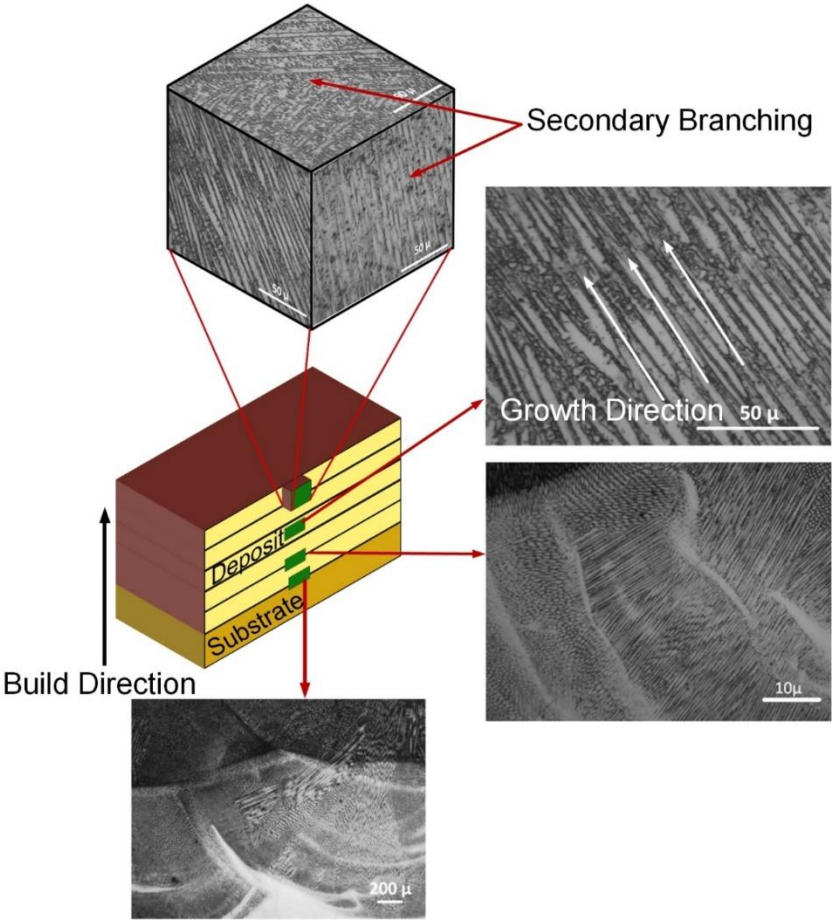
Secondary Branching
Growth Direction 50 µ
Deposit
Substrate
Build Direction
10µ
200 µ

(b)

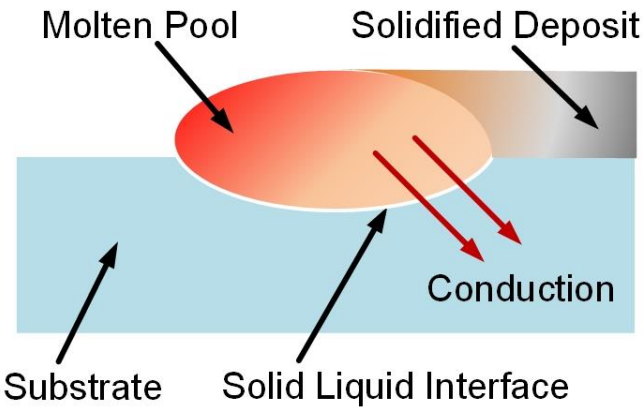

(c)

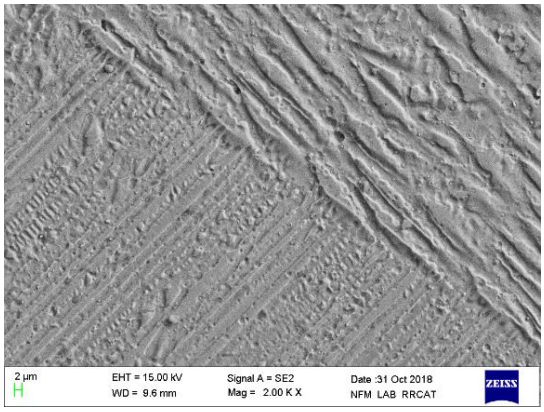

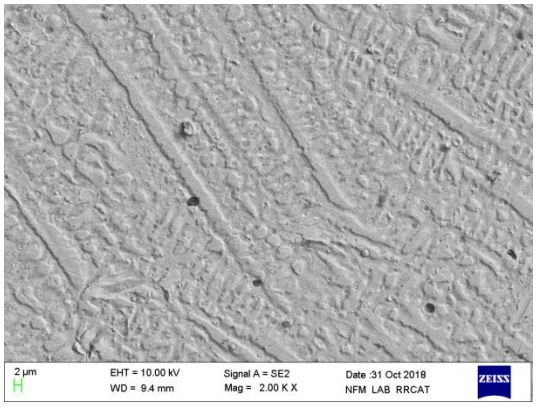

(d) (e)

Figure 6.4: Microstructure of as-built Hast-X (a) with layered separations (b) at different zones of deposition (c) Heat Transfer in molten pool d) SEM micrograph showing different directions of dendritic growth (e) SEM micrograph representing top layers with secondary branching

Figure 6.5 (a) and 6(b) present the Electron Back Scattered Diffraction (EBSD) images of LDED built Hast-X along the cross-section. Generally, there is a competitive growth between dendrites with different crystallographic orientations. Dendrites with easy-growth directions are allied closely with the highest heat flow path at the solid-liquid boundary attain lead in competitive growth during the solidification process. In the present case, it can be found that the orientation of the cells/ grains is random with slightly preferred texture along the <100>

orientation as per the inverse pole figure. The average grain size is 23 µm in the as-built samples, which is finer than the conventional Hastelloy-X. Typical grain size varies from 45 - 180 µm for wrought Hast-X components [37]. It can be seen that the proportion of low angle boundaries is high in the as-built samples, which is mainly due to the higher dislocation density generally seen in LDED built structures [187].

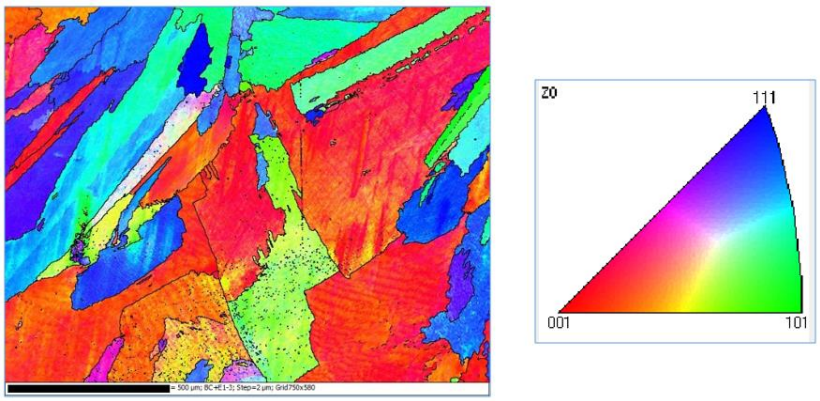

(a)

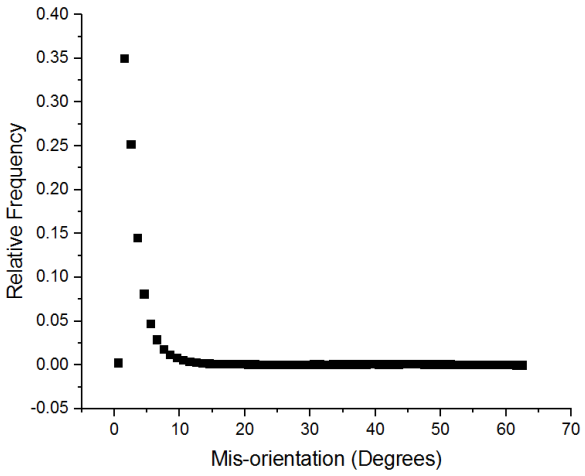

(b)

Figure 6.5: EBSD image of LDED built Hast-X (a) Direction of grain growth (b) Frequency vs misorientation plot

Figure 6.6 presents the elemental mapping carried out on the LDED built Hast-X measured along the cross-section. It can be inferred that the composition of Cr, Co, Fe and Ni are uniform

throughout the cross-section, with some regions indicating lack of Ni. It can also be seen that elements with higher chances of segregation, like – Mo, Si and C have segregated during the solidification. This is mainly due to the non-equilibrium/ rapid solidification during LDED and density differences inside the melt-pool. Further, LDED process undergoes continuous thermal cycling, which includes many heating and cooling cycles. Due to the continuous heating cycles, the temperature of the bulk retains at a higher temperature during the processing, which can aid the formation of carbides. It is understood from the elemental mapping analysis that Mo rich carbides are formed during LDED, which can be M_6C (M stands for Mo) as seen in literature [134].

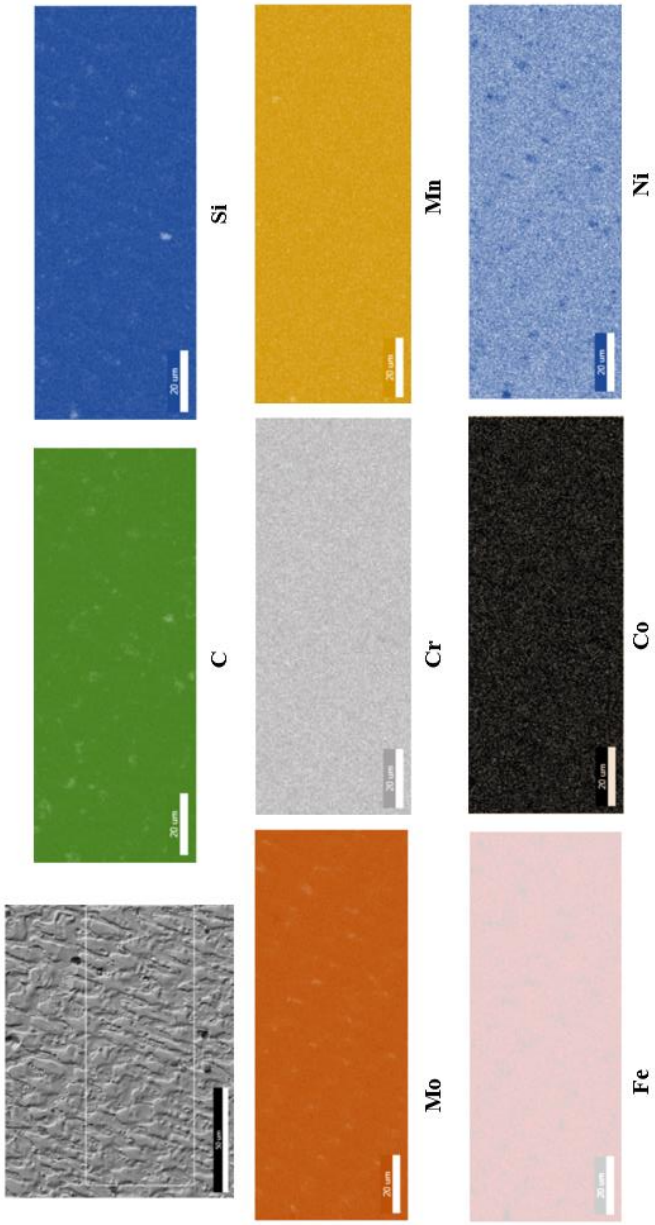

Figure 6.6: Elemental mapping of LDED built Hast-X

XRD studies of as-built Hast-X and Hast-X powder is performed from 30° to 80° to understand the presence of phases. Figure 6.7a presents the XRD pattern of LDED built Hast-X and Hast-X powder. It can be seen that the as-built sample reveal peaks similar to the peaks observed for Hast-X powders at 43.35°, 50.5° and 74.34° indexed to (111), (200), (220) planes, respectively revealing the presence of Ni γ-matrix (PDF number: 00-004-0850). The presence of Mo rich carbides is not observed during the XRD analysis. This indicates that the volume fraction of Mo rich carbides formed during LDED is relatively low. It can also be seen that (200) plane

has higher intensity as compared to other peaks. This indicates a slightly preferred texture as observed in EBSD analysis. Further, it can be seen that there is a slight variation in the peak position from the peak positions for Hast-X powder. The peak positions of the powder are 43.48°, 50.69° and 74.57° for (100), (200) and (220) planes, respectively. The deviation in the peak-position indicates the variation in the lattice spacing as per the Braggs law. Braggs law is presented in equation 6.1, where n is an integer, λ is the wavelength, d is the lattice spacing and Θ is the peak position. In the present case, a shift in the peak position towards the left side is observed, which indicates an increase in the lattice spacing. An increase in lattice spacing can be attributed to tensile strain present in the lattice due to tensile stresses generated on the surface of the built structures.

$$n\lambda = 2d\sin\theta \tag{6.1}$$

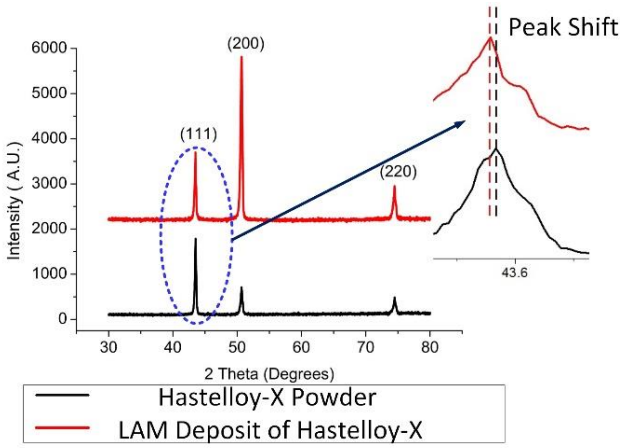

Figure 6.7: XRD pattern of as-built Hast-X and Hast-X powder

6.5 Surface Topography

Surface topography of the LDED built bulk structure is analysed in the as-built condition using stereo microscopy, scanning electron microscopy and laser scanning confocal microscopy. Figure 6.8a presents the microscopic images of the as-built surface. It can be seen that the surface is crack-free with the presence of partially melted powders and layer pattern. The observed pattern on the surface of the built structure is due to the overlapped laser scans during

unidirectional deposition. The distance between the two lines is in the range of 1.25 – 1.4 mm, which is equal to the hatch spacing or transverse traverse index used during LDED. Layer pattern during the deposition contributes to the waviness on the built surface. The roughness is mainly governed by the presence of partially melted powders present on the deposit surface. The major reasons for the presence of partially melted powders are:

- Lack of 100% powder catchment during LDED,
- Spattering due to the higher laser energy used for deposition,
- Powder particle size.

During LDED, 100% of the fed material is not melted and deposited even at higher laser energy density. Some of the particles gets sufficient energy to just have surface melting and they bond with the previously built tracks. However, they do not have enough energy to create continuous deposits. In addition, due to the higher energy density used in LDED, spatter or incompletely particles are rejected from the melt-pool, which gets into contact with the previously built tracks. Another factor governing the roughness is the powder particle size. As the powder particle size increases, the roughness on the surface increases. Figure 6.8b presents the SEM images of the surface at a higher magnification. The measured powder particle size is in the range of 60 - 80 μm. Further, surface roughness measurements using a laser scanning confocal microscope indicates an R_a value of 8.72 μm.

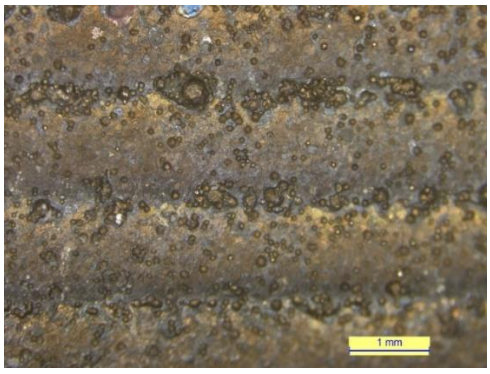

(a)

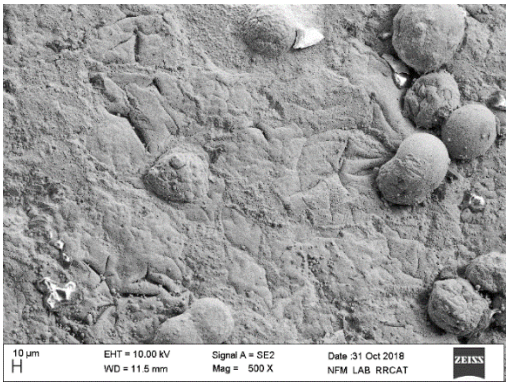

(b)

Figure 6.8: Surface Topography (a) Stereo microscopy image at low magnification (b) scanning electron microscopy images at low magnification

6.6 Surface Residual Stress

Surface residual stress measurements on Hast-X is measured using XRD method. Figure 6.9a presents the surface residual stress on Hast-X deposits at different points, where points on the surface refers to the point on the top surface, where the residual stress is measured. It can be observed that the top surface of the as-built sample is dominated by tensile residual stresses with a maximum magnitude of 252 MPa on the deposit surface. The reasons for residual stress in as-built LDED samples are primarily due to temperature gradient mechanism (TGM) initiated by the high temperature generated by the laser and the rapid cooling of the upper layers. Figure 6.9b presents the schematic diagram explaining the TGM mechanism during LDED process. During heating, the constraint on the expansion of the heated layers encourages elastic compressive strain in the material as represented in stage 1. This induces a compressive stress in the upper layers that may rise above the yield strength of the material and cause plastic deformation (Ɛ) in those layers as denoted in stage 2. During subsequent cooling, the upper molten layers tend to shrink due to thermal contraction, which is prevented by the lower

solidified layers. The above cooling mechanism generates tensile stress in the upper layer as represented in stage 3.

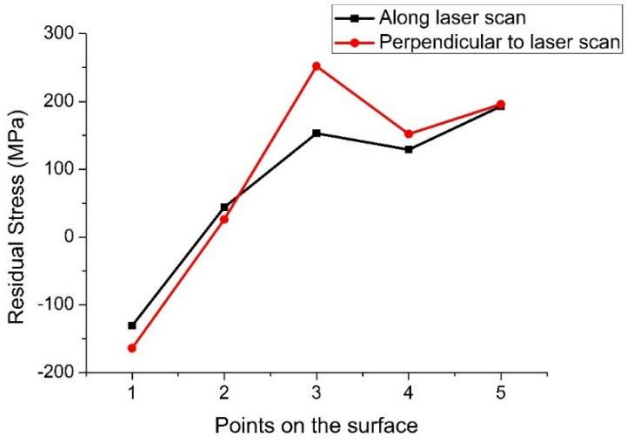

(a)

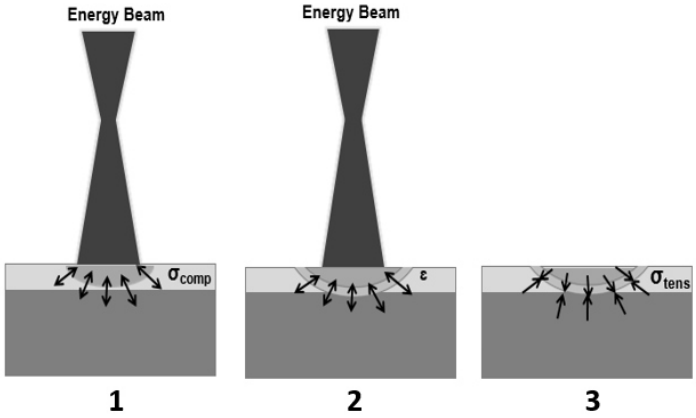

(b)

Figure 6.9: Residual stress on as-built Hast-X samples

6.7 Micro-hardness

Microhardness of as-built samples is measured using Vickers microhardness tester. The measurements are taken along the deposit cross-section from the top of the deposit to the bottom of the deposit. The measured value of micro-hardness varies between 230 HV – 252 HV, with an average micro-hardness of 239 $HV_{1.96N}$. The micro-hardness values of conventionally built Hast-X reported in the literature is 180 HV[37]. The higher micro-

hardness of LDED built Hast-X is primarily due to the finer grain structure generated during LDED process due to faster cooling rates. In addition, the dislocation density of LDED built components are generally higher due to the rapid solidification behaviour[188]. The higher dislocation density offers more resistance to the plastic deformation[189]. A comparison with Laser Powder Bed Fusion (LPBF) built parts show that the micro-hardness of LDED built Hast-X is lower than LPBF built components. It is reported in the literature that micro-hardness of the typical LPBF built Hast-X components is 317 HV[125]. The large difference in micro-hardness can be primarily attributed to the difference in the cooling rates between LDED and LPBF process. The major reason for the variation in cooling rate between the two processes is the difference in the melt-pool size. In LDED, the typical melt-pool size varies in the mm scale, while the LPBF process uses a laser spot diameter in the micron scale. In addition, LPBF uses a higher scan speed as compared to LDED, which results in finer melt-pool. As the size of the melt-pool increases, the time taken for cooling also increases [190]. Thus, LPBF built components have higher cooling rates, which results in higher hardness.

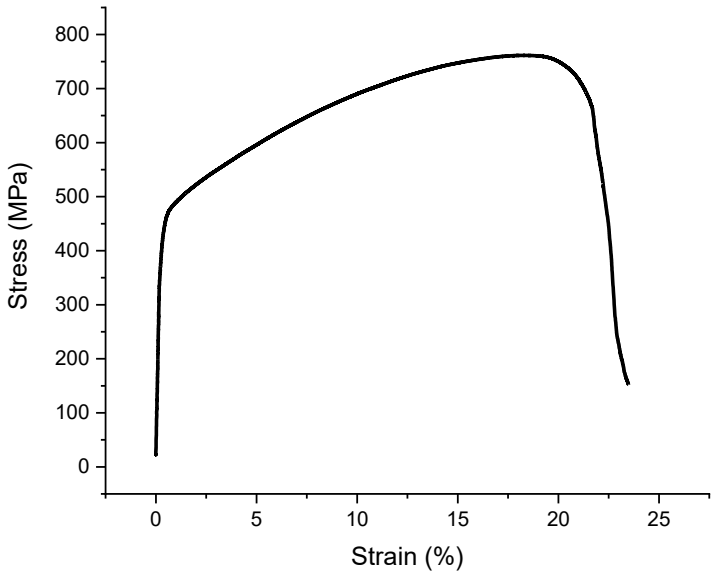

Figure 6.10: Stress-Strain curve from uni-axial test

6.8 Tensile Behaviour at Room Temperature

Figure 6.10 presents the stress-strain curve obtained from micro-tensile test. The yield strength and ultimate strength obtained for bulk LDED Hast-X structure are 455 MPa and 761 MPa, respectively. In order to confirm the suitability of the Automated Ball Indentation (ABI) for testing LDED samples, ABI tests are performed to estimate the mechanical properties at room temperature using non-destructive testing. A comparison between uni-axial test (from micro-tensile studies) and ABI test is carried out on LDED built Hast-X bulk structures.

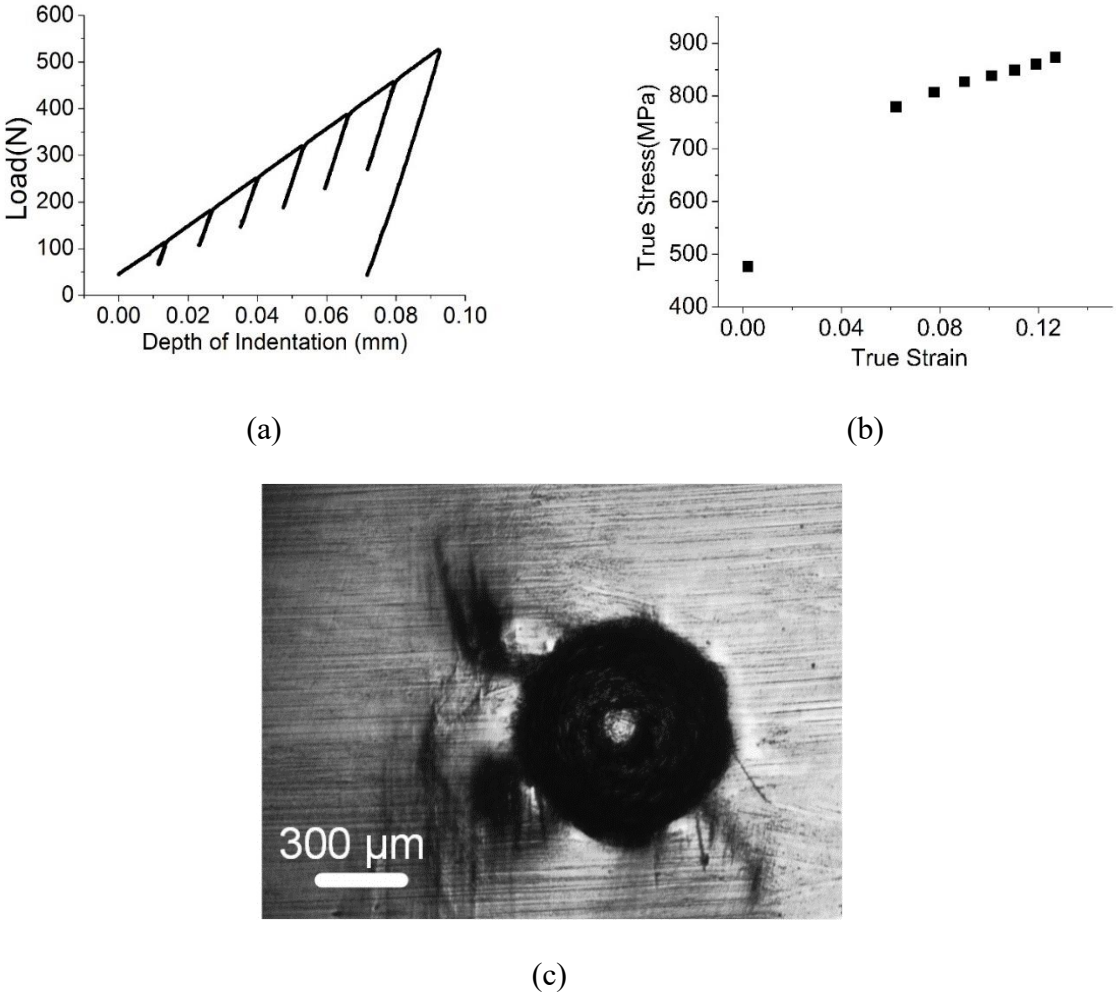

(a) (b)

(c)

Figure 6.11: Ball Indentation test of Hast-X a) Load-depth of indentation plot b) Flow Curve at room temperature (c) ABI Indentation

It is observed in Figure 6.11a that seven cycles of loading and unloading are applied on Hast-X sample. Subsequently, the yield strength and ultimate strength of the material is calculated from the procedure provided in chapter 3. Flow curve obtained from the calculation for Hast-X at room temperature using ABI technique is presented in Figure 6.11b. The estimated value of yield strength and ultimate strength using ABI testing is found to be 478 MPa and 765 MPa, respectively for LDED built Hast-X material. It is observed that a maximum deviation of 3.6% and 0.5% is obtained between uni-axial results and ABI test results for yield strength and ultimate strength, respectively. Thus, it is confirmed that ABI is a reliable technique for estimating the mechanical properties of LDED built samples in a non-destructive manner. Figure 6.11(c) presents the ABI indentation on the surface of the as-built sample. Pile-up is observed around the indentation due to the plastic flow that has taken place during the ABI indentation.

As ABI provides the flow curve of the material, yield ratio (YR) is calculated to understand the ductility of the material. YR is the ratio between yield strength and ultimate strength of the material and it represents the uniform elongation of the material. Lower YR value indicates higher ductility[183], higher capacity for plastic deformation and safe margin against fracture. It is also an indication of the stress level the material will endure beyond yield point before reaching the ultimate point. It can be seen from Table 6.1 that LDED built Hast-X has lower YR as compared to LPBF built samples and higher YR than conventionally built samples. Thus, it can be concluded that LDED built Hast-X has higher ductility as compared to LPBF and lower ductility as compared to conventionally built Hast-X samples. It can be observed from Table 6.1 that the properties of LDED built Hast-X is intermediate to the properties of Hast-X built through conventional route [37] and LPBF [129] as observed in micro-hardness studies also. The reason for the variation in the mechanical properties from LPBF and conventional samples are discussed in the previous section.

Table 6.1: Comparison of yield strength, ultimate strength and yield ratio for Hast-X through different fabrication routes

Condition	Yield Strength (MPa)	Ultimate Strength (MPa)	Yield Ratio
LDED - Present Study	478 ± 2	765 ± 4	0.62
Conventional [37]	340	760	0.44
LPBF [129]	600	788	0.75

It is also observed that the mechanical properties of the LDED built Hast-X bulk structures is higher than the mechanical properties of the wall structures built at same LEPF (reported in chapter 5). The lower value of strength for wall structures is primarily due to slower cooling rate during LDED of wall structures. During LDED of wall structures, heat transfer only takes place through the previously deposited layers, which are relatively at higher temperature due to the deposition process. However, during LDED of bulk structures, the heat transfer takes places through the substrate/previously deposited layer (Q_v) and along the adjacent layers (Q_h) and thus, the effective heat transfer increases. This results in faster cooling rate in bulk structures as compared to wall structures leading to finer grain structure and higher values of mechanical strength.

6.9 Tensile Behaviour at High Temperature

Figures 6.12 present the load-displacement curves obtained for LDED built Hast-X in the as-built condition at different test temperatures from ambient to 873 K. The maximum temperature for testing is selected by considering one of the applications of LDED built Hast-X for Supercritical CO_2 cycle [30]. It can be observed that for the same displacement, the applied load decreases with an increase in the test temperature. In other words, the resistance to plastic deformation decreases with an increase in the test-temperature. This can be primarily due to

the easy movement of the dislocations at the higher test temperature. A reduction of 33 % in the maximum load is observed when the temperature is increased from 300 K to 873 K. In addition, the load-displacement slope reduced from 6 kN/mm to 3.8 kN/mm with an increase in the test temperature from 300 K to 873 K. This behaviour is mainly due to the easy dislocation movement due to reduced plastic deformation resistance, as the test temperature increases. It can also be noted that there is a slight scatter in the final displacement of the indenter, even though the final indenter displacement and indentation diameter are the same for all the tests. This can be mainly attributed to the slight difference in microstructure at different locations considered for the study.

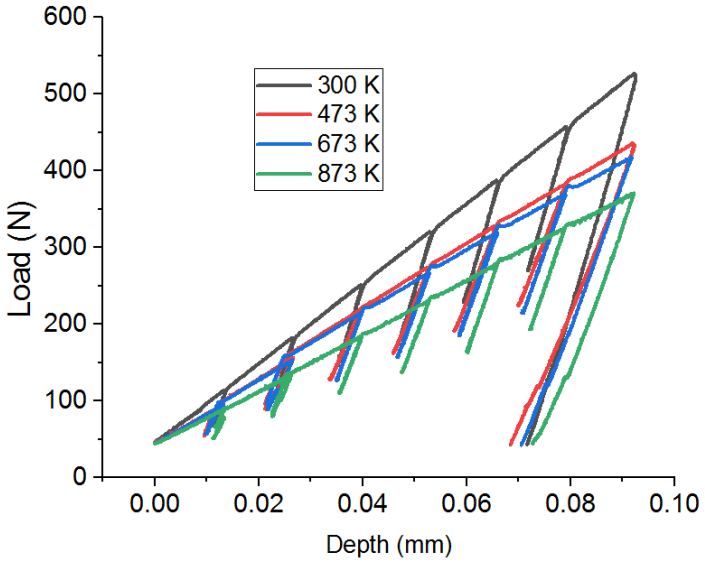

Figure 6.12: Load-displacement plot showing the effect of test temperature

The flow curves obtained for LDED built Hast-X estimated at various temperatures are presented in Figures 6.13(a) for as-built samples. As expected, the true stress values reduce with an increase in the test temperature for the same true plastic strain. It can be observed that the yield strength and ultimate strength decreases with an increase in test temperature (refer Figure 6.13(b)), due to the reduced hindrance for dislocation motion at elevated temperatures. The yield strength is higher than conventional wrought samples[37], which can be due to higher

dislocation density typically seen in LDED and fine microstructural features. In addition, it can be noted here that the difference in the yield strength between the conventional and LDED sample reduces with an increase in test temperature primarily due to dislocation annihilation that can happen at the higher temperature.

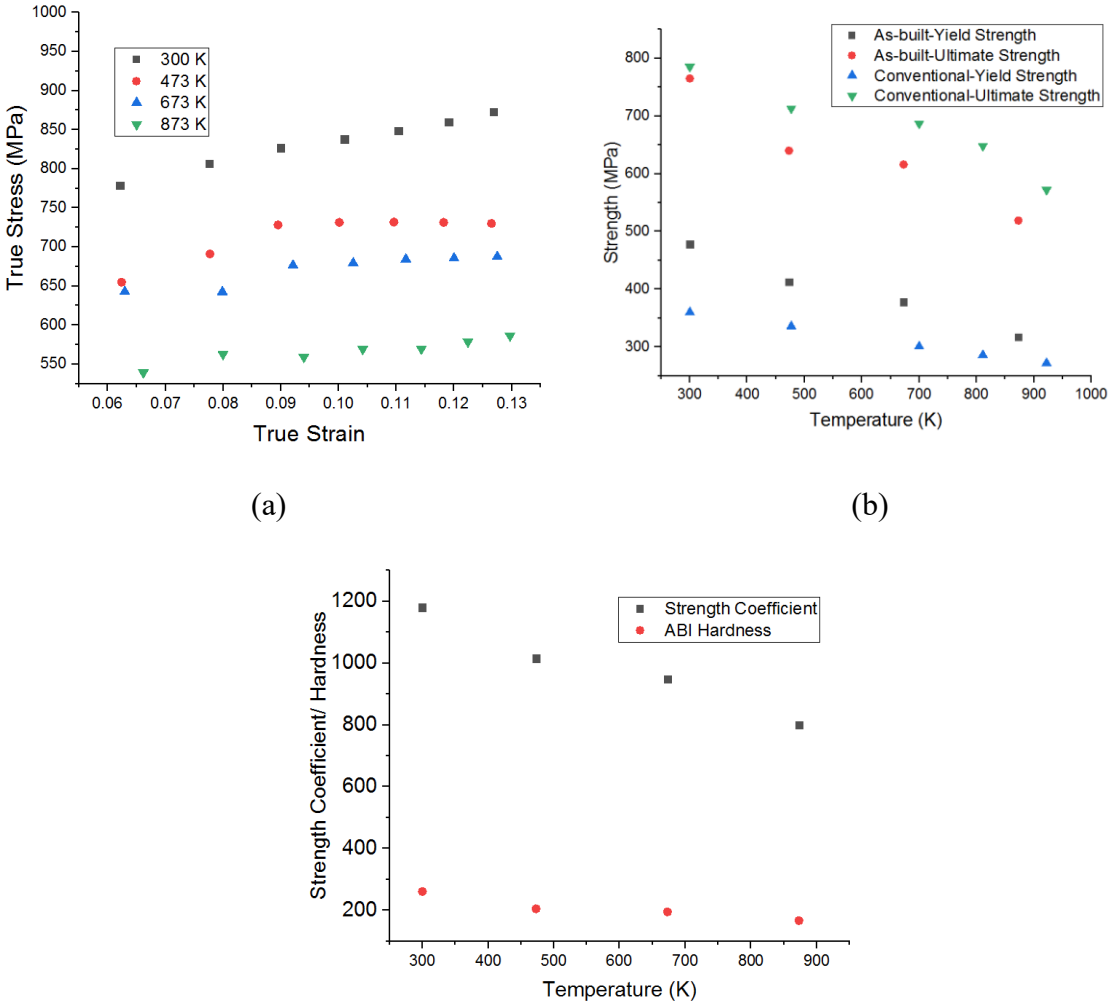

Figure 6.13: ABI results at different test temperatures (a) True-stress vs True plastic strain of as-built sample (b) Yield strength and ultimate strength of as-built and conventional sample (c) Strength coefficient and ABI hardness

Generally, the stress-strain characteristic of metals follows the Hollomon's equation, which relates the true stress and plastic strain using a power law. The strength coefficient (K) and

strain hardening exponent (n) are derived from the plot between the true stress and plastic strain. The values of strength coefficient and strain hardening exponent are estimated by fitting equation 6.2 for different values of test temperature.

$$\sigma_t = K\varepsilon_P^n \tag{6.2}$$

It is observed that the strength coefficient shows a decreasing trend with an increase in the test temperature as presented in Figure 6.13(c), similar to the trend followed by yield strength and ultimate strength. This is mainly due to the reduction in dislocation density in the material at a higher temperature. ABI hardness also shows the similar trend and a reduction of 36% is observed for as-built samples from 300 K to 873 K. It is observed that the strain hardening exponent shows a small increasing trend with an increase in test temperature for as-built samples. Strain hardening exponent increased from 0.13 to 0.15 for as-built samples, when the test temperature is increased up to 873 K. Strain hardening generally occur in metals under loading and takes place when the hindrance due to the interaction between the dislocations resists the dislocation movement. The strain hardening exponent shows the capability of a material to resist continuous plastic deformation. Strain hardening exponent mainly depends on the microstructure of the material and typically it increases with a decrease in the yield strength of the material. Strain hardening exponent is primarily a function of the dislocation density and strain hardening takes place due to the rapid increase in dislocation density during plastic deformation. If the initial dislocation density is lower, faster will be the increase in dislocation density during the plastic deformation. As the dislocation density decreases with an increase in test temperature, strain hardening exponent increases[191]. Moreover, the work hardening processes seem to be dominating more than the competing flow softening in the temperature regime studied. Figure 6.14 presents the microstructure of the as-built samples

after ABI testing. It is observed that the microstructure is retained after high-temperature ABI testing, with as-built samples showing a mix of cellular and dendritic growth.

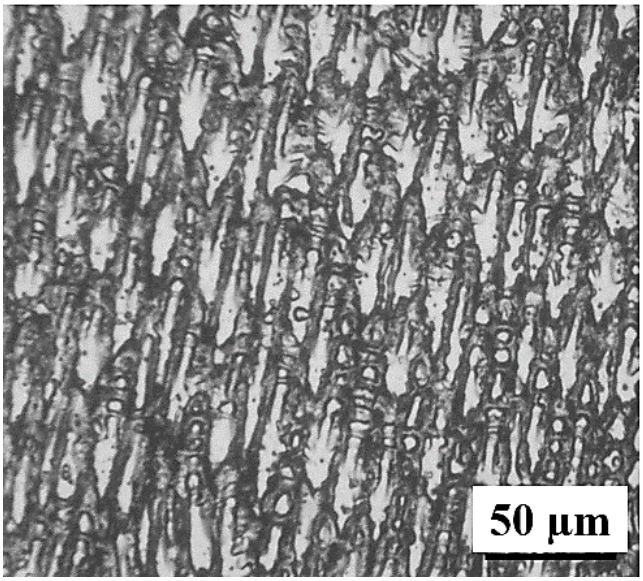

Figure 6.14: Microstructure of ABI sample after testing

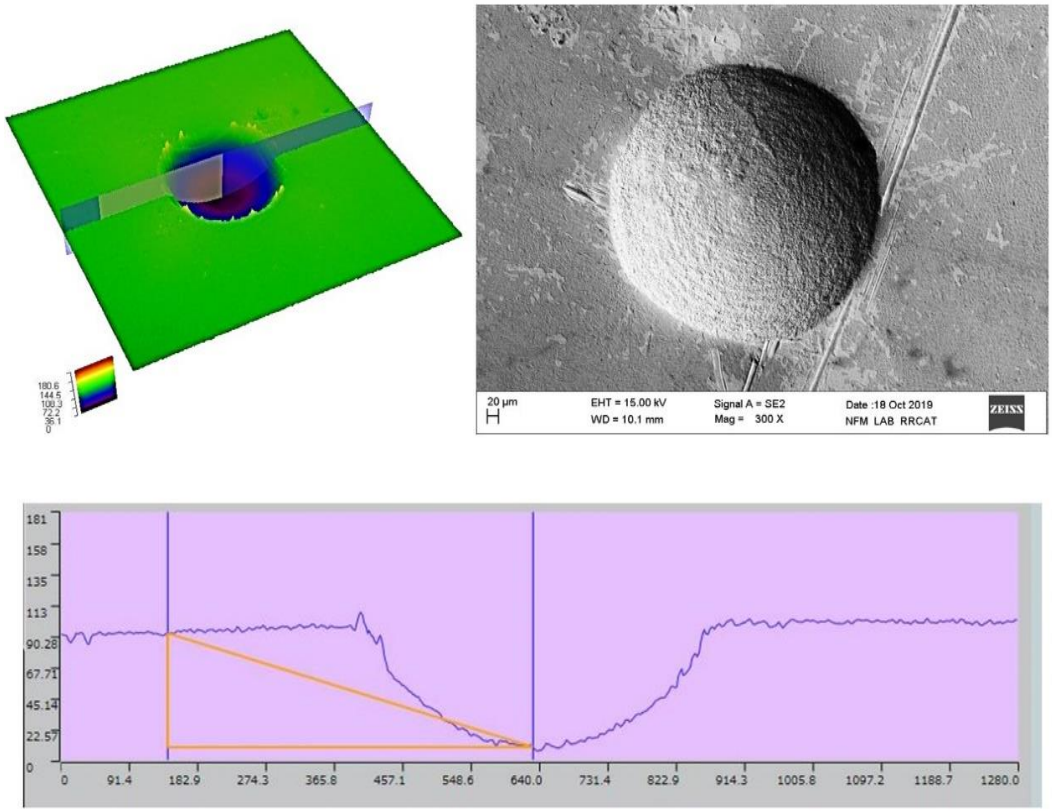
180.6
144.5
108.3
72.2
36.1
0
20 µm
EHT = 15.00 kV
WD = 10.1 mm
Signal A = SE2
Mag = 300 X
Date :18 Oct 2019
NFM LAB RRCAT
ZEISS
181
158
135
113
90.28
67.71
45.14
22.57
0
0
91.4
182.9
274.3
365.8
457.1
548.6
640.0
731.4
822.9
914.3
1005.8
1097.2
1188.7
1280.0

(a)

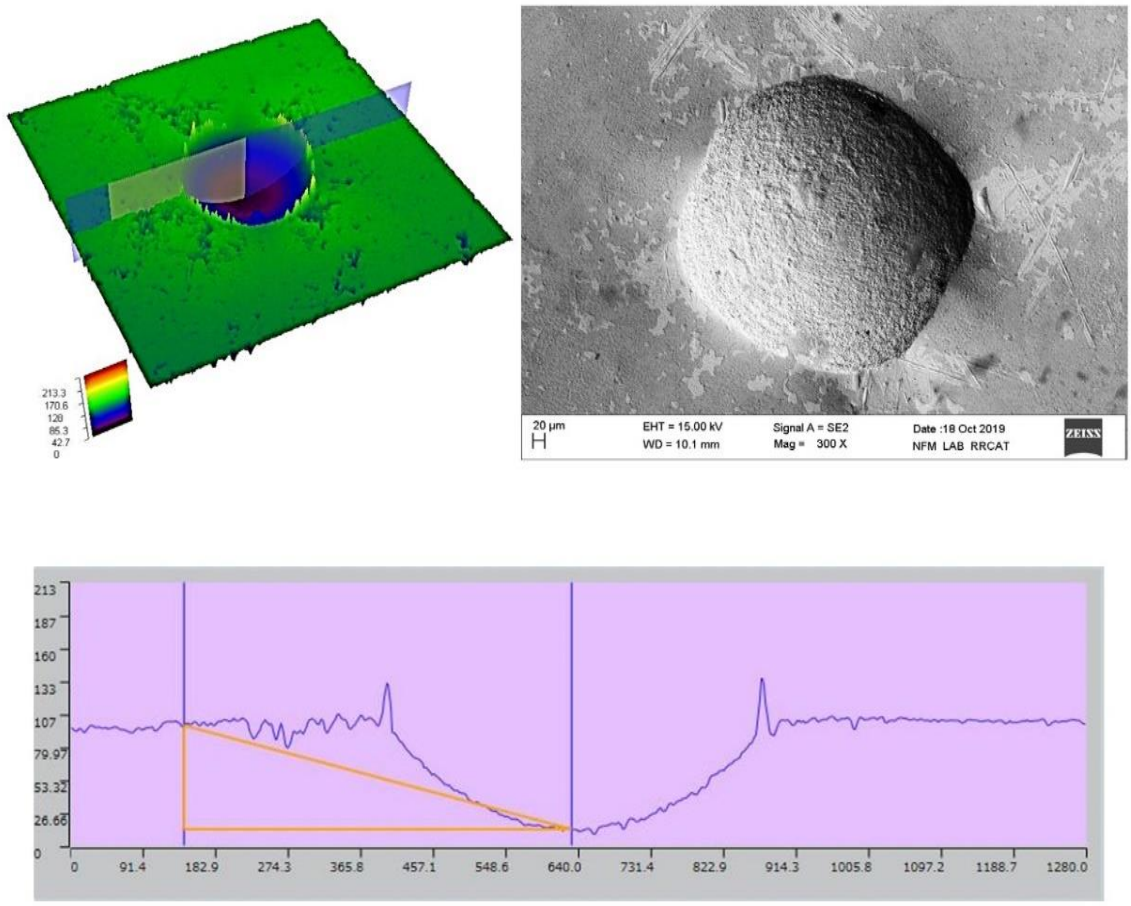

(b)

Figure 6.15: ABI indentation of LDED built Hast-X at (a) 473 K (b) 673 K

The indentation profile is analysed using a laser confocal microscope and SEM. Figure 6.15a and 6.15b presents the indentation profile of as-built sample tested at 473 K and 673 K. No crack formation is observed around the indentation region for the samples. Material pile-up is seen around the indentation area and it is observed that the pile-up increases with an increase in test-temperature. This is because as the test temperature increases, the material softens, which leads to the growth and outward spreading of the plastic zone[192]. A small increase in the indentation diameter is observed with an increase in test temperature indicating lower resistance to deformation. The measured indentation diameter for the as-built sample tested at

473 K and 673 K is 490 μm and 501 μm, respectively. These observations indicate that with an increase in the test temperature, hardness, yield strength and resistance to the plastic deformation reduces.

6.10 Summary

Bulk Hast-X structures are built using the identified process parameters and subjected to the microstructural, surface and mechanical characterisations in the as-built condition to understand its behaviour. Microscopic analysis shows the presence of fine cellular and dendritic growth and the samples revealed random grain orientation with slightly preferred texture along the <100> plane. The samples revealed the elemental segregation of Mo, Si and C showing the precipitation of Mo-rich carbides. The presence of FCC matrix is revealed during X-ray diffraction studies. Surface characterisations reveal the presence of partially melted powders on the surface of the built structures. Residual stress measurement reveals predominantly tensile stress on the deposited surface with a maximum value of 252 MPa. Micro-tensile test results at ambient temperature showed excellent agreement with the mechanical properties obtained from automated ball indentation (ABI) tests of LDED built Hast-X in as-built condition. Subsequently, ABI tests are used to evaluate the mechanical properties in as-built and heat-treated conditions from ambient temperature to 873 K. It is observed that the strength and ABI hardness decreased with increase in test temperature, while the strain hardening exponent showed an opposite trend. The yield strength of as-built sample is higher than the conventional sample. Further, the indentation size and material pile up around the indentation also increased with an increase in the test temperature.

Chapter 7 : Understanding the effect of In-situ Sequential Layer by Layer Re-melting (SLLR) and post heat-treatment of Hast-X bulk structures[5]

7.1 Introduction

LDED being a high energy density and fast process, it generates various processing issues, like - cracking, porosity, surface roughness, non-homogenous microstructure, etc. This reduces the useful life and strength of the built component and limits their deployment in duty critical circumstances. Solidification cracking during LDED process can be primarily due to the larger thermal stress owing to higher input energy and subsequent higher temperature gradients [47]. Porosity generation during LDED can be either or a combination of gas-induced porosity and process-induced, which are generated mainly due to gas entrapment during the deposition and lack of fusion at isolated locations, respectively. Surface roughness in LDED built structures can be due to the non-flat layer edges [47] and partially melted metal powders. Non-homogenous microstructure formation and elemental segregation during LDED are mainly due to non-equilibrium solidification conditions. Thus, to resolve the above issues and make the components ready for applications, LDED built components are exposed to various treatments, commonly known as post-processing techniques.

[5] This chapter is partially reproduced with permission from Elsevier (Journal – S. No. 2 and 8) – See Letters of Copyright Permission (Page No. 208 and 212)

Some of the common post-processing techniques are machining, hot isostatic pressing (HIPing), shot peening, laser peening, heat-treatment, etc. CNC machining is the most commonly used finishing technique to improve the surface quality and requisite dimension within the acceptable tolerance of LDED built components. HIPing is the post-processing technique generally applied to improve the density and mechanical properties of the components using high pressure and temperature. The component is raised to elevated temperature and high pressure is applied using Argon gas, which closes the sub-surface cracks/ pores. Shot peening and laser shock peening are techniques used to induce compressive residual stress on the surface of LDED built component to eradicate the tensile residual stress developed during LDED[193,194]. The tensile residual stress on the component surface can reduce the fatigue life of the component by allowing crack propagation. By deploying shot peening or laser shock peening, compressive residual stresses are induced on the surface and sub-surface region, which improves the fatigue life of the built structures. In addition, the grain structure gets finer and surface hardness, wear-resistance and corrosion behaviour improve with laser peening[194].

Laser remelting is a surface treatment technique to modify the surface properties, like – microstructure, microhardness, wear resistance, surface roughness, etc. Laser remelting can be carried out in-situ after LDED processing and it results in rapid melting and cooling that takes place instantly once the laser moves away, which results in high cooling rate (self quenching). This leads to a finer grain structure at the surface and increases the surface hardness and wear resistance[195]. Researchers have attempted laser remelting of LDED built structures. Yang et al. investigated the effect of laser remelting on the microstructure and magnetic properties of single-layer laser deposits of Fe-Co-based alloys. It was observed that laser remelting leads to higher saturation magnetization and lower coercivity. In addition, finer microstructure, improved microhardness and improved wear resistance were observed after laser

remelting[196]. Yasa et al. investigated laser remelting of LDED built Inconel 625 wall structures after 10-layer deposition intervals. A reduction by 61 % in porosity and an improvement by 26 % in hardness is observed[195]. Xin et al. investigated the microstructure and mechanical properties of SS 316L thin-wall structure by combining LDED and laser remelting. Laser remelting of single track laser clad layer show reduction in the porosity, improvement in hardness and increase in dendrite length[197].

Sequential Layer-by-layer Laser Remelting (SLLR), an extension of laser remelting process, can be a possible option to improve the surface and bulk properties of LDED components by avoiding post-processing step. SLLR involves laser remelting after LDED of each layer. SLLR deploys the same laser source used for LDED and scans the laser beam over the previously deposited layer. The difference between SLLR and LDED is that powder feeding is turned off during SLLR, which leads to complete exposure of previously deposited layers with the laser heat source. Yu et al. [198] investigated the effect of SLLR on the microstructure and mechanical properties of LDED built 17-4 PH stainless steel. The deployment of SLLR reduced the porosity level and mechanical anisotropy in the LDED built sample. SLLR at 15 J/mm^2 revealed the least porosity and near isotropous UTS. However, it was concluded that the effect of SLLR to remove the anisotropy in ductility is less because of the unavoidable interlayer defects.

In the case of non-homogeneity in the microstructure, the most suitable solution can be the thermal post-processing of the built structures. The most common and globally used thermal post-processing is the heat-treatment. Generally, the major goal behind performing heat-treatments are: stress reduction, allowing redistribution of alloying elements, grain growth, promote the formation of new recrystallized grains, dissolving phases, generation of new phases, etc. [199]. Hast-X being a solid solution strengthened alloy, the prescribed heat-

treatment procedure is the solution treatment. Solution treatment is used to reset the previous phase precipitations and dissolve the secondary phases. It also aids to achieve a homogenous microstructure by rearranging the compositional segregation experienced during the solidification process. Thus, solution treatment/ annealing serves the following purposes, like - recrystallization of alloy, homogenization of alloy and dissolving approximately all phases in the face centred cubic matrix[199].

In the previous chapter, the LDED built structures are systematically characterised using various tools to understand the behaviour of the LDED built Hast-X structures. It is observed that the micro-pores are present at isolated locations, which are a mix of process-induced and gas-induced pores. Further, the surface of as-built samples show the presence of partially melted powders leading to higher surface roughness and non-uniformity at several locations. In addition, the non-homogenous microstructure is observed in the as-built samples along with the presence of elemental segregations. In the present chapter, two separate investigations are carried out on LDED built Hast-X bulk structures.

Thus, there is limited work available in the public domain on the deployment of SLLR on bulk LDED built nickel superalloys to improve the surface and bulk properties. Further, there is no literature available in the public domain on the effect of solution treatment on the behaviour of LDED built Hast-X structures. Therefore, in the present work, SLLR of LDED built Hast-X is used to elucidate the effect of SLLR on the porosity, surface topography, microstructural characteristics and mechanical properties. Subsequently, to understand the effect of solution treatment on LDED built Hast-X bulk structures, a systematic investigation is carried out on the microstructure and mechanical characteristics of solution treated Hast-X structures and the mechanical properties are compared with that of conventional counterparts as available in the literature. Further, the mechanical properties at elevated temperature are carried out using

Automated Ball Indentation for heat-treated samples and the behaviour is also compared with as-built samples and conventional counterparts.

7.2 In-situ SLLR of Hast-X Bulk Structures

7.2.1 Experimental Details

Trial experiments are carried out to select the process parameters for SLLR by using single tracks. Single tracks are deposited by varying the laser power at a constant scan speed of 1.2 m/min. A higher scan speed of 1.2 m/min is used for remelting to obtain a finer melt-pool size, which can aid to improve the surface topography. At lower values of laser power, the partially melted powders on the surface were not completely melted, while at higher laser power excessive oxidation/ burning of tracks are observed. Thus, a laser power of 1500 W is selected for SLLR considering the surface quality of the built tracks. Figure 7.1 presents the comparison between the surface topography of single tracks with and without remelting.

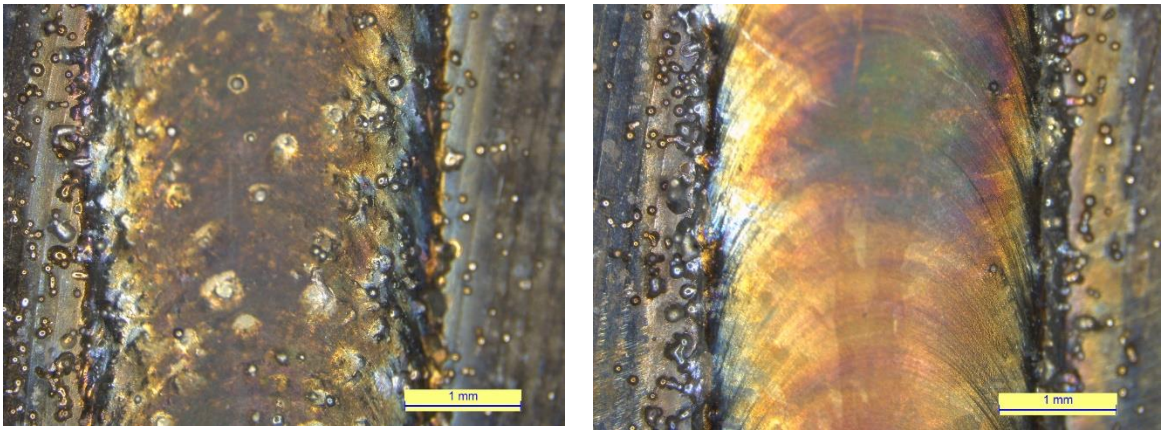

(a) (b)

Figure 7.1: LDED single tracks deposited at a laser power of 1600 W (a) without remelting (b) with remelting at laser power of 1500 W

Based on the trial experiments, laser power of 1500 W and a scan speed of 1.2 m/min, with 50 % overlap between adjacent scans is used for SLLR experiments. The process parameters used for bulk deposition are laser power (P): 1.6 kW; scan speed (V): 0.5 m/min; powder feed

rate (F): 8 g/min with 50 % overlap between adjacent tracks as discussed in chapter 4. Table 7.1 presents the process parameters used for LDED and SLLR experiments. Both LDED and SLLR experiments are performed using the unidirectional scanning strategy as presented in Figure 7.2. After every layer of LDED deposition, the delay period of ~ 2.5 seconds is used before the SLLR experiment. Argon gas is fed at 6 litres per minute for feeding the powder to the deposition zone during LDED and to protect the melt pool from oxidation during LDED and SLLR. Rectangular Hast-X blocks of size 50 mm x 20 mm x 5 mm are deposited with and without SLLR using LDED system. Samples without SLLR and with SLLR will be designated as LDED and SLLR samples, respectively hereafter in the chapter.

Table 7.1: Process parameters used for LDED and SLLR

LDED of Hastelloy-X	***SLLR***
Laser Power - 1600 W	*Laser Power – 1.5 kW*
Scan Speed – 0.5 m/min	*Scan Speed – 1.2 m/min*
Powder Feed Rate – 8 g/min	*Overlap Percentage - 50 %*
Overlap Percentage - 50 %	

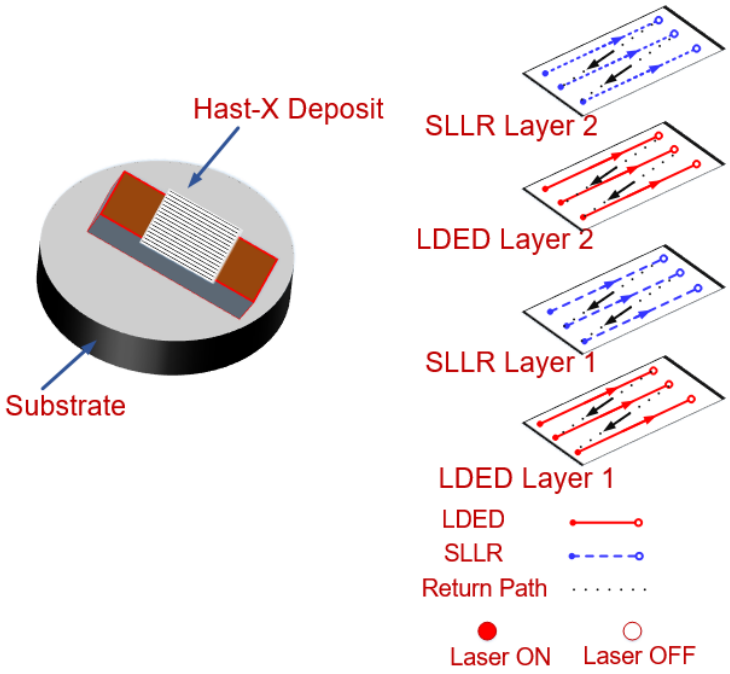

Figure 7.2: Scheme of SLLR during LDED

The deposited bulk structures are characterized to understand the effect of SLLR on the porosity, surface topography, microstructure and mechanical properties of LDED built Hast-X bulk structures.

7.2.2 Porosity

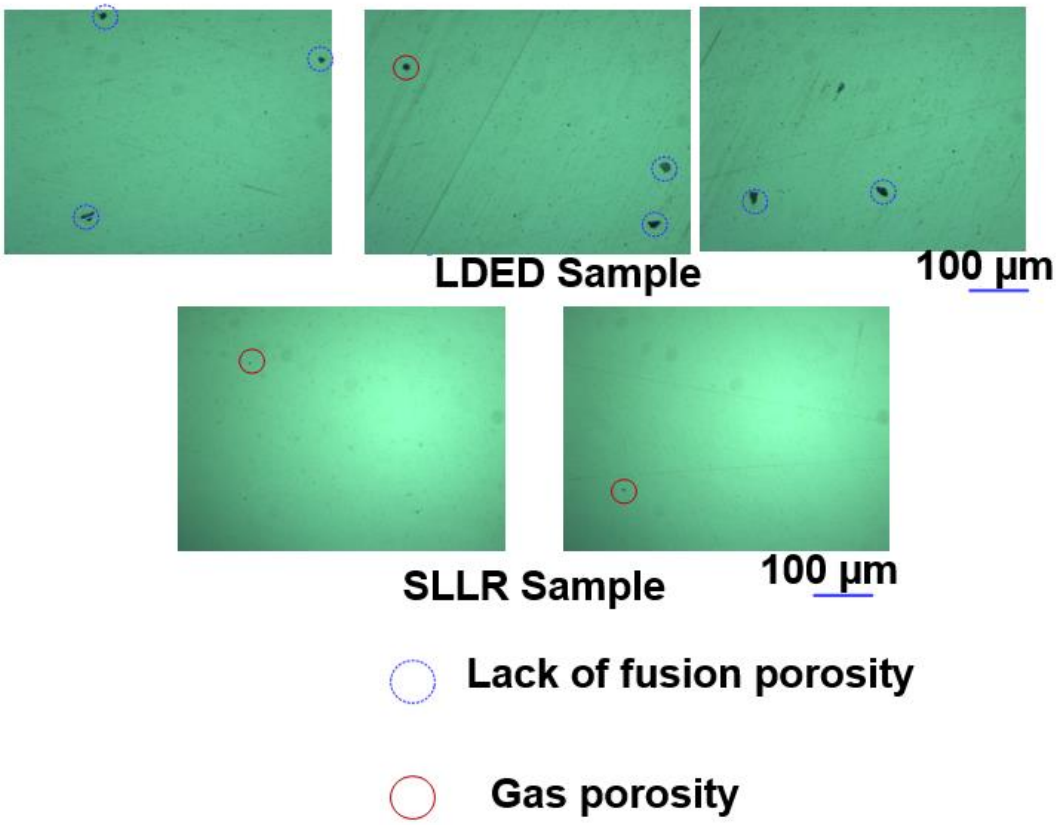

Figure 7.3: Porosity of LDED and SLLR samples

Figure 7.3 presents the porosity of LDED and SLLR samples and the measured area fraction porosity of LDED samples is ~ 0.5% with random porosity at isolated locations. These localized pores are a mix of small spherical and irregular pores. Spherical pores are mainly gas porosities, which are generated due to either gas atomisation of feedstock material (a prior step to LDED) or trapped gas/ metallic vapour volumes generated during fast cooling. Irregular pores are process-induced porosities and they are mainly seen due to the lack of fusion at localized regions or incomplete material consolidation. The maximum size of these pores in LDED built samples is measured as 30 µm.

In SLLR samples, the size and the number of the pores reduced with the maximum size of pores is found as 5 µm. The pores observed in SLLR samples are mainly gas-induced pores,

with no process-induced pores. SLLR could reduce the porosity observed in LDED samples significantly to ~ 0.01 %. During SLLR, porosity tries to move up to the top of the melt pool and disappear during the subsequent remelting. This results in the filling up of pores with molten material and reduces pore size due to the release of trapped gases. SLLR also yields a good metallurgical fusion between neighbouring tracks and layers. Further, the reduction in the porosity is also achieved due to increased melt pool duration leading to more wetting period causing the release of trapped volumes during SLLR. This results in better densification behaviour for LDED samples after SLLR[197,200].

7.2.3 Surface Topography

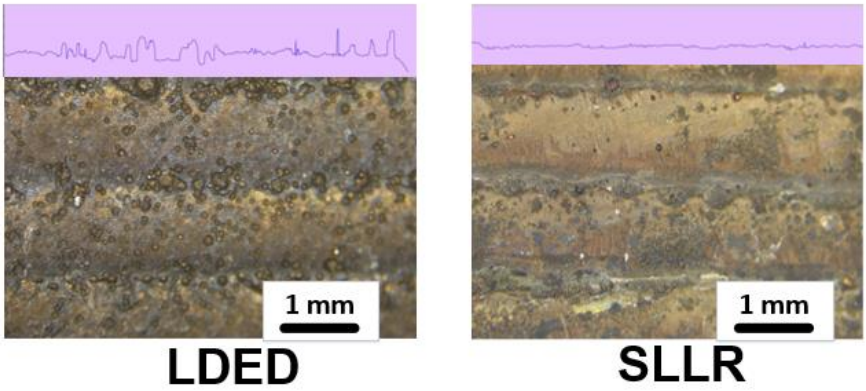

Figure 7.4: Surface Topography of LDED and SLLR samples

The surface topography of the samples is analysed using a stereomicroscope as presented in Figure 7.4. The as-built LDED samples revealed partially melted powders on the top surface. However, the amount of partially melted powders on the sample surface reduced in SLLR samples. Table 7.2 presents the surface roughness values and it is seen that the R_a value reduced by 71.5 % after SLLR. The higher value of R_a in LDED sample is mainly due to the partially melted powders on the deposit surface as seen in Figure 7.4. It is observed that SLLR reduced the surface roughness significantly due to relatively less number of partially melted powders on the surface of SLLR sample. It can also be noted that the R_p value reduces significantly as

compared to R_v value. Laser remelting results in the complete melting of the partially melted powders on the LDED sample surface and redistribution of materials takes place from the peaks and valleys resulting in a flatter surface with an improved surface finish. In addition, the melt pool tends to spread wetting due to the increased melt pool duration[200]. This leads to smoothening of the surface and the uniform sample surface is obtained as shown in Figure 7.4.

Table 7.2: Surface Roughness Parameters of LDED and SLLR samples

Condition/ Parameter	R_a (µm)	R_p (µm)	R_v (µm)	R_z (µm)
As-built	10.54	61.48	19.14	80.62
SLLR	3	12.79	14.03	26.83

7.2.4 Microstructural and Phase Analysis

Macrostructure of the samples shows clear melt pool boundaries as labelled in figure 7.5a. The layered structure with the melt pool boundaries and distinct interface among the LDED layers is due to the reheat and re-melt effect during the layer-by-layer deposition in LDED. The melt pool boundaries are observed to be defect-free (without cracks) in the LDED and SLLR samples at the macro-scale. It may be seen that in SLLR samples the depth of melt-pool is relatively lower than LDED samples. This is primarily due to the lower melt-pool temperature in SLLR samples owing to lower laser absorptivity and relatively lower energy per unit length used for remelting.

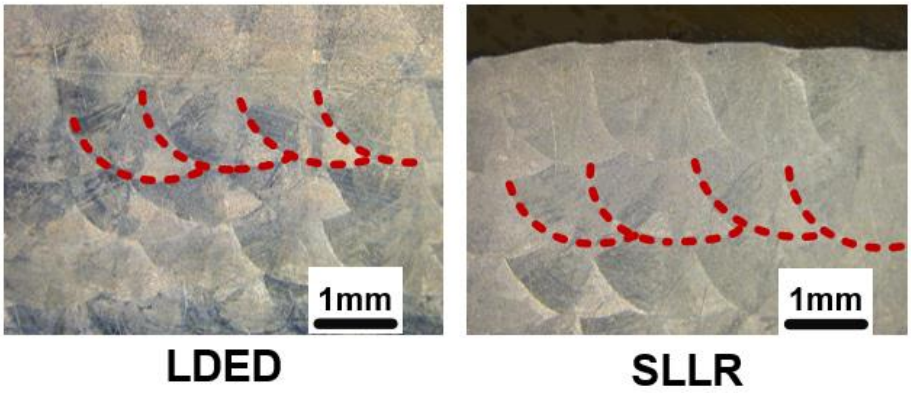

(a)

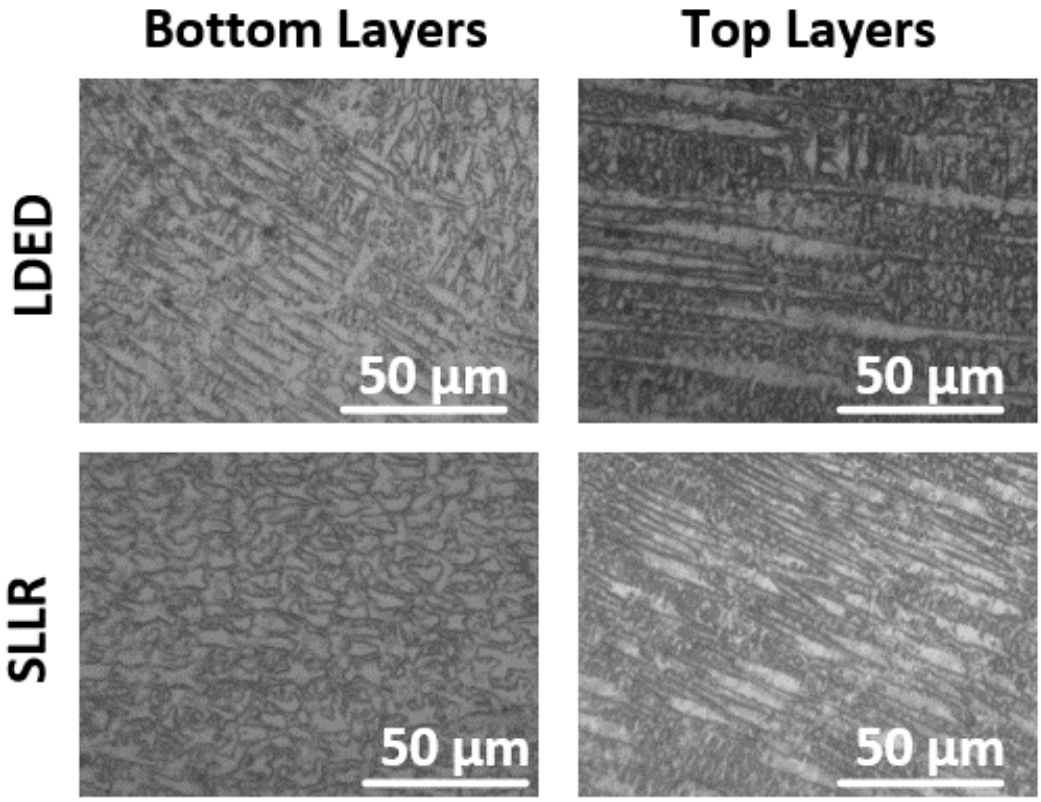

(b)

Figure 7.5: LDED and SLLR sample (a) Macrostructure (b) Microstructure

Figure 7.5b presents the microstructure of the samples and it is seen that the microstructure is a mix of cellular and dendritic structure with classical secondary arms at the top layers. Both LDED and SLLR samples are observed to be defect-free without cracks in the microscale also. During LDED, the dendrites at the bottom layers are finer due to the larger thermal gradient

primarily because of the substrate effect. During the initial layers, the substrate (initially at room temperature) acts as a heat sink with larger thermal gradient and the epitaxial growth of columnar dendrites is seen in the direction almost perpendicular to the solidification interface. The growth takes place opposite to direction of heat transfer, where the temperature gradient is the largest. It is observed that the columnar dendrites get coarser as the deposition moves from the bottom layers to the top layers. This is mainly due to the increase in the preheat temperature at the previously deposited layers leading to a reduction in the cooling rate of the material[105]. The calculated dendrite width varies from 4 μm to 7 μm as the deposition moves from the bottom layers to top layers.

The microstructure of the SLLR sample is similar to LDED. However, SLLR results in slightly finer grain structure as compared to LDED samples and the dendrite width varies from 3 μm to 5 μm as the deposition moves from the bottom layers to top layers in SLLR samples. The slight reduction in the dendrite size after SLLR is mainly due to the faster cooling rate during SLLR as compared to LDED. During LDED, the laser energy is absorbed by the substrate and powder cloud, with powder having more laser absorptivity as compared to the substrate/ bulk material. During SLLR, since powder feed is off and complete exposure of laser beam to the substrate takes place. This can result in less amount of energy used for melting in SLLR as compared to LDED due to lower laser absorptivity of the bulk layers as compared to the powder cloud, which results in smaller melt pool size and higher cooling rates in SLLR. In addition, the relatively low laser energy per unit length used for SLLR can also result in smaller melt pool and faster cooling.

Figure 7.6(a) and 7.6(b) presents the EBSD images of LDED and SLLR samples, respectively. It can be found that the orientation of the growth shows preferred texture along the (100) orientation for the LDED built sample as per the inverse pole diagram. The average grain size

is measured to be 23 µm in the LDED sample. In SLLR samples, the orientation of grains become random, which shows that the anisotropy of the sample is reduced with SLLR. The redistribution of the temperature gradient due to the subsequent melting of an overlying layer can significantly weaken the pre-solidified texture, which leads to relatively smaller polar density. This is in line with the observations by Yu et al. [198]. In addition, the average grain size is reduced in the SLRR sample to 14 µm, which is due to the faster cooling rate during SLLR. This is also in line with microscopy analysis.

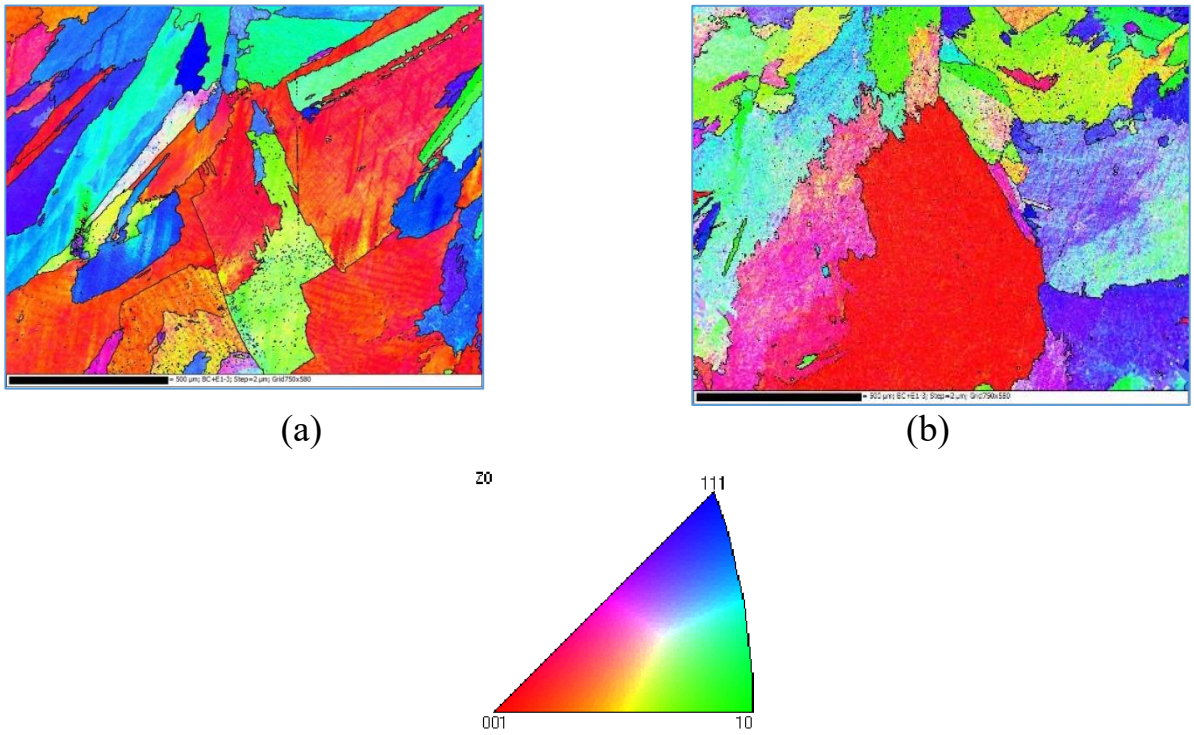

Figure 7.6: EBSD analysis (a) LDED sample (b) SLLR sample

Figure 7.7 presents the elemental mapping carried out on the LDED and SLLR samples. As discussed in chapter 6, Ni, Cr, Fe and Mn elements are uniformly distributed along the cross-section of the LDED sample. In addition, Mo, Si and C segregations are observed in the LDED samples and the presence of Mo rich carbides is also detected in LDED samples primarily due to continuous thermal cycling during the process. Similar results are also observed in the SLLR samples. However, the amount of segregation slightly reduced with SLLR, which can be co-

related with the relatively higher cooling rate in SLLR samples as compared to that of LDED samples[180]. At very high cooling rates, solute atoms are trapped by fast-advancing solidification interface, and as a result, the micro-segregation gets reduced[180].

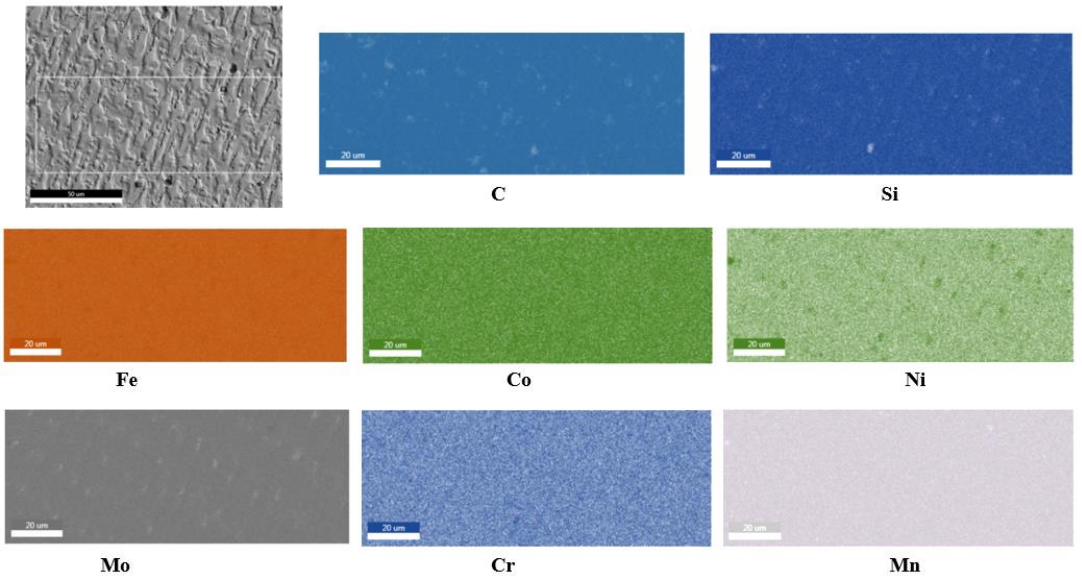

(a)

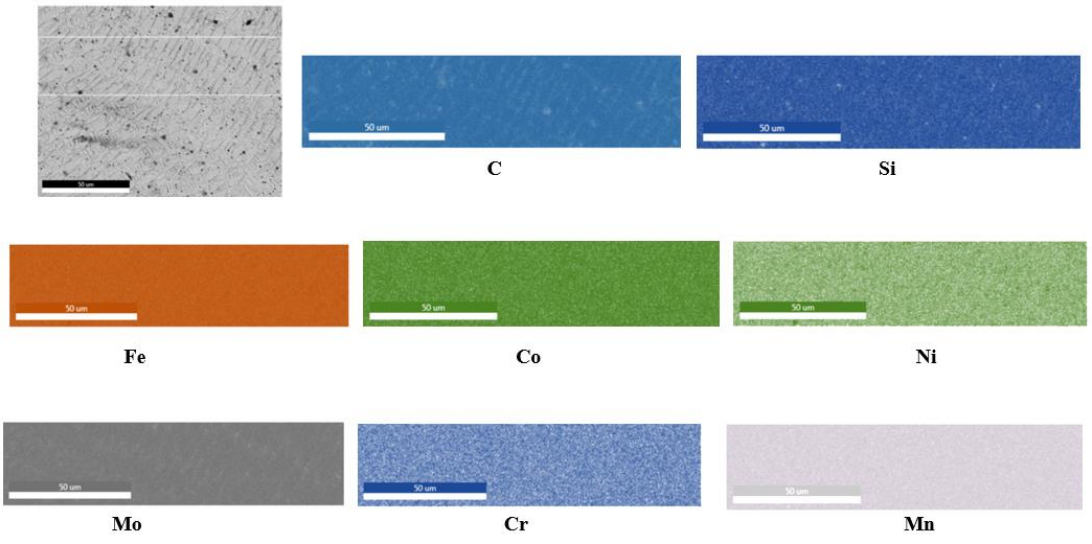

(b)

Figure 7.7: Element mapping of (a) LDED and (b) SLLR samples

Figure 7.8 (a) presents the XRD studies carried out on LDED and SLLR samples. LDED samples show peaks at 43.51°, 50.68° and 74.48° indexed to (111), (200), (220) planes, respectively revealing the presence of Ni γ-matrix (PDF number: 00-004-0850). SLLR samples also revealed similar peaks with an increase in the peak width. The increase in peak width can be attributed to the presence of finer crystallites in SLLR samples as compared to LDED sample. As seen in EBSD, preferential growth along the (100) plane is observed in the LDED sample, which is indicated by the highest intensity peak of (200). However, the preferential growth along (100) is reduced in SLLR samples. This confirms the observations from EBSD analysis. It can also be seen in Figure 7.8(b) that a peak shift towards the left is observed for SLLR samples as compared to LDED samples. This is primarily due to the increase in the d-spacing according to Braggs law as shown in equation 7.1, where, n is an integer, λ is the wavelength, and Θ is the Bragg angle. The increase in d-spacing indicates an increase in the tensile residual stress for SLLR samples as compared to LDED samples[181].

$$n\lambda = 2dsin\theta \tag{7.1}$$

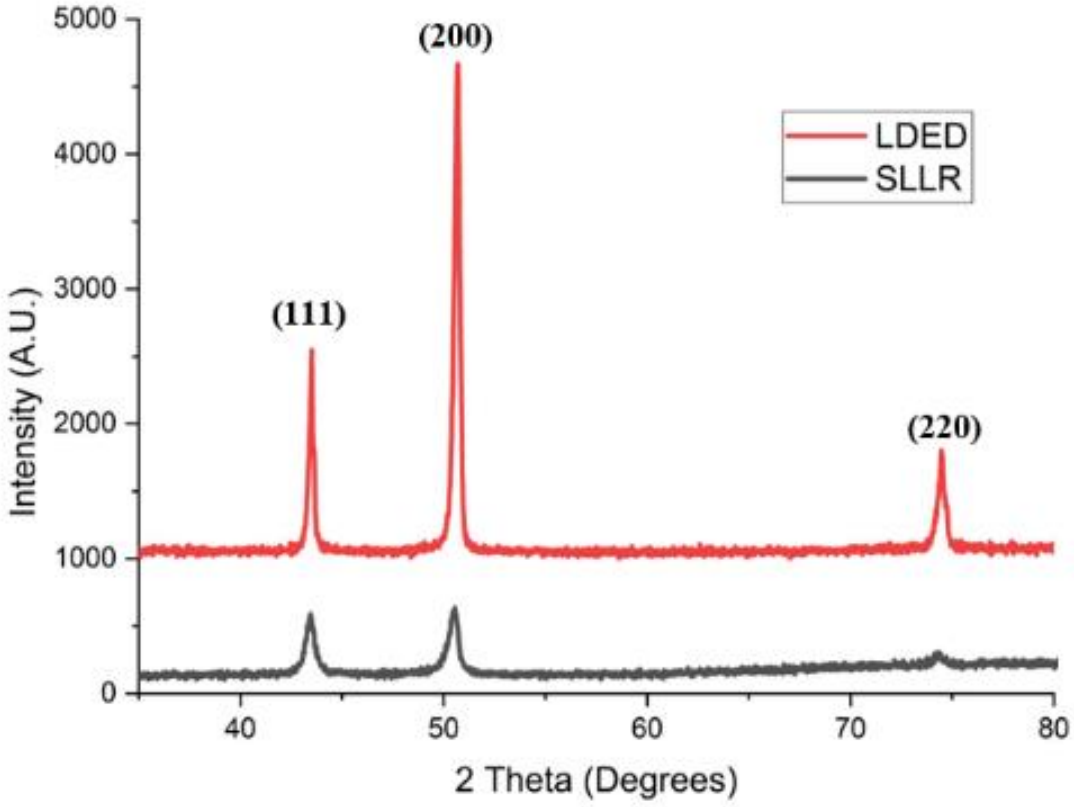

(a)

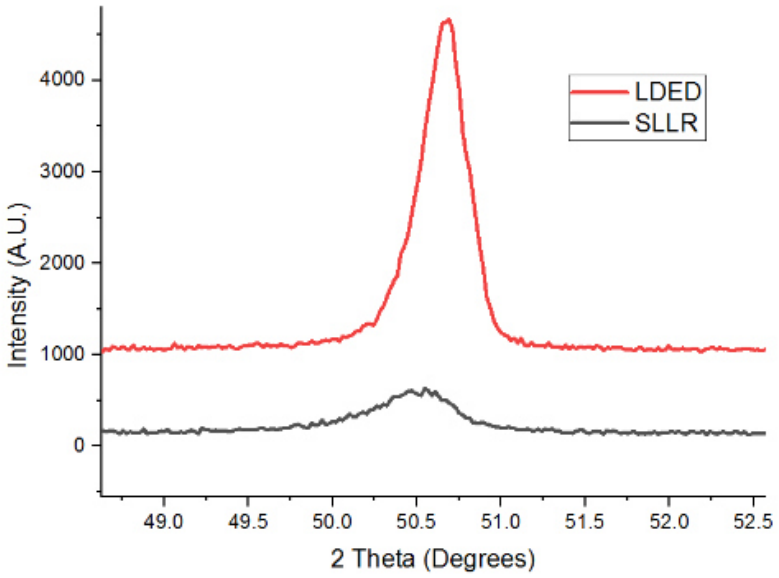

(b)

Figure 7.8: XRD (a) peaks of LDED and SLLR samples (b) peak shift

7.2.5 Mechanical Properties

Mechanical properties are evaluated using microhardness and Automated Ball Indentation technique to elucidate the effect of SLLR on the mechanical behaviour of LDED samples. Figure 7.9a presents the average microhardness of LDED and SLLR sample. The obtained value of the average microhardness for LDED built Hast-X is 239 $HV_{1.96N}$. The microhardness measurements of the SLLR samples show an increase of 12 % as compared to LDED samples, which is mainly due to the relatively finer dendritic structure in SLLR samples. The micro-hardness in LDED and SLLR conditions are higher than conventional Hast-X samples[37].

ABI testing is carried out along and normal to the build direction of LDED and SLLR samples to estimate the effect of SLLR on the tensile behaviour. Load - indentation depth plot obtained normal to the build direction is presented in Figure 7.9b. It is seen that the load required for obtaining the same indentation depth is higher for SLLR sample as compared to that of LDED sample. These are in line with micro-hardness and microstructural examinations. This is mainly due to relatively higher resistance to deformation offered by samples built with SLLR as compared to LDED sample due to relatively finer microstructure as discussed in the previous results. Figure 7.9c presents the flow curves of the structures and it can be seen that the sample built with SLLR shows slightly higher tensile strength than LDED sample. The variation in yield strength and ultimate strength with SLLR is presented in Figure 7.9d and it is seen that there is a slight increase in the yield strength by 4% and ultimate strength by 1.25% after SLLR. It can be seen in Figure 7.9e that the yield strength and ultimate strength measured along the build direction. The points on the x-axis refers to different points along the cross-section of the deposition from the substrate to top surface, where the measurements are taken. It shows a small declining trend from the bottom layers to top layers primarily due to variation in

microstructure from bottom to top layers as explained in the previous section. It is observed that the effect of SLLR on the yield strength and ultimate strength is less and the maximum improvement in yield strength and ultimate strength obtained along the build direction are 7% and 5%, respectively. It can also be noted that the range of yield strength and ultimate strength values along the cross-section decreased with SLLR. The range of yield strength and ultimate strength are 51 MPa and 43 MPa for LDED samples, respectively. However, the range of yield strength and ultimate strength reduced to 23 MPa and 32 Mpa, respectively for SLLR samples. The obtained value of yield strength at all the conditions is higher than the yield strength of the conventionally built Hast-X (340 MPa)[37]. These are in line with the results obtained during microhardness measurements. In addition, the yield ratio (ratio of yield strength to ultimate strength) is estimated to compare the ductility of the LDED and SLLR samples. Generally, a lower value of yield ratio indicates higher ductility of the material. It can be seen that yield ratio in SLLR samples vary between 0.59 – 0.62 and 0.59 – 0.60 in LDED sample. Thus, the relatively higher value of yield ratio for SLLR samples indicate a reduction in the ductility[183].

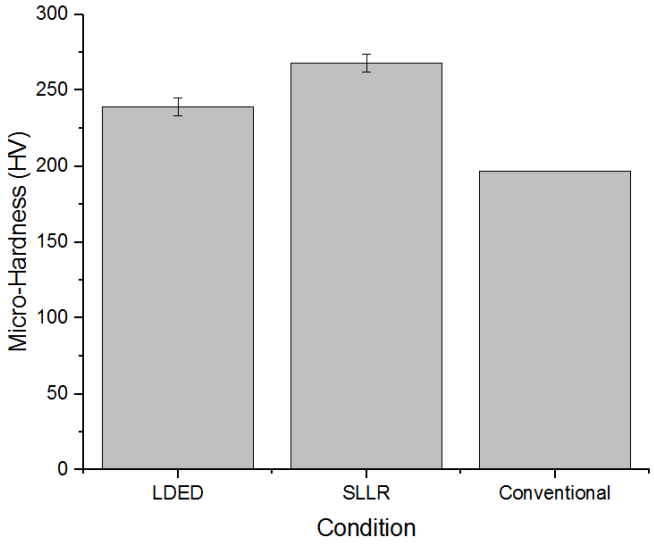

(a)

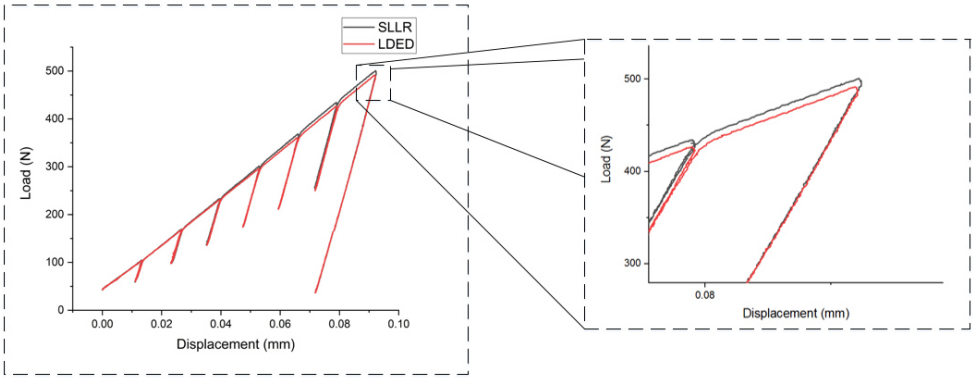
SLLR
LDED
Load (N)
Displacement (mm)
Load (N)
Displacement (mm)

(b)

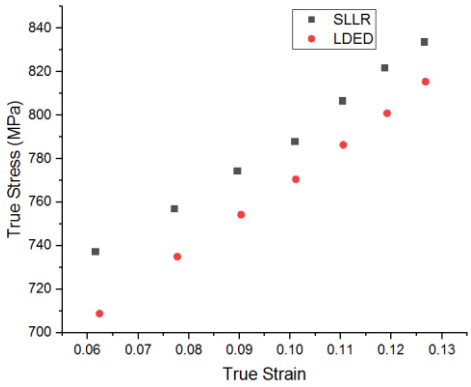
SLLR
LDED
True Stress (MPa)
True Strain

(c)

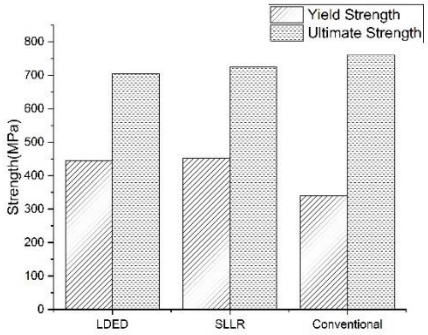
Yield Strength
Ultimate Strength
Strength(MPa)
LDED
SLLR
Conventional

(d)

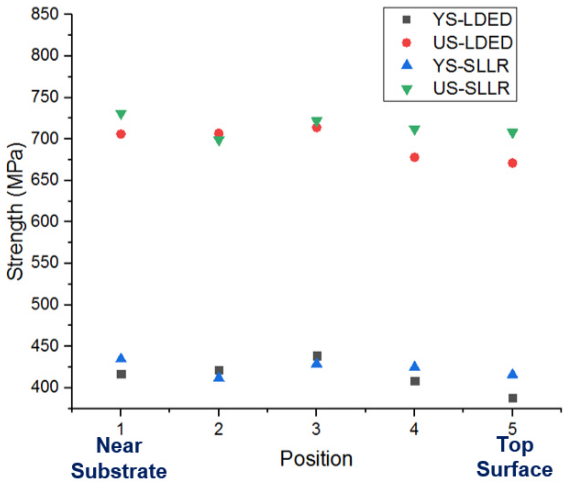
YS-LDED
US-LDED
YS-SLLR
US-SLLR
Strength (MPa)
Near Substrate
Position
Top Surface

(e)

Figure 7.9: ABI tests on LDED built Hast-X with and without SLLR a) Micro-hardness b) load-displacement plot of top surface c) True stress-strain plot of top surface c) Yield and ultimate Strength of top surface e) Yield and Ultimate Strength along the cross-section

Figure 7.10a and 7.10b present the microscopy images of the ABI indentations on LDED and SLLR samples. Pile-up is observed around the indentation in both the cases, with LDED samples having more pile-up as compared to SLLR samples. This can be due to the higher hardness of SLLR samples, which retards the plastic flow of materials leading to reduced pileup formation.

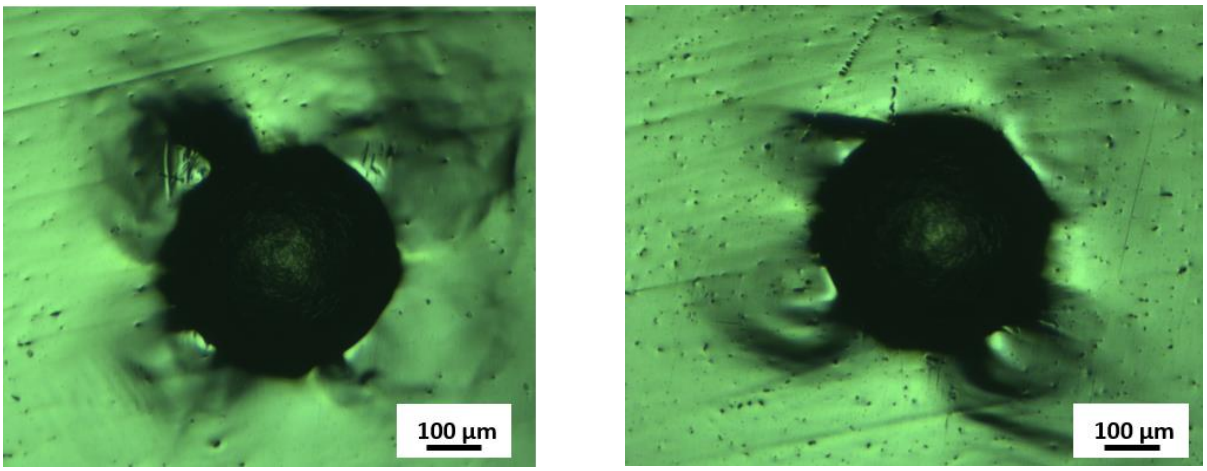

(a) (b)

Figure 7.10: ABI Indentations of (a) LDED (b) SLLR samples

7.3 Solution Treatment of LDED built Hast-X

7.3.1 Experimental Details

LDED process parameters deployed for depositing bulk and cylindrical Hast-X structures are laser power – 1600 W, scan speed – 0.5 m/min and powder feed rate – 8 g/min, with 50 % overlap between adjacent tracks. Subsequently, deposited samples are subjected to heat-treatment at 1450 K [37] for a soaking period of 2 hours followed by water quenching.

7.3.2 Macro Analysis

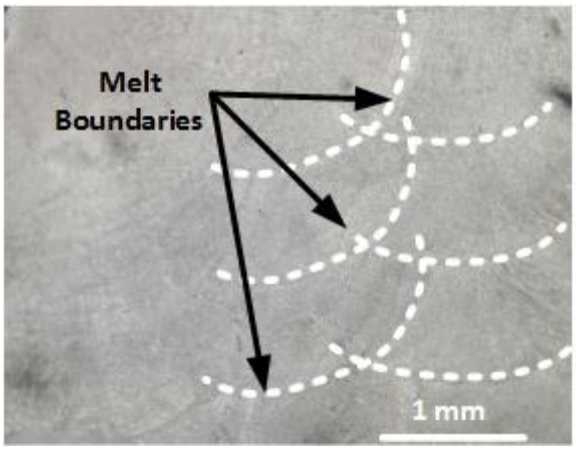

(b)

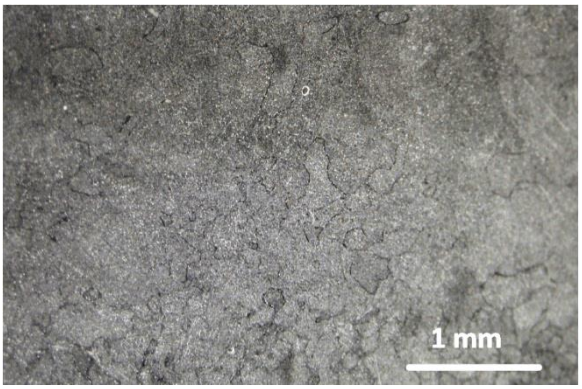

(c)

Figure 7.11: Macro-analysis (a) Melt-pool boundaries of as-built samples (b) Dissolved melt-pool in heat-treated samples

It is observed that the LDED samples are free from macro-defects such as cracks and voids. As discussed in chapter 6, LDED built Hast-X has overlapping melt-pool between the layers and tracks as seen in Figure 7.11a. However, it can be seen from figure 7.11b that the molten pool boundaries disappeared after the homogenization taken place during the heat treatment.

7.3.3 Microstructural and Phase Analysis

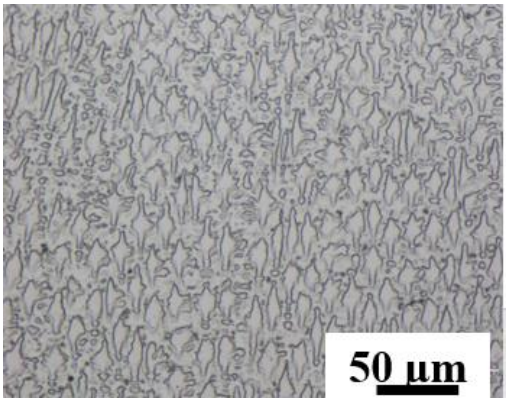

(a)

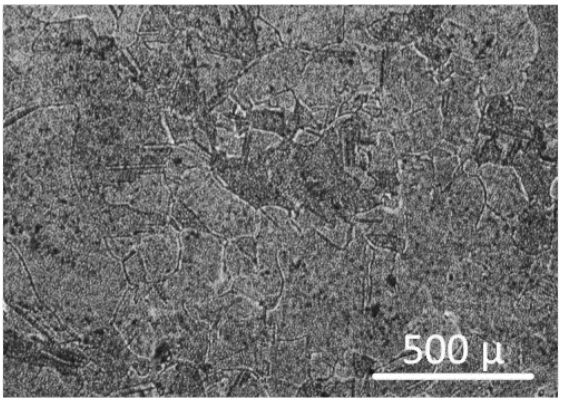

(b)

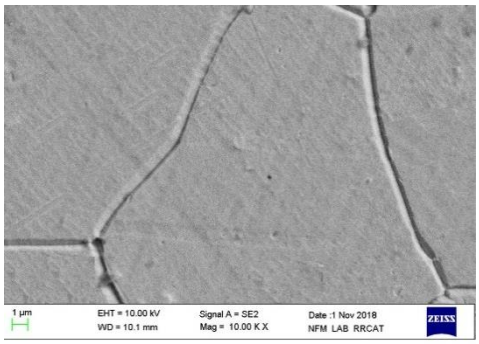

(c)

Figure 7.12: Microstructural analysis (a) as-built sample (b) heat-treated using optical microscopy (c) heat-treated using scanning electron microscopy

Figure 7.12 present the microstructure of LDED built Hast-X in as-built condition and heat-treated. As discussed in chapter 6, the microstructure of the as-built sample reveals fine columnar growth with a mix of cellular and dendritic structure (refer to Figure 7.12a). Figure 7.12b and 7.12c present the microstructure of the heat-treated sample and it shows the presence of recrystallized equiaxed grains due to homogenization during solution treatment. Recovery, recrystallization and grain growth takes place during heat treatment. During recovery, the internal stresses are relieved and it mainly takes place at a lower temperature. During recrystallization, new grains are formed with the same lattice structure with approximately the same dimensions in all directions as appropriate conditions are provided. Thus, the recrystallized equiaxed grains are formed during heat treatment. Further, the coalescence of grains during grain growth increases the size of grains.

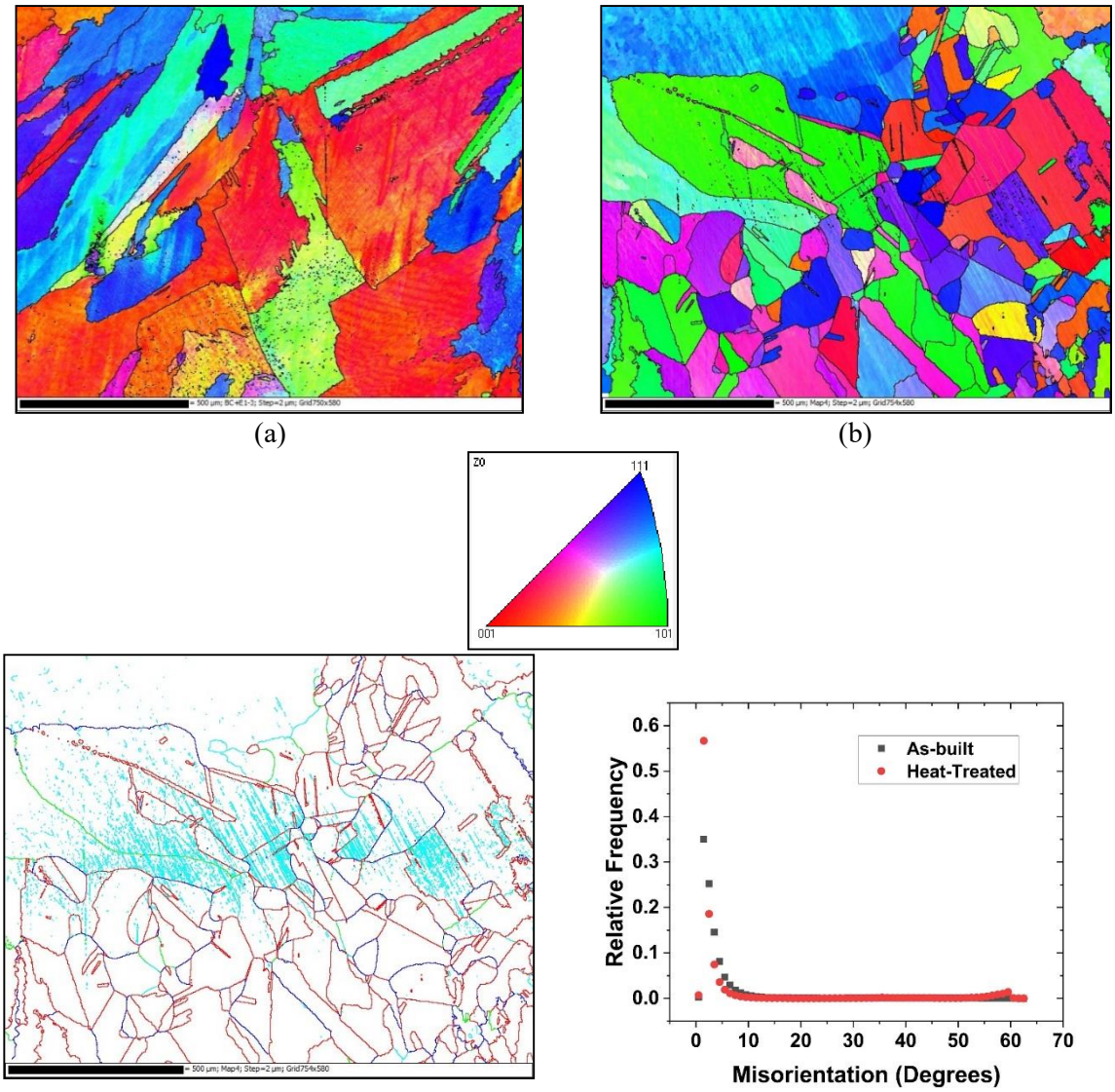

Figure 7.13: EBSD images (a) as-built sample (b) heat-treated sample (c) twinning in heat-treated sample (d) variation of the mis-orientation angle

Figure 7.13(a) and 7.13(b) present the EBSD images of as-built and heat-treated Hast-X. It can be observed that the orientation of the cells/ grains is random in nature with slightly preferred texture along the <100> orientation for the as-built sample as per the inverse pole figure for as-built samples. However, the slightly preferred texture along the <100> direction gets weaker with heat–treatment and thus, the orientation of grains becomes random in the heat-treated samples. Further, recrystallization of grains is visible in the heat-treated samples, with twin boundary formation as seen in Figure 7.13(c). This confirms the static recrystallization of

LDED built Hast-X after heat-treatment. During LDED, due to repetitive heating and cooling cycles, residual stresses and dislocations are generated in the material. These residual stresses and dislocations act as driving force for the recrystallization of grains and annealing twins[102]. In addition, the average grain size increased with heat-treatment due to the grain growth after recrystallization occurring during heat-treatment. The average grain size is 23 μm and 44 μm in the as-built and heat-treated samples, respectively. Further, it can be seen from Figure 7.13(d) that the proportion of low angle boundaries shows a reducing trend and proportion of high angle boundaries shows an increasing trend with heat-treatment due to the recrystallization and grain growth occurring during heat-treatment.

Figure 7.14 presents the elemental mapping carried out on the heat-treated samples. As discussed in chapter 6, the presence of Mo, Si and C segregation is observed along with the formation of Mo-rich carbides in the as-built samples. However, heat-treated samples show a significant reduction in segregation, with the presence of fewer carbon segregations at isolated locations. During solution treatment, all the elements are brought to the matrix and the fast-cooling rate during the quenching does not allow any precipitates to grow at a lower temperature. In addition, the Mo-based carbides are not observed in heat-treated samples. This is primarily due to the fast-cooling rate during quenching providing insufficient period for the carbide precipitation/growth.

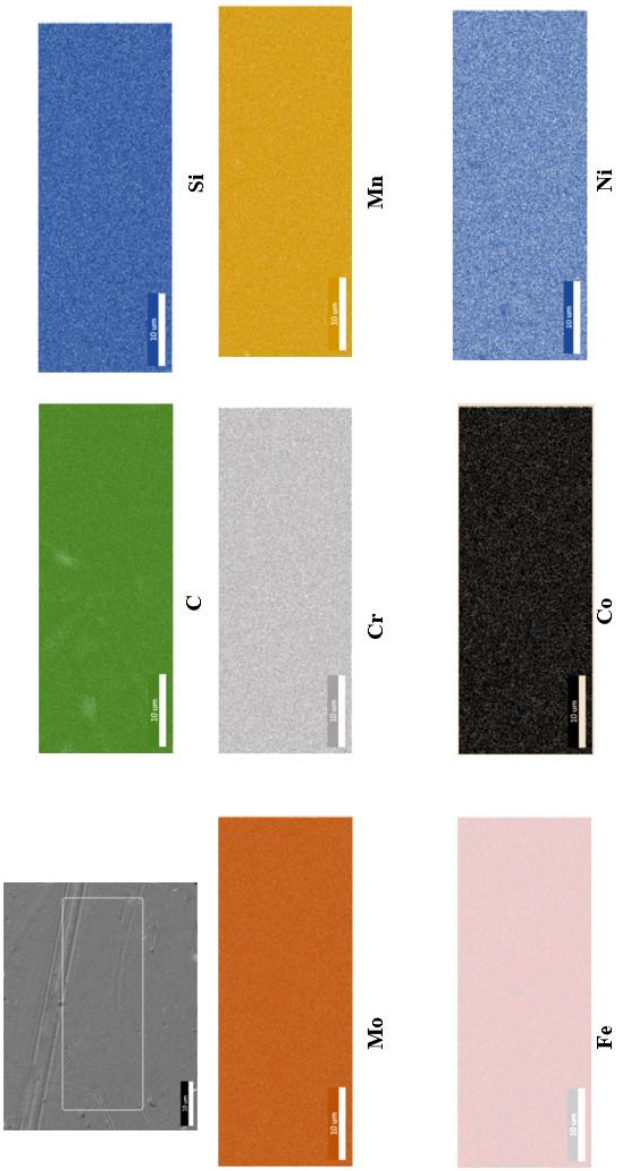

Figure 7.14: Elemental mapping of LDED built Hast-X in heat-treated condition

XRD studies of as-built and heat-treated Hast-X is performed from 30° to 80° and XRD pattern is presented in Figure 7.15a. It can be seen that the similar to the XRD pattern of the as-built sample, same peaks indexed to (111), (200), (220) planes, respectively revealing the presence of Ni γ-matrix are observed in heat-treated samples. However, a reduction in the peak width is seen in heat-treated samples. The reduction in peak width may be primarily due to the increase in the crystallite size of the material. It can be seen in figure 7.15b that the peaks of heat-treated samples shifted towards the right as compared to the as-built sample. A shift of 0.09°, 0.08°

and 0.1° towards the right is observed for the (111), (220) and (200) plane, respectively. This shows the variation in the lattice spacing of the material according to Braggs law (refer to equation 7.1). The increase in 2θ infers a reduction in the distance between nearby lattice planes (d), which reveals a reduction in the tensile stress on the surface of the heat-treated sample[181].

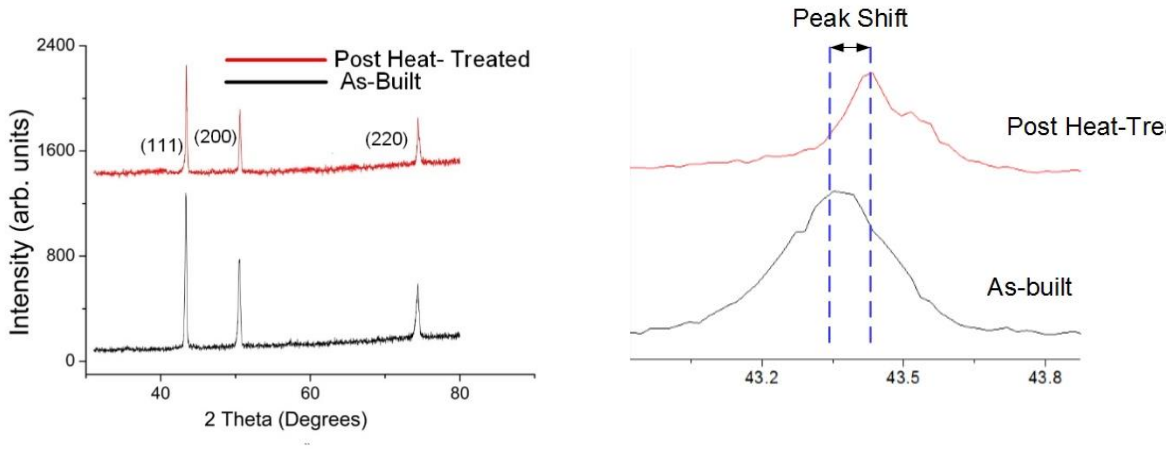

(a) (b)

Figure 7.15: XRD pattern presenting a) As-built and heat-treated Hast-X b) diffraction peak positions of (111) crystal plane after heat treatment

7.3.4 Micro-hardness

Microhardness of as-built and heat-treated samples are measured using Vickers microhardness tester. Table 7.3 presents the comparison of micro-hardness of as-built and heat-treated samples. It is observed that an average microhardness of 239 $HV_{1.96N}$ is obtained for the as-built samples. This is primarily due to finer dendritic microstructure generated in the as-built Hast-X deposits at higher cooling rate. The microhardness measurements on heat-treated samples present the reduction of ~13%in its value with an average micro-hardness of 208 $HV_{1.96N}$. This is primarily due to homogenization of microstructure and coarsening of grains during heat-treatment. This confirms Hall-petch criteria that the material hardness is inversely

related to the grain size of the material[175]. Further, the standard deviation of 6.45 and 2.07 is observed for the as-built and heat-treated samples, respectively. The reduction in standard deviation also indicates microstructure homogenization after heat treatment. The micro-hardness of conventional Hast-X is approximately 180 HV[37], which is lower than that of as-built samples. The heat-treatment of Hast-X reduced the microhardness and it is comparable with that of conventionally built samples.

Table 7.3: Microhardness of Hast-X samples under as-built, heat-treated and conventionally built conditions

Condition	Value
As-built	$239 \pm 6.45\ HV_{1.96N}$
Heat-treated	$208 \pm 2.07\ HV_{1.96N}$
Conventional [37]	180 HV

7.3.5 Single-Cycle Ball Indentation Testing

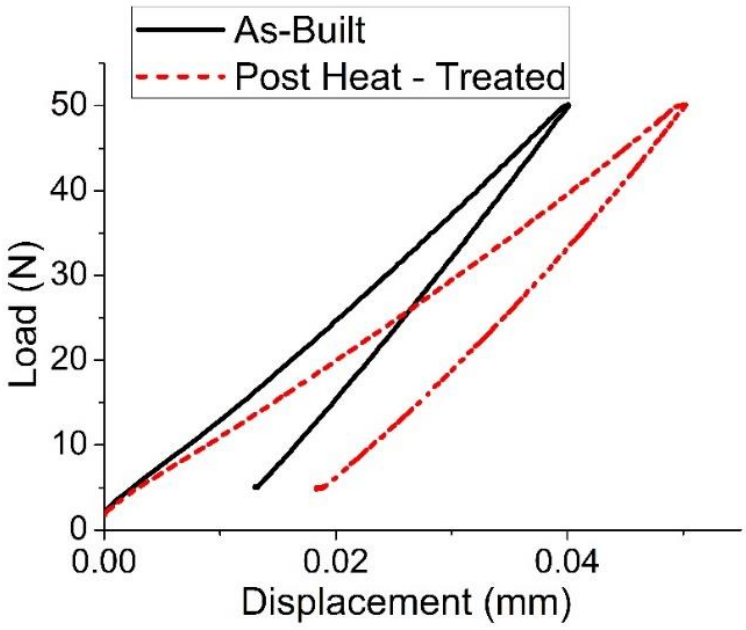

Figure 7.16: SCBI on as-built and heat-treated Hast-X

Single-cycle ball indentation testing (SCBI) is used for comparing the energy storage ability of the material. SCBI is carried out at a maximum cycle load of 50 N with a loading rate of 0.1

mm/min and unloading until 2 N load. Figure 7.16 presents the typical load-displacement curve obtained during the SCBI of LDED samples. The area under the loading and unloading curve represents the entire work performed during loading and the reversible elastic contribution of the total work, respectively. The difference between the two areas provides the energy absorbed in plastic deformation, which can be related to the energy stored by the material. The area under the curves of as-built is 0.29 N-mm, while the area under the curve for the heat-treated sample is 0.45 N-mm. SCBI studies reveal improvement in energy storage capacity by 1.55 to that of as-built.

7.3.6 Tensile Behaviour at Room and Elevated Temperatures

Figures 7.17(a) and 7.17(b) present the load-displacement curves obtained for LDED built Hast-X in the as-built and heat-treated condition at different test temperatures. It can be observed that for the same displacement, the applied load decreases with an increase in the test temperature. Further, it can also be seen that the load required for a given displacement decreases with heat-treatment. In other words, the as-built sample reveals higher resistance to plastic deformation as compared to the heat-treated sample. This can be primarily due to a reduction in the dislocation density and an increase in grain size after heat-treatment. In addition, the migration of the grain boundaries is pinned by the Mo-rich carbides, which increases the strength of the as-built samples as compared to heat-treated samples[186]. Similarly, the resistance to plastic deformation decreases with an increase in the test temperature. A reduction of 33 % and 24 % in the maximum load is observed when the temperature is increased from 300 K to 873 K in as-built and heat-treated conditions, respectively. Thus, it can be inferred that the formation of recrystallized and coarsened grains after heat-treatment helped in retaining the high-temperature properties of the material. In addition, the load-displacement slope reduced from 6 kN/mm to 3.8 kN/mm for as-built LDED

sample, while it reduced from 5.1 kN/mm to 3.4 kN/mm for heat-treated samples with an increase in the test temperature from 300 K to 873 K. This behaviour is mainly due to the easy dislocation movement due to reduced plastic deformation resistance, as the test temperature increases.

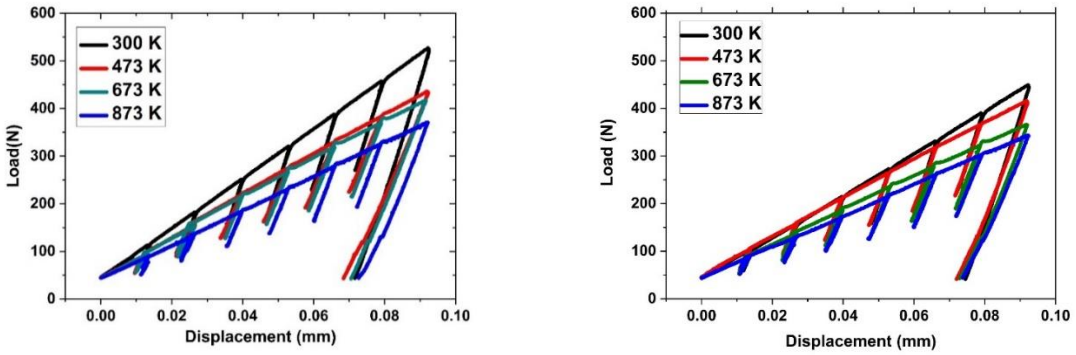

(a) (b)

Figure 7.17: Load-displacement plot showing the effect of test temperature for (a) as-built sample (b) heat-treated sample

The flow curves obtained for LDED built Hast-X estimated at various temperatures are presented in Figures 7.18(a) and 7.18(b) for as-built and heat-treated conditions, respectively. As expected, the true stress values reduce with an increase in the test temperature and with heat-treatment for the same true plastic strain. It can be observed that the yield strength and ultimate strength decreases with an increase in test temperature (refer Figure 7.19(c)), due to the reduced hindrance for dislocation motion at elevated temperatures. Moreover, higher strength in the as-built condition can be due to the rapid cooling rate in LDED process, which can lead to increase in yield strength from solid solution strengthening and/or from fine microstructural features that are altered after heat-treatment. As mentioned earlier, the reduction in dislocation density with an increase in the test temperature and with heat-treatment also governs the variation in mechanical properties. It can also be seen in Figure 7.18(c) that the yield strength of LDED Hast-X in the as-built condition is higher than the conventional

samples [37] at all conditions, while the value of yield strength of LDED built Hast-X is similar to conventional sample after heat-treatment. The ultimate strength of the conventional sample is found to be slightly higher than as-built and heat-treated samples at room temperature can be due to a better solid solution strengthening in the conventional sample.

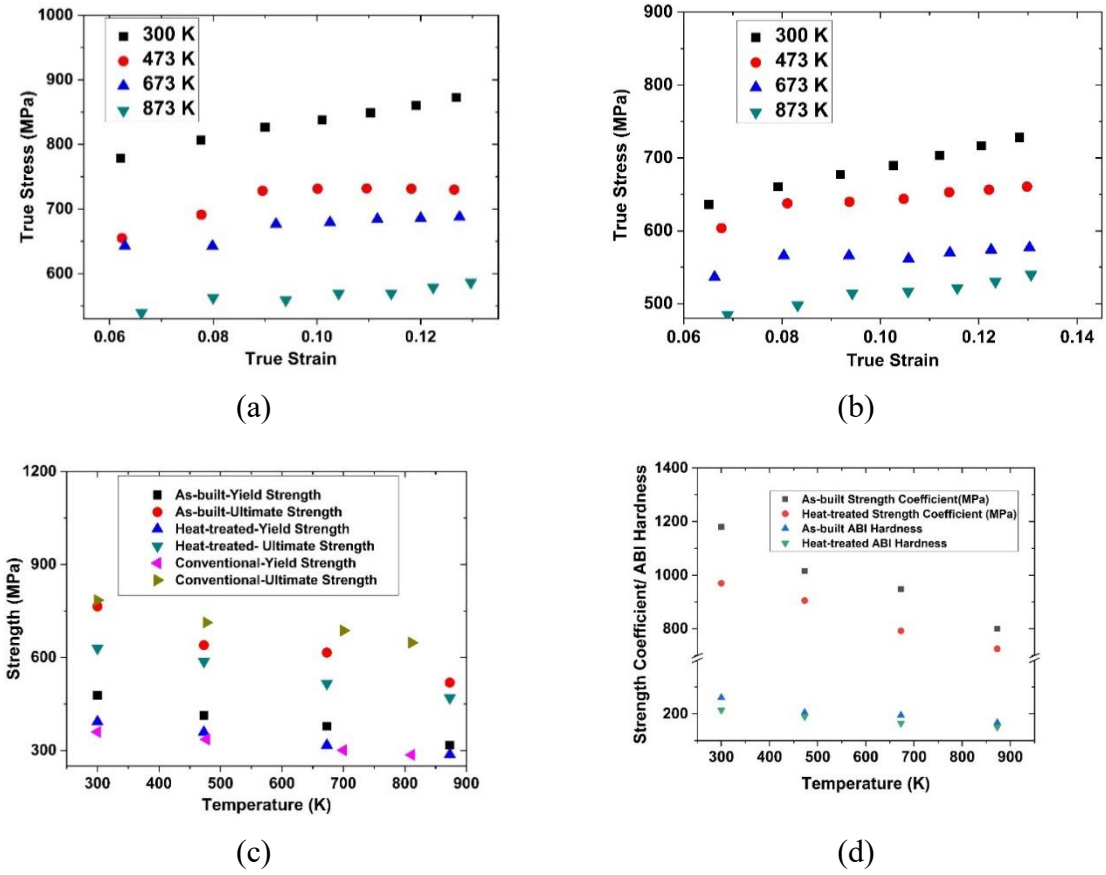

Figure 7.18: ABI results at different test temperatures (a) True-stress vs True plastic strain of as-built sample (b) True-stress vs True-strain of the heat-treated sample (c) Yield strength and ultimate strength of as-built, heat-treated and conventional sample (d) Strength coefficient and ABI hardness

The strength coefficient (K) and strain hardening exponent (n) are derived from the plot between the true stress and plastic strain. It is observed that the strength coefficient shows a decreasing trend with an increase in the test temperature as presented in Figure 7.18(d), similar to the trend followed by yield strength and ultimate strength. This is mainly due to the reduction in dislocation density in the material at a higher temperature. ABI hardness also shows the

similar trend and a reduction by 36% and 26% is observed for as-built and heat-treated samples, respectively for temperature change from 300 K to 873 K. This also shows that the coarse recrystallized grains in the heat-treated samples helped in retaining the high-temperature properties of LDED built Hast-X. It is observed that the strain hardening exponent shows a small increasing trend with an increase in test temperature for as-built samples. Strain hardening exponent increased from 0.13 to 0.15 for as-built samples and 0.14 to 0.15 for heat-treated samples, when the test temperature is increased up to 873 K.

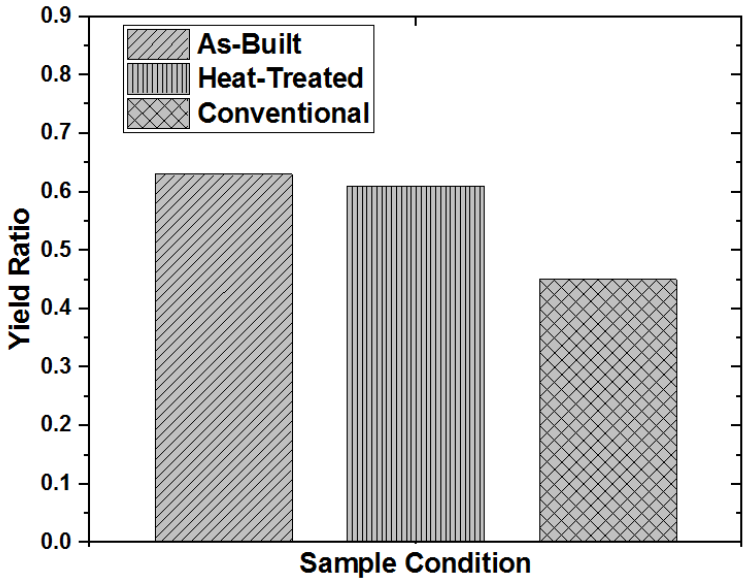

Figure 7.19: Comparison of yield ratio of LDED built Hast-X in different conditions

The average value of room temperature yield ratio at the three different conditions are compared and it is seen in Figure 7.19 that the yield ratio is lowest for conventional samples [37] followed by heat-treated and as-built samples. It shows that the ductility is highest for conventional samples followed by heat-treated and as-built samples.

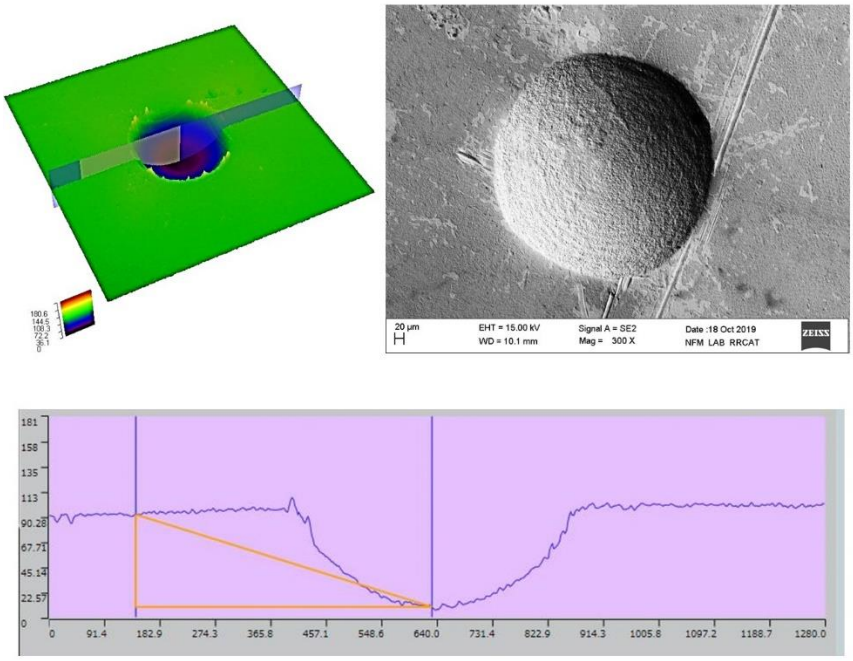

(a)

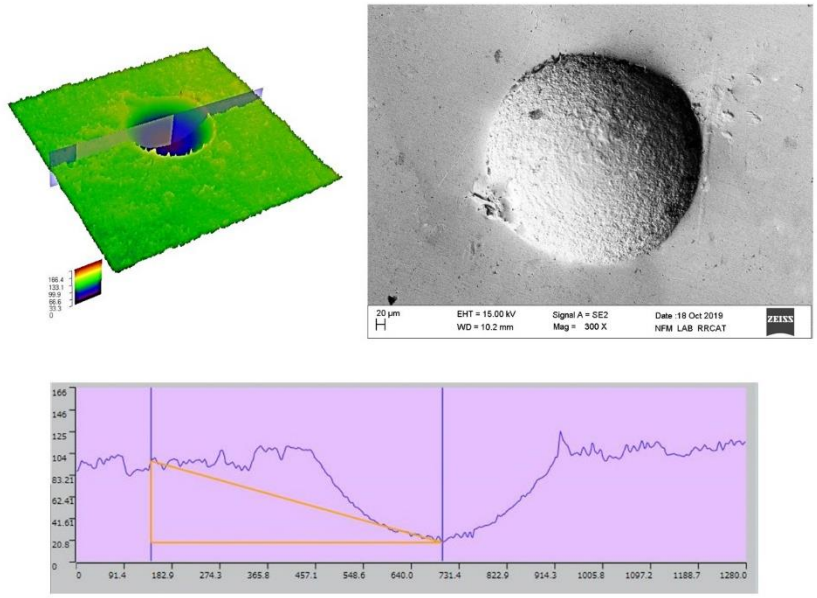

(b)

Figure 7.20: ABI indentation at 473 K (a) as-built sample (b) heat-treated sample

The indentation profile is analysed using a laser confocal microscope and SEM. Figure 7.20a and 7.20b present the indentation profile of as-built sample tested at 473 K and heat-treated sample tested at 473 K, respectively. No crack formation is observed around the indentation region for any of the samples. Material pile-up is seen around the indentation area and it is observed that the pile-up increases with heat-treatment. A slight increase in the indentation diameter is observed with heat-treatment indicating lower resistance to deformation. The measured indentation diameter for the as-built and heat-treated sample tested at 473 K is 490 μm and 510 μm, respectively. These observations indicate that heat-treatment reduces the strength values of the material, which leads to an increase in indentation diameter and pileup with heat-treatment. These findings are in agreement with the ABI test results.

7.4 Summary

SLLR during LDED of each layer is deployed to overcome the bulk and surface-related issues observed in LDED built samples. A significant reduction in porosity, 71.5% reduction in surface roughness, reduction in grain size and reduction in dendrite size is observed in SLLR samples as compared to LDED samples. EBSD and XRD analysis show preferential growth along (100) direction in LDED samples, which is eradicated in SLLR samples. XRD studies show that there is no phase change after SLLR. Mo, Si and C segregations and the presence of Mo rich carbides are present in LDED and SLLR samples. It is also seen that the segregation slightly decreases after SLLR due to higher cooling rate. An increase in the microhardness by 12% and yield strength by 7 % along the build direction is observed in SLLR samples as compared to samples without SLLR. A slight increase in yield ratio is observed after SLLR indicating a reduction in the ductility. It can be concluded that SLLR significantly reduces porosity and surface roughness, while the effect of SLLR on the mechanical properties is not highly predominant.

In the present chapter, investigations are carried out on the microstructural and mechanical

properties of LDED built Hast-X bulk structures in heat-treated conditions and compared with as-built samples. The microstructure of heat-treated samples shows recrystallized and coarsened equiaxed grains with an average grain size of ~44 μm and a lower fraction of low angle boundaries microstructure as opposed to cellular-dendritic growth for as-built samples with an average grain size of ~23 μm and a higher fraction of low angle boundaries. The heat-treated samples revealed random grain orientation as opposed to as-built samples with slightly preferred texture along the <100> plane. Also, the elemental segregation of Mo, Si and C and precipitation of Mo-rich carbides are not seen in the heat-treated samples. ABI test results showed that the yield strength of the heat-treated sample is similar to the yield strength of conventional Hast-X and lower than as-built samples at all test temperatures. Yield strength, ultimate strength, strength coefficient and ABI hardness reduced with an increase in temperature, while strain hardening exponent and uniform ductility showed an opposite trend for both as-built and heat-treated samples. The microstructure of the as-built and heat-treated samples did not reveal any significant change after ABI testing at 873 K. The effect of test temperature and heat-treatment on the indentation geometry is analysed and it is observed that pile-up and width of indentation increases with an increase in test-temperature and with heat-treatment.

Chapter 8 : Process methodology for LDED of Printed Circuit Heat Exchanger using wall and bulk structures

8.1 Introduction

In the previous chapters, various studies are carried out on wall structures and bulk structures from parametric investigations to effect of treatments (in-situ and ex-situ) on the geometry, microstructural and mechanical properties. In the present chapter, Laser Directed Energy Deposition (LDED) methodology is developed for building channels and Printed Circuit Heat Exchanger (PCHE). The name PCHE is derived from the technique generally deployed for manufacturing the plates that form the principal component of the heat exchanger. Generally, the channels are produced using chemical milling, a method analogous to that employed to develop printed circuit boards in the electronics industry[201].

In this work, PCHE is built using a combination of straight walls, overhang walls and bulk structures using the know-how developed from the comprehensive studies as presented in Figure 8.1. The 3-axis configuration is used to provide a generalized methodology for building the component and to avoid complexity in the LDED programming. The chapter also includes the LDED of overhang walls and studies on the process methodology for building proof of concept and prototype component.

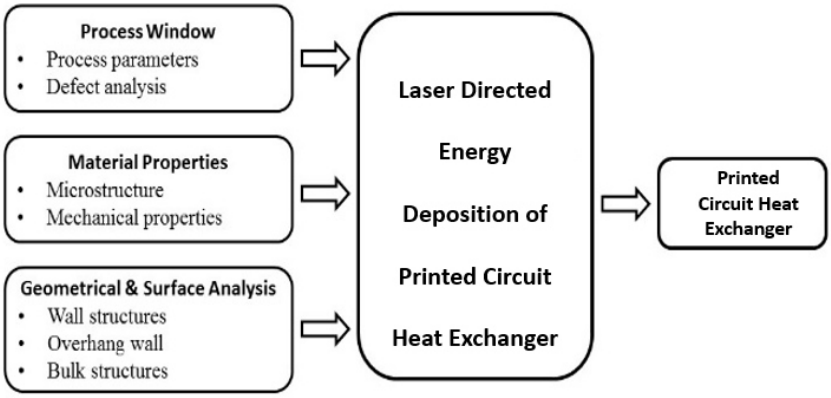

Figure 8.1: Workflow leading to the development of PCHE

8.2 Need for LDED Strategy

An intermediate heat exchanger is one of the key components of the power generation system to effectively and reliably transfer heat from the primary cycle (solar, nuclear, steam) to the power generation cycle. The elevated temperature and pressure at which they operate limit the use of joining techniques, like – brazing. The conventional shell and tube heat exchangers are not ideal for the above application due to the space constraints and low compactness (heat transfer area available per unit volume) of the heat exchanger. Printed Circuit Heat Exchanger (PCHE) is ideal as an intermediate heat exchanger mainly due to large compactness values. Printed Circuit Heat Exchangers (PCHE) is one of the commonly used compact heat exchangers with high compactness. They are generally fabricated using a two-stage process called: photochemical etching and diffusion bonding. In the first stage, channels are etched out on plates using photochemical etching. This is followed by diffusion bonding (a solid-state bonding technique) to join the plate together[30,202]. Figure 8.2 presents the typical diagram of a PCHE. The inherent advantages of PCHE over brazed heat exchangers make it an ideal choice for high-temperature power sector due to lack of welded joints or weakening spots. The major limitations associated with the above fabrication technique are the slow nature of the process due to the slow etching rate, non-green nature of the process as it involves material removal by acid etching from the plate, multiple-stage processing for developing a single unit

of PCHE and channel geometry limitations. In general, more stages of operation lead to more probability of failure. Hence, the use of LDED for fabricating PCHE is ideal due to the following:

- LDED is relatively fast as compared to photochemical etching,
- As the process does not involve material removal using acids, LDED is a greener route for manufacturing PCHE
- A single unit of PCHE can be fabricated using a single-step manufacturing process.
- LDED offers high design and material freedom

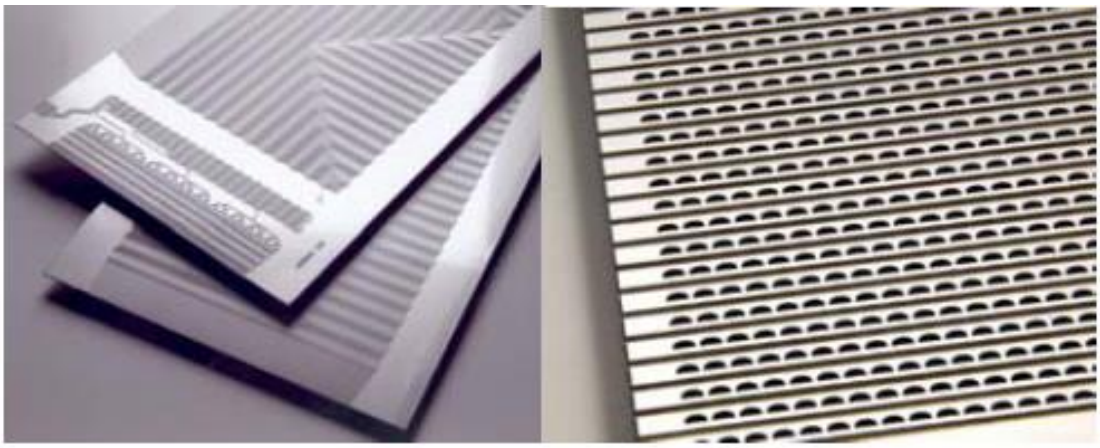

Figure 8.2: Etched channels and diffusion bonded structure of PCHE [202]

8.3 Overhang Wall Strategy

The major challenge in deploying LDED for fabricating CHE is the difficulty in fabricating completely overhang parts using a 3 axis configuration. It can be seen in Figure 8.2 that it is difficult to fabricate complete overhang parts using LDED without support structures. The structure tends to collapse, while depositing a solid layer on top of the wall structures as labelled in Figure 8.3. Thus, an alternate method is developed by using overhang walls as presented in Figure 8.3b. Figure 8.3c presents the methodology deployed for fabricating PCHE channels by combining overhang walls with straight walls and bulk deposits for fabricating

PCHE. Laser spot centre is shifted by a fraction of the track width after each layer to fabricate overhang walls. The overlap percentage between each layer in the overhang wall is a function of the design of PCHE and channel dimensions. Figure 8.4 presents the typical overhang wall deposited using LDED.

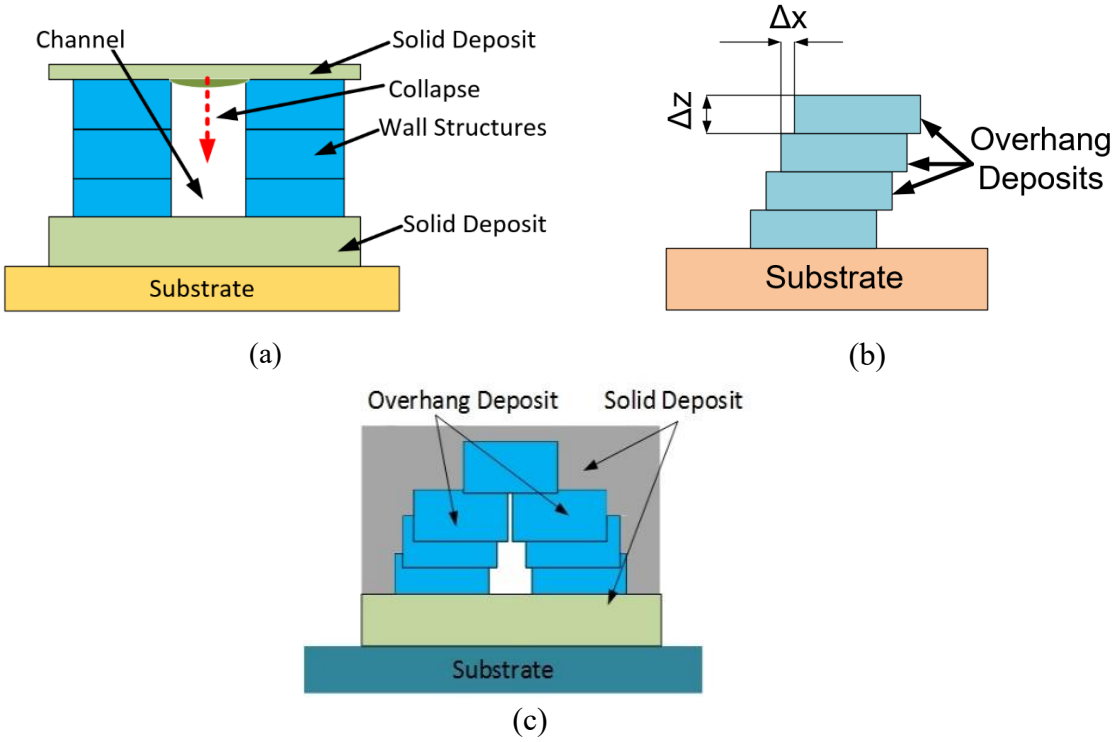

Figure 8.3: LDED Strategy a) Failure during complete overhang b) Strategy to fabricate overhang walls c) Overhang walls for successful fabrication of PCHE

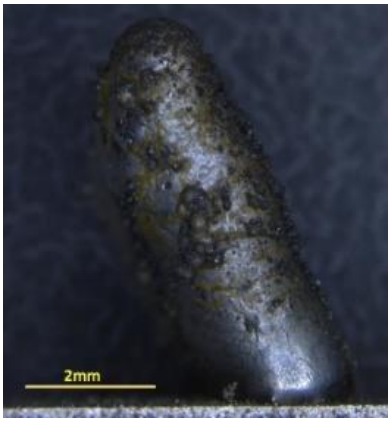

Figure 8.4: Typical Overhang wall built using LDED

Δx and Δz shift is provided by shifting the nozzle by a fraction of the measured track width and track height values, respectively as shown in Table 8.1. The observed track width and track height are 1.85 mm and 0.42 mm, respectively. It is observed that for all other process parameters remaining constant, the maximum value of lateral shift (Δx) that can be deployed for fabricating overhang walls without failure is 15%. When the value of Δx is above 15%, the wall collapsed after the initial few layers. This is primarily due to the domination of gravitational force over the surface and viscous forces in the overhang portion of the wall. The gravitational force of the unsupported molten mass acts downwards, while the viscous and surface forces hold the molten mass from spreading by opposing the gravitational force. After a particular overhang percentage, the gravitational force of the unsupported mass exceeds the surface and viscous forces, which leads to the collapse of the wall.

Table 8.1: Control factors and corresponding observations

Experiment No.	Δx (%)	Δz (%)	Measured Angle (degrees)	Maximum Width Variation (mm)
1	10	100	67.07	0.13
2	10	85	64.66	0.17
3	10	70	63.96	0.18
4	12.5	100	62.21	0.14
5	12.5	85	59.27	0.19
6	12.5	70	57.81	0.20
7	15	100	55.15	0.39
8	15	85	53.64	0.66
9	15	70	51.48	0.75

In order to investigate the angle and width variation of overhang deposition at constant processing parameters, a series of overhangs with different desired inclined angles are deposited using unidirectional deposition strategy by controlling Δx and vertical shift (Δz). The range of desired inclination angles of overhangs (θ_d) is 66° to 46° with the horizontal plane. Table 8.1 presents the control factors and experimentally obtained angle and width variation along the length of the wall. It can be seen that in the present study the minimum angle made by the wall with the horizontal is 51° at the desired angle of 46°.

The effects of Δx on angle and uniformity of overhang wall deposition are investigated at different Δz. It can be observed from Table 8.1 that overhangs are made at three levels of Δx. The angle made by the wall with the horizontal plane decreases with an increased value of Δx for the same Δz. This is in accordance with equation 8.1, which reveals that a reduction in Δx can reduce the angle made by the wall with horizontal. Dimensional inspection of the overhang walls revealed non-uniformity on the walls along the length with an increase in Δx. It is also revealed from Table 8.1 that the width variation along the length of the wall increased significantly as Δx is increased, which presents the increased non-uniformity of the walls. This may be due to lack of balance between surface tension forces, viscous forces and gravitational forces during the deposition of overhang structures. It can also be seen from Table 8.1 that the effect of Δx on the width variation is more profound as compared to the effect of Δz.

$$\tan\theta = \frac{\Delta z}{\Delta x} \tag{8.1}$$

The effects of Δz on angle accuracy and uniformity of overhang deposition are investigated at different Δx. The overhangs were fabricated with three different Δz and Table 8.1 presents the variation of angle with different Δz. It can be observed that the angle made by the walls reduces as Δz decreases. Dimensional inspection of the overhang walls revealed significant non-uniformity of the walls along the length with the reduction in Δz as compared to change in Δx.

It is also revealed from Table 8.1 that the width variation increased significantly as Δz is reduced, which presents the increased non-uniformity of the walls. This can be due to relatively higher laser energy density resulting in larger distortion in width.

The overhang angle observed using optical microscopy is compared with the calculated angle as presented in Figure 8.5. It is seen that the deviation from the calculated angle during the deposition increases with a reduction in the value of Δz. The maximum deviation observed in the present study is 11.5%. Reduction in Δz reduces the defocussing distance during deposition. When the defocusing height decreases, the deposition height increases due to more concentration of powder, which results in enhanced powder utilization and this resulted in large variation between calculated angle and the observed angle at a lower value of Δz.

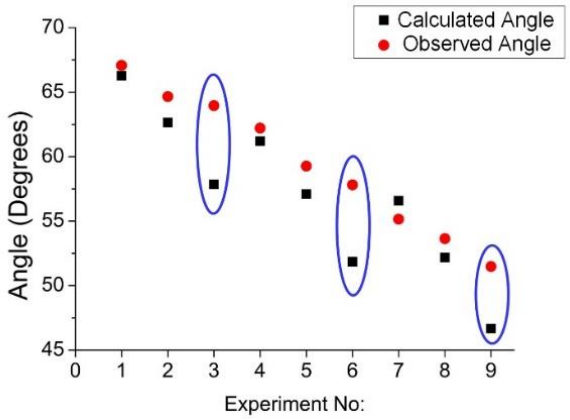

Figure 8.5: Deviation between the calculated and observed inclination angle

8.4 LDED of Channels

LDED is used to build channels at different combinations of process parameters. Figure 8.6 presents the macroscopic images of the channels built using inclined walls. The shift in x-direction and z-direction is kept constant during the study. The beam diameter in the range of 1 -1.25 mm is used for the present study to build finer features using LDED. However, LEPF values are kept within the range developed in chapter 4. Figure 8.6a and 8.6b presents the effect of powder feed rate at constant laser power (500 W), scan speed (0.6 m/min) and the number

of layers. Figure 8.6a and 8.6b presents the channel built using a powder feed rate of 2.5 g/min and 3 g/min, respectively. It can be seen that the channel presented in figure 8.6a collapsed due to insufficient height in the deposition, while at higher feed rate, the channel is found to be close from the top and open at the ends. The presence of partially melted powders is seen inside the channels, which can be removed using post-processing. Figure 8.6c presents the channels built at a laser power of 600 W, scan speed of 0.6 m/min and powder feed rate of 3 g/min. It is observed that the channel height is increased with an increase in laser power due to an increase in the powder catchment efficiency. The channels are observed to be defect-free and open from both the ends. Figure 8.6d and 8.6e present the channels built at different values of the gap between the channels. It can be seen that as the gap between the channels reduced from 2.5 mm to 1.5 mm, the quality of channels reduced and channels are observed to be closed from both the ends.

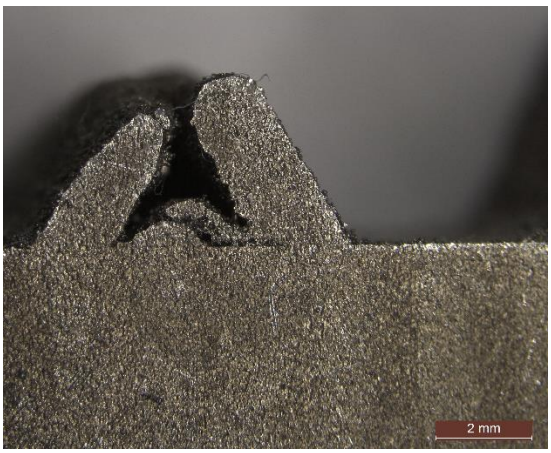

(a)

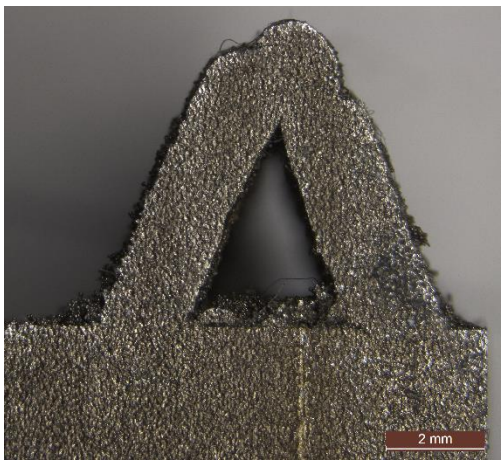

(b)

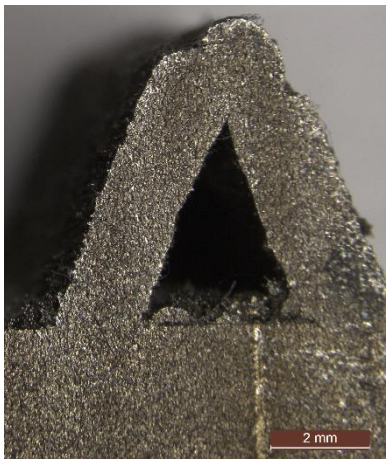

(c)

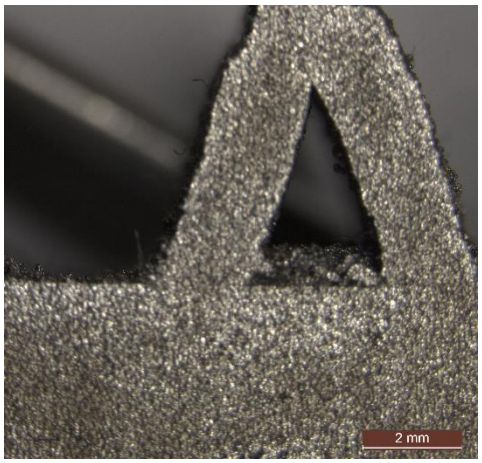

(d)

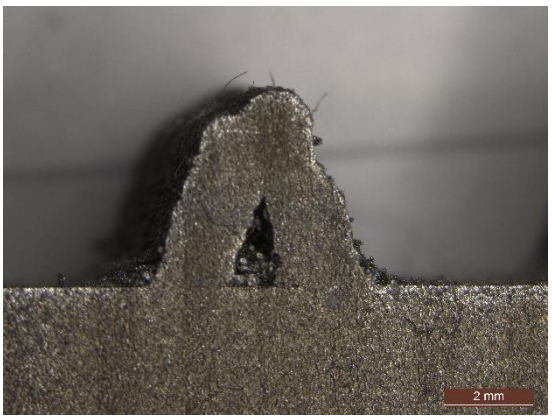

(e)

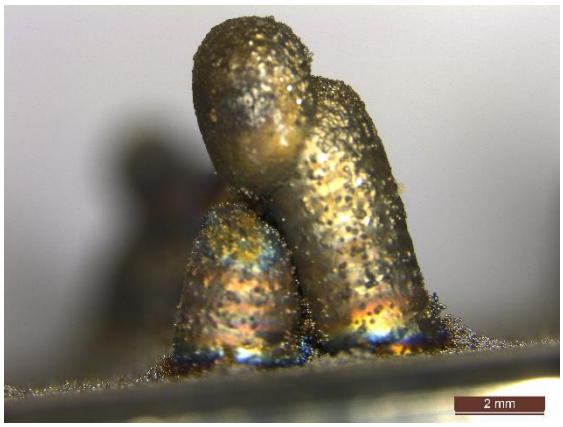

(f)

Figure 8.6: LDED built channels at different process conditions and parameters

Figure 8.7 presents the channels built using a combination of straight walls and inclined walls. The channels are built by varying the overlap percentage and it is observed that the channels built with the overlap of 85% between the tracks provide channels with partially melted powders inside the channels. As the percentage of overlap between the tracks are increased to 90%, a reduction in the amount of partially melted powders inside the channel is observed as shown in Figure 8.7b.

8.5 LDED Methodology for PCHE Fabrication

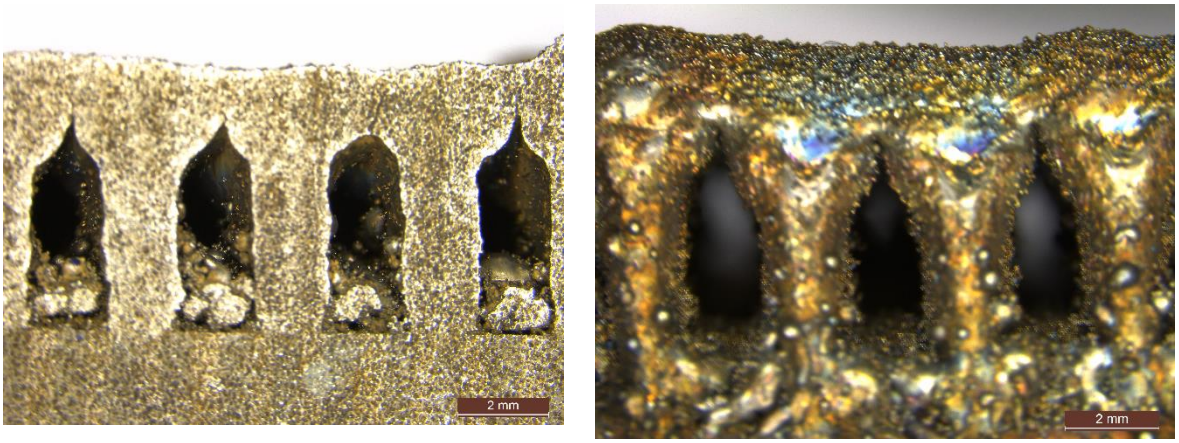

(a) (b)

Figure 8.7: LDED fabricated channels (a) 85% overlap (b) 90% overlap

Subsequent to the above analysis, the proof of concept of PCHE is developed. Figure 8.8a and 8.8b presents the proof of concept of PCHE built using LDED. The PCHE was analysed using microscopy and it was observed that the channels are open from both the ends.

(a) (b)

Figure 8.8: Proof of concept of LDED built PCHE

Subsequently, a cross-flow prototype PCHE of size 200 mm × 200 mm × 170 mm is developed using LDED for methodology validation. The strategy used for building the PCHE is presented in figure 8.9a. It involves the followings:

a) Building of uniform straight walls

b) Building of overhang walls on top of straight walls by providing x shift

c) Bulk deposition

To build a single unit of the channel, i.e. channels in the y-direction, the straight walls are built in the y-direction, followed by double overhang wall deposition (2 sided overhang) to build the channels in the y-direction by providing a shift in the x-direction (refer Figure 8.9a). Subsequently, bulk deposition is carried out to bring uniform layer deposition. The same procedure is repeated in the x-direction to build the x-direction unit. The units are built one over the other following YXYXYX fashion. Figure 8.9b presents the CNC program developed for the overhang wall geometry and 8.9c presents the simulation of the program. Subsequently, the PCHE is built and the different stages of PCHE fabrication are presented in figure 8.9d and 8.9e. Figure 8.9f presents the photographic view of 200 mm × 200 mm × 170 mm PCHE built using LDED.

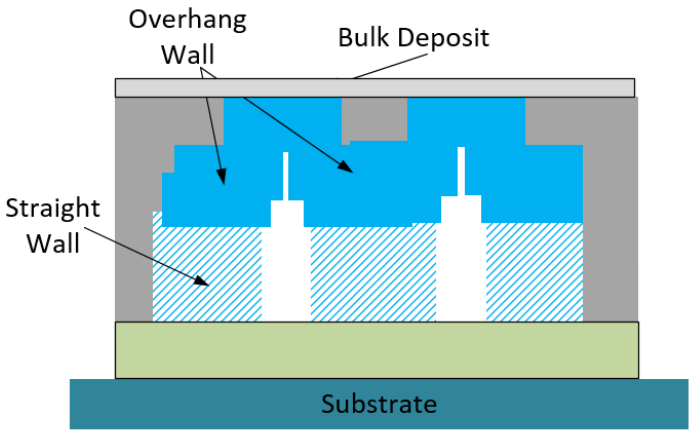

(a)

```
N1 R1 =3.4; WIDTH of the channel
N2 R4 =10; No of the layer of wall
N3 R5 = 0.10; Overlap
N4 R6 = 0.1; track height
N5 R8 =150; length of channel
N6 R9 =6; no of channel
N7 R10=11;No of layers for channel WALL
N8 R15 = 0;X  value
N9 R16 =0; Y value
N10 R17 = 200; z value
N11 R18 = 1000; feed rate
N12 G90 G01 G54 X=R15 Y=R16 Z=R17 F=2*R18
N13 M53
N14 M57 G04 F5
N29 R16=0
N30 R53=0
N31 While (R53<R10)
N32 R16=0
N33 R52=0
N34 While (R52<(R9+1))
N35 G90 G01 G54 Y=R16+(R5*(R53+1)) X=R15 Z=R17-(R6*((R53+1))) F=2*R18
N36 M71
N37 G91 G01 X=-R8 F=R18
N38 M72
N39 G90 G01 G54 Y=R16-(R5*(R53+1)) X=R15 Z=R17-(R6*((R53+1))) F=2*R18
N40 M71
N41 G91 G01 X=-R8 F=R18
N42 M72
N43 R52=R52+1
N44 R16=R16-R1
N45 ENDWHILE
N46 R53=R53+1
N47 ENDWHILE
N48 R16=0
N49 G90 G01 G54 X=R15 Y=R16 F=2*R18
N50 R54=0
N51 While (R54<(R9+1))
N52 M71
N53 G91 G01 X=-R8 F=667
N54 M72
N55 G91 G01 X=R8 Y=-R1 F=2*R18
N56 R54= R54+1
N57 ENDWHILE
N48 M30
```

(b)

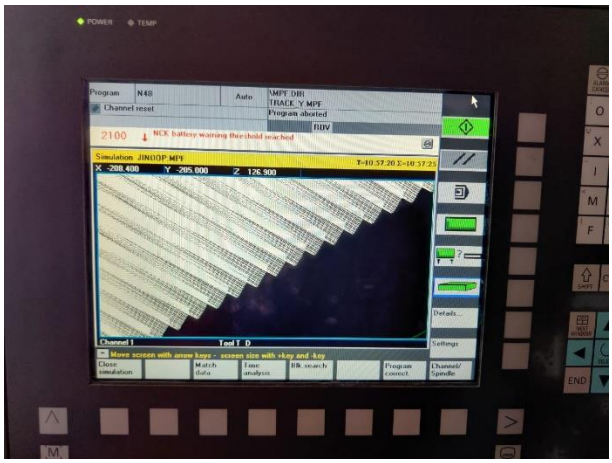

(c)

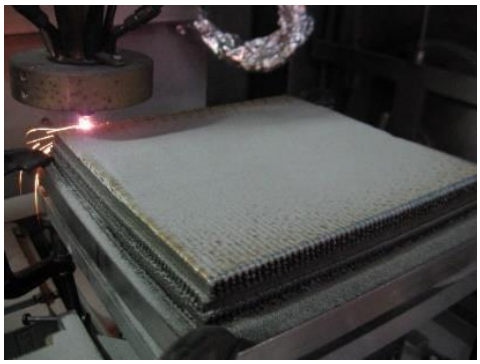

(d)

(e)

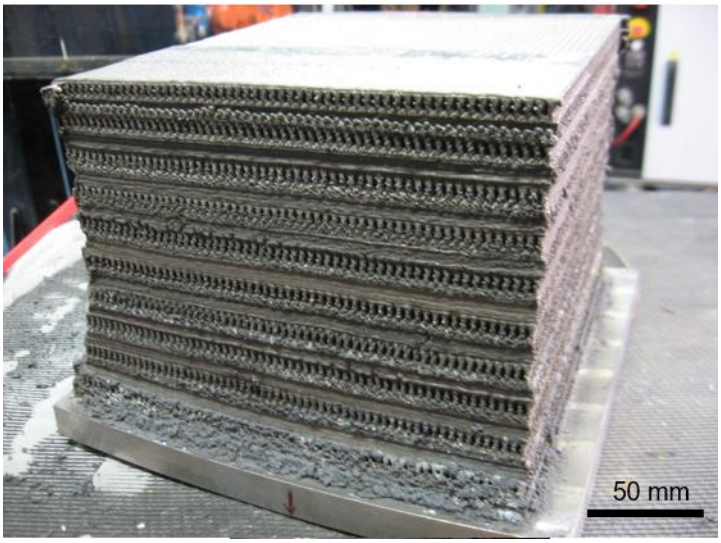

(f)

Figure 8.9: LDED built PCHE (b) G & M Code for overhang wall (c) Simulation of G & M code for PCHE fabrication (d) LDED of PCHE in progress (e) closer view of the channels (f) Prototype PCHE

8.6 Summary

This chapter presented LDED methodologies adopted for building overhang walls, channels and PCHE. While building the overhang walls using LDED, it was observed that the maximum Δx possible for fabricating overhang structures without failure or external support is 15 % of the track width. Overhang walls making a minimum overhang angle of 51^{o} with the horizontal plane is obtained at 15 % Δx and 70 % Δz. Further, the study is extended to the LDED of channels by varying the process parameters. Further, fabrication of a PCHE prototype is carried out and the feasibility of PCHE fabrication using LDED is substantiated. The channels in the

PCHE are observed to be open from both the ends. Thus, LDED can be considered as a green technology for fabricating PCHE with minimal material wastage and complex shaped channel geometry for various applications.

Chapter 9 : Conclusions and Future Scope

9.1 Conclusions

The present research work comprehends and contributes to the existing understanding on the Laser Directed Energy Deposition (LDED) of Hast-X structures from single tracks to multiple overlapped and multi-layer tracks under different process conditions yielding thin walls and bulk structures in terms of processing, geometry, microstructural and mechanical characteristics. It provides insights on to the effect of in-situ treatments and ex-situ post-processing on the behaviour of LDED built Hast-X components. The work also contributes to the development of process methodology for building Printed Circuit Heat Exchangers (PCHEs) using LDED. On the basis of the research work, the followings are the conclusions:

a) The geometry of LDED built single tracks show that the track width and track height increase with an increase in laser power and powder feed rate, while the same effect in track width and track height is observed with the reduction in scan speed. Laser power is found to be dominant process parameter for track width, while powder feed rate is the significant process parameter for controlling track height. The developed analytical modelling confirms the parametric dependence of track width and track height.
b) The identified processing window indicates that an optimum value of Laser Energy per unit Powder Feed (LEPF) is mandatory for defect free deposition of Hast-X. For higher values of LEPF, cracks are observed primarily due to combination of higher thermal stresses and elemental segregations. For lower values of LEPF, the deposits are found to be discontinuous primarily due to unavailability of sufficient laser energy. The optimum value of LEPF for Hast-X is identified in the range of 8.2 - 13.2 kJ/g for continuous and crack free deposition. Within the process window, the area fraction density of continuous tracks

is found to be > 99.5% and the porosity increases with a reduction in LEPF and increase in scan speed. The process parameter combination yielding higher area fraction density and build rate are deployed for overlapped multi-track deposition.Defect-free deposition in the micro scale with fine cellular and dendritic grain structure is achieved.

c) One of the exciting applications of LDED is the development of wall structures and the properties of the wall structures can be tailored by varying the thermal conditions, which can be achieved by depositing at different process parameters or providing interlayer delay between layers using idle time period. The effect of LEPF on the geometry of the wall structures shows that the variation in wall height increases with an increase in LEPF, while the variation in wall width decreases with an increase in LEPF. It is also observed that the average wall height decreases and average wall width increases with an increase in LEPF due to increase in the outward flow of melt pool. The microstructural studies show that grain structure is a mix of cellular and dendritic growth within the range of LEPF used for the study. The size of cellular/dendritic growth increases slightly with an increase in LEPF due to reduction in the cooling rate. Investigations on the mechanical properties illustrates that the micro-hardness, yield strength and ultimate strength decreases slightly with an increase in LEPF, with higher values of yield strength and micro-hardness as compared to conventional wrought sample. Numerical simulation aids to elucidate the above results and show that the preheat temperature on the previously built layer increases with an increase in LEPF.

d) In case of walls built with different interlayer delay, it is observed that the average wall height increases and average wall width decreases with an increase in the interlayer delay period due to reduction in the outward flow of melt pool. The cellular and dendritic growth is observed at all conditions and it is observed that size of growth decreases slightly with an increase in the interlayer delay period primarily due to higher cooling rate. In addition,

the studies on mechanical properties show that strength values increase with an increase in interlayer delay supporting the observations from the microstructural studies. Numerical simulation aids to the explanation of the above results and shows that the pre-heat temperature on the previously built layer reduces with an increase in interlayer delay leading to an increase in cooling rate.

e) Bulk structures are integral for building dense Hast-X engineering components using LDED. Thus built bulk structures show few pores at isolated locations (relative density ~ 99.5%), which are a mix of lack of fusion porosity and gas porosity. The microstructural analysis shows the presence of cellular and dendritic growth, with an increase in the size of growth from the bottom layer to the top layer owing to reduction in cooling rate as the deposition moves from bottom layer to top layer. The elemental segregations of C, Si and Mo are observed in the samples due to non-equilibrium solidification in LDED and the presence of Mo based carbides are also observed, which are formed due to higher number of thermal cycling experienced by the material during the layer-by-layer deposition. The orientation of the grain growth is largely random orientation with some preferred texture along the (100) plane and the grain size is observed to be finer that the conventional wrought samples. Surface analysis of the built structure show that the residual stress on the sample surface is primarily tensile and the higher surface roughness on the as-built surface is attributed to the presence of partially melted powders on the sample surface. The micro-hardness, yield strength and ultimate tensile strength of LDED built Hast-X are higher than that of conventionally processed wrought samples and wall structures deposited at same process parameters. Further, mechanical properties measured at elevated temperature show that the yield strength and ultimate strength decreased by 33% and 32%, respectively with an increase in test temperature to 873 K. The yield strength of LDED samples is greater

than the conventional counterparts at all temperature conditions mainly due to higher dislocation densities in LDED samples.

f) LDED built bulk components are observed to have higher surface roughness, localized lack of fusion porosity and non-equilibrium microstructure. Thus, LDED built structures are subjected to SLLR (a process involving laser remelting after LDED of each layer) to improve the density and surface quality; and solution treatment to achieve uniform microstructure. It is observed that relative density of LDED built Hast-X structures increased with SLLR and the lack of fusion porosity disappeared primarily due to localized material re-distribution during SLLR. The average surface roughness reduced by 71.5% after SLLR due to melting of partially melted powders observed on as-built LDED surface. The cellular and dendritic growth of LDED samples show a little refinement with SLLR. Presence of random grain orientation is observed after SLLR due to re-distribution of thermal history generated during LDED. A small increase in the microhardness by 12% and yield strength by 7% is observed after SLLR due to relatively finer dendritic microstructures in SLLR samples.

g) Microstructural and mechanical studies on the solution treated Hast-X structures show the presence of recrystallized and coarsened equiaxed grains with random orientation and significant reduction in segregation and carbide precipitation. Reduction in the average micro-hardness is observed after solution treatment and the hardness values are found to be closer to micro-hardness of conventional wrought Hast-X. The yield strength of solution treated sample is similar to the yield strength of conventionally wrought Hast-X taken from literature at all test temperatures from room temperature to 873 K, which can be due to coarsened grain structure and reduction in the dislocation density. It is observed that the yield strength and ultimate strength of the solution treated samples reduced by 27% and 25%, respectively with an increase in test temperature from room temperature to 873 K.

h) One of the potential applications of Hast-X is the development of PCHE. LDED of PCHE is challenging due to the difficulty in building completely overhang parts using the generic 3-axis configuration. To achieve the same, overhang walls are built by varying the distance between the laser spot centre and vertical shift of the co-axial nozzle after each layer. The maximum lateral shift possible for fabricating overhang structures without failure is found to be 15%. PCHE channels built at different combination of process parameter show that the process parameter selection, channel size and overlap percentage between layers influences the quality of channels. Further, PCHE is built using a combination of straight walls, overhang walls and bulk structures using the acquired know-how from the above comprehensive studies.

9.2 Future Scope

The future scope of the work includes the following:

a) The fatigue, corrosion and oxidation behaviour of LDED built Hast-X in as-built and post-processed conditions may be explored.
b) Effect of LEPF and preheat on the properties of LDED built bulk Hast-X structures may be analyzed.
c) Effect of different SLLR parameters and solution treatment temperatures on LDED built bulk structures may be investigated.
d) Studies may also be carried out on the development of PCHEs for design duty conditions using LDED and its performance evaluation.
e) Studies may be carried out to explore the optimization of machining parameters for LDED built Hast-X as it can pave a path for hybrid LDED process.
f) Studies on the effect of slurry-based machining may be carried to out to improve the surface quality of LDED built channels.
g) Uncertainty analysis of track geometry can be performed.

h) Effect of channel surface roughness on the performance of the PCHE can be carried out.

i) Accelerated testing of LDED built Hast-X can be performed.

Letter of Copyright Permissions

Copyright Clearance Center | RightsLink®

Home | Help | Email Support | Jinoop A N

Laser assisted direct energy deposition of Hastelloy-X

Author: A.N. Jinoop,C.P. Paul,K.S. Bindra
Publication: Optics & Laser Technology
Publisher: Elsevier
Date: January 2019

© 2018 Elsevier Ltd. All rights reserved.

Please note that, as the author of this Elsevier article, you retain the right to include it in a thesis or dissertation, provided it is not published commercially. Permission is not required, but please ensure that you reference the journal as the original source. For more information on this and on your other retained rights, please visit: https://www.elsevier.com/about/our-business/policies/copyright#Author-rights

BACK | CLOSE WINDOW

Copyright Clearance Center | RightsLink®

Home | Help | Email Support | Jinoop A N

Effect of post heat-treatment on the microstructure and mechanical properties of Hastelloy-X structures manufactured by laser based Directed Energy Deposition

Author: A.N. Jinoop,J. Denny,C.P. Paul,J. Ganesh Kumar,K.S. Bindra
Publication: Journal of Alloys and Compounds
Publisher: Elsevier
Date: 15 August 2019

© 2019 Elsevier B.V. All rights reserved.

Please note that, as the author of this Elsevier article, you retain the right to include it in a thesis or dissertation, provided it is not published commercially. Permission is not required, but please ensure that you reference the journal as the original source. For more information on this and on your other retained rights, please visit: https://www.elsevier.com/about/our-business/policies/copyright#Author-rights

BACK | CLOSE WINDOW

11/19/2020 Rightslink® by Copyright Clearance Center

Copyright Clearance Center | RightsLink®

Home | Help | Email Support | Jinoop A N

Laser-assisted directed energy deposition of nickel super alloys: A review

Author: AN Jinoop, CP Paul, KS Bindra
Publication:
Proceedings of the Institution of Mechanical Engineers, Part L: Journal of Materials: Design and Applications
Publisher: SAGE Publications
Date: 11/01/2019

Copyright © 2019, © SAGE Publications

Gratis Reuse

If you are a SAGE journal author requesting permission to reuse material from your journal article, please note you may be able to reuse your content without requiring permission from SAGE. Please review SAGE's author re-use and archiving policies at https://us.sagepub.com/en-us/nam/journal-author-archiving-policies-and-re-use for more information.

If your request does not fall within SAGE's reuse guidelines, please proceed with submitting your request by selecting one of the other reuse categories that describes your use. Please note, a fee may be charged for reuse of content requiring permission. Please submit a ticket through the SAGE Permissions Portal if you have questions.

BACK | CLOSE WINDOW

Copyright Clearance Center | RightsLink®

Home | Help | Email Support | Jinoop A N

Laser Additive Manufacturing using directed energy deposition of Inconel-718 wall structures with tailored characteristics

Author: A.N. Jinoop,C.P. Paul,S.K. Mishra,K.S. Bindra
Publication: Vacuum
Publisher: Elsevier
Date: August 2019

Please note that, as the author of this Elsevier article, you retain the right to include it in a thesis or dissertation, provided it is not published commercially. Permission is not required, but please ensure that you reference the journal as the original source. For more information on this and on your other retained rights, please visit: https://www.elsevier.com/about/our-business/policies/copyright#Author-rights

BACK | CLOSE WINDOW

Copyright Clearance Center | RightsLink®

Home | Help | Email Support | Jinoop A N

Hot deformation behavior of Hastelloy-X preforms built using directed energy deposition based laser additive manufacturing

Author: A.N. Jinoop,V. Anil Kumar,C.P. Paul,Ravi Ranjan,K.S. Bindra
Publication: Materials Letters
Publisher: Elsevier
Date: 1 July 2020

Please note that, as the author of this Elsevier article, you retain the right to include it in a thesis or dissertation, provided it is not published commercially. Permission is not required, but please ensure that you reference the journal as the original source. For more information on this and on your other retained rights, please visit: https://www.elsevier.com/about/our-business/policies/copyright#Author-rights

BACK | CLOSE WINDOW

1/1/2021 Gmail - Re: Permission to reuse article for thesis

Gmail — Jinoop A N <anjinoop18@gmail.com>

Re: Permission to reuse article for thesis

Ian Mellanby <ian@oldcitypublishing.com> Tue, Nov 24, 2020 at 8:46 AM
To: Jinoop A N <anjinoop18@gmail.com>

Dear Jinoop,

We hereby give you permission for you to use content from your article in your thesis providing full reference is given to the original publication.

Good luck with your PhD and we look forward to publishing your research work in the future.

Best regards

Ian

Dr. Ian Mellanby
Publishing Director
Old City Publishing Inc.
628 North 2nd Street,
Philadelphia PA 19123 USA
Tel: +1 215 925-4390
Cell/Mobile: +1 215 208-8701
Fax: +1 215 925-4371
e-mail: ian@oldcitypublishing.com
www.oldcitypublishing.com
Like us on Facebook
Follow us on twitter

From: Jinoop A N <anjinoop18@gmail.com>
Date: Thursday, 19 November 2020 05:20
To: Ian Mellanby <info@oldcitypublishing.com>
Subject: Permission to reuse article for thesis

Dear Sir/ Madam,

I am Jinoop A N, a PhD Scholar at Homi Bhabha National Institute, Raja Ramanna Centre for Advanced Technology, India. I am also the author of the article titled "Laser Additive Manufacturing (LAM) of Hastelloy-X Thin Walls Using Directed Energy Deposition (DED): Parametric Investigation and Multi-objective Analysis." published in "Lasers in Engineering" journal in the 46th volume.

I would like to reuse the contents of the above manuscript for my PhD thesis. I request you to kindly grant me permission for the same.

Thanks and regards,

Jinoop

Copyright Clearance Center | RightsLink®

Home | Help | Email Support | Jinoop A N

Effect of laser energy per unit powder feed on Hastelloy-X walls built by laser directed energy deposition based additive manufacturing

Author: A.N. Jinoop,C.P. Paul,S.K. Nayak,J. Ganesh Kumar,K.S. Bindra

Publication: Optics & Laser Technology

Publisher: Elsevier

Date: June 2021

Please note that, as the author of this Elsevier article, you retain the right to include it in a thesis or dissertation, provided it is not published commercially. Permission is not required, but please ensure that you reference the journal as the original source. For more information on this and on your other retained rights, please visit: https://www.elsevier.com/about/our-business/policies/copyright#Author-rights

BACK | CLOSE WINDOW

PLS Clear

PARTIES:

1. **Taylor and Francis Group LLC (Books) US** [CompanyNumber] (Licensor); and
2. **Jinoop A N** (Licensee).

Thank you for your recent permission request. Some permission requests for use of material published by the Licensor, such as this one, are now being facilitated by PLSclear.

Set out in this licence cover sheet (the **Licence Cover Sheet**) are the principal terms under which Licensor has agreed to license certain Licensed Material (as defined below) to Licensee. The terms in this Licence Cover Sheet are subject to the attached General Terms and Conditions, which together with this Licence Cover Sheet constitute the licence agreement (the **Licence**) between Licensor and Licensee as regards the Licensed Material. The terms set out in this Licence Cover Sheet take precedence over any conflicting provision in the General Terms and Conditions.

Free Of Charge Licence Terms

Licence Date:	31/12/2020
PLSclear Ref No:	45624

The Licensor

Company name:	Taylor and Francis Group LLC (Books) US
Address:	711 3rd Avenue New York 10017 United States US

The Licensee

Licensee Contact Name:	Jinoop A N
Licensee Address:	RRCAT 452013 India

Licensed Material

title:	Additive Manufacturing Applications and Innovations
ISBN:	9781138050600
publisher:	Taylor and Francis Group LLC (Books) US
Chapter name or number	Metal Additive Manufacturing using Lasers

Number of words	17940
Page numbers	37-94
Number of pages	57
Are you requesting permission to reuse your own work?	Yes

For Use In Licensee's Publication(s)

usage type	Book, Journal, Magazine or Academic Paper-Thesis / Dissertation
Will your dissertation be placed in an online repository?	No
Author	Jinoop A N
Language	English
Title of dissertation/thesis	Experimental studies and Parametric Investigation on Laser Directed Energy Deposition based Additive Manufacturing of Hastelloy-X Thin Walls and Bulk Structures
University or institution	Homi Bhabha National Institute
Unlimited circulation?	Yes

Rights Granted

Exclusivity:	Non-Exclusive
Format:	Thesis / Dissertation
Language:	English
Territory:	World
Duration:	Lifetime of Licensee's Edition
Maximum Circulation:	Unlimited

GENERAL TERMS AND CONDITIONS

1. Definitions and Interpretation

1.1 Capitalised words and expressions in these General Terms and Conditions have the meanings given to them in the Licence Cover Sheet.

1.2 In this Licence any references (express or implied) to statutes or provisions are references to those statutes or provisions as amended or re-enacted from time to time. The term including will be construed as illustrative, without limiting the sense or scope of the words preceding it. A reference to in writing or written includes faxes and email. The singular includes the plural and vice versa.

2. Grant of Rights

2.1 The Licensor grants to Licensee the non-exclusive right to use the Licensed Material as specified in the Licence Cover Sheet.

2.2 The rights licensed to Licensee under this Licence do not include the right to use any third party copyright material incorporated in the Licensed Material. Licensee should check the Licensed Material carefully and seek permission for the use of any such third party copyright material from the relevant copyright owner(s).

2.3 Unless otherwise stated in the Licence Cover Sheet, the Licensed Material may be:

2.3.1 subjected to minor editing, including for the purposes of creating alternative formats to provide access for a beneficiary person (provided that any such editing does not amount to derogatory treatment); and/or

2.3.2 used for incidental promotional use (such as online retail providers' search facilities).

2.4 Save as expressly permitted in this Licence or as otherwise permitted by law, no use or modification of the Licensed Material may be made by Licensee without Licensor's prior written permission.

3. Copyright Notice and Acknowledgement

3.1 Licensee must ensure that the following notices and acknowledgements are reproduced prominently alongside each reproduction by Licensee of the Licensed Material:

3.1.1 the title and author of the Licensed Material;

3.1.2 the copyright notice included in the Licensed Material; and

3.1.3 the statement "Reproduced with permission of The Licensor through PLSclear."

4. Reversion of Rights

4.1 The rights licensed to Licensee under this Licence will terminate immediately and automatically upon the earliest of the following events to occur:

4.1.1 the Licensed Material not being used by Licensee within 18 months of the Licence Date;

4.1.2 expiry of the Licence Duration; or

4.1.3 the Maximum Circulation being reached.

5. Miscellaneous

5.1 By using the Licensed Material, Licensee will be deemed to have accepted all the terms and conditions contained in this Licence.

5.2 This Licence contains the entire understanding and agreement of the parties relating to its subject matter and supersedes in all respects any previous or other existing arrangements, agreements or understandings between the parties whether oral or written in relation to its subject matter.

5.3 Licensee may not assign this Licence or any of its rights or obligations hereunder to any third party without Licensor's prior written consent.

5.4 This Licence is governed by and shall be construed in accordance with the laws of England and Wales and the parties hereby irrevocably submit to the non-exclusive jurisdiction of the Courts of England and Wales as regards any claim, dispute or matter arising under or in relation to this Licence.

Influence of heat treatment on the microstructure evolution and elevated temperature mechanical properties of Hastelloy-X processed by laser directed energy deposition

Author: A.N. Jinoop,C.P. Paul,J. Ganesh Kumar,V. Anilkumar,R. Singh,S. Rao,K.S. Bindra
Publication: Journal of Alloys and Compounds
Publisher: Elsevier
Date: 5 July 2021

Journal Author Rights

Annexure -1: Composition and Mechanical properties of common Nickel Superalloys

	Composition														Ultimate Strength (MPa)	Yield Strength (MPa)
Alloy	Cr	Co	Mo	W	Nb	Al	Ti	Ta	Fe	Hf	C	B	Zr	Ni		
Hastelloy X	22	1.5	9	0.6	-	0.25	-	-	18.5	-	0.1	-	-	Bal.	760	340
Inconel 625	21.5	-	9	-	3.6	0.2	0.2	-	2.5	-	0.05		-	Bal.	965	490
Inconel 690	29	-	-	-	-	-	-	-	9	-	0.025		-	Bal.	724	348
Inconel 100	10	15	3	-	-	5.5	5	-	-	-	0.18	0.01	0.06	Bal.	795	655
Inconel 718	19	-	3	-	5.1	0.5	0.9	-	18.5	-	0.04		-	Bal.	1435	1185
Inconel 738	16	8.5	1.75	2.6	0.9	3.4	3.4	1.7	-	-	0.11	0.01	0.05	Bal.	945	765
Rene 41	19	11	1	-		1.5	3.1	-	14.5	-	0.09	0.005	-	Bal.	1420	1060
Rene 95	14	8	3.5	3.5	3.5	3.5	2.5	-	-	-	0.15	0.01	0.05	Bal.	1620	1310
Waspaloy	19.5	13.5	4.3	-	-	1.3	3	-	-	-	0.08	0.006	-	Bal.	1275	795

Annexure -2: Properties of Hastelloy-X

Properties (Unit)	Values
Density (kg/m^3)	8220
Melting Temperature Range (K)	1530 – 1628
Thermal Conductivity (W/m.K)	10
Specific Heat (J/(kg·K)	450
Mean Coefficient of Thermal Expansion (m/m-°C)	13.9 10^{-6} (26 -100 °C)
Modulus of Elasticity (GPa)	205
Poisson's Ratio	0.32
Hardness	86-88 HRBW

References

[1] S. Keating, N. Oxman, Compound fabrication: A multi-functional robotic platform for digital design and fabrication, Robot. Comput. Integr. Manuf. 29 (2013) 439–448. https://doi.org/https://doi.org/10.1016/j.rcim.2013.05.001.

[2] F. Wimmer, Application Cases and Integration of Additive Manufacturing Processes into Conventional Process Chains by the Example of Tool Repair Using the Controlled Metal Build-Up Process, Fraunhofer Institute for Production Technology, Aachen, 2015.

[3] S. Mohd Yusuf, S. Cutler, N. Gao, Review: The Impact of Metal Additive Manufacturing on the Aerospace Industry, Met. . 9 (2019). https://doi.org/10.3390/met9121286.

[4] P.K. Saha, Aerospace Manufacturing Processes, First Edit, CRC Press, Boca Raton, 2016. https://doi.org/https://doi.org/10.1201/9781315367965.

[5] A. Del Prete, R. Franchi, F. Antermite, I. Donatiello, Development of an automatic procedure for machining distortions improvement on an aeronautic axisymmetric component, AIP Conf. Proc. 2113 (2019) 80008. https://doi.org/10.1063/1.5112616.

[6] M.J. Bermingham, S. Palanisamy, M.S. Dargusch, Understanding the tool wear mechanism during thermally assisted machining Ti-6Al-4V, Int. J. Mach. Tools Manuf. 62 (2012) 76–87. https://doi.org/https://doi.org/10.1016/j.ijmachtools.2012.07.001.

[7] International Organization for Standardization/ASTM International, ISO/ASTM

52900: 2017-06 additive manufacturing—general principles—terminology, 2017.

[8] A. Gisario, M. Kazarian, F. Martina, M. Mehrpouya, Metal additive manufacturing in the commercial aviation industry: A review, J. Manuf. Syst. 53 (2019) 124–149. https://doi.org/https://doi.org/10.1016/j.jmsy.2019.08.005.

[9] R.M. Mahamood, E.T. Akinlabi, Achieving Mass Customization Through Additive Manufacturing BT - Advances in Ergonomics of Manufacturing: Managing the Enterprise of the Future, in: C. Schlick, S. Trzcieliński (Eds.), Springer International Publishing, Cham, 2016: pp. 385–390.

[10] S. Ford, M. Despeisse, Additive manufacturing and sustainability: an exploratory study of the advantages and challenges, J. Clean. Prod. 137 (2016) 1573–1587. https://doi.org/https://doi.org/10.1016/j.jclepro.2016.04.150.

[11] L.J. Kumar, C.G. Krishnadas Nair, Current Trends of Additive Manufacturing in the Aerospace Industry BT - Advances in 3D Printing & Additive Manufacturing Technologies, in: D.I. Wimpenny, P.M. Pandey, L.J. Kumar (Eds.), Springer Singapore, Singapore, 2017: pp. 39–54. https://doi.org/10.1007/978-981-10-0812-2_4.

[12] G.M. ınez de Frutos, Product development process for additive manufacturing Considerations on the design of final products for 3D printing, Instituto Superior Técnico Lisboa, 2015.

[13] C P Paul, Parametric Studies of Laser Metal Deposition for Fabrication Engineering Components, Devi Ahilya Vishwavidyalaya, 2005.

[14] Royal Academy of Engineering, Additive manufacturing: opportunities and constraints, London S, 2013.

[15] T. McCue, Significant 3D Printing Forecast Surges To $35.6 Billion, Forbes. (2019).

[16] T. Wohlers, Wohlers Report 2019. 3D Printing and Additive Manufacturing State of the Industry, 2019.

[17] C.P. Paul, P. Bhargava, A. Kumar, A.K. Pathak, L.M. Kukreja, Laser Rapid Manufacturing: Technology, Applications, Modeling and Future Prospects, Lasers Manuf. (2013) 1–67. https://doi.org/https://doi.org/10.1002/9781118562857.ch1.

[18] A.J. Pinkerton, [INVITED] Lasers in additive manufacturing, Opt. Laser Technol. 78 (2016) 25–32. https://doi.org/https://doi.org/10.1016/j.optlastec.2015.09.025.

[19] A. du Plessis, C. Broeckhoven, I. Yadroitsava, I. Yadroitsev, C.H. Hands, R. Kunju, D. Bhate, Beautiful and Functional: A Review of Biomimetic Design in Additive Manufacturing, Addit. Manuf. 27 (2019) 408–427. https://doi.org/https://doi.org/10.1016/j.addma.2019.03.033.

[20] S.M. Banait, C.P. Paul, A.N. Jinoop, H. Kumar, R.S. Pawade, K.S. Bindra, Experimental investigation on laser directed energy deposition of functionally graded layers of Ni-Cr-B-Si and SS316L, Opt. Laser Technol. 121 (2020) 105787. https://doi.org/https://doi.org/10.1016/j.optlastec.2019.105787.

[21] Y. Zhang, A. Bandyopadhyay, Direct fabrication of compositionally graded Ti-Al2O3 multi-material structures using Laser Engineered Net Shaping, Addit. Manuf. 21 (2018) 104–111. https://doi.org/https://doi.org/10.1016/j.addma.2018.03.001.

[22] M. Akbari, N. Ha, Impact of additive manufacturing on the Vietnamese transportation industry: An exploratory study, Asian J. Shipp. Logist. 36 (2020) 78–88. https://doi.org/https://doi.org/10.1016/j.ajsl.2019.11.001.

[23] I. Bahnini, M. Rivette, A. Rechia, A. Siadat, A. Elmesbahi, Additive manufacturing technology: the status, applications, and prospects, Int. J. Adv. Manuf. Technol. 97 (2018) 147–161. https://doi.org/10.1007/s00170-018-1932-y.

[24] T. Parent-Simard, A. Landry-Blais, P.K. Dubois, M. Picard, V. Brailovski, Effect of Surface Roughness Induced by Laser Powder Bed Fusion Additive Manufacturing in a Mini-Channel Heat Exchanger, (2019). https://doi.org/10.1115/GT2019-90978.

[25] Z. Min, S.N. Parbat, L. Yang, B. Kang, M.K. Chyu, Fabrication and Characterization of Additive Manufactured Nickel-Based Oxide Dispersion Strengthened Coating Layer for High-Temperature Application, J. Eng. Gas Turbines Power. 140 (2018). https://doi.org/10.1115/1.4038351.

[26] M. Binder, L. Kirchbichler, C. Seidel, C. Anstaett, G. Schlick, G. Reinhart, Design Concepts for the Integration of Electronic Components into Metal Laser-based Powder Bed Fusion Parts, Procedia CIRP. 81 (2019) 992–997. https://doi.org/https://doi.org/10.1016/j.procir.2019.03.240.

[27] S. Yadav, A.N. Jinoop, N. Sinha, C.P. Paul, K.S. Bindra, Parametric investigation and characterization of laser directed energy deposited copper-nickel graded layers, Int. J. Adv. Manuf. Technol. 108 (2020) 3779–3791. https://doi.org/10.1007/s00170-020-05644-9.

[28] T. Petrat, B. Graf, A. Gumenyuk, M. Rethmeier, Laser Metal Deposition as Repair Technology for a Gas Turbine Burner Made of Inconel 718, Phys. Procedia. 83 (2016) 761–768. https://doi.org/https://doi.org/10.1016/j.phpro.2016.08.078.

[29] Y. Ahn, S.J. Bae, M. Kim, S.K. Cho, S. Baik, J.I. Lee, J.E. Cha, Review of supercritical CO2 power cycle technology and current status of research and

development, Nucl. Eng. Technol. 47 (2015) 647–661. https://doi.org/https://doi.org/10.1016/j.net.2015.06.009.

[30] X. Li, R. Le Pierres, S.J. Dewson, Heat exchangers for the next generation of nuclear reactors, Proc. 2006 Int. Congr. Adv. Nucl. Power Plants, ICAPP'06. 2006 (2006) 201–209.

[31] I. Del Sol, A. Rivero, L.N. López de Lacalle, A.J. Gamez, Thin-Wall Machining of Light Alloys: A Review of Models and Industrial Approaches, Mater. . 12 (2019). https://doi.org/10.3390/ma12122012.

[32] X. Xu, G. Mi, L. Chen, L. Xiong, P. Jiang, X. Shao, C. Wang, Research on microstructures and properties of Inconel 625 coatings obtained by laser cladding with wire, J. Alloys Compd. 715 (2017) 362–373. https://doi.org/https://doi.org/10.1016/j.jallcom.2017.04.252.

[33] S. Singh, D.K. Goyal, P. Kumar, A. Bansal, Laser cladding technique for erosive wear applications: a review, Mater. Res. Express. 7 (2020) 12007. https://doi.org/10.1088/2053-1591/ab6894.

[34] P. Popoola, Laser Engineering Net Shaping Method in the Area of Development of Functionally Graded Materials (FGMs) for Aero Engine Applications - A Review, in: G. Farotade (Ed.), IntechOpen, Rijeka, 2016: p. Ch. 17. https://doi.org/10.5772/61711.

[35] V. Kulkarni, Advances of Additive Manufacturing in Aerospace Application, AM Chron. (2020).

[36] A.P.B.T.-I. to A.M. Mouritz, ed., 12 - Superalloys for gas turbine engines, in: Woodhead Publishing, 2012: pp. 251–267.

https://doi.org/https://doi.org/10.1533/9780857095152.251.

[37] HAYNES INTERNATIONAL, HASTELLOY® X Principal Features, (2020).

[38] Haynes International, Power Generation, (2020).

[39] Y. Kondo, K. Fukaya, K. Kunitomi, Y. Miyamoto, Tensile and impact properties changes of HASTELLOY X after exposure in high-temperature helium environment, Metall. Trans. A. 19 (1988) 1269–1275. https://doi.org/10.1007/BF02662588.

[40] H.E. McCoy, J.P. Strizak, J.F. King, Hastelloy-X for High Temperature Gas-Cooled Reactor Applications, Nucl. Technol. 66 (1984) 161–174. https://doi.org/10.13182/NT84-A33464.

[41] I. Gibson, D.W. Rosen, B. Stucker, Additive Manufacturing Technologies 3D Printing, Rapid Prototyping, and Direct Digital Manufacturing, Second, Springer-Verlag, New York, 2015. https://doi.org/10.1007/978-1-4939-2113-3.

[42] S.A.M. Tofail, E.P. Koumoulos, A. Bandyopadhyay, S. Bose, L. O'Donoghue, C. Charitidis, Additive manufacturing: scientific and technological challenges, market uptake and opportunities, Mater. Today. 21 (2018) 22–37. https://doi.org/https://doi.org/10.1016/j.mattod.2017.07.001.

[43] S.K. Nayak, S.K. Mishra, A.N. Jinoop, C.P. Paul, K.S. Bindra, Experimental Studies on Laser Additive Manufacturing of Inconel-625 Structures Using Powder Bed Fusion at 100 μm Layer Thickness, J. Mater. Eng. Perform. 29 (2020) 7636–7647. https://doi.org/10.1007/s11665-020-05215-9.

[44] J. Gonzalez-Gutierrez, F. Arbeiter, T. Schlauf, C. Kukla, C. Holzer, Tensile properties of sintered 17-4PH stainless steel fabricated by material extrusion additive

manufacturing, Mater. Lett. 248 (2019) 165–168. https://doi.org/https://doi.org/10.1016/j.matlet.2019.04.024.

[45] H. Miyanaji, D. Ma, M.A. Atwater, K.A. Darling, V.H. Hammond, C.B. Williams, Binder jetting additive manufacturing of copper foam structures, Addit. Manuf. 32 (2020) 100960. https://doi.org/https://doi.org/10.1016/j.addma.2019.100960.

[46] S. Verploegh, M. Coffey, E. Grossman, Z. Popović, Properties of 50–110-GHz Waveguide Components Fabricated by Metal Additive Manufacturing, IEEE Trans. Microw. Theory Tech. 65 (2017) 5144–5153. https://doi.org/10.1109/TMTT.2017.2771446.

[47] W.J. Sames, F.A. List, S. Pannala, R.R. Dehoff, S.S. Babu, The metallurgy and processing science of metal additive manufacturing, Int. Mater. Rev. 61 (2016) 315–360. https://doi.org/10.1080/09506608.2015.1116649.

[48] R.J. Friel, R.A. Harris, Ultrasonic Additive Manufacturing – A Hybrid Production Process for Novel Functional Products, Procedia CIRP. 6 (2013) 35–40. https://doi.org/https://doi.org/10.1016/j.procir.2013.03.004.

[49] T. DebRoy, H.L. Wei, J.S. Zuback, T. Mukherjee, J.W. Elmer, J.O. Milewski, A.M. Beese, A. Wilson-Heid, A. De, W. Zhang, Additive manufacturing of metallic components – Process, structure and properties, Prog. Mater. Sci. 92 (2018) 112–224. https://doi.org/https://doi.org/10.1016/j.pmatsci.2017.10.001.

[50] N. Seema, N.A. Arun, K. Sajan, J.P. Shreekant, R. Manivannan, K. K.P., B. Parag, Review on electron beam based additive manufacturing, Rapid Prototyp. J. 26 (2019) 485–498. https://doi.org/10.1108/RPJ-07-2019-0182.

[51] H. Geng, J. Li, J. Xiong, X. Lin, F. Zhang, Optimization of wire feed for GTAW based additive manufacturing, J. Mater. Process. Technol. 243 (2017) 40–47. https://doi.org/https://doi.org/10.1016/j.jmatprotec.2016.11.027.

[52] N. Resnina, I.A. Palani, S. Belyaev, S.S.M. Prabu, P. Liulchak, U. Karaseva, M. Manikandan, S. Jayachandran, V. Bryukhanova, A. Sahu, R. Bikbaev, Structure, martensitic transformations and mechanical behaviour of NiTi shape memory alloy produced by wire arc additive manufacturing, J. Alloys Compd. 851 (2021) 156851. https://doi.org/https://doi.org/10.1016/j.jallcom.2020.156851.

[53] B. Wu, Z. Pan, D. Ding, D. Cuiuri, H. Li, J. Xu, J. Norrish, A review of the wire arc additive manufacturing of metals: properties, defects and quality improvement, J. Manuf. Process. 35 (2018) 127–139. https://doi.org/https://doi.org/10.1016/j.jmapro.2018.08.001.

[54] FisicaNET, LASER AND ITS APPLICATIONS, (n.d.).

[55] W. Steen, J. Mazumder, Laser Material Processing, Fourth Edi, Springer-Verlag, London, 2010.

[56] C.P. Paul, A. Kumar, P. Bhargava, L.M. Kukreja, Laser-Assisted Manufacturing: Fundamentals, Current Scenario, and Future Applications BT - Nontraditional Machining Processes: Research Advances, in: J.P. Davim (Ed.), Springer London, London, 2013: pp. 1–34. https://doi.org/10.1007/978-1-4471-5179-1_1.

[57] A. Mazzoli, Selective laser sintering in biomedical engineering, Med. Biol. Eng. Comput. 51 (2013) 245–256. https://doi.org/10.1007/s11517-012-1001-x.

[58] E.O. Olakanmi, Selective laser sintering/melting (SLS/SLM) of pure Al, Al–Mg, and

Al–Si powders: Effect of processing conditions and powder properties, J. Mater. Process. Technol. 213 (2013) 1387–1405. https://doi.org/https://doi.org/10.1016/j.jmatprotec.2013.03.009.

[59] D. Gu, Laser Additive Manufacturing of High-Performance Materials, Springer-Verlag, Berlin Heidelberg, 2015. https://doi.org/10.1007/978-3-662-46089-4.

[60] E. Toyserkani, A. Khajepour, S.F. Corbin, Laser Cladding, First, CRC Press, Boca Raton, 2004. https://doi.org/https://doi.org/10.1201/9781420039177.

[61] Fraunhofer-Institut für Werkstoff- und Strahltechnik IWS Dresden, Coaxial laser wire cladding head COAXwire, (n.d.). https://www.iws.fraunhofer.de/en/business_fields/surface_treatment/laser_cladding/system_technology/COAXwire.html (accessed January 1, 2021).

[62] C.P. Paul, P. Ganesh, S.K. Mishra, P. Bhargava, J. Negi, A.K. Nath, Investigating laser rapid manufacturing for Inconel-625 components, Opt. Laser Technol. 39 (2007) 800–805. https://doi.org/https://doi.org/10.1016/j.optlastec.2006.01.008.

[63] rp-photonics, Optical Intensity, (n.d.). https://www.rp-photonics.com/ (accessed January 1, 2021).

[64] S. Donadello, M. Motta, A.G. Demir, B. Previtali, Monitoring of laser metal deposition height by means of coaxial laser triangulation, Opt. Lasers Eng. 112 (2019) 136–144. https://doi.org/https://doi.org/10.1016/j.optlaseng.2018.09.012.

[65] X. Chen, Modelling of directed energy deposition processes, MISSOURIUNIVERSITY OF SCIENCE AND TECHNOLOGY, 2014.

[66] C. Zhang, F. Chen, Z. Huang, M. Jia, G. Chen, Y. Ye, Y. Lin, W. Liu, B. Chen, Q.

Shen, L. Zhang, E.J. Lavernia, Additive manufacturing of functionally graded materials: A review, Mater. Sci. Eng. A. 764 (2019) 138209. https://doi.org/https://doi.org/10.1016/j.msea.2019.138209.

[67] A. Carrozza, A. Aversa, F. Mazzucato, M. Lombardi, S. Biamino, A. Valente, P. Fino, An Innovative Approach on Directed Energy Deposition Optimization: A Study of the Process Environment's Influence on the Quality of Ti-6Al-4V Samples, Appl. Sci. . 10 (2020). https://doi.org/10.3390/app10124212.

[68] A.C. Paul, A.N. Jinoop, C.P. Paul, P. Deogiri, K.S. Bindra, Investigating build geometry characteristics during laser directed energy deposition based additive manufacturing, J. Laser Appl. 32 (2020) 42002. https://doi.org/10.2351/7.0000004.

[69] J.C. Najmon, S. Raeisi, A. Tovar, 2 - Review of additive manufacturing technologies and applications in the aerospace industry, in: F. Froes, R.B.T.-A.M. for the A.I. Boyer (Eds.), Elsevier, 2019: pp. 7–31. https://doi.org/https://doi.org/10.1016/B978-0-12-814062-8.00002-9.

[70] C. Li, Z.Y. Liu, X.Y. Fang, Y.B. Guo, Residual Stress in Metal Additive Manufacturing, Procedia CIRP. 71 (2018) 348–353. https://doi.org/https://doi.org/10.1016/j.procir.2018.05.039.

[71] M. Alimardani, E. Toyserkani, J.P. Huissoon, C.P. Paul, On the delamination and crack formation in a thin wall fabricated using laser solid freeform fabrication process: An experimental–numerical investigation, Opt. Lasers Eng. 47 (2009) 1160–1168. https://doi.org/https://doi.org/10.1016/j.optlaseng.2009.06.010.

[72] I. Mingareev, T. Bonhoff, A.F. El-Sherif, W. Meiners, I. Kelbassa, T. Biermann, M. Richardson, Femtosecond laser post-processing of metal parts produced by laser

additive manufacturing, J. Laser Appl. 25 (2013) 52009. https://doi.org/10.2351/1.4824146.

[73] C.B. D. Manfredi, F. Calignano, E. P. Ambrosio, M.Krishnan, R. Canali, S. Biamino, M. Pavese, E. Atzeni, L. Iuliano, P. Fino, Direct Metal Laser Sintering: an additive manufacturing technology ready to produce lightweight structural parts for robotic applications, La Metall. Ital. 10 (2014).

[74] E. Chlebus, K. Gruber, B. Kuźnicka, J. Kurzac, T. Kurzynowski, Effect of heat treatment on the microstructure and mechanical properties of Inconel 718 processed by selective laser melting, Mater. Sci. Eng. A. 639 (2015) 647–655. https://doi.org/https://doi.org/10.1016/j.msea.2015.05.035.

[75] H.A.R. M. Thöne, S. Leuders, A. Riemer, T. Tröster, Influence of heat-treatment on Selective Laser Melting products – e.g. Ti6Al4V, in: Int. Solid Free. Fabr. Symp., Texas, 2012.

[76] H. Attia, S. Tavakoli, R. Vargas, V. Thomson, Laser-assisted high-speed finish turning of superalloy Inconel 718 under dry conditions, CIRP Ann. 59 (2010) 83–88. https://doi.org/https://doi.org/10.1016/j.cirp.2010.03.093.

[77] K. Moussaoui, W. Rubio, M. Mousseigne, T. Sultan, F. Rezai, Effects of Selective Laser Melting additive manufacturing parameters of Inconel 718 on porosity, microstructure and mechanical properties, Mater. Sci. Eng. A. 735 (2018) 182–190. https://doi.org/https://doi.org/10.1016/j.msea.2018.08.037.

[78] E. Schlienger, D. Dimos, M. Griffith, J. Michael, M. Oliver, T. [Sandia N.L. Romero Albuquerque, NM (United States)], J. [Sandia N.L. Smugeresky Livermore, CA (United States)], Near Net Shape production of metal components using LENS, in:

Pacific Rim Int. Conf. Adv. Mater. Process., United States, 1998.

[79] M. Hedges, N. Calder, Near net shape rapid manufacture & repair by LENS, Meet. Proc. RTO-MP-AVT-139. 2 (2006) 13.

[80] Optomec Inc., Optomec Releases Pure Copper Directed Energy Deposition (DED) Additive Manufacturing Process, (2019).

[81] A. Dass, A. Moridi, State of the Art in Directed Energy Deposition: From Additive Manufacturing to Materials Design, Coatings . 9 (2019). https://doi.org/10.3390/coatings9070418.

[82] A. Saboori, D. Gallo, S. Biamino, P. Fino, M. Lombardi, An Overview of Additive Manufacturing of Titanium Components by Directed Energy Deposition: Microstructure and Mechanical Properties, Appl. Sci. . 7 (2017). https://doi.org/10.3390/app7090883.

[83] J. Ni, H. Ling, S. Zhang, Z. Wang, Z. Peng, C. Benyshek, R. Zan, A.K. Miri, Z. Li, X. Zhang, J. Lee, K.-J. Lee, H.-J. Kim, P. Tebon, T. Hoffman, M.R. Dokmeci, N. Ashammakhi, X. Li, A. Khademhosseini, Three-dimensional printing of metals for biomedical applications, Mater. Today Bio. 3 (2019) 100024. https://doi.org/https://doi.org/10.1016/j.mtbio.2019.100024.

[84] F. Trevisan, F. Calignano, A. Aversa, G. Marchese, M. Lombardi, S. Biamino, D. Ugues, D. Manfredi, Additive manufacturing of titanium alloys in the biomedical field: processes, properties and applications, J. Appl. Biomater. Funct. Mater. 16 (2017) 57–67. https://doi.org/10.5301/jabfm.5000371.

[85] B.V. Krishna, S. Bose, A. Bandyopadhyay, Laser Processing of Net-Shape NiTi Shape

Memory Alloy, Metall. Mater. Trans. A. 38 (2007) 1096–1103. https://doi.org/10.1007/s11661-007-9127-4.

[86] S. Poeppel, Laser Cladding Advancements for Pressurized Boiler Components, (2017).

[87] J. Bennett, D. Garcia, M. Kendrick, T. Hartman, G. Hyatt, K. Ehmann, F. You, J. Cao, Repairing Automotive Dies With Directed Energy Deposition: Industrial Application and Life Cycle Analysis, J. Manuf. Sci. Eng. 141 (2018). https://doi.org/10.1115/1.4042078.

[88] R. Vilar, A. Almeida, Repair and manufacturing of single crystal Ni-based superalloys components by laser powder deposition—A review, J. Laser Appl. 27 (2014) S17004. https://doi.org/10.2351/1.4862697.

[89] E. Díaz, M.J. Tobar, A. Yáñez, J. García, J. Taibo, Laser Powder Welding with a Co-based alloy for repairing steam circuit components in thermal power stations, Phys. Procedia. 5 (2010) 349–358. https://doi.org/https://doi.org/10.1016/j.phpro.2010.08.156.

[90] Adrian P. Mouritz, Introduction to Aerospace Materials, Woodhead Publishing, Sawston, Cambridge, 2012.

[91] H. K. D. H. Bhadeshia, Nickel Based Superalloys, (n.d.).

[92] C.H. Lund, PHYSICAL METALLURGY OF NICKEL-BASE SUPER-ALLOYS, United States, 1961.

[93] F. Liu, X. Lin, G. Yang, M. Song, J. Chen, W. Huang, Microstructure and residual stress of laser rapid formed Inconel 718 nickel-base superalloy, Opt. Laser Technol. 43 (2011) 208–213. https://doi.org/https://doi.org/10.1016/j.optlastec.2010.06.015.

[94] Z. Liu, T. Li, F. Ning, W. Cong, H. Kim, Q. Jiang, H. Zhang, Effects of deposition variables on molten pool temperature during laser engineered net shaping of Inconel 718 superalloy, Int. J. Adv. Manuf. Technol. 102 (2019) 969–976. https://doi.org/10.1007/s00170-018-03245-1.

[95] P.L. Blackwell, The mechanical and microstructural characteristics of laser-deposited IN718, J. Mater. Process. Technol. 170 (2005) 240–246. https://doi.org/https://doi.org/10.1016/j.jmatprotec.2005.05.005.

[96] H. Xiao, S. Li, X. Han, J. Mazumder, L. Song, Laves phase control of Inconel 718 alloy using quasi-continuous-wave laser additive manufacturing, Mater. Des. 122 (2017) 330–339. https://doi.org/https://doi.org/10.1016/j.matdes.2017.03.004.

[97] H. Xiao, S.M. Li, W.J. Xiao, Y.Q. Li, L.M. Cha, J. Mazumder, L.J. Song, Effects of laser modes on Nb segregation and Laves phase formation during laser additive manufacturing of nickel-based superalloy, Mater. Lett. 188 (2017) 260–262. https://doi.org/https://doi.org/10.1016/j.matlet.2016.10.118.

[98] Y. Chen, K. Zhang, J. Huang, S.R.E. Hosseini, Z. Li, Characterization of heat affected zone liquation cracking in laser additive manufacturing of Inconel 718, Mater. Des. 90 (2016) 586–594. https://doi.org/https://doi.org/10.1016/j.matdes.2015.10.155.

[99] B.E. Carroll, R.A. Otis, J. Paul, J. Suh, R.P. Dillon, A.A. Shapiro, D.C. Hofmann, Z. Liu, A.M. Beese, Functionally graded material of 304L stainless steel and inconel 625 fabricated by directed energy deposition : Characterization and thermodynamic modeling, Acta Mater. 108 (2016) 46–54. https://doi.org/10.1016/j.actamat.2016.02.019.

[100] B. Zhang, G. Bi, P. Wang, J. Bai, Y. Chew, M.S. Nai, Microstructure and mechanical

properties of Inconel 625/nano-TiB2 composite fabricated by LAAM, Mater. Des. 111 (2016) 70–79. https://doi.org/https://doi.org/10.1016/j.matdes.2016.08.078.

[101] R. Koike, T. Misawa, T. Aoyama, M. Kondo, Controlling metal structure with remelting process in direct energy deposition of Inconel 625, CIRP Ann. 67 (2018) 237–240. https://doi.org/https://doi.org/10.1016/j.cirp.2018.04.061.

[102] Y.L. Hu, X. Lin, S.Y. Zhang, Y.M. Jiang, X.F. Lu, H.O. Yang, W.D. Huang, Effect of solution heat treatment on the microstructure and mechanical properties of Inconel 625 superalloy fabricated by laser solid forming, J. Alloys Compd. 767 (2018) 330–344. https://doi.org/https://doi.org/10.1016/j.jallcom.2018.07.087.

[103] G. Puppala, A. Moitra, S. Sathyanarayanan, R. Kaul, G. Sasikala, R.C. Prasad, L.M. Kukreja, Evaluation of fracture toughness and impact toughness of laser rapid manufactured Inconel-625 structures and their co-relation, Mater. Des. 59 (2014) 509–515. https://doi.org/https://doi.org/10.1016/j.matdes.2014.03.013.

[104] J. Tuominen, P. Vuoristo, T. Mäntylä, J. Latokartano, J. Vihinen, P.H. Andersson, Microstructure and corrosion behavior of high power diode laser deposited Inconel 625 coatings, J. Laser Appl. 15 (2003) 55–61. https://doi.org/10.2351/1.1536652.

[105] G.P. Dinda, A.K. Dasgupta, J. Mazumder, Laser aided direct metal deposition of Inconel 625 superalloy: Microstructural evolution and thermal stability, Mater. Sci. Eng. A. 509 (2009) 98–104. https://doi.org/https://doi.org/10.1016/j.msea.2009.01.009.

[106] D. Ma, A.D. Stoica, Z. Wang, A.M. Beese, Crystallographic texture in an additively manufactured nickel-base superalloy, Mater. Sci. Eng. A. 684 (2017) 47–53. https://doi.org/https://doi.org/10.1016/j.msea.2016.12.028.

[107] K. Feng, Y. Chen, P. Deng, Y. Li, H. Zhao, F. Lu, R. Li, J. Huang, Z. Li, Improved high-temperature hardness and wear resistance of Inconel 625 coatings fabricated by laser cladding, J. Mater. Process. Technol. 243 (2017) 82–91. https://doi.org/https://doi.org/10.1016/j.jmatprotec.2016.12.001.

[108] G. Bi, C.-N. Sun, H. Chen, F.L. Ng, C.C.K. Ma, Microstructure and tensile properties of superalloy IN100 fabricated by micro-laser aided additive manufacturing, Mater. Des. 60 (2014) 401–408. https://doi.org/https://doi.org/10.1016/j.matdes.2014.04.020.

[109] J.O. Milewski, P.G. Dickerson, R.B. Nemec, G.K. Lewis, J.C. Fonseca, Application of a manufacturing model for the optimization of additive processing of Inconel alloy 690, J. Mater. Process. Technol. 91 (1999) 18–28. https://doi.org/https://doi.org/10.1016/S0924-0136(98)00412-9.

[110] T. Baldridge, G. Poling, E. Foroozmehr, R. Kovacevic, T. Metz, V. Kadekar, M.C. Gupta, Laser cladding of Inconel 690 on Inconel 600 superalloy for corrosion protection in nuclear applications, Opt. Lasers Eng. 51 (2013) 180–184. https://doi.org/https://doi.org/10.1016/j.optlaseng.2012.08.006.

[111] J.M. Wilson, Y.C. Shin, Microstructure and wear properties of laser-deposited functionally graded Inconel 690 reinforced with TiC, Surf. Coatings Technol. 207 (2012) 517–522. https://doi.org/https://doi.org/10.1016/j.surfcoat.2012.07.058.

[112] M. Zhong, H. Sun, W. Liu, X. Zhu, J. He, Boundary liquation and interface cracking characterization in laser deposition of Inconel 738 on directionally solidified Ni-based superalloy, Scr. Mater. 53 (2005) 159–164. https://doi.org/https://doi.org/10.1016/j.scriptamat.2005.03.047.

[113] J. Xu, X. Lin, P. Guo, Y. Hu, X. Wen, L. Xue, J. Liu, W. Huang, The effect of

preheating on microstructure and mechanical properties of laser solid forming IN-738LC alloy, Mater. Sci. Eng. A. 691 (2017) 71–80. https://doi.org/https://doi.org/10.1016/j.msea.2017.03.046.

[114] J. Li, H.M. Wang, H.B. Tang, Effect of heat treatment on microstructure and mechanical properties of laser melting deposited Ni-base superalloy Rene′41, Mater. Sci. Eng. A. 550 (2012) 97–102. https://doi.org/https://doi.org/10.1016/j.msea.2012.04.037.

[115] J. Li, H.M. Wang, Microstructure and mechanical properties of rapid directionally solidified Ni-base superalloy Rene′41 by laser melting deposition manufacturing, Mater. Sci. Eng. A. 527 (2010) 4823–4829. https://doi.org/https://doi.org/10.1016/j.msea.2010.04.062.

[116] J. Yang, F. Li, Z. Wang, X. Zeng, Cracking behavior and control of Rene 104 superalloy produced by direct laser fabrication, J. Mater. Process. Technol. 225 (2015) 229–239. https://doi.org/https://doi.org/10.1016/j.jmatprotec.2015.06.002.

[117] J. Liang, Y. Liu, J. Li, Y. Zhou, X. Sun, Epitaxial growth and oxidation behavior of an overlay coating on a Ni-base single-crystal superalloy by laser cladding, J. Mater. Sci. Technol. 35 (2019) 344–350. https://doi.org/https://doi.org/10.1016/j.jmst.2018.10.011.

[118] R.J. Moat, A.J. Pinkerton, L. Li, P.J. Withers, M. Preuss, Crystallographic texture and microstructure of pulsed diode laser-deposited Waspaloy, Acta Mater. 57 (2009) 1220–1229. https://doi.org/https://doi.org/10.1016/j.actamat.2008.11.004.

[119] A.J. Pinkerton, M. Karadge, W. Ul Haq Syed, L. Li, Thermal and microstructural aspects of the laser direct metal deposition of waspaloy, J. Laser Appl. 18 (2006) 216–

226. https://doi.org/10.2351/1.2227018.

[120] Mega Mex, Hastelloy® X, (2020).

[121] Haynes International, Our Company History, (n.d.).

[122] Heanjia Super Metal Co. Ltd., Hastelloy X Alloy- Complete Guide, (2015).

[123] B. C.R., R. P.L., C. W.R., S. J.P., L. A., D. J.R., Application of Hastelloy X in Gas-Cooled Reactor Systems, Tennessee, 1976.

[124] F. Wang, X.H. Wu, D. Clark, On direct laser deposited Hastelloy X: dimension, surface finish, microstructure and mechanical properties, Mater. Sci. Technol. 27 (2011) 344–356. https://doi.org/10.1179/026708309X12578491814591.

[125] F. Wang, Mechanical property study on rapid additive layer manufacture Hastelloy® X alloy by selective laser melting technology, Int. J. Adv. Manuf. Technol. 58 (2012) 545–551. https://doi.org/10.1007/s00170-011-3423-2.

[126] D. Tomus, T. Jarvis, X. Wu, J. Mei, P. Rometsch, E. Herny, J.-F. Rideau, S. Vaillant, Controlling the Microstructure of Hastelloy-X Components Manufactured by Selective Laser Melting, Phys. Procedia. 41 (2013) 823–827. https://doi.org/https://doi.org/10.1016/j.phpro.2013.03.154.

[127] N.J. Harrison, I. Todd, K. Mumtaz, Reduction of micro-cracking in nickel superalloys processed by Selective Laser Melting: A fundamental alloy design approach, Acta Mater. 94 (2015) 59–68. https://doi.org/https://doi.org/10.1016/j.actamat.2015.04.035.

[128] T. Etter, K. Kunze, F. Geiger, H. Meidani, Reduction in mechanical anisotropy through high temperature heat treatment of Hastelloy X processed by Selective Laser

Melting (SLM), IOP Conf. Ser. Mater. Sci. Eng. 82 (2015) 12097. https://doi.org/10.1088/1757-899x/82/1/012097.

[129] D. Tomus, Y. Tian, P.A. Rometsch, M. Heilmaier, X. Wu, Influence of post heat treatments on anisotropy of mechanical behaviour and microstructure of Hastelloy-X parts produced by selective laser melting, Mater. Sci. Eng. A. 667 (2016) 42–53. https://doi.org/https://doi.org/10.1016/j.msea.2016.04.086.

[130] D. Tomus, P.A. Rometsch, M. Heilmaier, X. Wu, Effect of minor alloying elements on crack-formation characteristics of Hastelloy-X manufactured by selective laser melting, Addit. Manuf. 16 (2017) 65–72. https://doi.org/https://doi.org/10.1016/j.addma.2017.05.006.

[131] G. Marchese, G. Basile, E. Bassini, A. Aversa, M. Lombardi, D. Ugues, P. Fino, S. Biamino, Study of the microstructure and cracking mechanisms of hastelloy X produced by laser powder bed fusion, 2018. https://doi.org/10.3390/ma11010106.

[132] R. Mertens, S. Dadbakhsh, J. Van Humbeeck, J.-P. Kruth, Application of base plate preheating during selective laser melting, Procedia CIRP. 74 (2018) 5–11. https://doi.org/https://doi.org/10.1016/j.procir.2018.08.002.

[133] Q. Han, R. Mertens, M.L. Montero-Sistiaga, S. Yang, R. Setchi, K. Vanmeensel, B. Van Hooreweder, S.L. Evans, H. Fan, Laser powder bed fusion of Hastelloy X: Effects of hot isostatic pressing and the hot cracking mechanism, Mater. Sci. Eng. A. 732 (2018) 228–239. https://doi.org/https://doi.org/10.1016/j.msea.2018.07.008.

[134] G. Marchese, E. Bassini, A. Aversa, M. Lombardi, D. Ugues, P. Fino, S. Biamino, Microstructural Evolution of Post-Processed Hastelloy X Alloy Fabricated by Laser Powder Bed Fusion, Mater. . 12 (2019). https://doi.org/10.3390/ma12030486.

[135] D. Kong, X. Ni, C. Dong, L. Zhang, J. Yao, C. Man, L. Wang, Anisotropic response in mechanical and corrosion properties of hastelloy X fabricated by selective laser melting, Constr. Build. Mater. 221 (2019) 720–729. https://doi.org/10.1016/j.conbuildmat.2019.06.132.

[136] M.L. Montero-Sistiaga, Z. Liu, L. Bautmans, S. Nardone, G. Ji, J.-P. Kruth, J. Van Humbeeck, K. Vanmeensel, Effect of temperature on the microstructure and tensile properties of micro-crack free hastelloy X produced by selective laser melting, Addit. Manuf. 31 (2020) 100995. https://doi.org/https://doi.org/10.1016/j.addma.2019.100995.

[137] M.L. Montero-Sistiaga, S. Pourbabak, J. Van Humbeeck, D. Schryvers, K. Vanmeensel, Microstructure and mechanical properties of Hastelloy X produced by HP-SLM (high power selective laser melting), Mater. Des. 165 (2019) 107598. https://doi.org/https://doi.org/10.1016/j.matdes.2019.107598.

[138] A. Keshavarzkermani, R. Esmaeilizadeh, U. Ali, P.D. Enrique, Y. Mahmoodkhani, N.Y. Zhou, A. Bonakdar, E. Toyserkani, Controlling mechanical properties of additively manufactured hastelloy X by altering solidification pattern during laser powder-bed fusion, Mater. Sci. Eng. A. 762 (2019) 138081. https://doi.org/https://doi.org/10.1016/j.msea.2019.138081.

[139] R. Esmaeilizadeh, A. Keshavarzkermani, U. Ali, Y. Mahmoodkhani, B. Behravesh, H. Jahed, A. Bonakdar, E. Toyserkani, Customizing mechanical properties of additively manufactured Hastelloy X parts by adjusting laser scanning speed, J. Alloys Compd. 812 (2019) 152097. https://doi.org/10.1016/j.jallcom.2019.152097.

[140] Special Metals Corporation, INCONEL®alloy 718, 2007.

[141] J. A.N., P. C.P., B. S., D. J., N. S.K., K. S., B. K.S., Investigating effects of Solution Treatment on Powder Bed Laser Additive Manufactured Inconel 718, in: Natl. Laser Symp., Bhabha Atomic Research Centre, Mumbai, India., 2017.

[142] V. Kenneth, B. Lucas, M. Karen, C. Tom, POWDER BED FUSION vs. DIRECTED ENERGY DEPOSITION BENCHMARK STUDY: MID-SIZE PART with SIMPLE GEOMETRY, New Mexico, 2018.

[143] M. Pakniat, F.M. Ghaini, M.J. Torkamany, Hot cracking in laser welding of Hastelloy X with pulsed Nd:YAG and continuous wave fiber lasers, Mater. Des. 106 (2016) 177–183. https://doi.org/https://doi.org/10.1016/j.matdes.2016.05.124.

[144] A.K. Nath, C.P. Paul, P. Bhargava, P. Ganesh, T. Reghu, Laser rapid manufacturing at the raja ramanna centre for advanced technology, India, Int. Congr. Appl. Lasers Electro-Optics. 2007 (2007) P530. https://doi.org/10.2351/1.5061201.

[145] P. Ganesh, R. Kaul, C.P. Paul, P. Tiwari, S.K. Rai, R.C. Prasad, L.M. Kukreja, Fatigue and fracture toughness characteristics of laser rapid manufactured Inconel 625 structures, Mater. Sci. Eng. A. 527 (2010) 7490–7497. https://doi.org/https://doi.org/10.1016/j.msea.2010.08.034.

[146] C.P. Paul, A. Jain, P. Ganesh, J. Negi, A.K. Nath, Laser rapid manufacturing of Colmonoy-6 components, Opt. Lasers Eng. 44 (2006) 1096–1109. https://doi.org/https://doi.org/10.1016/j.optlaseng.2005.08.005.

[147] S. Mondal, C.P. Paul, L.M. Kukreja, A. Bandyopadhyay, P.K. Pal, Application of Taguchi-based gray relational analysis for evaluating the optimal laser cladding parameters for AISI1040 steel plane surface, Int. J. Adv. Manuf. Technol. 66 (2013) 91–96. https://doi.org/10.1007/s00170-012-4308-8.

[148] C.P. Paul, S.K. Mishra, C.H. Premsingh, P. Bhargava, P. Tiwari, L.M. Kukreja, Studies on laser rapid manufacturing of cross-thin-walled porous structures of Inconel 625, Int. J. Adv. Manuf. Technol. 61 (2012) 757–770. https://doi.org/10.1007/s00170-011-3742-3.

[149] S. Shiva, I.A. Palani, C.P. Paul, B. Singh, Comparative Investigation on the Effects of Laser Annealing and Laser Shock Peening on the As-Manufactured Ni–Ti Shape Memory Alloy Structures Developed by Laser Additive Manufacturing BT - Application of Lasers in Manufacturing, in: U.S. Dixit, S.N. Joshi, J.P. Davim (Eds.), Springer Singapore, Singapore, 2019: pp. 1–20.

[150] T. Bhardwaj, M. Shukla, N.K. Prasad, C.P. Paul, K.S. Bindra, Direct Laser Deposition-Additive Manufacturing of Ti–15Mo Alloy: Effect of Build Orientation Induced Surface Topography on Corrosion and Bioactivity, Met. Mater. Int. 26 (2020) 1015–1029. https://doi.org/10.1007/s12540-019-00464-3.

[151] K. Benarji, Y. Ravi Kumar, A.N. Jinoop, C.P. Paul, K.S. Bindra, Effect of Heat-Treatment on the Microstructure, Mechanical Properties and Corrosion Behaviour of SS 316 Structures Built by Laser Directed Energy Deposition Based Additive Manufacturing, Met. Mater. Int. (2020). https://doi.org/10.1007/s12540-020-00838-y.

[152] K. Benarji, Y.R. Kumar, C.P. Paul, A.N. Jinoop, K.S. Bindra, Parametric investigation and characterization on SS316 built by laser-assisted directed energy deposition, Proc. Inst. Mech. Eng. Part L J. Mater. Des. Appl. 234 (2019) 452–466. https://doi.org/10.1177/1464420719894718.

[153] T. Bhardwaj, M. Shukla, C.P. Paul, K.S. Bindra, Direct Energy Deposition - Laser Additive Manufacturing of Titanium-Molybdenum alloy: Parametric studies,

microstructure and mechanical properties, J. Alloys Compd. 787 (2019) 1238–1248. https://doi.org/https://doi.org/10.1016/j.jallcom.2019.02.121.

[154] A.A. Siddiqui, A.K. Dubey, C.P. Paul, A study of metallurgy and erosion in laser surface alloying of AlxCu0.5FeNiTi high entropy alloy, Surf. Coatings Technol. 361 (2019) 27–34. https://doi.org/https://doi.org/10.1016/j.surfcoat.2019.01.042.

[155] S. Shiva, I.A. Palani, C.P. Paul, B. Singh, Laser annealing of laser additive–manufactured Ni-Ti structures: An experimental–numerical investigation, Proc. Inst. Mech. Eng. Part B J. Eng. Manuf. 232 (2016) 1054–1067. https://doi.org/10.1177/0954405416661582.

[156] S. Shiva, I.A. Palani, C.P. Paul, S.K. Mishra, B. Singh, Investigations on phase transformation and mechanical characteristics of laser additive manufactured TiNiCu shape memory alloy structures, J. Mater. Process. Technol. 238 (2016) 142–151. https://doi.org/https://doi.org/10.1016/j.jmatprotec.2016.07.012.

[157] T. Yu, J. Sun, W. Qu, Y. Zhao, L. Yang, Influences of z-axis increment and analyses of defects of AISI 316L stainless steel hollow thin-walled cylinder, Int. J. Adv. Manuf. Technol. 97 (2018) 2203–2220. https://doi.org/10.1007/s00170-018-2083-x.

[158] C.P. Paul, S.K. Mishra, A. Kumar, L.M. Kukreja, Laser rapid manufacturing on vertical surfaces: Analytical and experimental studies, Surf. Coatings Technol. 224 (2013) 18–28. https://doi.org/https://doi.org/10.1016/j.surfcoat.2013.02.044.

[159] Y. Huang, M.B. Khamesee, E. Toyserkani, A new physics-based model for laser directed energy deposition (powder-fed additive manufacturing): From single-track to multi-track and multi-layer, Opt. Laser Technol. 109 (2019) 584–599. https://doi.org/https://doi.org/10.1016/j.optlastec.2018.08.015.

[160] K.C. Mills, Ni - Hastelloy-X, in: K.C.B.T.-R.V. of T.P. for S.C.A. Mills (Ed.), Woodhead Publ. Ser. Met. Surf. Eng., Woodhead Publishing, 2002: pp. 175–180. https://doi.org/https://doi.org/10.1533/9781845690144.175.

[161] P. Promoppatum, S.-C. Yao, P.C. Pistorius, A.D. Rollett, A Comprehensive Comparison of the Analytical and Numerical Prediction of the Thermal History and Solidification Microstructure of Inconel 718 Products Made by Laser Powder-Bed Fusion, Engineering. 3 (2017) 685–694. https://doi.org/https://doi.org/10.1016/J.ENG.2017.05.023.

[162] A. Kumar, C.P. Paul, A.K. Pathak, P. Bhargava, L.M. Kukreja, A finer modeling approach for numerically predicting single track geometry in two dimensions during Laser Rapid Manufacturing, Opt. Laser Technol. 44 (2012) 555–565. https://doi.org/https://doi.org/10.1016/j.optlastec.2011.08.026.

[163] A. Kumar, C.P. Paul, A.S. Padiyar, P. Bhargava, G. Mundra, L.M. Kukreja, Numerical Simulation of Laser Rapid Manufacturing of Multi-Layer Thin Wall Using an Improved Mass Addition Approach, Numer. Heat Transf. Part A Appl. 65 (2014) 885–910. https://doi.org/10.1080/10407782.2013.850968.

[164] T. Mukherjee, W. Zhang, T. DebRoy, An improved prediction of residual stresses and distortion in additive manufacturing, Comput. Mater. Sci. 126 (2017) 360–372. https://doi.org/https://doi.org/10.1016/j.commatsci.2016.10.003.

[165] Y.S. Lee, D.F. Farson, Surface tension-powered build dimension control in laser additive manufacturing process, Int. J. Adv. Manuf. Technol. 85 (2016) 1035–1044. https://doi.org/10.1007/s00170-015-7974-5.

[166] Z. Xu, L. Jiang, J. Dong, Z. Li, X. Zhou, The effect of silicon on precipitation and

decomposition behaviors of M6C carbide in a Ni–Mo–Cr superalloy, J. Alloys Compd. 620 (2015) 197–203. https://doi.org/https://doi.org/10.1016/j.jallcom.2014.09.112.

[167] Z. Li, R. Xu, Z. Zhang, I. Kucukkoc, The influence of scan length on fabricating thin-walled components in selective laser melting, Int. J. Mach. Tools Manuf. 126 (2018) 1–12. https://doi.org/https://doi.org/10.1016/j.ijmachtools.2017.11.012.

[168] L. Peng, J. Shengqin, Z. Xiaoyan, H. Qianwu, X. Weihao, Direct laser fabrication of thin-walled metal parts under open-loop control, Int. J. Mach. Tools Manuf. 47 (2007) 996–1002. https://doi.org/https://doi.org/10.1016/j.ijmachtools.2006.06.017.

[169] F. Wang, X. Cheng, G.M. Zheng, X.H. Yang, Q.J. Guo, Q.L. Sun, Study of micromilling parameters and processes for thin wall fabrications, Precis. Eng. 56 (2019) 246–254. https://doi.org/https://doi.org/10.1016/j.precisioneng.2018.12.005.

[170] J. Liu, L. Li, Direct Fabrication of Thin-Wall Parts by Laser Cladding, J. Manuf. Process. 8 (2006) 1–7. https://doi.org/https://doi.org/10.1016/S1526-6125(06)70096-2.

[171] H. Zhang, L. Zhu, P. Xue, Laser direct metal deposition of variable width thin-walled structures in Inconel 718 alloy by coaxial powder feeding, Int. J. Adv. Manuf. Technol. 108 (2020) 821–840. https://doi.org/10.1007/s00170-020-05434-3.

[172] I. Alexander, G. Vladimir, P. Petr, K. Mihail, I. Yuriy, V. Andrey, Machining of Thin-walled Parts Produced by Additive Manufacturing Technologies, Procedia CIRP. 41 (2016) 1023–1026. https://doi.org/https://doi.org/10.1016/j.procir.2015.08.088.

[173] X. Wang, D. Deng, Y. Hu, F. Ning, H. Wang, W. Cong, H. Zhang, Overhang structure and accuracy in laser engineered net shaping of Fe-Cr steel, Opt. Laser Technol. 106 (2018) 357–365. https://doi.org/https://doi.org/10.1016/j.optlastec.2018.04.015.

[174] S. Sun, M. Brandt, M. Easton, 2 - Powder bed fusion processes: An overview, in: M.B.T.-L.A.M. Brandt (Ed.), Woodhead Publ. Ser. Electron. Opt. Mater., Woodhead Publishing, 2017: pp. 55–77. https://doi.org/https://doi.org/10.1016/B978-0-08-100433-3.00002-6.

[175] M. Furukawa, Y. Iwahashi, Z. Horita, M. Nemoto, N.K. Tsenev, R.Z. Valiev, T.G. Langdon, Structural evolution and the Hall-Petch relationship in an Al□Mg□Li□Zr alloy with ultra-fine grain size, Acta Mater. 45 (1997) 4751–4757. https://doi.org/https://doi.org/10.1016/S1359-6454(97)00120-1.

[176] M. Zhang, C. Chen, C. Liu, S. Wang, Study on Porous Mg-Zn-Zr ZK61 Alloys Produced by Laser Additive Manufacturing, Met. . 8 (2018). https://doi.org/10.3390/met8080635.

[177] K. Shah, H. Khurshid, I. ul Haq, S. Anwar, S.A. Shah, Numerical modelling of pulsed and continuous wave direct laser deposition of Ti-6Al-4V and Inconel 718, Int. J. Adv. Manuf. Technol. 95 (2018) 847–860. https://doi.org/10.1007/s00170-017-1224-y.

[178] H. Gedda, Laser Cladding: An Experimental and Theoretical Investigation, PhD Thesis, Luleå Univ. Technol. 2004. (2004) 99.

[179] S. Shiva, N. Yadaiah, I.A. Palani, C.P. Paul, K.S. Bindra, Thermo mechanical analyses and characterizations of TiNiCu shape memory alloy structures developed by laser additive manufacturing, J. Manuf. Process. 48 (2019) 98–109. https://doi.org/https://doi.org/10.1016/j.jmapro.2019.11.003.

[180] Y. Wang, J. Shi, Influence of laser scan speed on micro-segregation in selective laser melting of an iron-carbon alloy: A multi-scale simulation study, Procedia Manuf. 26 (2018) 941–951. https://doi.org/https://doi.org/10.1016/j.promfg.2018.07.121.

[181] Q. Jia, D. Gu, Selective laser melting additive manufacturing of Inconel 718 superalloy parts: Densification, microstructure and properties, J. Alloys Compd. 585 (2014) 713–721. https://doi.org/https://doi.org/10.1016/j.jallcom.2013.09.171.

[182] S. Dryepondt, K. Mike, F.A. List, Microstructure and Properties of Hastelloy X Fabricated by Additive Manufacturing, 2018.

[183] J. Jang, Y. Choi, Y.-H. Lee, D. Kwon, Instrumented microindentation studies on long-term aged materials: work-hardening exponent and yield ratio as new degradation indicators, Mater. Sci. Eng. A. 395 (2005) 295–300. https://doi.org/https://doi.org/10.1016/j.msea.2004.12.033.

[184] R.W. Messler, Principles of Welding, Wiley, 1999. https://doi.org/10.1002/9783527617487.

[185] M.N. Ahsan, C.P. Paul, L.M. Kukreja, A.J. Pinkerton, Porous structures fabrication by continuous and pulsed laser metal deposition for biomedical applications; modelling and experimental investigation, J. Mater. Process. Technol. 211 (2011) 602–609. https://doi.org/https://doi.org/10.1016/j.jmatprotec.2010.11.014.

[186] S. Li, Q. Wei, Y. Shi, Z. Zhu, D. Zhang, Microstructure Characteristics of Inconel 625 Superalloy Manufactured by Selective Laser Melting, J. Mater. Sci. Technol. 31 (2015) 946–952. https://doi.org/https://doi.org/10.1016/j.jmst.2014.09.020.

[187] E. Tochigi, A. Nakamura, N. Shibata, Y. Ikuhara, Dislocation Structures in Low-Angle Grain Boundaries of α-Al2O3, Cryst. . 8 (2018). https://doi.org/10.3390/cryst8030133.

[188] S. Gorsse, C. Hutchinson, M. Gouné, R. Banerjee, Additive manufacturing of metals: a brief review of the characteristic microstructures and properties of steels, Ti-6Al-4V

and high-entropy alloys, Sci. Technol. Adv. Mater. 18 (2017) 584–610. https://doi.org/10.1080/14686996.2017.1361305.

[189] T. Ronneberg, C.M. Davies, P.A. Hooper, Revealing relationships between porosity, microstructure and mechanical properties of laser powder bed fusion 316L stainless steel through heat treatment, Mater. Des. 189 (2020) 108481. https://doi.org/https://doi.org/10.1016/j.matdes.2020.108481.

[190] R.M. Mahamood, E.T. Akinlabi, S. Akinlabi, Laser power and Scanning Speed Influence on the Mechanical Property of Laser Metal Deposited Titanium-Alloy, Lasers Manuf. Mater. Process. 2 (2015) 43–55. https://doi.org/10.1007/s40516-014-0003-y.

[191] Y.L. Hu, Y.L. Li, S.Y. Zhang, X. Lin, Z.H. Wang, W.D. Huang, Effect of solution temperature on static recrystallization and ductility of Inconel 625 superalloy fabricated by directed energy deposition, Mater. Sci. Eng. A. 772 (2020) 138711. https://doi.org/https://doi.org/10.1016/j.msea.2019.138711.

[192] S. Arunkumar, A Review of Indentation Theory, Mater. Today Proc. 5 (2018) 23664–23673. https://doi.org/https://doi.org/10.1016/j.matpr.2018.10.156.

[193] B. AlMangour, J.-M. Yang, Improving the surface quality and mechanical properties by shot-peening of 17-4 stainless steel fabricated by additive manufacturing, Mater. Des. 110 (2016) 914–924. https://doi.org/https://doi.org/10.1016/j.matdes.2016.08.037.

[194] A.N. Jinoop, S.K. Subbu, C.P. Paul, I.A. Palani, Post-processing of Laser Additive Manufactured Inconel 718 Using Laser Shock Peening, Int. J. Precis. Eng. Manuf. 20 (2019) 1621–1628. https://doi.org/10.1007/s12541-019-00147-4.

[195] E. Yasa, J.P. Kruth, J. Deckers, Manufacturing by combining Selective Laser Melting and Selective Laser Erosion/laser re-melting, CIRP Ann. - Manuf. Technol. 60 (2011) 263–266. https://doi.org/10.1016/j.cirp.2011.03.063.

[196] X. Yang, J. Liu, X. Cui, G. Jin, Z. Liu, Y. Chen, X. Feng, Effect of remelting on microstructure and magnetic properties of Fe-Co-based alloys produced by laser additive manufacturing, J. Phys. Chem. Solids. 130 (2019) 210–216. https://doi.org/https://doi.org/10.1016/j.jpcs.2019.03.001.

[197] B. Xin, X. Zhou, G. Cheng, J. Yao, Y. Gong, Microstructure and mechanical properties of thin-wall structure by hybrid laser metal deposition and laser remelting process, Opt. Laser Technol. 127 (2020) 106087. https://doi.org/10.1016/j.optlastec.2020.106087.

[198] Z. Yu, Y. Zheng, J. Chen, C. Wu, J. Xu, H. Lu, C. Yu, Effect of laser remelting processing on microstructure and mechanical properties of 17-4 PH stainless steel during laser direct metal deposition, J. Mater. Process. Technol. 284 (2020) 116738. https://doi.org/10.1016/j.jmatprotec.2020.116738.

[199] D. Matthew J., Donachie, Stephen J., Superalloys: A Technical Guide, Second Edi, ASM International, Cleveland, 2002.

[200] K. Wei, M. Lv, X. Zeng, Z. Xiao, G. Huang, M. Liu, J. Deng, Effect of laser remelting on deposition quality, residual stress, microstructure, and mechanical property of selective laser melting processed Ti-5Al-2.5Sn alloy, Mater. Charact. 150 (2019) 67–77. https://doi.org/10.1016/j.matchar.2019.02.010.

[201] B. Sundén, J. Fu, Chapter 6 - Aerospace Heat Exchangers, in: B. Sundén, J.B.T.-H.T. in A.A. Fu (Eds.), Academic Press, 2017: pp. 89–115.

https://doi.org/https://doi.org/10.1016/B978-0-12-809760-1.00006-5.

[202] D. Southall, R. Le Pierres, S.J. Dewson, Design considerations for compact heat exchangers, Int. Conf. Adv. Nucl. Power Plants, ICAPP 2008. 3 (2008) 1953–1968.

Thesis Highlight

Name of the Student: Jinoop A N

Name of the CI/OCC: Raja Ramanna Centre for Advanced Technology, Indore.

Enrolment No.: ENGG03201604001

Thesis Title: Experimental Studies and Parametric Investigation on Laser Directed Energy Deposition based Additive Manufacturing of Hastelloy-X Thin Walls and Bulk Structures

Discipline: Engineering Sciences **Sub-Area of Discipline: Mechanical Engineering**

Date of viva voce: 25th May 2021

Laser Additive Manufacturing (LAM) is one of the advanced manufacturing technologies witnessing a rising demand in aerospace and power sector to build high-performance components subjected to extreme duty conditions. Hastelloy-X (Hast-X) is one of the nickel-based superalloys suitable for high-temperature applications due to the appropriate blend of high-temperature strength, toughness and resistance to degradation in a corrosive or oxidizing environment. Laser Directed Energy Deposition (LDED) based LAM has potential for building Hast-X components used in aerospace and power sector. The present thesis is focused on the engagement of the versatile LDED to build defect free Hast-X thin-wall and bulk structures, and comprehensively investigate their behavior at different process and service conditions experimentally.

The present research work comprehends and contributes to the existing understanding on the LDED of Hast-X structures from single tracks to multiple overlapped multi-layer tracks under different process conditions yielding thin walls and bulk structures in terms of processing, geometry, microstructural and mechanical characteristics. The quality of deposition (cracking, continuity, surface quality and porosity) and properties (geometric, microstructural and mechanical) can be tailored by varying the process parameters. A simple analytical is developed for faster predictions of track geometry at various processing parameters and finite element based numerical tool is deployed to get the process insight. The obtained theoretical results find good match with the experimental results. The investigated mechanical properties of LDED built Hast-X structures are found to be higher than conventionally build Hast-X structures. The microstructures are found to be non-homogenous with finer grain size. It is found that in-situ treatment , i.e. Sequential Layer by Layer Remelting (SLLR) can improve the density and surface finish of the built components and ex-situ treatments such as solution treatment can aid to achieve homogenization and properties close to conventional components. One of the potential applications of Hast-X is the development of Printed Circuit Heat Exchanger (PCHE), generally used in advanced power sectors. A protoype PCHE is build as shown in Figure 1 using LDED by deploying straight walls, overhang walls and bulk structures to demonstrate the process capabilty. The acquired know-how from the above comprehensive studies in single tracks, wall structures and bulk structures is used for building the PCHE.

Figure 1. Photographic view of LDED built Printed Circuit Heat Exchanger of size 200 mm x 200 mm x 170 mm.